UNIVERSITÀ DI PARMA

UNIVERSITÀ DEGLI STUDI DI PARMA

DOTTORATO DI RICERCA IN FISICA

XXXVI CICLO

Looking for non-standard cosmologies: the critical role of numerical tools

---

Coordinatore:
Chiar.mo Prof. Stefano Carretta
Tutore:
Chiar.mo Prof. Guido D'Amico

Dottorando:
Lorenzo Piga

Anni accademici 2020/2021-2022/2023

Home is behind, the world ahead,
And there are many paths to tread
Through shadows to the edge of night,
Until the stars are all alight.

J.R.R. Tolkien, *A Walking Song*

Acknowledgments

These last three years have been full of many emotions and challenges for me. I am deeply conscious that it would have not been the same without the people I met and those that have always been there for me.

I am truly thankful to my supervisor, Guido. My formation as a scientist would have not been the same without such an example and lead. Most of all, I have truly appreciated the independence and guidance offered to me. I am also grateful for the detailed comments on this manuscript, which have greatly improved its quality.

I am forever in debt with Riccardo, that many years ago has shown me the beauty of Cosmology. His encouragement and his ideas have been a powerful pull to make it through this PhD.

I promised to Marco a special mention in this thesis. His friendship and his collaboration were sincerely the cornerstone of these years of PhD. I enjoyed his way of working and living the life, and the many serious (but, honestly, mostly fun!) discussions we had. I hope we will continue working together in the following years!

Of course, special thanks to both Massimo and Filippo, for welcoming me with kindness and respect. I have learnt a lot from their experience and their way of doing research and I hope to continue working together in the future.

During these last years I collaborated with many different groups and researchers. I have learnt a lot from every of them and I would like to them all: Nicola Bellomo, Valentì Bosch-Ramòn, Ben Bose, Luciano Burderi, Melita Carbone, Deanna C. Hooper, Matteo Lucca, Sabino Matarrese, Chiara Moretti, Vivian Poulin, Nils Schönberg, Alvise Raccanelli, Licia Verde, Matteo Viel and Bill Wright.

The periods I've spent abroad and the PhD schools were moments I particularly enjoyed

during my PhD. I have met a lot of people I want to remember: Arsalam Alam, Marco Bonici, Marina Cagliari, Alessandro Carones, Javier Carrón Duque, Alba Kalaja. Even though I can't list them all here, each one of my AstroMundus friends knows how much I care for and miss them.

I want to thank the University of Parma and the INFN for providing me the great opportunity to pursue my research and to participate at many workshops and conferences. Most of the analyses were performed on the HPC (High Performance Computing) facility of the University of Parma, whose support team I want also to thank.

I am also particularly grateful to Francisco Villaescusa-Navarro and to the CCA. The time spent in New York has been one of the best in my life and I could never forget that.

I am so grateful to all my friends, who, to my great fortune, are too numerous to mention one by one. I will be eternally grateful for the support and love!

Thank you Mamma, Papà and Giuse. Your love and support is everything for me. Thank you zia Tetta, for all the spoons of honey. Thanks to Laura's family, who has warmly welcome and supported me in all these years. Thanks to all of my family, that is extended well beyond the simple blood relationship. You all are the family I have chosen.

Finally, thank you Laura. I cannot write much because I know you'll start blushing, but I loved having you with me during this adventure. I cannot wait for all the others to come!

Contents

Articles and copyright permissions

The results of this thesis have produced two papers:

1. **L. Piga**, M. Marinucci, G. D'Amico, M. Pietroni, F. Vernizzi, B. S. Wright
   "Constraints on modified gravity from the BOSS galaxy survey"
   JCAP (2022), DOI: https://doi.org/10.1088/1475-7516/2023/04/038

2. **L. Piga**, M. Lucca, N. Bellomo, V. Bosch-Ramon, S. Matarrese, A. Raccanelli, L. Verde
   "The effect of outflows on CMB bounds from Primordial Black Hole accretion"
   JCAP (2022), DOI: https://doi.org/10.1088/1475-7516/2022/12/016

The papers were published on the Journal of Cosmology and Astrophysics (JCAP). As author of the article I have the permission to use them or a portion of them in my thesis or dissertation, as specified by the IOP's Author rights policy, that can be found here.

Chapter 1

Introduction

1.1 The ΛCDM model

The attempt to understand the universe has led to the formulation of the current standard cosmological model, known as the Λ-Cold Dark Matter model (hereafter ΛCDM).

The cosmos seems to possess structures on dimensions up to several tens of Mpc, but the data strongly supports isotropy and homogeneity at larger scales. This can be regarded as the primary evidence for the Cosmological Principle: on vast scales, the universe manifests as both homogeneous and isotropic, thus presenting the same characteristics to any observer at a specific cosmic moment. As a consequence, on cosmological scales, the distribution of matter in the universe is both homogeneous and isotropic. Looking for a solution to Einstein's field equations with these symmetries, we get the Friedmann-Robertson-Walker (FRW) metric, which predicts the expansion of the Universe.

While on smaller scales the universe manifests as non-uniform, these postulates are corroborated on larger and intermediary scales from evidences such as the Cosmic Microwave Background (CMB), galaxy clusters, and observations in the radio and X-ray spectra among others [1]. The CMB radiation is emblematic of an almost perfect black body radiation, populated by photons with a mean temperature given by $T_{\mathrm{CMB}} \approx 2.7\,\mathrm{K}$. This radiation is a relic of the early phases of the universe when it was opaque to radiation. As the universe became transparent during the hydrogen recombination epoch, approximately $380,000$ years after to the Big Bang, these photons could stream freely and we observe them at the present time. An

experimental proof of universe's predominant isotropy and homogeneity are the little relative temperature variations ($\frac{\delta T}{T} \approx 10^{-5}$) that can be found uniformly across the sky.

The constituents contributing to the matter-energy composition of the universe are primarily five. The amount of a particular species can be quantified via the abundance parameter $\Omega \equiv \frac{\rho}{\rho_c}$, where ρ represents the density of the species in question, and ρ_c denotes the critical density. As postulated in the ΛCDM model, the current constitution of our universe is:

- Baryonic Matter ($\Omega_b \simeq 0.05$): this is the ordinary matter composed of electrons, protons, and neutrons.

- Cold Dark Matter ($\Omega_{cdm} \simeq 0.26$): this represents a portion of matter whose composition remains elusive, potentially including non-baryonic elements. It does not interact with radiation, hence its designation as "dark". The adjective "cold" comes from the understanding that this matter decoupled from other components when its constituent particles were non-relativistic.

- Dark Energy ($\Omega_\Lambda \simeq 0.69$): this component was introduced to explain the observed accelerated expansion of the universe, evidence for which can be derived from Type Ia Supernovae observations. In General Relativity, dark energy corresponds to the cosmological constant (Λ) postulated by Einstein.

- Radiation ($\Omega_r \simeq 10^{-5}$): the radiation fraction of the universe, mainly photons, offers a minor contribution to today's overall energy.

- Neutrinos: in the early universe, neutrinos were highly relativistic and contributed to the radiation density. However, as the universe expanded and cooled, neutrinos decoupled from other particles and became non-relativistic. Their free-streaming nature can suppress the growth of matter fluctuations on small scales, leaving small imprints in the large scale structure. The impact of neutrinos on the CMB anisotropies and matter power spectrum makes them a target of precision cosmology.

According to the ΛCDM model, roughly 26% of the universe's total mass-energy content is thought to be dark matter. This constituent was historically proposed to reconcile observations

related to galaxy velocity curves. The luminous mass density in a spiral galaxy diminishes as one progresses from its center to its outer periphery. Consequently, based on Kepler's second law, one would anticipate the rotational velocities of stars orbiting the galaxy's center to decrease as their distance from the center increases. However, the predicted velocity curve diverges from the observed data. Experimental results show that the rotation curves of spiral galaxies maintain a flat trajectory well beyond zones dominated by luminous matter [2, 3]. This discrepancy is resolved by theorizing that spiral galaxies are surrounded by large dark matter halos. The mass of these halos is presumed to range between 3 to 10 times the mass associated with a galaxy's luminous segment.

Further indications of dark matter's presence in the universe come from galaxy clusters analyses. Within these clusters, the gravitational mass responsible for keeping galaxies in their orbits is inconsistent with the luminous mass. This discordance suggests the necessity for an additional, dark matter component. Another piece of evidence comes from weak gravitational lensing observations. In the absence of dark matter, the power spectrum associated with temperature anisotropies in the CMB would manifest a different structural composition. Finally, a critical proof for the existence of dark matter comes from the fact that the universe's structures could form by today. In fact, up to recombination, if the matter were only baryonic, radiation pressure would smooth out density fluctuations and gravitational potentials. Since dark matter remains inert to radiation, it could establish the gravitational potential wells, starting from long before recombination. In such a way, gravitational potentials were deep enough during the dark ages for gas cooling and condensation, ending in the genesis of galaxies.

The second ingredient in our understanding of the universe is the evidence for its expansion. This expansionary hypothesis was first theoretically proposed by Friedmann in 1922. It was later highlighted in 1927 by Lemaitre and subsequently in 1929 by Hubble, who used the period-luminosity correlation pertaining to Cepheid variables discovered by Leavitt in 1908. Their collective observations established a direct proportional relationship between an object's (proper) distance D and its velocity along the line of sight (LOS) denoted as v. This relationship shows that the universe is in a state of expansion, such that objects positioned farther away from us recede at a more rapid velocity. Such observations were included into the formulation

of the Hubble(-Lemaitre) law:

$$v = H_0 D \tag{1.1}$$

where H_0 is the proportionality constant between distance and speed, also known as Hubble(-Lemaitre) constant. The Hubble parameter is often parameterized in terms of its dimensionless equivalent

$$h = \frac{H_0}{100\,\mathrm{km/(s\,Mpc)}} \tag{1.2}$$

The cosmological constant Λ is a component with constant energy density, at first introduced by Einstein. Originally, it was meant to describe a static universe solution in General Relativity, which is however unstable. Recently, the cosmological constant has been reintroduced to describe cosmological dynamics. This was mainly based on observations of high-redshift Type-1A supernovae, which are standardizable candles in cosmology. The Hubble diagram derived from these supernovae observations shows inferred absolute luminosities decreasing with the redshift. This would suggest an acceleration in the Hubble expansion, counter to the intuitive deceleration induced by self-gravity. In order to reconcile observations with an accelerating expansion, one needs a positive cosmological constant.

In the epoch characterized by matter's dominance, cosmic structures, like galaxy clusters, materialized as a consequence of gravitational instability. In later cosmic epochs, roughly around $z \sim O(0.5)$, the prevailing influence shifted towards the dark energy, represented by Λ. This transition is the driving force behind the universe's ongoing phase of accelerated expansion.

1.1.1 The inflationary universe

The standard narrative of the universe's history is filled with numerous challenges. One of the most important is the observed uniformity and flatness of the universe: we need to understand why and how the cosmos is so homogeneous, isotropic, and flat. A universe with only radiation cannot smooth out perturbations, making it difficult to understand how different regions of

the universe appear causally connected. This link is shown by the uniform temperature of the cosmic microwave background (CMB) radiation observed from every direction in the sky.

Another problem lies in the measured curvature of the universe. The fact that its value is so close to zero suggests a fine-tuning that is not easily justifiable without some underlying reason.

Additionally, numerous advanced theoretical models, such as Grand Unified Theories (GUTs) and string theory, predict phenomena like domain walls, cosmic strings, and magnetic monopoles — yet these remain absent from our observations.

According to the ΛCDM model, a potential resolution to these fine-tuning dilemmas is an early period of accelerated cosmic expansion. This inflationary phase could ensure causal connectivity across the universe and effectively "reset" any initial conditions that would clash with current observations, reconciling theory with our data. The idea is that during the early stages of the universe, the expansion of the universe was driven by a scalar field named the *inflaton*. The quantum perturbations linked to this inflaton field acted as seeds, giving rise to density variations. After this inflationary phase, the inflaton experienced decay, filling the universe with relativistic particles. This event is known as the *reheating* process, subsequent to which the traditional *hot big bang* epoch was inaugurated.

1.2 Beyond ΛCDM

Besides a few tensions in the data currently under discussion (see e. g. in [4]), the ΛCDM model is in good agreement with a large number of observations. These range from measurements associated with the late-time accelerated expansion gleaned from type Ia Supernovae [5, 6], to the anisotropies in the cosmic microwave background (CMB) [7, 8, 9], and extending to the baryon acoustic oscillations (BAO) evident in galaxy distribution studies [10, 11]. Due to its exceptionally precise predictive capabilities across a spectrum of observables - be it the CMB radiation or the genesis and evolution of large cosmic structures [12, 13, 14] - provided with a limited number of parameters, the ΛCDM model has firmly established itself as the reigning cosmological paradigm.

Nevertheless, the phenomenological ΛCDM model does not provide any fundamental ex-

planation for the nature of its dark components, i.e., cold dark Matter and dark energy, despite the fact that they make up for the vast majority of the energy density of the universe today. Therefore, in order to find an origin for these fundamental, yet elusive, components of the universe, proposals suggesting physics beyond the ΛCDM model are frequently presented.

The nature of dark matter is still unknown and many are the proposed candidates, such as baryonic candidates involving neutral hydrogen gas and massive compact halo objects (MACHOs) [15], which are however in strong disagreement with observations, or non-baryonic candidates that invoke hypothetical particles such as axions [16], sterile neutrinos [17], weakly interacting massive particles (WIMPs) [18], gravitationally-interacting massive particles (GIMPs) [19], or supersymmetric particles [20]. Nonetheless, these possibilities have found no experimental evidence so far.

A promising candidate for dark matter is represented by Primordial Black Holes (PBHs): this possibility have regained interest in recent years [21, 22, 23] after the first LIGO detection of a Gravitational Wave (GW) signal emitted from a binary BH merger [24].

Generally DM candidates are classified based on their mass. Within this framework, DM models extend across a vast range, from ultra-light axion-like entities to macroscopic compact structures such as BHs. In this work we focused on PBHs possessing masses exceeding $1\ M_{\odot}$. These PBHs are of interest due to their potential detectability by present and upcoming GW observatories.

With this perspective, we explored additional constraints on the PBH abundance within this mass range, especially focusing on bounds from matter accretion into a PBH. The consequent radiation emission from the accretion activity modulates the universe's thermal evolution, delaying recombination and altering reionization. As a consequence this can be constrained with CMB data. Nevertheless, the theoretical modeling of accretion is accompanied by significant uncertainties, leading to considerable margins of error in the final constraints. The geometry of accretion and the ionization model, which defines the local temperature gradient near the BH, are examples of these sources of uncertainty.

In our study [25], we have devised an accretion model that incorporates the influence of outflows, particularly focusing on their impacts on the universe's thermal history and on the

CMB anisotropies. We focused on various accretion geometries, ionization mechanisms and PBH mass distributions. The main result is that the large theoretical uncertainties underlying the modelling of the outflows significantly enlarge those already present due to the other variables. This causes the upper limits on the PBH mass to be large, lying between roughly 0.01 to 100 $M_\odot$ (under the assumption that PBHs constitute the entirety of DM), contingent on the selected accretion and outflow models. Such fluctuations have strong implications for the observational window of LVK. Our results justify the need for a more comprehensive and rigorous modeling approach to PBH accretion, necessary to explore the possibility of PBHs as DM candidates and potential sources of LVK detected occurrences [25].

The lack of a deep understanding of the fundamental nature of dark energy leaves also open the possibility of alternative scenarios, such as for instance modified gravity models; see e.g. [26]. Nevertheless, the cosmological constant remains a problem which revolves around the discrepancy between the observed value of the cosmological constant (or dark energy) and its "natural" value. Despite a plethora of modified gravity theories introduced over the past decades, none have provided a satisfactory resolution to this issue. In fact, while these theories can successfully reproduce the observed expansion history of the universe and can explain the acceleration without the need for a cosmological constant, they often introduce other naturalness or fine-tuning problems. These complications can arise from the additional degrees of freedom or the specific functional forms introduced to modify the gravitational action.

In the realm of cosmological theories that go beyond the standard ΛCDM model, certain scenarios maintain scale-independent linear growth: this includes, but is not limited to, Jordan-Brans-Dicke theories [27], scalar-tensor theories with scalar fields having horizon-sized Compton wavelengths, and clustering quintessence models [28, 29]. Other models that fit within this framework are the EFT of dark energy beyond the linear regime [30, 31, 32], dark scattering paradigms [33], and k-mouflage models [34, 35, 36, 37].

The *normal branch* of the Dvali, Gabadadze, and Porrati (nDGP) model and the Effective Field Theory (EFT) for dark energy beyond a linear approach stand out as notable examples. These frameworks introduce additional nonlinear interactions. The nDGP model proposes

that our universe is a four-dimensional brane within a five-dimensional Minkowski space. This implies that gravity functions in five dimensions on broader scales and shifts to a four-dimensional force in line with General Relativity (GR) on more smaller scales. The transition between these is identified by the crossover scale r_c, which is determined by the ratio of the gravitational constants in five and four dimensions.

As explored in the following sections, in this analysis we deduce $\Omega_{\rm rc} \leq 0.65$ at the 95% C.L. [38] using the BOSS dataset. This constraint is achieved by fixing the primordial amplitude of fluctuations A_s to values coming from Planck's measurements.

These constraint is dependent from the selection of a prior for the $\Omega_{\rm rc}$ parameter. To generalize our results, we also provided a prior-independent constraint on the nDGP parameter utilizing the Bayes factor [39]. This methodology proves advantageous when constraining parameters exhibiting non-Gaussian posteriors. Employing this technique, we deduce an upper limit of $\Omega_{\rm rc} \leq 0.2$ at the 95% C.L..

Even though our analysis [38] primarily focuses on the nDGP model, a direct expansion to other scale-independent models is possible. For instance, models described by the comprehensive single-field framework of the EFT of dark energy [40, 41, 42, 43, 44] and further extrapolated beyond linear order [31, 30]. This method allows for improved constraints on various dark energy and modified gravity theories by combining Planck data with forthcoming surveys. Upcoming research is projected to cover wider regions and capture more galaxies compared to SDSS-III.

Moving ahead in the direction of using different sources to test beyond-ΛCDM models, we can focus on the so-called Inter-Galactic Medium (IGM). The primary observable manifestation of the IGM is the Lyman-α forest, an excellent tracer of the underlying DM distribution [45, 46, 47]. As such, it has been fundamental in setting tight constraints on various non-standard DM (NSDM) models, including thermal warm DM (WDM) [48], axion-like particles [49], (self-)interacting DM [50], and PBHs [51].

The central physical observable in Lyman-α forest analyses is the flux power spectrum, which is influenced by both astrophysical and cosmological factors. However, establishing the relationship between the parameters characterizing the astrophysical and cosmological

model, and the expected Lyman-α flux is highly intricate. Typically, the alternative DM models mentioned above can be constrained by the deviation from the ΛCDM linear matter power spectrum at small scales. This phenomenological parameterization captures the small-scale deviations induced by a wide range of models [52].

Also a broad range of alternative DM models exhibit the same asymptotic behavior as the ΛCDM model on intermediate and large scales, rendering their small-scale characteristics largely independent of the underlying parameters. Even in a purely ΛCDM analysis, Lyman-α data can provide valuable insights into long-standing discrepancies between early- and late-universe estimates of cosmological parameters [53], offering independent measurements of the amplitude of the linear perturbations, smoothed on a $8\,\mathrm{Mpc}/h$ scale, parametrized by the σ_8 parameter and the primordial spectral index, denoted as n_s.

In our work, one of our primary goals is to introduce a dynamic and efficient tool that facilitates the evaluation of diverse alternative cosmological frameworks using a combined set of Lyman-α forest data. This data originates from both intermediate and high-resolution surveys, spanning a redshift range $3.0 \leq z \leq 5.4$ and encompasses various IGM thermal histories. These results are accomplished thanks to an innovative collection of N-Body hydrodynamic simulations. Additionally, we have designed a new interpolation scheme, enhanced with Machine Learning (ML) techniques. This approach surpasses previous methods in terms of precision, theoretical model diversity, and the assimilation of supplementary data.

1.3 Numerical tools for beyond-ΛCDM cosmologies

The synergy between theoretical models and observational data is essential in the scientific process. The goal is to identify which theories match the observed data. In cosmology, as models and observational methods have become more complex, there has been a need for advanced tools for accurate comparisons. Looking ahead to the next decade in cosmology, with expected vast data from current and future surveys, there is a push to develop quicker, more accurate codes and enhance data sampling.

At this stage, the constraints might arise more from the limitations of statistical and data-driven methodologies than from the data itself. Modern computational codes, particularly

those based on Bayesian statistics and machine learning techniques, are emerging as valuable tools for cosmological research.

In this thesis we explore the role played by these numerical tools and how they can contribute to find answers to the most fundamental questions that still remain in cosmology.

1.3.1 CLASS

The Cosmic Linear Anisotropy Solving System, hereafter CLASS [54, 55], is a Boltzmann solver that can be generalized to non-minimal cosmological models. A Boltzmann solver is a computational tool used to solve the Boltzmann equation for the evolution of cosmic perturbations in the universe. These solvers play a crucial role in modern cosmology by allowing theorists to compute the theoretical predictions of various cosmological models and then compare them with observations, especially the temperature and polarization anisotropies in the Cosmic Microwave Background (CMB) and the distribution of galaxies in large-scale structure surveys. All the relevant cosmological quantities for this thesis, such as the CMB power spectra, are computed employing the latest version (v. 3.2) of the CLASS code [56].

In particular, exploring the effects of outflows on accretion of PBHs, we make use of the energy injection treatment discussed in ref. [57], which is largely based on the ExoCLASS extension of CLASS [58]. Recombination is solved using the HYREC [59, 60] implementation of CLASS, while the energy injection and deposition process is computed using the prescriptions detailed in section 2.4.

1.3.2 PyBird

In this section we introduce the code used to get constraints on different cosmological models, like LCDM or the nDGP modified gravity model. `PyBird` [61] is a code[1] based on Refs. [62, 63], written in Python. The program is developed for the computation computation of the power spectrum and correlation function of matter and biased tracers in real and redshift space.

The theoretical model is built on the EFTofLSS and a perturbative bias expansion presented

[1] See here for the public GitHub repository.

explicitly in [62, 63], and generalized in [64] to go beyond EdS approximation. For a rapid evaluation, the loop integrals (and the resummation integrals) are computed using the FFTLog method [65]. See [66, 67, 68] for other publicly available codes based on the EFTofLSS.

PyBird has been crafted for efficient power spectrum evaluation, easily adaptable within data analysis pipelines. It operates independently, primarily relying on the linear matter power spectrum, which can be sourced from Boltzmann solvers like CAMB [69] or CLASS [54, 55]. PyBird's structure is modular, allowing for straightforward adjustments for various tasks, including two-loop power spectrum or bispectrum calculations.

1.3.3 Optimized Kriging

In this work we also utilize measurements of the power spectrum of the Lyman-α forest, derived from two distinct QSO spectral samples, the XQ-100 and the combined MIKE/HIRES datasets. To exploit these data, we built a newly interpolation scheme to be used for Bayesian inference, enhancing the interpolation method used in prior studies, specifically the Ordinary Kriging method [70, 71, 72, 73]. The interpolation process involves calculating optimal weights, which are then used to predict ratios of flux power spectra with respect to a given fiducial model. This improvement is accomplished through the integration of machine learning techniques, as elaborated in Section 5.1.3. Furthermore, we have built a grid of simulations to encompass a finer and more extensive range of mean transmitted flux values, denoted as $\bar{F}(z)$. This expansion serves to further reduce the theoretical errors associated with our newly developed Optimized Kriging method.

To determine the optimal values for the hyperparameters, we employ a machine learning-based optimization process. The primary goal is to minimize the average relative error in theoretical predictions. To accomplish this, we leverage the Optuna package [74] coupled with a *Tree of Parzen Estimator* (TPE) sampler [75, 76] to select the most suitable hyperparameter values.

1.4 Outline of this work

The thesis is structured as follows.

Chapter 2 presents the impact of outflows on Primordial Black Hole accretion and, subsequently, on the constraints for these objects to constitute a relevant fraction of DM. We obtain constraints on the PBH abundance from CMB data, considering different accretion patterns, ionization models, and mass distributions. We also account for both mechanical feedback and non-thermal emissions from outflows. Our results indicate that these outflows add uncertainty when determining cosmological limits on the PBH abundance. This is especially relevant for observations in the LIGO-Virgo-KAGRA range.

In chapter 3 we introduce briefly the EFTofLSS and the nDGP model and present the novel implementation of this model within the public code PyBird [61], which will be used for MCMC analysis. We evaluate our pipeline using synthetic and simulated data to identify potential biases in the extracted cosmological parameters from marginalization and theoretical errors. Our application to the normal branch of the DGP model with a ΛCDM background reveals a strong degeneracy between the nDGP parameter $\Omega_{\rm rc}$ and the primordial fluctuation amplitude A_s, leading to biased posteriors.

In chapter 4 we study the extraction of cosmological parameters for beyond ΛCDM models using simulated CDM halos mocks, in preparation for the future analysis of space satellite missions like *Euclid* [77]. These surveys offer an unprecedented opportunity to rigorously test cosmological models [77, 78, 79]. The analysis is performed with Markov-Chain Monte-Carlo techniques and is conducted using the `PyBird` software, using the EFTofLSS as our theoretical framework.

In chapter 5 we present a newly developed interpolation scheme refined with ML techniques, to test a variety of alternative cosmological models with a joint set of Lyman-α forest data. This advanced tool could help us to assess various alternate cosmological models using a combined Lyman-α forest dataset from both intermediate and high-resolution surveys, covering different IGM thermal histories.

We conclude in chapter 6 with some remarks and possible future developments of this research.

Chapter 2

Primordial Black Holes Accretion

Should Primordial Black Holes (PBHs) exist in nature, they would inevitably accrete baryonic matter in their vicinity. In turn, the consequent emission of high-energy radiation could affect the thermal history of the universe to an extent that can be probed with a number of cosmological observables such as the Cosmic Microwave Background (CMB) anisotropies. However, our understanding of the accretion and radiation emission processes in the context of PBHs is still in its infancy, and very large theoretical uncertainties affect the resulting constraints on the PBH abundance. Building on state-of-the-art literature, in this chapter we take a step towards the development of a more realistic picture of PBH accretion by accounting for the contribution of outflows. Specifically, we derive CMB-driven constraints on the PBH abundance for various accretion geometries, ionization models and mass distributions in absence and in presence of mechanical feedback and non-thermal emissions due to the outflows. As a result, we show that the presence of such outflows introduces an additional layer of uncertainty that needs to be taken into account when quoting cosmological constraints on the PBH abundance, with important consequences in particular in the LIGO-Virgo-KAGRA observational window.

The chapter is organized as follows. In section 2.1 we briefly introduce the generalities of PBH and in 2.2 we describe the mechanism of accretion and outline the current status of the field, while in section 2.3 we present the outflow model considered here in its details, adopting and extending the main results of [80, 81]. In section 2.4 we succinctly explain how the accretion process affects the thermal history of the universe. In section 2.5 we discuss the nu-

merical implementation of the accretion models, while in section 2.6 we calculate the resulting CMB anisotropy constraints for monochromatic and extended PBH mass functions, and discuss their implications for the LVK observed mass range. Finally, we conclude in section 2.7 with a summary of our analysis and closing remarks.

2.1 Primordial Black Holes framework

PBHs are BHs that formed in the very early universe, much before the appearance of the first stars. Their existence was first suggested in the late '60s [82, 83, 84, 85] and they have since become one of the most popular candidates to make up for at least a fraction of the total DM content of the universe (see, e.g., refs. [86, 87, 88, 89] for recent reviews). Moreover it has been suggested that PBHs could also be the seeds for the formation of intermediate mass [90] as well as super massive [91, 92] BHs, which are believed to reside at the center of most galaxies. Other *observational conundra* that are possibly solved by the potential presence of PBHs are discussed in refs. [93, 88].

Despite these arguments in support of the presence of PBHs, many of their properties, such as their formation mechanism, abundance or mass distribution, are still unknown [88, 93, 94]. As a consequence, existing constraints on the PBH abundance heavily rely on assumptions about the BH phenomenology. For instance, it is well known that PBHs, if existing, would inevitably accrete matter and convert a fraction of the energy released by the accretion into radiation. The resulting injection of high-energy photons into the cosmological photon bath would then affect the thermal history of the universe and, thus, observables that depend upon it, such as the CMB anisotropies. However, the impact of this energy injection on the CMB varies depending on the details of the accretion and energy injection mechanisms considered, for instance on the assumed geometry of the accretion [95, 96, 97], or on the properties of the environment surrounding the PBH [98, 99]. Furthermore, the potential presence of magnetic fields and/or the excess of thermal energy in part of the accreted matter might lead to the formation of outflows, like winds or jets. Such outflows are expected to dilute the medium surrounding the BH reducing the total amount of accreted material, effect known as mechanical feedback (MF), and to be potential accelerators of non-thermal particles ca-

pable to effectively boost the total luminosity of the BH [100, 101, 102, 80, 81]. Overall, the resulting CMB constraints on the PBH abundance cover approximately the $\mathcal{O}(1 - 10^4)\ M_\odot$ mass range, with vastly different outcomes depending on the accretion and emission mechanisms [96, 103, 97, 99]. These CMB anisotropy constraints are also complemented by bounds derived from CMB spectral distortions [96], galactic emission [104, 105, 106], interstellar gas heating [107], and the 21-cm line [108, 109, 110].

Yet, an accurate modelling of the accretion mechanism is fundamental to test the consistency between cosmological constraints and astrophysical hints in support of the PBH hypothesis. In fact, the range of PBH masses that would explain the origin of the LIGO-Virgo-KAGRA (LVK) observations lays between 1 and 100 $M_\odot$ [111, 112, 113], which is precisely the region of parameter space of relevance for CMB anisotropy constraints on matter accretion onto PBHs depending on the underlying assumptions of the accretion process [96, 97] (see, e.g., figure 2 of ref. [93] for a graphical representation).

Currently, the two most popular models of accretion mechanism onto a PBH assume spherical [114, 96] or disk [97] accretion, with the latter leading to a significantly higher radiation luminosity than the former, hence to more stringent bounds. Similarly, also the type of ionization mechanism at play in the vicinity of the PBH has been shown to be able to affect the radiation luminosity by orders of magnitude [96]. However, in previous analysis the contribution from potentially present outflows has been neglected and it is therefore possible that their inclusion might alter the aforementioned conclusions. For instance, it is *a priori* unclear whether the dominant effect of the outflows is the reduction of the accretion rate via MF or the enhancement of the radiation luminosity due to the non-thermal emission of photons. The relative importance of these effects is very likely to depend not only on the PBH mass, but also on other assumptions regarding the geometry of the accretion, the ionization model and the characteristics of the outflows.

In this chapter we investigate these open questions by constructing an accretion model that accounts for both MF and non-thermal outflows, building on the analysis previously carried out in refs. [80, 81]. We then study their impact on the thermal history of the universe and the CMB anisotropies in the context of both accretion geometries and ionization models, as well as for various PBH mass distributions. As a result, we find that the large theoretical uncertainties

underlying the modelling of the outflows significantly enlarge those already present due to the other variables, leading to upper bounds on the PBH mass that can vary from approximately 0.01 to 100 $M_\odot$ (assuming PBHs make all of the DM) depending on the chosen accretion model and outflow properties. This in turn bears important consequences for the LVK observability window. The chapter presented here shows that a more robust and complete modelling of PBH accretion is necessary to draw meaningful conclusions on PBHs being realistic DM candidates and progenitors of the LVK detected events.

2.2 State of the art of PBH accretion

A PBH is moving supersonically in a homogeneously distributed gas accretes matter though an accretion column forming opposite to the direction of motion. In this scenario the accretion at the BH horizon is conveniently described by the Bondi-Littleton rate [115, 116, 117]

$$\dot{M}_{\rm PBH} = 4\pi\rho_\infty\, v_{\rm rel}\, \lambda\, r_B^2\,, \tag{2.1}$$

where ρ_∞ is the mass density of the gas far away from the point mass, $v_{\rm rel}$ is the relative velocity between the PBH and the gas, λ is the dimensionless accretion rate (which takes into account deviations from the idealised Bondi scenario due to the presence of e.g., pressure, viscosity, radiation feedback, MF, etc.), and r_B is the Bondi radius, which characterizes the size of the BH sphere of influence and is defined as $r_B = GM_{\rm PBH}/v_{\rm rel}^2$. The consequent radiation luminosity of the system is typically parametrized as

$$L_{\rm rad} = \epsilon\, \dot{M}_{\rm PBH}\,, \tag{2.2}$$

where ϵ is a dimensionless parameter that accounts for the radiation efficiency of the accretion process.[1]

While the PBH mass is a free parameter of the model, quantities like $v_{\rm rel}$, λ and ϵ are determined by the properties of the environment close the PBH, such as, for instance, the temperature profile of the infalling gas, as well as by the geometry of the accretion or the details of the energy emission. Although there is no consensus on the exact form that these quantities

[1] In equations (2.1)-(2.2) we have assumed $c = 1$, convention that we will apply throughout the manuscript.

should take, several ideas have been proposed so far in the literature (see e.g., refs. [96, 97]). In order to set the stage for the accretion model described in section 2.3, where we focus more closely on the role of outflows, in this section we briefly review the state of the art of PBH accretion. Specifically, we focus on the role of the relative velocity between PBH and surrounding gas in section 2.2.1, on that of the gas ionization model in section 2.2.2 and on that of the geometry of the accretion in section 2.2.3, since these are the main aspects that affect the final accretion radiation luminosity in absence of outflows. The possible impact of other physical effects is discussed in section 2.2.4.

2.2.1 Accounting for PBH velocities

Constraints on the PBH abundance have been reported for different choices of the PBH velocities. Since the different assumptions can change the resulting constraints by orders of magnitude, we analyze and motivate here the approach employed in this chapter.

The first possibility is to consider that PBHs are at rest or moving at sub-sonic speed, hence the only relevant velocity is that of the surrounding medium, i.e., the speed of sound far away from the accretion region $c_{s,\infty}^2 = \gamma v_B^2 = \gamma P_\infty/\rho_\infty$, where $\gamma = 5/3$ is the polytropic equation of state index for an ideal monoatomic gas and $v_B = \sqrt{P_\infty/\rho_\infty}$ is the Bondi velocity. Therefore, in the $v_{\rm PBH} = 0$ scenario, where $v_{\rm PBH}$ is the PBH proper velocity, we have

$$v_{\rm rel} = c_{s,\infty} \,. \tag{2.3}$$

However, under the assumption that the PBHs are the DM, PBHs are expected to be supersonic given that their velocity would effectively be the DM-baryon linear relative velocity v_L, at least on large scales.[2] In this case the relative velocity reads

$$v_{\rm rel} = \sqrt{c_{s,\infty}^2 + v_{\rm PBH}^2} \,. \tag{2.4}$$

Since velocities are stochastic variables, the radiation luminosity of a PBH population is

[2]Following ref. [96], we only consider the large-scale linear velocity of the PBHs, neglecting the effects of the small-scale non-linear contribution from PBH clustering. As shown in ref. [118], this approach is accurate for $z \gtrsim 100$, which is also the redshift range CMB data are the most sensitive to (see, e.g., ref. [119]). We therefore do not expect this approximation to affect our results significantly.

in fact a velocity-averaged[3] luminosity $\langle L_{\rm rad}\rangle$. So far two different averaging procedures have been presented in the literature [120, 96]. In the first one, which we refer to as approximated average in the rest of the chapter, the relative velocity is approximated as

$$v_{\rm rel} \simeq \sqrt{c_{s,\infty}\langle v_{\rm PBH}^2\rangle^{1/2}}, \tag{2.5}$$

with

$$\langle v_{\rm PBH}^2\rangle^{1/2} = \langle v_L^2\rangle^{1/2} = \min[1, (1+z)/10^3] \times 30\ {\rm km/s}, \tag{2.6}$$

z being the redshift, and this result is used in equation (2.1) to obtain the radiation luminosity of the population. This approximation is well motivated in the cases where the radiation luminosity is proportional to $\dot{M}_{\rm PBH}^2 \propto (c_{s,\infty}^2 + v_{\rm PBH}^2)^{-3}$, however in different scenarios its validity has to be assessed on a case-by-case basis. The approximation in equation (2.5) holds for all redshifts below $z \simeq 10^4$ and can therefore be safely applied for all times of interest for this chapter.

The second, more exact and general way of averaging over relative velocities is to consider that a transformation of the form $c_{s,\infty}^2 \rightarrow c_{s,\infty}^2 + v_{\rm PBH}^2$ (which is the same as going from equation (2.3) to equation (2.4)) corresponds to a transformation of the gas temperature far away from the PBH of the form

$$T_\infty \rightarrow T_\infty + \frac{m_p\, v_{\rm PBH}^2}{\gamma(1+\bar{x}_e)}\,, \tag{2.7}$$

where m_p is the proton mass and $\bar{x}_e$ is the background free electron fraction.[4] In this case we express $v_{\rm rel}$ in terms of T_∞ and average the resulting radiation luminosity over the distribution of the relative velocities to obtain the total radiation luminosity $\langle L_{\rm rad}\rangle$. In the following we refer to this approach as exact average.

[3] For the cases presented in this chapter velocities are assumed to be Gaussian distributed.

[4] This transformation follows from the fact that $c_{s,\infty}^2 = \gamma T_\infty(1+\bar{x}_e)/m_p$, and hence $T_\infty = m_p c_{s,\infty}^2/(1+\bar{x}_e)\gamma$.

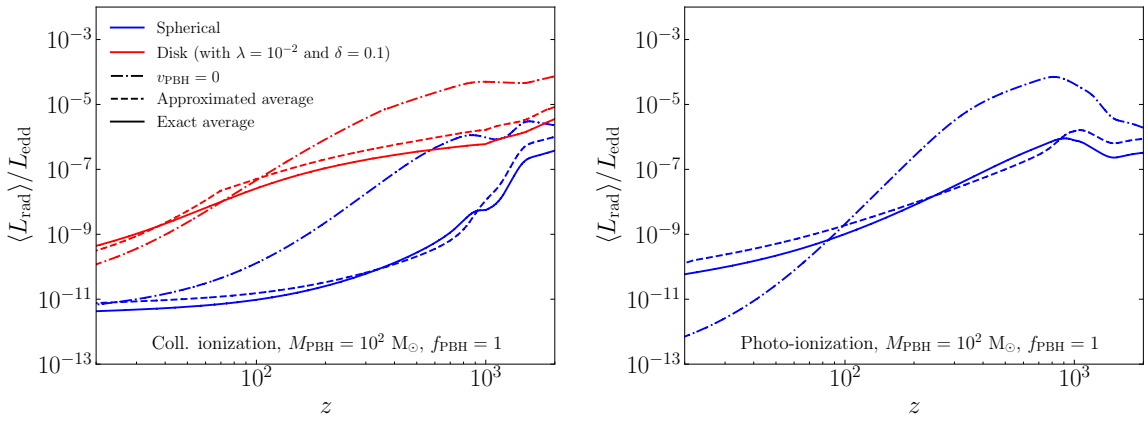

Figure 2.1: Graphical illustration of the impact that the three possible choices for the computation of the relative velocity between PBH and surrounding matter have on the final luminosity of the system, for both the collisional (left) and photo-ionization (right) models. As term of reference, we compare the average radiation luminosity $\langle L_{\rm rad}\rangle$ to the Eddington luminosity $L_{\rm edd}$.

We show in figure 2.1 the effect that these three choices for the relative velocity ($v_{\rm PBH} = 0$, approximated and exact average) have on the averaged total luminosity $\langle L_{\rm rad}\rangle$. In the figure we consider the two types of ionization mechanisms described in section 2.2.2 as well as both the spherical and disk accretion scenarios detailed in section 2.2.3, for the representative case of $M_{\rm PBH} = 10^2\, M_\odot$ and $f_{\rm PBH} = 1$, where $f_{\rm PBH} = \rho_{\rm PBH}/\rho_{\rm DM}$ is the fractional PBH energy density normalized to the DM abundance.[5] As can be clearly seen from the figure, the two methods to account for $v_{\rm rel}$ when $v_{\rm PBH} \neq 0$ are overall almost equivalent, although differences (roughly of order two for the cases considered in the figure) can appear in particular for the disk accretion scenario, as in this case the radiation luminosity is not necessarily proportional to $\dot{M}^2_{\rm PBH}$. Moreover, we find that the exact approach is the most conservative. The figure further highlights the importance of including the PBH proper velocity, since the predictions of equation (2.3) always significantly deviate (even by orders of magnitude) from the exact approach. Therefore, for the sake of generality and being conservative, henceforth (unless

[5] Although not explicitly present in the definition of the radiation luminosity, $f_{\rm PBH}$ affects its value since $L_{\rm rad}$ depends on the background temperature of the accreted matter, which is in turn sensitive to the total amount of injected energy and hence to $f_{\rm PBH}$, as discussed in section 2.4. We will therefore explicitly report the employed value of $f_{\rm PBH}$ in all figures presented in the manuscript.

stated otherwise) we always employ the exact averaging procedure to account for relative velocities, as done for instance in ref. [96].

2.2.2 Ionization models

In the scenarios of interest for this chapter, the radiation luminosity of an accreting PBH mostly comes from free-free radiation originated in the region close to the Schwarzschild radius [96]. The energy of the photons emitted in that region depends on the plasma temperature close to and around the compact object, which in turn depends on the dynamics of the infalling gas. Therefore, an accurate estimate of the temperature profile of the accreting region is necessary to determine the PBH radiation luminosity.

Before recombination, when the medium is already ionized, the temperature increases adiabatically the closer the gas gets to the BH. After recombination, when the medium far from the compact object becomes neutral, two scenario are possible, depending on the relative importance of two potentially competing effects: medium compression, which increases the temperature adiabatically, and ionization, which reduces the temperature proportionally to the energy lost in the ionization process and hence to the amount of initial neutral gas. In the first scenario the temperature of the infalling gas increases until it reaches $T_{\rm ion} \sim 10^4\ K$, then it stops increasing until all the gas gets ionized (since the balance between compression and ionization is maintained), and finally it resumes increasing. In this scenario the neutral gas is ionized through collisions with the free electrons and it is therefore referred to as "collisional ionisation". On the other hand, in the second scenario the radiation produced near the Schwarzschild radius is intense enough to directly photo-ionize the infalling gas before it reaches the ionization temperature $T_{\rm ion}$. Therefore in this scenario, which is conveniently called "photo-ionization", the temperature increases monotonically. In both scenarios radiative cooling is not expected to be relevant on scales close to the PBH.

Given that determining a realistic profile of the temperature around the PBH is very challenging and would require dedicated numerical simulations, we follow the simplifying approach of ref. [96]: we consider these two limiting scenarios of purely collisional or photo-ionization and report our results for both of them, knowing that they would bracket the realistic results.

2.2.3 Geometry of the accretion mechanism

The geometry of the accretion plays a crucial role in determining both the dimensionless accretion rate λ and the radiation efficiency ϵ. As in the previous section, also in this case we treat the spherical and disk accretion scenarios as the limits that encompass the true results. The extensive treatment of the physics of the accretion mechanism is reported in H.

In the spherical accretion scenario, most of the calculations can be performed semi-analytically (see, e.g., ref. [96] for a recent treatment of the problem). The accretion efficiency can be expressed as a function of the Compton drag and cooling rate by CMB photons, finding limiting cases where these rates are either very efficient (isothermal accretion with $\lambda \simeq 1.1$) or negligible (adiabatic accretion with $\lambda \simeq 0.1$). It is also possible to study the evolution of the dimensionless accretion rate depending on the mass of the PBH and on the epoch of the universe, as can be seen in e.g., figure 4 of ref. [96]. Similarly, the radiation efficiency reduces to a function of the mass accretion rate and the temperature of the gas close to the PBH, which in turn depends on the ionization mechanism as discussed in the previous section. Typical values for the radiation efficiency in the spherical case are displayed in the left panel of figure 2.2 for difference choices of the PBH mass and both ionization models.

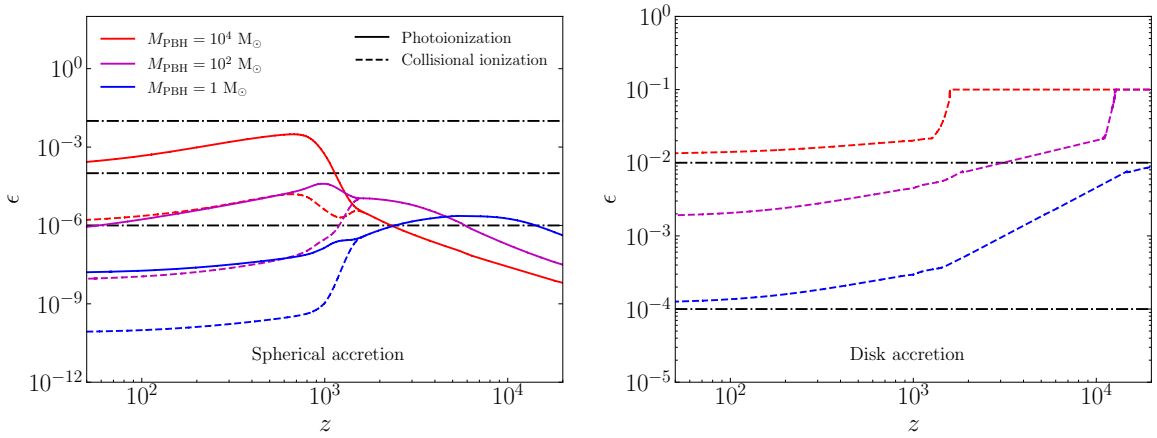

Figure 2.2: Graphical illustration of the dependence of the emission efficiency ϵ on the geometry of the accretion (spherical on the left, disk on the right) as well as on the ionization mechanism (photoionization as solid lines, collisional ionization as dashed lines) for different choices of the PBH mass. In all cases we assume $f_{\rm PBH} = 1$. The horizontal dashed-dotted lines represent the benchmark outflow efficiencies $\epsilon_{\rm non-th}$ discussed in section 2.3.2.

The other accretion mechanism we consider assumes the formation of a disk around the PBH [97]. Given that PBHs are expected to form binary systems already at early times [121], it seems natural to expect that the gas around the PBH experiences tidal forces that lead to the formation of a disk. Unfortunately, the details of disk accretion are very difficult to determine semi-analytically and only educated estimates have been used so far in the literature to determine quantities such as λ or ϵ. Following ref. [97], we fix as (arbitrary) benchmark value for the dimensionless accretion rate $\lambda = 0.01$, which has been argued to roughly take into account the role of viscosity and outflows close to the BH.[6] Similarly, we employ a parametric form of the radiation efficiency ϵ provided by ref. [122] (see in particular equation (11) and table 1 therein). However, there is an order-of-magnitude uncertainty in the estimate of the energy in electrons, characterized as the fraction of energy present in ions, which we assume here to have the representative value of $\delta = 0.1$, as done in ref. [97]. The redshift evolution of ϵ in the disk accretion scenario for these benchmark choices is displayed in the right panel of figure 2.2. Note that these values are up to six orders of magnitude higher than those typical of the spherical accretion scenario. The figure also highlights that, while in the spherical accretion scenario $\epsilon \propto \dot{M}_{\rm PBH}/L_{\rm edd} \propto M_{\rm PBH}$, in the disk accretion scenario $\epsilon \propto (\dot{M}_{\rm PBH}/L_{\rm edd})^a \propto M_{\rm PBH}^a$ where $a \sim 0.3 - 0.6$ is a parameter fitted to match numerical simulations of ref. [122], and hence the radiation efficiency scales differently as a function of the PBH mass in the two cases.

In summary, the unknown geometry of the accretion introduces an enormous source of uncertainty - potentially of orders of magnitude - in assessing the final radiation luminosity. This uncertainty is to be added on top of the uncertainty due to the ionization processes, although so far the disk accretion setup has been analyzed only in the context of collisional ionization. Due to these not completely understood physical processes, the constraints on the abundance of PBHs can vary substantially depending on the underlying choices made to describe the accretion process. Additional effects (discussed in detail in section 2.2.4) only

[6] The role of outflows in the works upon which ref. [97] is based is different than what is considered in section 2.3 (i.e., MF). In that context, outflows play a role only close to the BH, on scales of order approximately $10 - 100$ times the Schwarzschild radius, by removing material close to the compact object, thus reducing the accretion rate onto the BH. Hence they act at small scales, not at large scales reducing the available gas beyond the PBH sphere of influence. Moreover, in those works, the luminosity efficiency is boosted because of the increased energy transferred to electrons in the vicinity of the BH, not because of the acceleration of particles.

further add to this uncertainty budget.

2.2.4 Additional effects

Besides these main factors, the accretion process can potentially be affected by several other contributions that have been considered in the literature. In this section we briefly outline a number of them, highlighting the regimes where they become relevant or can be neglected.

- *The role of the Hubble expansion.* This effect acts on the accretion process as a form of viscosity and introduces an additional redshift dependence of the background energy density and sound speed [123]. However, these contributions become important only for $M_{\rm PBH} \gtrsim 10^4\,M_\odot$, threshold above which the quasi-steady flow approximation breaks down and so does the underlying mathematical setup. Therefore, in particular since in our analysis we focus on the LVK mass range, we do not consider masses above $10^4\,M_\odot$.

- *The gravitational effect of the gas surrounding the PBH.* The effect of self-gravity of the accreting gas can be neglected as long as the PBH mass is much larger than that of the surrounding medium, which is always the case for $M_{\rm PBH} \lesssim 10^5\,M_\odot$ [123] (as for these masses the PBH can only attract a relatively low amount of matter) and therefore also for the range of PBH masses considered in this chapter. The same kind of consideration applies also for the gravitational impact of the background matter on the PBH (which could in principle affect the motion of the PBH, effect known as dynamical friction) as long as one considers PBH masses below $10^4\,M_\odot$ [99, 107].

- *The role of super-Eddington accretion.* Another possibility to consider for very massive PBHs is for them to accrete at a super-Eddington rate (see, e.g., refs. [124, 125, 126] and references therein for recent reviews). The Eddington accretion rate is the limit at which the gravitational force of the BH and the radiation pressure compensate (under the assumption of spherical symmetry), defining therefore the threshold for the maximum luminosity of the object. However, in practice, this limit can be exceeded for instance within proto- and massive galaxies at redshifts $z \lesssim 20$, leading to periods of enhanced but variable luminosity. For spherical accretion, the transition to super-Eddington accretion is believed to happen for PBH masses roughly above $10^4\,M_\odot$, although in more

realistic situations this value would strongly depend on the characteristics of the surrounding environment and on the geometry of the accretion (see, e.g., ref. [127]). Nevertheless, since this is a mainly low-redshift effect, our CMB bounds are largely unaffected by this source of uncertainty.

- *The role of large-scale structure formation and DM halos.* Once large-scale structures start to form at redshifts $\mathcal{O}(10)$, the non-trivial dynamics of PBHs and their interaction with the medium requires numerical simulations to be properly assessed [128, 129, 130, 131], even if semi-analytical arguments can be made regarding how the accretion proceeds (see, e.g., ref. [132, 133]). Furthermore, in the scenario where PBHs represent just a sub-dominant component of the DM and the rest is described by some new beyond-the-Standard-Model particle, DM halos are expected to form around the PBHs [134]. In this case, the formation of DM halos and of large-scale structures more in general can boost both the accretion of material [98, 123, 95] and the PBH proper velocities [97]. While the former effect enhances the radiation luminosity [99], the latter reduces it [133]. However, since these competing effects are strongly reliant on the assumptions made to describe the relevant late-time physics, we will neglect them in the current analysis for sake of clarity and leave their inclusion for future work.

- *PBH mutual interactions.* In the absence of large primordial non-Gaussianity, PBHs do not cluster over cosmic times [135] (see e.g., ref. [136] for further discussions) and PBH evolution can be effectively considered in isolation for masses below $10^4\ M_\odot$ [96]. Furthermore, although early works suggested the existence of a large number of PBH binaries forming at early times [137], these are in contradiction with more recent numerical simulations [138, 139]. Hence, PBH mutual interactions can be safely neglected in the mass range considered in this chapter.

- *The role of the PBH spin.* The radiation emitted by fastly rotating PBHs is enhanced by a factor of order ten percent with respect to the non-rotating case [140]. However, the majority of Kerr PBHs are realistically expected to have a dimensionless Kerr parameter much lower than unity [141, 142], especially in the scenarios where PBHs form from the collapse of large primordial density fluctuations (see, e.g., refs. [143, 144, 145] for

possible exceptions). Hence this effect can be neglected for the purpose of this chapter.

- *The effect of inhomogeneuos energy injections.* Recently, it has also been shown that the impact of PBH accretion on the photon bath can be very sensitive to the inhomogeneous spatial distribution of PBHs [146]. Nevertheless, since further important theoretical and numerical steps will be necessary to fully understand this effect, as also pointed out in the reference, we leave its inclusion in the analysis for future work.

2.3 The role of outflows

Another key physical effect that has been neglected in many of the previous analyses is the presence of outflows and their effect on large scales, where hereafter in this context "large" implies approximately the PBH scale of influence $r_{\rm acc} \simeq 2GM_{\rm PBH}/v^2_{\rm PBH} = 2r_B$. Recent analytical estimates and numerical simulations [80, 81] suggest that even relatively weak jets and winds, i.e., outflows with different degree of collimation, might be able to sweep away some of the material around the PBH, thus reducing the flow of gas entering the BPH sphere of influence. Therefore, if present and carrying as little power as $10^{-6}\dot{M}_{\rm PBH}$ [80], outflows could reduce the available material for accretion through this mechanical feedback effect. Despite the fact that the magnetic field in the primordial gas and the spin of the PBH are likely to be small, even pure hydrodynamical effects could drive outflows in a non-rotating black hole under small anisotropies of the accretion structure Bosch-Ramon:2020pcz,Aguayo-Ortiz2019,Tejeda2020,Waters2020. Taking this and the uncertainties on accretion physics at very high z into account, the role of mechanical feedback deserves to be considered.

Furthermore, if outflows are produced during the accretion process, they can also potentially accelerate particles that can radiate and inject an additional amount of energy into the thermal bath. Such radiation from the outflows can compete with that produced in the accretion process itself, however, only for outflows that are relatively powerful. Therefore, outflows with a rather low power in terms of $\dot{M}_{\rm PBH}$ could still produce mechanical feedback but generate negligible amounts of radiation. These two phenomena, analyzed separately in sections 2.3.1 and 2.3.2, are in fact competing effects: while decreasing the accretion rate intrinsically reduces the PBH radiation luminosity, such loss of luminosity is potentially compensated

by the energy deposited into the medium by non-thermal particles accelerated by the outflows.

In this chapter we analyze the impact outflows potentially have on the two different accretion geometries presented in section 2.2.3. As explained before, these models have to be understood as limiting cases, presented to illustrate where the real physical scenario potentially lays in the PBH parameter space. Therefore, even if strictly speaking in the perfectly spherically symmetric scenario we cannot have outflows, it is still useful to consider that case as the benchmark reference for the scenario where some very low amount of angular momentum is present, which is expected in a cosmological scenario with small inhomogeneities, as outlined in ref. [80].

2.3.1 Impact on the accretion rate

As discussed in ref. [80], many different mechanisms promote the formation of outflows as, for instance, the existence of a magnetic field and/or the presence of some accreted gas with an excess of thermal energy. A (small) magnetic field can be generated by the Biermann battery mechanism, in which case the magnetorotational instability could enhance the magnetization and the turbulence, creating the required conditions for outflow formation [147]. In the presence of magnetic fields, outflows and jets can be fed by the rotational energy of the PBH or by the inner regions of an accretion disk [148, 149], even when the accretion is quasi-spherical [150, 151, 152]. On the other hand, the production of an outflow from an excess of thermal energy in the gas is related to the formation of a thick and radiatively inefficient accreting disk, which forms winds through thermal pressure gradients. These outflows are expected to be broad and largely independent of the details of the magnetic field [101].

As demonstrated in ref. [80], once launched, outflows can overcome the ram pressure of the infalling gas and escape the PBH sphere of influence even when they are relatively weak and non-relativistic. Once outflows reach large scales, they compress and heat the medium by depositing energy and momentum into the gas. This phenomenon, called mechanical feedback (MF), is potentially responsible for a decrease in the accretion rate because the material is effectively heated and swept away from the PBH, implying that the amount of material that is available at scales of order $r_{\rm acc}$ is reduced with respect to the standard case presented in section 2.2.

In order to account for this new large-scale effect, we modify the PBH accretion rate in equation (2.1) by introducing a new fractional rescaling $f_{\rm LS}$, so to obtain

$$\dot{M}_{\rm PBH} = 4\pi\rho_\infty v_{\rm rel}\,\lambda\,f_{\rm LS}\,r_B^2\,. \tag{2.8}$$

This new parameter specifically accounts for physical effects happening at large scales. Therefore, in the case with no MF, we have by definition that $f_{\rm LS} \equiv 1$ and we recover the cases presented in section 2.2. Conversely, when MF is present, $f_{\rm LS}$ is expected to be lower than unity with a value that depends on the outflow ejected material velocity $v_{\rm o}$, the angle between the outflow and the PBH velocity θ and outflow half-opening angle χ (even if this latter dependence is weaker than the first two) [81].

Numerical simulations in 3D [81] suggest that a conservative choice for the fractional rescaling benchmark value (after averaging over all the possible values of the outflow orientation θ) is $f_{\rm LS} = 0.1$. Despite implying an order-of-magnitude reduction of the accretion rate, this choice is still cautious since phenomena such as the potential fast variation of the outflow orientation may further reduce the value of $f_{\rm LS}$ and hence of the accretion rate (as discussed in [81]). Moreover, once PBHs become trans- or sub-sonic, the value of the fractional rescaling may be further reduced since the system becomes more axi-symmetric, and the accumulated internal energy and thus pressure within the outflow-medium interaction region can diminish accretion further (see, e.g., Zeilig-Hess2019,Bosch-Ramon:2020pcz). The in-depth analysis of such additional phenomena is left for future work.

2.3.2 Impact on the total luminosity

The presence of outflows might not only lead to MF, but also to the acceleration of non-thermal particles which later deposit energy and momentum into the medium. Therefore the total luminosity of the PBH receives contributions both from the radiation luminosity and the "non-thermal" luminosity induced by the outflow, i.e.,

$$L_{\rm tot} = L_{\rm rad} + L_{\rm non-th}\,, \tag{2.9}$$

where $L_{\rm rad}$ is the same of equation (2.2) and the non-thermal contribution is conveniently parametrized by an additional efficiency parameter $\epsilon_{\text{non-th}}$ as

$$L_{\text{non-th}} = \epsilon_{\text{non-th}}\, \dot{M}_{\rm PBH}\,. \tag{2.10}$$

An upper-limit on $\epsilon_{\text{non-th}}$ can be derived assuming that most of the energy released by the accretion gets released as outflows, which upon interaction with the environment (interaction by which MF is realized) converts most of its energy into non-thermal accelerated particles. In such a scenario, $\epsilon_{\text{non-th}}$ would be ultimately determined by the relation between the dominant radiation channel, likely inverse Compton (IC) scattering off CMB photons, non-radiative losses via escape and adiabatic losses. Given the dense CMB photon field at $z \sim 10^2 - 10^3$, IC could efficiently cool relativistic electrons, with most of the radiation peaking somewhere within the range from soft X-rays to gamma rays. Such a scenario, which would imply $\epsilon_{\text{non-th}} \sim 0.1$, is however highly optimistic, with more reasonable values for $\epsilon_{\text{non-th}} \lesssim 10^{-2}$ (though values $\ll 10^{-2}$ are also possible). A similar scenario has been explored in ref. Bosch-Ramon2018 for the case of super-massive BH jets interacting with the medium at high z.

Due to the lack of quantitative predictions based on first principles, a robust (and not highly model-dependent) estimate of $\epsilon_{\text{non-th}}$ has not been obtained yet. Therefore, in order to parametrize its impact on the cosmic medium, we consider three different benchmark values for $\epsilon_{\text{non-th}}$, namely $\epsilon_{\text{non-th}} = 10^{-2},\ 10^{-4},\ 10^{-6}$. As a reference, the intermediate case, $\epsilon_{\text{non-th}} = 10^{-4}$, may be interpreted as a scenario where 10% of the accretion energy goes to the outflows, of which 10% goes to non-thermal particles, which in turn can radiate through IC about 10% of their energy, 10% of which in the form of photons with suitable energies (see ref. [151] for a discussion in the context of isolated black holes in our galaxy). These benchmark values are compared to the radiation efficiencies obtained for the scenarios in absence of outflows in figure 2.2. As it can be observed in the figure, the chosen non-thermal emission efficiencies are of the same order of magnitude (depending on the PBH mass) of the radiation efficiencies obtained in the represented cases, hinting to a tight interplay between the two terms contributing to equation (2.9).

Finally, we note that in this case the gas can be easily ionized through compression by the

shock generated by the outflow on large scales. Hence, since the gas cooling time is not small enough for the gas to recombine, the photo-ionization model provides a more realistic description of the physical picture. Nevertheless, we will also consider the collisional ionization model for sake of completeness.

2.3.3 Combined effect

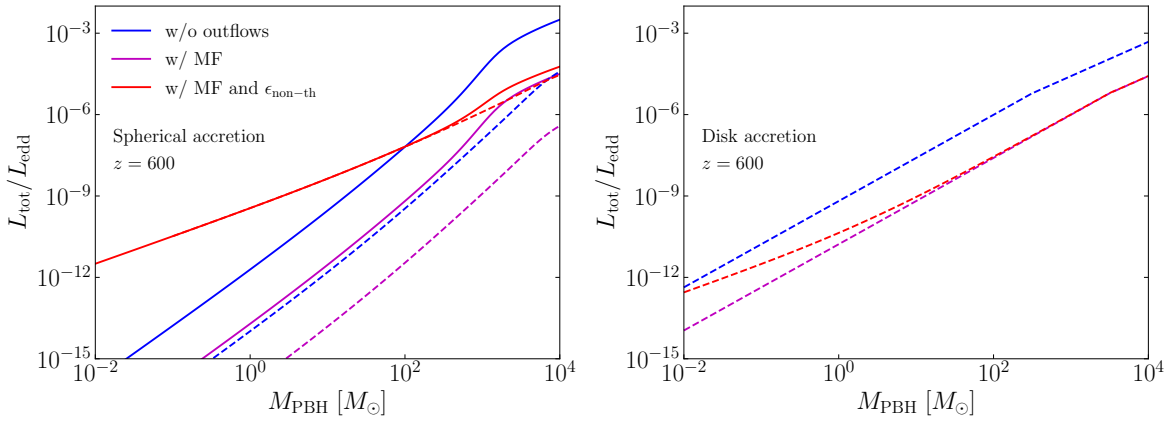

Figure 2.3: Graphical representation of the impact of the outflow effects (MF and non-thermal emissions) on the total luminosity of the system as a function of the PBH mass. As in figure 2.2, both the spherical and disk accretion scenarios are shown (on the left and on the right, respectively) as well as the different possible ionization models (photo-ionization in solid and collisional ionization in dashed). In all cases we assume $f_{\rm PBH} = 10^{-3}$, $\epsilon_{\rm non-th} = 10^{-4}$ and we restrict ourselves only to the representative redshift $z = 600$ (as justified in the text).

The impact of MF and non-thermal emissions on the total luminosity is shown in figure 2.3 for both accretion geometries (spherical on the left, disk on the right) and ionization models. For sake of succinctness (but with no loss of generality), here we assume $f_{\rm PBH} = 10^{-3}$ and $\epsilon_{\rm non-th} = 10^{-4}$. Furthermore, we also show the results only for the representative case of $z = 600$, which has been shown to be the time around which the CMB anisotropies are most responsive to (almost constant in time) energy injections such as the ones considered here [153]. A more general redshift dependence can be qualitatively inferred from figure 2.2.

In figure 2.3, the various predictions in absence of outflows are shown in blue and match the expected linear dependence of the radiation luminosity on $M_{\rm PBH}$ (with different powers

depending on the geometry as explained in section 2.2.3) over almost the full PBH mass range. These curves are then suppressed by orders of magnitude when including the role of MF[7], as represented by the magenta lines. However, this reduction of luminosity can be partially compensated, in particular in the low mass range, when non-thermal emissions are taken into account (red lines).

This implies that when including the effect of outflows there are three possible outcomes.

1. First of all, if non-thermal emissions are very efficient, their contribution to the total luminosity always dominates over the radiation luminosity and results in an enhanced energy injection with respect to the case in absence of outflows (unless very low $f_{\rm LS}$ values, say $\ll 1$, are considered). This scenario is represented, for instance, in the left panel of figure 2.3 in the collisional ionization case.

2. On the other hand, the opposite is true if non-thermal emissions are relatively inefficient, as observable in the disk accretion case represented in the right panel of the figure.

3. Finally, as can be seen from the left panel of the figure for the photoionization case, there might be a range of PBH masses where the total luminosity is enhanced with respect to the case in absence of outflows due to non-thermal emissions (low mass range) and regions where this is instead suppressed because of MF (high mass range).

As discussed in section 2.6, the balance between these regimes dictates how the final CMB constraints are affected by the presence of outflows.

2.4 Impact on thermal history and CMB anisotropies

The last ingredient to factor in our analysis is the description of how the emitted radiation impacts the thermal history of the universe. A population of PBHs *injects* energy into the

[7]That is, since $L_{\rm rad} \propto \dot{M}^2_{\rm PBH} \propto f^2_{\rm LS}$ in the spherical accretion case and $L_{\rm rad} \propto \dot{M}^{1+a}_{\rm PBH} \propto f^{1+a}_{\rm LS}$ in the disk accretion case. By assuming $f_{\rm LS} = 0.1$ (as argued in the previous section) one obtains a suppression of a factor 100 and 40, respectively.

cosmic medium at a rate

$$\left.\frac{dE}{dtdV}\right|_{\rm inj} = \bar{\rho}_{\rm PBH}\,\frac{\langle L_{\rm tot}\rangle}{M_{\rm PBH}} = \bar{\rho}_{\rm cdm}\,f_{\rm PBH}\,\frac{\langle L_{\rm tot}\rangle}{M_{\rm PBH}}, \tag{2.11}$$

where $\bar{\rho}_{\rm PBH}$ is the PBH background energy density, $f_{\rm PBH} = \bar{\rho}_{\rm PBH}/\bar{\rho}_{\rm cdm}$ is its fractional form with respect to the DM abundance, and $\langle L_{\rm tot}\rangle$ is the velocity-averaged total luminosity. However, the amount of energy that is actually *deposited* into the thermal bath can in principle be different, for instance depending on the transparency and energy density of the medium or on the type of emitted particles [154, 155]. Furthermore, different deposition channels have to be accounted for, since the additional energy might not only heat up the medium but also ionize and excite it if the injection happens after recombination [156, 157, 158]. Following [57, 159, 160], we express the deposited energy rate in a channel c as

$$\left.\frac{dE}{dtdV}\right|_{{\rm dep},c} = \left.\frac{dE}{dtdV}\right|_{\rm inj} f_{\rm eff}\,\chi_c\,, \tag{2.12}$$

where $f_{\rm eff}$ and χ_c are the deposition efficiency and deposition fraction for the specific channel, respectively.[8] In this chapter we parameterize $f_{\rm eff}$ as in section IV of ref. [96], while for the calculation of the different deposition fractions we rely on table V of ref. [158].

Once the relation between injected and deposited energy is set, one can analyze how the different accretion scenarios affect the reionization fraction x_e, which is ultimately the quantity that determines how much the CMB anisotropy power spectra are affected by the non-standard energy injection. In fact, the main effects of depositing energy into the cosmic medium are twofold: *(i)* delaying the time of last scattering, which induces a slight shift in the position of the peaks in the CMB temperature and polarization power spectra, and *(ii)* effectively increasing the ionization optical depth since the reionization of the universe starts at an earlier time. In figures 2.4 and 2.5 we highlight this behavior by comparing the effect on the free electron fraction x_e and the CMB anisotropy power spectra (computed as described in section 2.5) of the different accretion models considered in this chapter, with and without outflows, for three representative choices of PBH mass.

[8] Alternatively, one could have directly calculated the total deposition function $f_c(z, x_e)$, as in refs. [58, 161], but this approach is not currently implemented in the version of CLASS employed here.

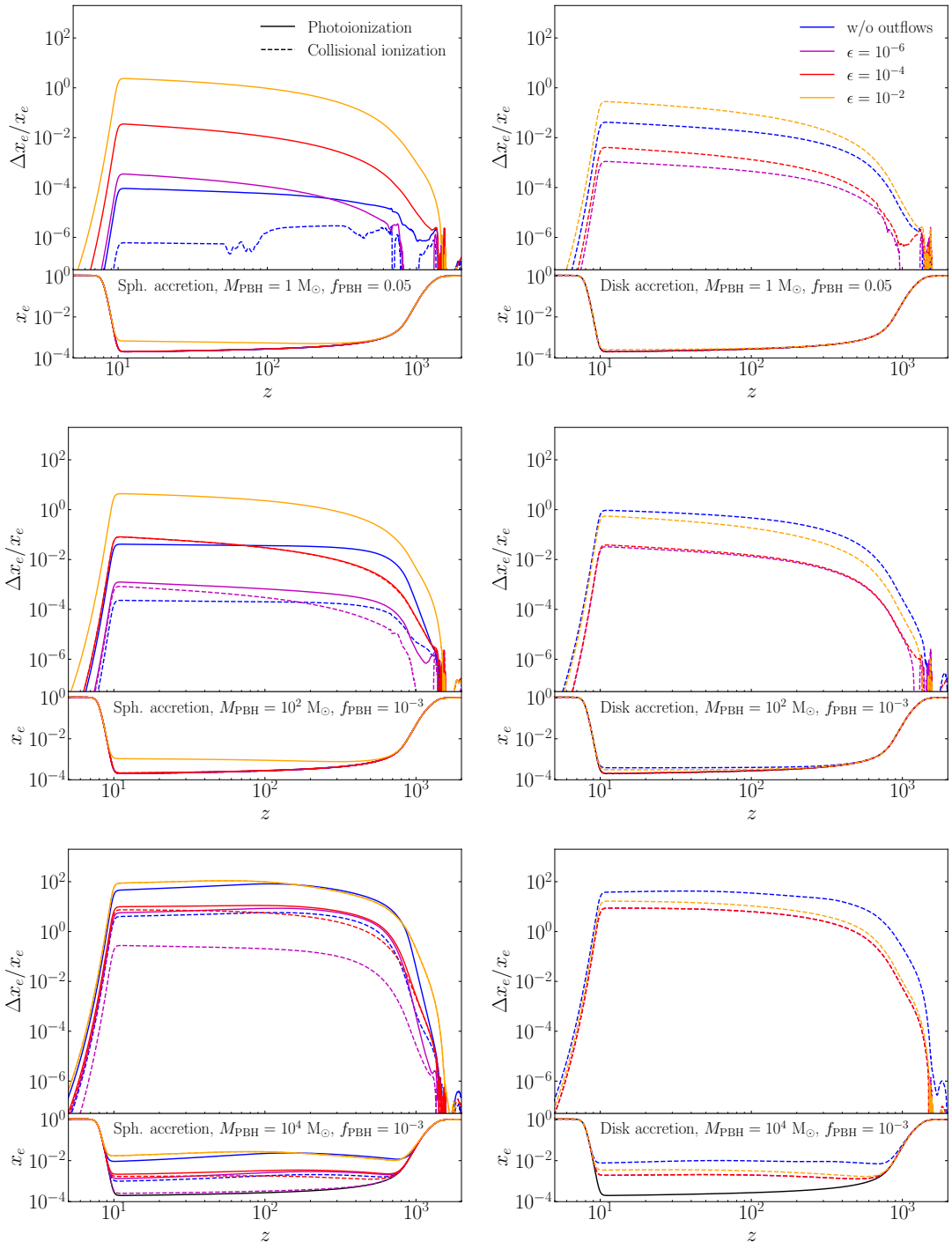

Figure 2.4: Role of the outflows in the impact on the free electron fraction of the accretion process (shown are the free electron fraction – lower panels – and its relative difference with respect to the ΛCDM prediction – upper panels). From top to bottom we compare three representative choices of the PBH mass (same as in figure 2.2), while from left to right we compare the spherical and disk accretion scenarios (for the latter we assumed $\lambda = 0.01$ and $\delta = 0.1$). In the bottom panels the ΛCDM prediction is shown in black. The irregular shape of the collisional ionization curve in the top left panel is due to numerical noise.

From the figures, several conclusions can be drawn. On the left panels of figure 2.4, which represent the spherical accretion case, we compare the cases with and without outflows and we find that for low PBH masses (upper panel) the contribution from the outflows always dominates over the radiation luminosity. In fact, once MF is accounted for, the mass accretion rate is suppressed by a factor 10 (assuming the fiducial values introduced in section 2.3.1), and the corresponding radiation efficiency becomes significantly lower than any of the cases with a non-zero $\epsilon_{\rm non-th}$. Interestingly, this is true for both ionization models discussed in section 2.2.2, so that no difference is to be seen between the collisional (dashed lines) and photo-ionization (solid lines) cases when including outflows in the low mass range. The situation slightly changes, however, for PBH masses of the order of $10^2\ M_\odot$ (middle panel) and non-thermal efficiencies lower than 10^{-4}, where the radiation luminosity in the photo-ionization case becomes comparable to that of the non-thermal outflows after the inclusion of MF and differences between the various ionization processes start to emerge. This behavior is further enhanced for larger PBH masses (bottom panel), although the non-thermal luminosity still dominates for $\epsilon_{\rm non-th} \sim 10^{-2}$.

On the other hand, because of the higher radiation efficiencies reached in the disk accretion scenario (see figure 2.2), already at relatively low PBH masses (upper panel) the intrinsic radiation efficiency of the accretion is comparable to the non-thermal contribution once MF is taken into account for $\epsilon_{\rm non-th} \sim 10^{-6}$. For higher PBH masses (middle and bottom panels) the role of the non-thermal emission becomes negligible and the curves for $\epsilon_{\rm non-th} < 10^{-4}$ perfectly overlap, with only a minor difference in the $\epsilon_{\rm non-th} = 10^{-2}$ case.

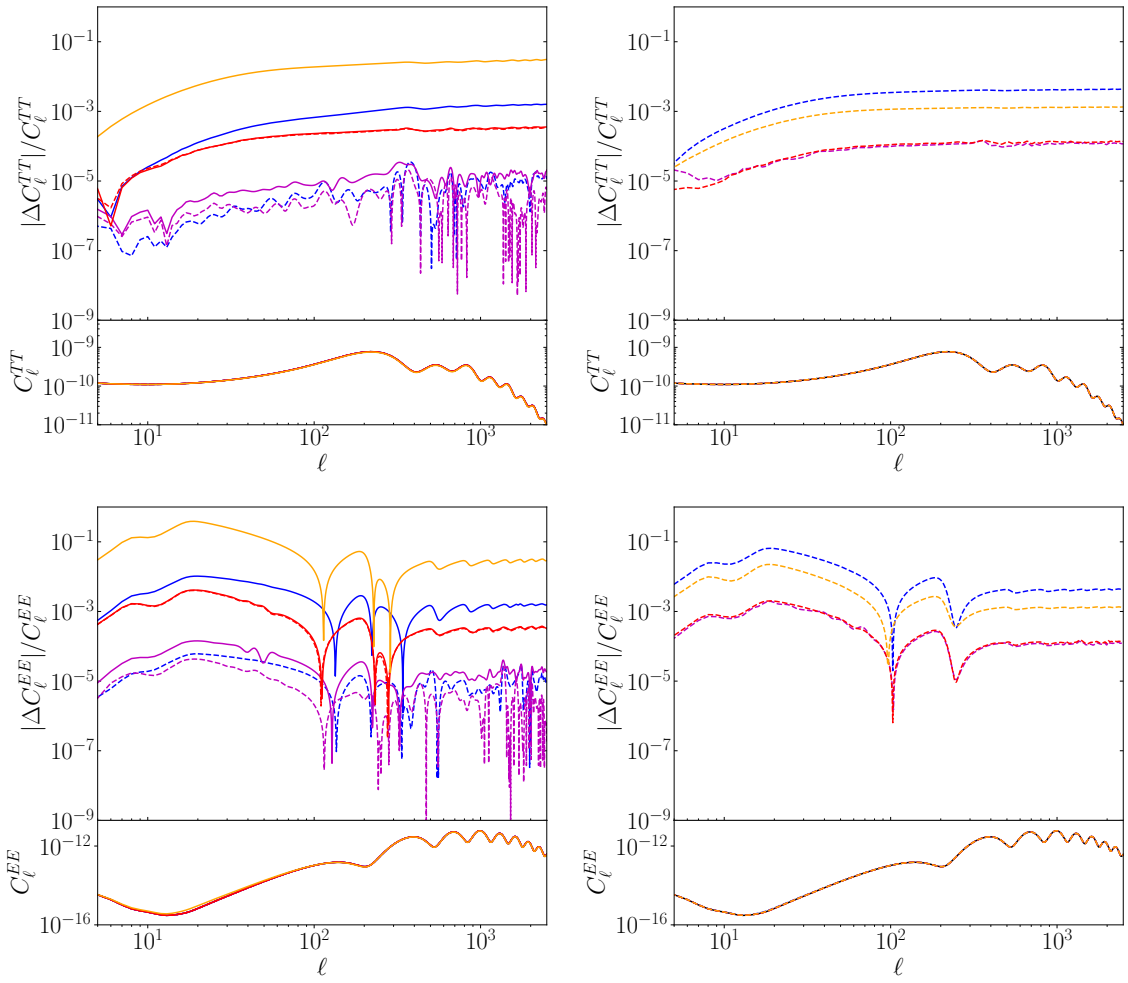

Figure 2.5: CMB temperature (upper panels) and polarization (lower panels) power spectra for $M_{\rm PBH} = 10^2\ M_\odot$ and $f_{\rm PBH} = 10^{-3}$. As in figure 2.4, the spherical and disk accretion scenarios are shown in the left and right panels, respectively, while solid and dashed lines represent the photo- and collisional ionization cases.

In summary, we expect the contribution from the outflows to be largely determining the luminosity of the system for low masses in the spherical accretion scenario, greatly reducing (if not erasing) the differences between the various ionization models in this regime, while for larger PBH masses the interplay between radiation luminosity, MF and non-thermal emissions starts to become apparent. This differs from the disk accretion case where the intrinsic radiation luminosity of the system is always relevant, and eventually dominates already for PBH masses of the order of $10^2\ M_\odot$.

In figure 2.5 we also show the impact that these modified thermal histories have on the CMB temperature and polarization anisotropy power spectra. For sake of succinctness, here we focus only on the $M_{\rm PBH} = 10^2\ M_\odot$ case, which we believe already suffices to convey the main message of the section. In particular, for both accretion geometries, we notice the same level of interplay between radiation efficiency, MF and non-thermal effects as in the corresponding panel of figure 2.4. Interestingly, the contribution of the outflows (visible for instance in the $\epsilon_{\rm non-th} = 10^{-2}$ case of the left panels) resembles very closely the smooth behavior already observed in ref. [97] for the disk accretion scenario (see figure 3 of the reference), while the purely spherical accretion case imprints a more oscillatory behavior in the residuals (see, e.g., figure 13 of ref. [96]). This might mean, for instance, that a potential observation of a similar signal might be unable to disentangle a spherical accretion scenario dominated by outflows from the disk accretion scenario, regardless of the impact of outflows.

2.5 Numerical setup

In terms of PBH accretion, we further improve upon the implementation of ref. [57] (and [58]) by including also the photo-ionization option for the spherical accretion case as well as the calculation for the average of the PBH luminosity over the PBH proper velocities, which we employ as default option for our analysis (see section 2.2.1 for further details). The impact of the outflows is implemented as an extension of the spherical and disk accretion cases, where we simply modify the definitions of the accretion rate $\dot{M}_{\rm PBH}$ and of the total luminosity $L_{\rm tot}$, as illustrated by equations (2.8) and (2.9), respectively. When considering disk accretion, we fix $\lambda = 0.01$ and $\delta = 0.1$, the benchmark values suggested in ref. [97].

The constraints on the cosmological parameters discussed in section 2.6 for the different accretion models are obtained using the parameter inference code MontePython [162, 163]. As commonly done in the literature, we perform a number of Markov Chain Monte Carlo (MCMC) scans of the parameter space for fixed values of the PBH mass, which reduces the problem to a 6+1 extension of the ΛCDM model with

$$\{\omega_b\,,\omega_{\rm cdm}\,,h\,,A_s\,,n_s\,,\tau_{\rm reio}\}+f_{\rm PBH}\,, \tag{2.13}$$

where ω_b and $\omega_{\rm cdm}$ are the baryon and DM physical energy densities, respectively, h is the dimensionless Hubble rate, A_s and n_s are the amplitude and scalar spectral index of the primordial power spectrum, and $\tau_{\rm reio}$ is the reionization optical depth.[9] In the scenarios of interest, PBHs are described by the abundance parameter $f_{\rm PBH} = \bar{\rho}_{\rm PBH}/\bar{\rho}_{\rm cdm}$, i.e., by the fraction of DM in form of PBHs. We consider temperature, polarization and lensing information from the Planck 2018 mission [9] (explicitly, we use the high-ℓ TTTEEE, low-ℓ EE, low-ℓ TT and lensing likelihoods) and determine the MCMCs to be converged with the Gelman-Rubin criterium $|R-1| < 0.02$ [164].

2.6 CMB constraints on PBH abundance

In this section we derive the corresponding CMB anisotropy constraints on the PBH abundance for both accretion geometries and ionization models described in section 2.2 and focusing on the impact of outflows for different choices of the non-thermal emission efficiency as explained in section 2.3. To ease the comparison with the literature, first of all we derive the aforementioned constraints in the context of a monochromatic PBH mass distribution in section 2.6.1. Then, for sake of generality, we also recast our constraints in terms of a popular choice of extended mass distribution in section 2.6.2. On the basis of these results, in section 2.6.3 we also comment on their implications for the LVK window.

2.6.1 Constraints for monochromatic mass distributions

We begin by assuming that PBHs have a monochromatic mass distribution (MMD), i.e., all PBHs have the same mass. In full generality, a PBH mass distribution is described by the fractional abundance function [165]

$$\frac{df_{\rm PBH}}{dM_{\rm PBH}} = f_{\rm PBH}\frac{d\Phi_{\rm PBH}}{dM_{\rm PBH}}, \tag{2.14}$$

[9] In figures 2.1-2.5 we always assume for these parameters the mean values reported in table 2 of ref. [9] for the Planck+BAO combination.

where $d\Phi_{\rm PBH}/dM_{\rm PBH}$ describes the shape of the PBH mass distribution, it is normalized to unity by construction and in the monochromatic case it reads as

$$\frac{d\Phi_{\rm PBH}}{dM_{\rm PBH}} = \delta^D(M_{\rm PBH} - M^\star_{\rm PBH}). \tag{2.15}$$

In this chapter we choose $M^\star_{\rm PBH}$ such that it scans the mass range $[10^{-2}, 10^4]\ M_\odot$, computing for each PBH mass the respective upper limit on the PBH abundance.

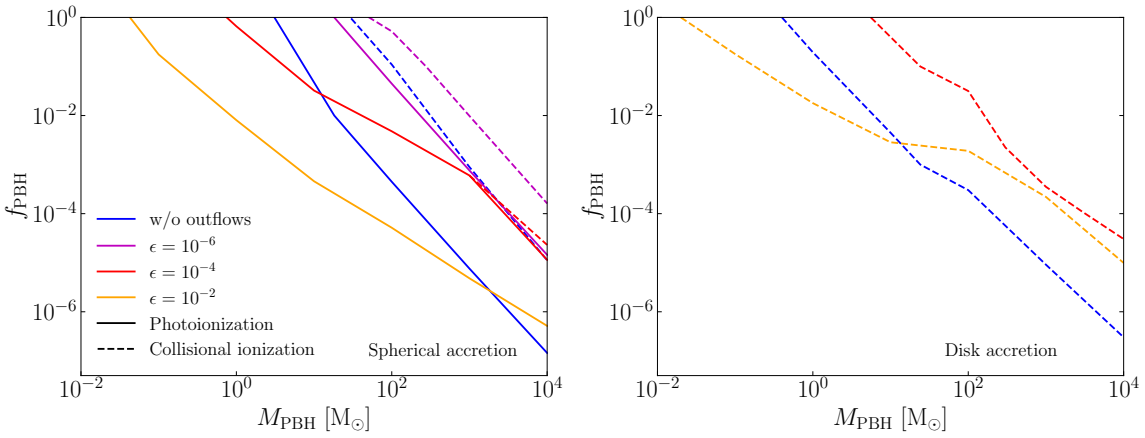

Figure 2.6: Impact of outflows on the CMB constraints on the fractional PBH abundance for the two main types of accretion geometry (spherical on the left and disk on the right) and ionization models (photo-ionization in solid and collisional ionization in dashed) assuming a MMD. The blue contours represent the scenarios without outflows and update the bounds first derived in [96] (left) and [97] (right), while the magenta, red and organge lines assume MF with $f_{\rm LS} = 0.1$ and non-thermal emissions with $\epsilon_{\rm non-th} = 10^{-6,-4,-2}$, respectively.

We show in figure 2.6 the corresponding 95% CL upper bounds on the fractional PBH abundance $f_{\rm PBH}$ for different accretion mechanisms, ionization choices and outflows scenarios. In particular, in each of the two subplots, which display the bounds for the spherical accretion case on the left and the disk accretion case on the right, we report the upper bounds on $f_{\rm PBH}$ for the two aforementioned ionization models (photo-ionization reported as solid lines and collisional ionization as dashed lines) as well as for different choices of the parameters describing the outflow modelling. As in the previous sections, we have the scenario without any outflow contribution in blue, while the contours including MF with the benchmarking value of $f_{\rm LS} = 0.1$ and non-thermal emissions are reported in magenta, red and orange for

$\epsilon_{\rm non-th} = 10^{-6,-4,-2}$, respectively.

Focusing first on the left panel of figure 2.6, i.e., on spherical accretion, we observe that the constraints obtained in absence of outflows are approximately one order of magnitude more stringent than those reported in ref. [96] for both ionization models. We attribute this discrepancy to the difference in methodology[10] and Planck data release employed here compared to the one in ref. [96]. The bounds for the collisional ionization case are in fact broadly consistent with those presented in ref. [99], where a more similar analysis was conducted. In terms of impact of the outflows, for low non-thermal efficiencies the role of MF alone is dominant, leading to an overall suppression of the constraints by approximately $1-2$ orders of magnitude, as explained in section 2.3.3. For intermediate values of $\epsilon_{\rm non-th}$ the interplay between MF and non-thermal emissions becomes more balanced, with the latter most predominately contributing to the total luminosity until PBH masses of the order of $10^3\ M_\odot$, above which the radiation luminosity dominates despite the presence of MF. Nevertheless, also in this scenario we observe a suppression of the bounds with respect to the case without outflows, with only a minor enhancement for masses below $10\ M_\odot$. The situation changes for very efficient non-thermal outflows, which dominate the accretion emission over the whole PBH mass range, thereby arasing the difference between photo- and collisional ionization (which perfectly overlap in the figure), and significantly strengthen the constraints down to PBH masses of the order of $0.1\ M_\odot$ for $f_{\rm PBH} = 1$.

On the other hand, since in the context of disk accretion the intrinsic radiation luminosity is much higher than in the spherical accretion case, in the right panel of figure 2.6 we notice that even for non-thermal efficiencies as high as 10^{-4} the only relevant impact of outflows is MF, which suppresses the constraints by about $1-2$ orders of magnitude. For this reason, the contours for the $\epsilon_{\rm non-th} = 10^{-4}$ and $\epsilon_{\rm non-th} = 10^{-6}$ cases perfectly overlap in the right panel of the figure. Only for $\epsilon_{\rm non-th}$ of the order of 10^{-2} non-thermal emissions start to play a significant role, enhancing the constraints for PBH masses below $10\ M_\odot$ but still leading to a suppression thereof for larger PBH masses.

Focusing on the shapes of the constraints, one expects the behaviour of the bounds to

[10] In ref. [96], for instance, an approach based on a Fisher-information matrix has been employed, while here we make use of an MCMC analysis.

follow the dependence of the deposited energy on the free parameters of the model, i.e., $f_{\rm PBH}$ and $M_{\rm PBH}$, which roughly boils down to $\mathrm{d}E/\mathrm{d}t\mathrm{d}V|_{\rm dep} \propto f_{\rm PBH} M_{\rm PBH} \lambda(\epsilon_{\rm non-th} + M_{\rm PBH}^2 \lambda)$. In the case of spherical accretion the values of λ at $z \sim \mathcal{O}(10 - 10^3)$ increase as a function of the mass (see figure 4 of ref. [96]), which explains why the relation between PBH abundance and mass is not linear, with the bounds becoming comparatively less stringent the lower the PBH mass (a similar behaviour is also to be observed in figure 2.3). This relation, and in particular the different dependence on the PBH mass, also explains the difference in slope of the $f_{\rm PBH} - M_{\rm PBH}$ upper bounds between the radiation and non-thermal emission dominated regimes. In the disk accretion scenario the value of λ is fixed to a fiducial value, and therefore the upper bounds approach a linear dependence more closely than in the spherical case. Nevertheless, as it becomes clear in particular in the $\epsilon_{\rm non-th} = 10^{-4,-6}$ cases, the parametric form of ϵ used in ref. [122] still introduces a non-trivial dependence of the constraints on the PBH mass.

2.6.2 Constraints for extended mass distributions

Even if for practical purposes it is more convenient to obtain constraints for MMDs, in reality it is well known that PBH populations would likely have an extended mass distribution (EMD). Different PBH formation mechanisms are generally responsible for different EMDs, although we can identify two popular benchmark classes of EMD: *power-law* and *lognormal*. Broadly speaking, the first class is typically associated with the collapse of large density perturbations or cosmic strings, see e.g., refs. [166, 167], while the latter is connected to the presence of large peaks in the primordial power spectrum, see e.g., refs. [168, 169, 170].

Recent works, as for instance refs. [171, 172, 173, 174, 175, 176, 177, 178, 179, 180, 181, 182, 183], have shown significant interest in models where PBHs are generated from peaks in the primordial curvature power spectrum. Such effort has been mainly driven by the intrinsic connection between the primordial power spectrum and inflationary dynamics, which is known to be compatible with the single-field slow-roll scenario only during $6/8$ e-folds of the at least 50 required to solve the horizon and flatness problems [184, 185, 186]. Therefore establishing robust bounds on the PBH abundance, or even just their presence, is a key ingredient in reconstructing the primordial power spectrum at scales of order $\mathcal{O}(10^5 - 10^{15})\ \mathrm{Mpc}^{-1}$ currently not accessible by other cosmological observables [187, 188, 189, 190, 191, 192, 193, 194,

195, 196, 197]. For this reason, here we focus on deriving abundance constraints for lognormal EMDs

$$\frac{d\Phi_{\rm PBH}}{dM_{\rm PBH}} = \frac{e^{-\frac{\log^2(M_{\rm PBH}/\mu)}{2\sigma^2}}}{\sqrt{2\pi}\sigma M_{\rm PBH}}, \tag{2.16}$$

characterized by two parameters, the mean μ and standard deviation σ. More realistic mass distribution models would require a greater number of parameters to describe the EMD [198], and therefore in this chapter we choose the simplest extension of the MMD case. The same procedure can be implemented also in the case of power-law EMDs, as done for instance in ref. [92].

Interpreting abundance constraints obtained for MMDs as abundance constraints for EMDs is not straightforward [199], although several methods have been proposed to infer the latter from the former (see e.g., refs. [165, 199, 200]). In this chapter we follow the approach of ref. [165], based on the concept of *equivalent mass*. In the case of interest, if PBHs have an EMD, equation (2.11) reads as

$$\left.\frac{dE}{dtdV}\right|_{\rm inj} = \bar{\rho}_{\rm cdm} f_{\rm PBH} \int dM_{\rm PBH} \frac{d\Phi_{\rm PBH}}{dM_{\rm PBH}} \frac{\langle L_{\rm tot}\rangle}{M_{\rm PBH}}, \tag{2.17}$$

showing that it is possible for different EMDs to inject the same amount of energy into the cosmic medium, making it possible for PBH populations in those models to be equally abundant. At a practical level, it is always possible to associate the impact on a cosmological observable of a given EMD, and therefore its abundance $f_{\rm PBH}^{\rm EMD}$, to the same-magnitude effect generated by a MMD with equivalent mass $M_{\rm eq}$, i.e., to its abundance $f_{\rm PBH}^{\rm MMD}$. Despite its simplicity, this method provides an easy analytical tool to compute constraints for EMDs starting from the MMD analysis of section 2.6.1. The validity of this method has been already explicitly proved in ref. [92] for the CMB case or, for instance, in ref. [105] for other abundance constraints also based on accretion physics.

In figure 2.7 we show the PBH abundance constraints for the lognormal EMD for all geometries, ionization models and non-thermal emission efficiencies already employed in the previous section. We report the new conversion formula used for all the cases at hand in appendix G. The gray shaded regions in the plots indicate the values of μ and σ for which the EMDs extend beyond $10^4\,M_\odot$ and the theoretical models employed in this chapter break down as discussed in section 2.2.4 (see ref. [165] for further details). By comparing the cases with

only radiative efficiency to the ones with also non-thermal emission, we note that as soon as the MF effect starts to play a role, the allowed parameter space increases significantly with respect to the case of radiative emission only. On the other hand, as soon as the non-thermal emission grows, the parameter space becomes very tightly constrained, as can be seen in the bottom panels. In other words, because of these two competing effects, the same EMD can be either ruled in or ruled out depending on the details of the accretion and emission models.

2.6.3 Theoretical uncertainties and implications for the LVK mass range

The analysis presented in this chapter clearly highlights what is one of the underlying issues with existing constraints on PBHs: the unknown magnitude of the theoretical error associated to the modelling of the accretion process. Reducing this uncertainty is crucial given that existing and future GW observatories are and will be sensitive in the $\mathcal{O}(10 - 10^4)$ Hz frequency range, i.e., the typical frequency range where the signal of coalescing compact objects with masses $\mathcal{O}(10 - 10^3)\ M_\odot$ is expected to be. An accurate estimation of the PBH abundance upper limits would in fact allow us to speculate more realistically about what amount of detected events can have a primordial origin.

Nevertheless, such an accurate description of the accretion process is still not available. Therefore, we present our findings in figure 2.8 as "uncertainty bands" around the true, unknown, upper bounds. These bands encapsulate the effects of the geometry and ionization models with (orange) and without (blue) the inclusion of outflows for a MMD. As shown in the figure, even before accounting for the outflow phenomenology, the width of the uncertainty band spans over two orders of magnitude, approximately between 1 and 100 $M_\odot$, for $f_{\rm PBH} \simeq 1$. This means that the intrinsic theoretical error in the modelling of the accretion makes these CMB anisotropy constraints unable to discern whether PBHs might be the progenitor of any observed BH merger, as they could either completely exclude or allow the LVK mass range. Once outflows are included in the modelling, the uncertainty band significantly enlarges both at large PBH masses, where MF dominates and the effect of non-thermal emission is negligible, and at low PBH masses, where the effect of non-thermal emission can be sizeable. Furthermore, the uncertainty due to the theoretical modelling in the case of EMDs can be easily seen when comparing the different panels of figure 2.7.

In this respect, we also note that the existing bounds on the PBH abundance deriving from the LVK estimate of the binary BH local merger rate are subject of an ongoing debate. In fact, semi-analytical estimates of the local merger rate R_0 of PBH binaries formed at early times suggest that it could be as high as $R_0 \sim 10^5\ \mathrm{Gpc}^{-3}\mathrm{yr}^{-1}$ [23, 137] for $f_{\mathrm{PBH}} = 1$, to be compared with the observational value of $R_0 \sim 20\ \mathrm{Gpc}^{-3}\mathrm{yr}^{-1}$ [201]. On the other hand, recent (and more accurate) numerical simulations reconcile the PBH early binary local merger rate value with the observed one for $f_{\mathrm{PBH}} = 1$ [138, 139].

The question of whether PBHs can be a significant component of the DM content of the universe and of the GW events detected by LVK is therefore still open and only a synergistic effort between different communities will help us find an answer to it. In fact, although in this chapter we focused only on CMB constraints, they are not the only relevant ones in the LVK mass range. For instance, there are many complementary constraints coming from supernova lensing [202], dwarf and ultra-faint dwarf galaxy dynamics [203, 204, 205], Lyman-α forest [206, 51] or wide binaries survival [207], which might help us shed light on the complexities of PBH phenomenology and ultimately determine their abundance.

2.7 Summary

Despite its remarkable success in explaining numerous cosmological observables, the ΛCDM model cannot provide any insight on what the true nature of DM is, allowing a vast plethora of models to fit observations. For the sake of convenience, DM candidates are typically categorized in terms of their mass: already in this context, DM models span many orders of magnitude, ranging from ultralight axion-like particles to macroscopic compact objects like BHs. Hence finding novel ways to constrain DM properties becomes fundamental in order to establish its nature.

In this chapter we focus on one of these popular candidates, PBHs. In particular, we focus on PBHs with masses larger than $1\ M_\odot$, since they have the potential to be detected by existing and future GW observatories. This class of PBHs had been previously thought to be ruled out by existing LVK constraints on the local merger rate, although recent numerical simulations have shown that the number of PBH merging binaries had been overestimated by several

orders of magnitude, reopening the possibility for PBHs to be a substantial component of the DM in the LVK mass range.

In this spirit, we turn our attention to other existing constraints on the PBH abundance in that same mass range, that is to those coming from the accretion of matter into a PBH. In fact, the emission of radiation following the accretion process affects the thermal history of the universe, by delaying recombination and anticipating reionization, and can therefore be constrained by CMB observations. However, large theoretical uncertainties underlay the modelling of accretion and this translates in large error bars on the final constraints. Examples of sources of such uncertainties are the geometry of the accretion as well as the ionization model determining the temperature profile close to the BH.

On top of these uncertainties, one aspect of the accretion physics that has not been considered extensively in the literature so far is the effect of outflows (winds and/or jets, depending on their degree of collimation) on the accretion. However, it has been shown both analytically and numerically that even relatively weak outflows can escape the BH sphere of influence and sweep away at least part of the cosmic medium around the PBH, thereby decreasing its accretion rate. At the same time, the very same outflows could also accelerate non-thermal particles and effectively enhance the luminosity of the BH. Therefore, these competing effects can significantly affect the total luminosity of the system and introduce an additional layer of uncertainty that needs to be taken into account when quoting cosmological constraints derived from PBH accretion.

In this chapter we attempt to model the largely unknown nature of these effects and to analyse how their balance affects the CMB constraints on PBH accretion. We do so for different choices of accretion geometry (spherical or disk) and ionization models (photo- and collisional ionization), as well as for both monochromatic and extend mass distributions. Our quantitative findings are shown in figures 2.6-2.7, which clarify that the final outcome heavily relies on the choice made in particular for the efficiency of the non-thermal emissions. This conclusion is graphically summarized in figure 2.8, where the cumulative uncertainty bands on the "true" bounds are shown with and without the inclusion of outflows.

Reionization history refers to the period in the early universe when the first stars and galaxies ionized the intergalactic medium. This process can affect the CMB in various ways,

particularly through the integrated Sachs-Wolfe effect and CMB polarization. Non-standard reionization histories, which deviate from the commonly accepted models, could potentially introduce variations in the CMB spectra. The effects of PBH accretion on the CMB, as discussed in this thesis, are specific to the scenario where PBHs are present in significant numbers in the early universe. The accretion of baryonic matter by PBHs could affect the CMB through additional radiation, which might alter the temperature and polarization anisotropies. While both mechanisms could potentially impact the CMB, the specific nature and scale of these effects could be quite different. Non-standard reionization histories would generally influence the CMB in a more global and uniform manner, whereas PBH accretion effects might be more stochastic and localized, depending on the PBH distribution. To determine if there are degenerate effects (i.e., similar observable impacts from different causes) between these two phenomena on the CMB, detailed cosmological simulations and observational data analysis would be required. This is a a very interesting topic worth exploring in the future.

Looking towards the future, several developments might have a significant impact on our results. On the one hand, should strongly compelling arguments be put forward in favour of one particular accretion geometry, it would significantly reduce the uncertainty on the PBH abundance upper bounds reported in figure 2.8. The same would be true also in the context of the ionization model. On the other hand, however, even more accurate simulations than the ones performed in [80, 81] might find indications for more complex outflow dynamics requiring, for instance, also information on outflow orientation or the transition to trans- or sub-sonic regimes. Taking into account for the potential role of these unknowns would inevitably further widen the size of the aforementioned uncertainty band. Similarly, the disk accretion scenario considered here is only restricted to the collisional ionization case, and extending it to the photo-ionization model would extend the uncertainty region towards low PBH masses.

Overall, we conclude that the path towards a realistic estimate of whether PBHs can make up for a sizeable fraction of the DM and of the events observed at the LVK facilities at the same time (i.e., in the same mass range) is still very long, as both the cosmological constraints and the merger rate estimates are subject to very large theoretical uncertainties. While this should discourage premature claims of exclusion or detection, it should also be seen as a source of

motivation for the improvements to come.

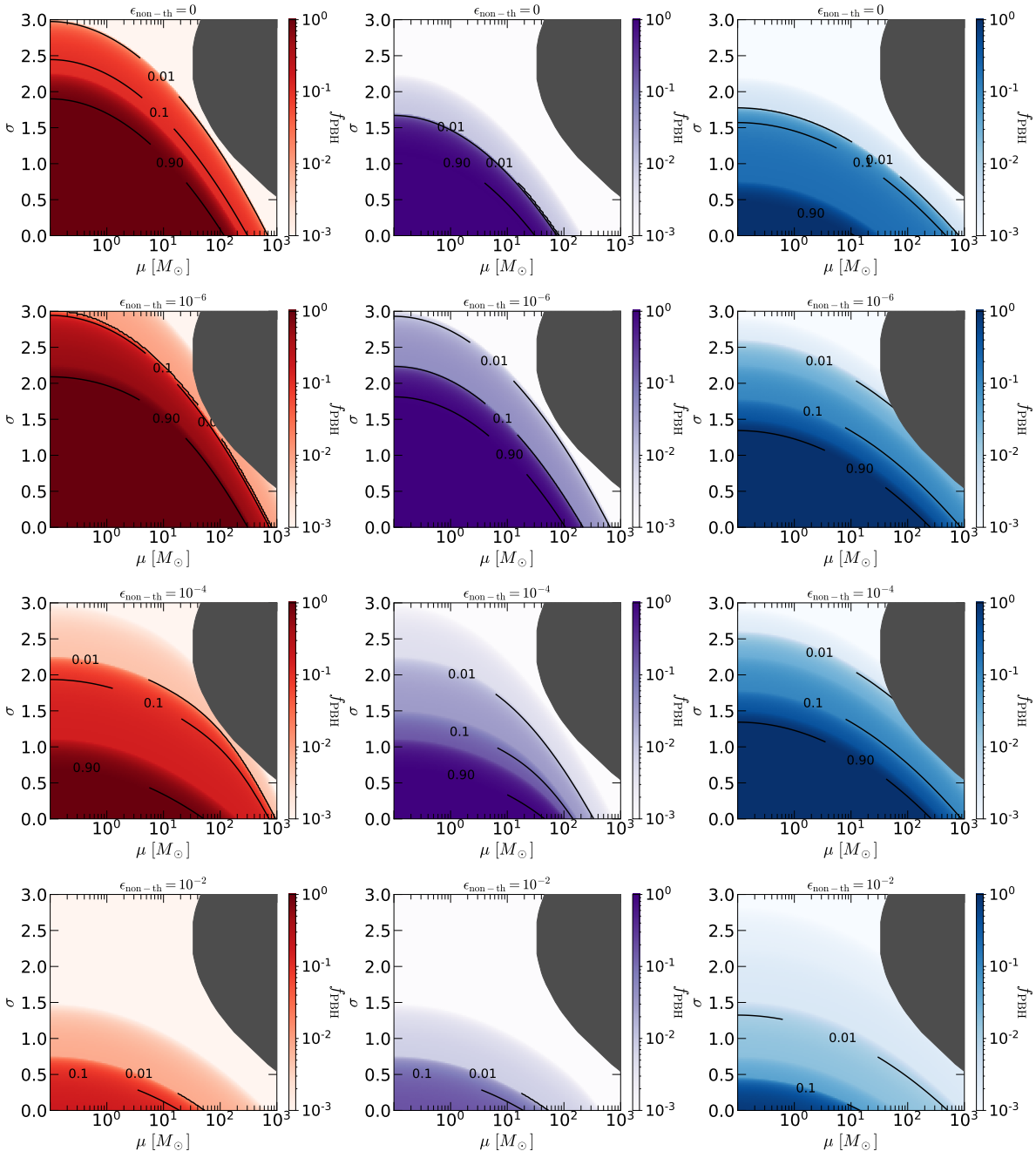

Figure 2.7: Same as in figure 2.6, but for a lognormal EMD. The figure shows the collisional and photoionization regimes for the spherical accretion case (left and center panels, respectively) and the disk accretion model (right panels). We report here all the cases in absence of MF and non-thermal emission (top panels), and with those effects included (middle and bottom panels) for different non-thermal efficiencies. The grey shaded area represents the region of parameter space that cannot be described appropriately by the theoretical model employed in this chapter.

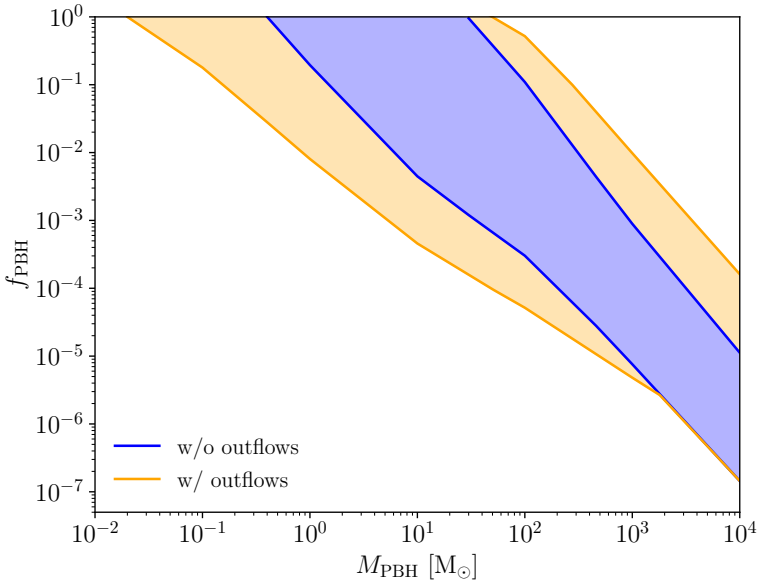

Figure 2.8: Uncertainty bands of both geometries and ionization models with (orange) and without (blue) the inclusion of outflows. The corresponding filled regions of parameter space represent the region where the true constraint lies.

Chapter 3

Large Scale Structure constraints on nDGP

In this chapter we develop a pipeline to set new constraints on scale-independent modified gravity, from the galaxy power spectrum in redshift space of BOSS DR12. The latter is modelled using the effective field theory of large-scale structure up to 1-loop order in perturbation theory. We test our pipeline on synthetic and simulated data, to assess systematic biases on the inferred cosmological parameters due to marginalization and theoretical errors, and we apply it to the normal branch of the DGP model with a ΛCDM background. When applied to synthetic data and cosmological simulations, we observe biased posteriors due to the strong degeneracy between the nDGP parameter $\Omega_{\rm rc}$ and the primordial amplitude of fluctuations A_s. Fixing the latter to the Planck central value, we obtain a posterior distribution with $\Omega_{\rm rc} \lesssim 0.65$ at 95% C.L., under the assumption of a flat prior on $\log_{10}\Omega_{\rm rc}$. This upper bound, however, depends strongly on the prior on $\Omega_{\rm rc}$. To alleviate this effect, we provide an upper bound based on the Bayes factor between the nDGP model and ΛCDM model, which gives $\Omega_{\rm rc} \lesssim 0.2$ at 95% C.L..

The chapter is structured as follows. In sec. 3.1 we briefly introduce the theoretical framework for the nDGP model, while in 3.2 we calculate the 1-loop power spectrum for galaxies in redshift space for a generic scale-independent modified gravity model. Section 3.3 describes the implementation and the validation of the nDGP model in `PyBird`. Before proceeding with the BOSS analysis, we devote sec. 3.4 to reveal the presence of projections effects, i.e. sys-

tematic biases on the 1-d posteriors due to marginalization over the other parameters. We do that by testing our pipeline on synthetic data and on simulations with known cosmological parameters and error specifications adapted to the two BOSS redshift samples. In particular, we use the so-called "PT Challenge" simulations, a set of high-resolution mocks mimicking the SDSS-III BOSS galaxy samples but covering a hundred times larger cumulative volume, which were employed in a blinded challenge consisting in inferring cosmological parameters from the power spectrum multipoles [208] (see sec. 3.4.3 for more details). Testing on simulations allows us also to study theory errors and the largest wavenumber $k_{\rm max}$ that we can reliably use within the effective theory. In sec. 3.5 we present the result of our analysis on the BOSS data and discuss the bounds on $\Omega_{\rm rc}$. We conclude in sec. 3.6. We relegate several discussions to the appendix. In particular, we display the full time-dependent functions of the nDGP scenario in app. A. Appendix B presents a comparison of the bias expansion used in this chapter with the one of the LSS bootstrap introduced in [209] that extends to modified gravity models. Moreover, we discuss how to choose the initial conditions for the linear growth factor in app. C.

We note that a pipeline analogous to the one presented here, based on the EFTofLSS, has been recently developed and used [210] to constrain the dark scattering model of interacting dark energy [211] with BOSS data.

3.1 Theoretical Framework

An important source of information about the universe comes from large-scale structure (LSS). Future surveys, such as DESI [79],*Euclid* [26], and LSST [78], will map the distribution of galaxies over huge volumes with unprecedented precision: they will likely become the major source of cosmological information in the coming decades. A major goal of these surveys is the study of the initial conditions and a measurement of neutrino masses, see e.g. [212]. But these data will also allow us to perform precision tests of the standard cosmological model and of the theory of general relativity (GR) on large scales, and to exclude many of their extensions.

For this task, it is important to have a robust understanding of the cosmic web at the scales where the data will be precise enough. Recently, progress has been made in modelling the

clustering of galaxies, notably the power spectrum, i.e. the Fourier transform of the 2-point function, of the galaxy distribution in redshift space. In particular, a fairly accurate modelling of the power spectrum can be obtained by using perturbation theory [213] up to 1-loop order, supplemented by the renormalization of large-scale fields due to unknown small-scale physics. In fact, the effect of small-scale physics on correlators can be modeled by the introduction of a set of counterterms [214, 215, 216, 217] and bias parameters [218, 219, 220, 221, 222, 223, 224, 225] (see [226] for a review), whose scale dependence can be predicted by symmetries.

This treatment goes under the name of effective field theory of large-scale structure (EFTofLSS) [214, 216], which has been recently used to model the power spectrum at 1-loop for the analysis of the Baryon Oscillation Spectroscopic Survey (BOSS) dataset [11], giving constraints on cosmological parameters with a good level of accuracy, see [63, 227, 228]. The results of these and subsequent analyses—e.g. regarding constraints on neutrino masses [229, 230], the H_0 tension [231, 232, 233], beyond-ΛCDM models [61, 234], redshift space distortions (RSD) [235, 236]—represent an important step forward in the study of LSS within the EFTofLSS. More recently, the bispectrum—i.e., the Fourier transform of the 3-point function—from BOSS observation has been analyzed using the tree-level [63, 237] and 1-loop EFTofLSS modelling [238], providing alternative constraints on primordial non-gaussianities [239, 240, 241]. For an extensive review of basic standard perturbation theory and EFTofLSS, we refer the reader to E.

In this chapter we show that current and future LSS data can be used to put reliable constraints on modified gravity as well. Specifically, we develop a pipeline to analyze the galaxy power spectrum in redshift space, that can be used to test general scale-independent extensions of the ΛCDM model. Then we apply it to BOSS data and constrain specifically the so-called normal branch[1] of the Dvali-Gabadadze-Porrati (DGP) model [246], or nDGP for short. Despite introducing a single additional parameter with respect to ΛCDM, it incorporates many interesting cosmological features: modifications in the background evolution, in the strength of the gravitational clustering and in the dynamics of the fluctuations, at linear order and beyond. For these reasons, this model is one of the most studied modification of GR and has been implemented in several N-body simulations, see e.g. [247] and references therein.

From a fundamental physics standpoint, the nDGP model is captivating because it proposes

[1]The self-accelerating branch [242] of the DGP model is unstable [243, 244, 245].

an alternative to GR at cosmological scales and it aims to explain the accelerated expansion of the universe. This model suggests a modification in the gravitational force law at distances beyond a crossover scale r_c, typically estimated to be on the order of the current Hubble scale, H_0^{-1}. The core idea of this model is its potential to replicate the ΛCDM model's predictions at certain scales while providing distinct outcomes at others. For instance, it predicts a deviation in the growth rate of cosmic structures and variations in gravitational lensing effects, which could be measurable through current and upcoming cosmological surveys. These deviations are particularly evident in the growth rate parameter f, where nDGP models tend to predict lower values compared to ΛCDM, especially at redshifts $z < 1$. Moreover, nDGP can be empirically tested through its unique signatures in the large-scale structure of the universe, such as galaxy distributions and CMB anisotropies. These observable differences from GR are crucial for the model's falsifiability and make it a candidate worthy of exploration in the quest to understand the nature of dark energy and the dynamics of cosmic expansions.

In the original DGP model, the universe is described by a 4d brane embedded in a 5d Minkowski spacetime. The cross-over scale between the 5d and 4d behaviour is given by the length scale r_c, which represents the fundamental extra parameter of this model, with GR being smoothly recovered by taking the cross-over scale much larger than the current Hubble scale H_0^{-1}, i.e., for $H_0 r_c \gg 1$. Constraints on this parameter are traditionally expressed in terms of the dimensionless quantity [248]

$$\Omega_{\rm rc} \equiv \frac{1}{4 r_c^2 H_0^2}. \tag{3.1}$$

For instance, ref. [248] puts an upper bound to the nDGP model of $\Omega_{\rm rc} < 0.020$ (95% C.L.) from WMAP and other available CMB data (including ISW-galaxy correlation), supernovae and measurements of H_0, assuming a cosmological constant in the background and a modified expansion history without spatial curvature. A more recent analysis with the same hypothesis was performed in [249] including CMB data from Planck, supernovae and BAO.

In contrast with these analyses, in the following we consider a version of the nDGP model where the background expansion history exactly reproduces the ΛCDM one in a spatially-flat universe. This is obtained by considering, instead of a cosmological constant, a dark energy component whose background dynamics exactly compensates the modified background evo-

lution of the nDGP model [250]. Deviations from ΛCDM take place only in the late-time evolution of perturbations, so that the model is weakly constrained by supernovae, sensitive only to the recent background expansion history. Similarly, it is weakly constrained by CMB data, whose dependence on late-time perturbations is only through the small integrated Sachs-Wolfe effect and lensing. Focusing on a nDGP model with ΛCDM background expansion allows us to probe the constraining power of LSS data, which are the most sensitive to the late-time evolution of perturbations.

Previous constraints on the nDGP model obtained in this setting are much weaker: for instance in [251] it was found $\Omega_{\rm rc} \lesssim 40$, using measurements of the monopole and the quadrupole of the correlation function from SDSS DR7 data, with fixed H_0. More recently, Ref. [252] used the values of the parameter combination $f\sigma_8$ estimated from the BOSS DR12 data [253] to set an upper bound of $\Omega_{\rm rc} \lesssim 0.25$ at 95% C.L. This constraint was obtained by setting tight Gaussian priors on both $\Omega_{\rm m0}$ and $\sigma_8^{\Lambda CDM}({\rm z}=0)$, corresponding to 1σ Planck constraints assuming flat ΛCDM.

As we will see below, in this chapter we obtain $\Omega_{\rm rc} \lesssim 0.65$ at 95% C.L. from the BOSS dataset. This constraint can be obtained only after fixing the primordial amplitude of fluctuations A_s derived from Planck's measurements. Relaxing A_s, the bound obtained is much looser and biased because the effect of modified gravity on the growth of structures is very degenerate with A_s. In principle, this degeneracy could be broken by combining data from different redshift bins, as the effect of $\Omega_{\rm rc}$ is time dependent. While this could be an effective strategy for future surveys such as DESI and *Euclid*, this is not the case for the BOSS data, as the two redshift bins analyzed in this chapter are very close.

The constraint presented above depends on the choice of prior for the $\Omega_{\rm rc}$ parameter. For this reason we also provide a prior-independent constraint on the nDGP parameter based on the so-called Bayes factor [39]. This procedure is particularly useful for constraining parameters with a non-Gaussian posterior. With this approach we obtain the upper value $\Omega_{\rm rc} \lesssim 0.2$ at 95% C.L..

We model the galaxy redshift-space power spectrum using the EFTofLSS implemented in `PyBird` [61], a fast Python code for the evaluation of the 1-loop power spectrum, developed for ΛCDM and modified here to include scale-independent modifications of gravity. We stress

that, although our analysis is restricted to the nDGP model alone, it can be straightforwardly extended to other scale-independent models, such as those described by the general single-field framework of the EFT of dark energy [40, 41, 42, 43, 44] extended beyond linear order [31, 30]. This opens the possibility of putting tighter constraints on a variety of dark energy and modified gravity scenarios by combining Planck data with future surveys that will scan larger volumes and will contain higher number of galaxies than SDSS-III.

3.2 Galaxy clustering in modified gravity

In this section we work out the expression of the galaxy power spectrum in redshift space for generic *scale-independent* modified gravity models. In sec. 3.2.1, following earlier works, see e.g. [254, 30], we first introduce the evolution equations of dark matter in modified gravity, focusing on standard perturbation theory without counterterms. The exact solutions to these equations in perturbation theory are derived in sec. 3.2.2. We then discuss the bias expansion in redshift space in sec. 3.2.3, following [64]. In this reference, the bias expansion was derived in the exact time dependent case (i.e. without assuming the commonly used Einstein-de Sitter approximation) for the ΛCDM model. In [209], some of us showed that this expansion also holds for scale-independent modified gravity models sharing the same symmetries as ΛCDM. Finally, in the last section, 3.2.4, we write down the 1-loop power spectrum, including all counterterms from the EFTofLSS used in `PyBird`.

3.2.1 Dark matter dynamics

We consider a perturbed spatially-flat Friedmann-Lemaître-Robertson-Walker metric in the Newtonian gauge, focusing on scalar perturbations, i.e.

$$ds^2 = -(1+2\Phi)dt^2 + a^2(t)(1-2\Psi)d\mathbf{x}^2 \,. \tag{3.2}$$

We work in the Jordan frame, where matter is minimally coupled to the gravitational metric. In this case test particles follow geodesics and the dark matter fluid is described by the standard

continuity and Euler equations

$$\dot{\delta} + a^{-1}\partial_i\left((1+\delta)v^i\right) = 0\,, \tag{3.3}$$

$$\dot{v}^i + Hv^i + \frac{1}{a}v^j\partial_j v^i + \frac{1}{a}\partial_i\Phi = -\frac{1}{a\rho_{\rm m}}\partial_j\tau^{ij}\,, \tag{3.4}$$

where $\rho_{\rm m}$ is the dark matter energy density, with background value $\bar{\rho}_{\rm m}$, $\delta \equiv \rho_{\rm m}/\bar{\rho}_{\rm m} - 1$ and v^i are respectively the energy density contrast and the velocity of dark matter, a dot denotes the derivative with respect to the cosmic time t and $H \equiv \dot{a}/a$ is the Hubble rate. Following [214, 215, 216], we have written down the smoothed continuity and Euler equations: the right-hand side of eq. (3.4) is the effective stress-energy tensor describing how the short modes affect the dynamics of the long modes resulting from this smoothing procedure. See [30] for a generalization to modified gravity models of this smoothing procedure and stress-energy tensor.

In GR, one closes these two equations with the Poisson equation. In modified gravity, however, the Poisson equation no longer holds. In order to proceed, we must thus discuss how to relate Φ to the fluid variables. To do so, in the following we specialize to scale-independent models, i.e. we assume that the mass of the scalar field responsible for modifying gravity is much smaller than the fundamental frequency of the survey. This is typically the case for Horndeski theories [255, 256], where higher-order derivative terms can lead to self-acceleration [243, 257] and display Vainshtein screening [258] around overdense regions. In this case, one can use the full field equations involving both Φ and Ψ([2]) to express the Laplacian of Φ in terms of the density contrast. This expression contains terms linear in δ, as in the Poisson equation, but in general there are also higher-order terms. Since we are interested in computing the 1-loop power spectrum, we will only consider terms up to third order in δ.

In summary, in a generic model one obtains (see e.g. [31, 30])

$$\begin{aligned}\frac{\partial^2\Phi}{H^2a^2} = {}& \frac{3\,\Omega_{{\rm m},a}}{2}\,\nu\,\delta + \left(\frac{3\,\Omega_{{\rm m},a}}{2}\right)^2\nu_2\left[\delta^2 - \left(\partial^{-2}\partial_i\partial_j\delta\right)^2\right] \\ & + \left(\frac{3\,\Omega_{{\rm m},a}}{2}\right)^3\nu_{22}\left[\delta - \left(\partial^{-2}\partial_i\partial_j\delta\right)\partial^{-2}\partial_i\partial_j\right]\left[\delta^2 - \left(\partial^{-2}\partial_k\partial_l\delta\right)^2\right] \\ & + \left(\frac{3\,\Omega_{{\rm m},a}}{2}\right)^3\nu_3\left[\delta^3 - 3\delta\left(\partial^{-2}\partial_i\partial_j\delta\right)^2 + 2(\partial^{-2}\partial_i\partial_j\delta)(\partial^{-2}\partial_k\partial_j\delta)(\partial^{-2}\partial_i\partial_k\delta)\right] + \mathcal{O}(\delta^4)\,,\end{aligned} \tag{3.5}$$

[2] In these theories Φ and Ψ are not necessarily the same.

where

$$\Omega_{\mathrm{m},a} \equiv \frac{\bar{\rho}_{\mathrm{m}}}{3M^2H^2} \tag{3.6}$$

is the *time-dependent* dark matter energy density in critical units and M is the effective Planck mass, which in general can depend on time. The functions $\nu(a)$, $\nu_2(a)$, $\nu_{22}(a)$, and $\nu_3(a)$ parametrize the time-dependent amplitude of the higher order terms. They can be related to the original parameters of the modified gravity model at hand[3] but from the viewpoint of the LSS equations, they are simply functions of time.[4] In general relativity $M = M_{\mathrm{Pl}} = (8\pi G)^{-1/2}$, $\nu = 1$, $\nu_2 = \nu_3 = \nu_{22} = 0$ and we recover the standard Poisson equation. Note that Ψ does not directly appear in the fluid equations in the non-relativistic limit considered here and we do not need it for this study.

At linear order one can neglect the higher-order terms in eqs. (3.3)–(3.5) and use these three equations to write a single (second-order in time) equation for the linearized density contrast $\delta^{(1)}(a)$. Its time dependence is captured by the growth factors $D(a)$, defined such that

$$\delta^{(1)}(a) = D(a)\delta^{(1)}(a_{\mathrm{in}}) \ , \tag{3.7}$$

satisfying

$$\frac{d^2D(a)}{d\ln a^2} + \left(2 + \frac{d\ln H}{d\ln a}\right)\frac{dD(a)}{d\ln a} - \frac{3}{2}\nu(a)\Omega_{\mathrm{m},a}(a)D(a) = 0 \ , \tag{3.8}$$

and normalized to unity at some initial time deep in matter domination era, $a = a_{\mathrm{in}}$. Assuming a ΛCDM background expansion rate, the difference with the standard ΛCDM case is captured by the function $\nu(a)$ in the last term, which modifies the strength of the gravitational interaction. In the following we assume that $\nu \to 1$ (i.e., GR is recovered) at early time. Since in this limit $\Omega_{\mathrm{m},a} \to 1$, at early time the solutions of this equation are the usual growing and decaying solutions in matter domination, i.e. $D_+ \propto a$ and $D_- \propto a^{-3/2}$, respectively. We can thus label the late-time solution as growing (decaying) if at early times it grows as a (decays as $a^{-3/2}$). The Green's functions of this equation are discussed in the next subsection.

[3] The derivation of eq. (3.5) is explicitly laid out in [31] for Horndeski models described in terms of the EFT of dark energy. There, one also finds the relations between ν, ν_2, ν_{22}, and ν_3 and the EFT of dark energy parameters, expressed in terms of the Horndeski Lagrangian. The analogous expression for the nDGP model is derived in [32].

[4] Note that this is only valid on length scales above the nonlinear scale where $\delta \sim 1$ and above the Vainshtein screening [258] scale where scalar field fluctuations enter the nonlinear regime, see [31].

To proceed, we also define the linear growth rate,

$$f \equiv \frac{d\ln D}{d\ln a} \,. \tag{3.9}$$

It satisfies the equation

$$\frac{df}{d\ln a} + f^2 + \left(2 + \frac{d\ln H}{d\ln a}\right) f - \frac{3}{2}\nu\Omega_{\mathrm{m},a} = 0 \,, \tag{3.10}$$

that can be straightforwardly derived from eq. (3.8). We define f_+ and f_- by eq. (3.9) with $D = D_+$ and $D = D_-$, respectively.

It is now convenient to go to Fourier space and study the dynamics of δ and v^i as a function of the scale factor. We neglect momentarily the stress-energy tensor on the right-hand side of eq. (3.4). Its effect will be discussed in sec. 3.2.4. Thus, we define the conformal Hubble rate $\mathcal{H} \equiv aH$ and use a prime to denote the derivative with respect to a. Moreover, we also introduce the rescaled velocity divergence θ, defined as

$$\theta \equiv -\frac{\partial_i v^i}{f_+ \mathcal{H}} \,. \tag{3.11}$$

Neglecting vorticity modes, the dynamics of δ and θ are now described by

$$a\,\delta'_{\mathbf{k}}(a) - f_+\theta_{\mathbf{k}}(a) = \int_{\mathbf{k}_1,\mathbf{k}_2} (2\pi)^3\delta_D(\mathbf{k}-\mathbf{k}_{12}) \times f_+\alpha(\mathbf{k}_1,\mathbf{k}_2)\theta_{\mathbf{k}_1}(a)\delta_{\mathbf{k}_2}(a) \,, \tag{3.12}$$

$$a\,\theta'_{\mathbf{k}}(a) - f_+\theta_{\mathbf{k}}(a) + \frac{3}{2}\frac{\nu\,\Omega_{\mathrm{m},a}}{f_+}\theta_{\mathbf{k}}(a) + \frac{1}{f_+}\frac{k^2}{\mathcal{H}^2}\Phi_{\mathbf{k}}(a) = \int_{\mathbf{k}_1,\mathbf{k}_2} (2\pi)^3\delta_D(\mathbf{k}-\mathbf{k}_{12}) \times f_+\beta(\mathbf{k}_1,\mathbf{k}_2)\theta_{\mathbf{k}_1}(a)\theta_{\mathbf{k}_2}(a) \,, \tag{3.13}$$

where to derive the second equation we have used eq. (3.10). Moreover, $\alpha(\mathbf{k}_1,\mathbf{k}_2)$ and $\beta(\mathbf{k}_1,\mathbf{k}_2)$ are the standard dark matter interaction vertices,

$$\alpha(\mathbf{k}_1,\mathbf{k}_2) = 1 + \frac{\mathbf{k}_1\cdot\mathbf{k}_2}{k_1^2} \qquad \text{and} \qquad \beta(\mathbf{k}_1,\mathbf{k}_2) = \frac{|\mathbf{k}_1+\mathbf{k}_2|^2\mathbf{k}_1\cdot\mathbf{k}_2}{2k_1^2k_2^2} \,, \tag{3.14}$$

and we have used the notation $\int_{\mathbf{k}_1,\ldots,\mathbf{k}_n} \equiv \int \frac{d^3k_1}{(2\pi)^3}\cdots\int\frac{d^3k_n}{(2\pi)^3}$ and $\mathbf{k}_{1\ldots n} \equiv \mathbf{k}_1 + \ldots + \mathbf{k}_n$.

In Fourier space, the generalized Poisson equation (3.5) reads

$$
\begin{aligned}
-\frac{k^2}{\mathcal{H}^2}\Phi_{\mathbf{k}}(a) &= \nu\frac{3\,\Omega_{\mathrm{m},a}}{2}\,\delta_{\mathbf{k}}(a) \\
&+ \nu_2\left(\frac{3\,\Omega_{\mathrm{m},a}}{2}\right)^2\int_{\mathbf{k}_1,\mathbf{k}_2}(2\pi)^3\delta_D(\mathbf{k}-\mathbf{k}_{12})\,\gamma(\mathbf{k}_1,\mathbf{k}_2)\delta_{\mathbf{k}_1}(a)\delta_{\mathbf{k}_2}(a) \\
&+ \nu_3\left(\frac{3\,\Omega_{\mathrm{m},a}}{2}\right)^3\int_{\mathbf{k}_1,\mathbf{k}_2,\mathbf{k}_3}(2\pi)^3\delta_D(\mathbf{k}-\mathbf{k}_{123})\gamma_3(\mathbf{k}_1,\mathbf{k}_2,\mathbf{k}_3)\delta_{\mathbf{k}_1}(a)\delta_{\mathbf{k}_2}(a)\delta_{\mathbf{k}_3}(a) \\
&+ \nu_{22}\left(\frac{3\,\Omega_{\mathrm{m},a}}{2}\right)^3\int_{\mathbf{k}_1,\mathbf{k}_2,\mathbf{q}_1,\mathbf{q}_2}(2\pi)^3\delta_D(\mathbf{k}-\mathbf{k}_{12})(2\pi)^3\delta_D(\mathbf{k}_2-\mathbf{q}_{12}) \\
&\qquad\qquad\times\gamma(\mathbf{k}_1,\mathbf{k}_2)\gamma(\mathbf{q}_1,\mathbf{q}_2)\delta_{\mathbf{k}_1}(a)\delta_{\mathbf{q}_1}(a)\delta_{\mathbf{q}_2}(a)\,,
\end{aligned}
\tag{3.15}
$$

where the new kernels inside the integrals are given by

$$
\begin{aligned}
\gamma(\mathbf{k}_1,\mathbf{k}_2) &= 1-\left(\hat{\mathbf{k}}_1\cdot\hat{\mathbf{k}}_2\right)^2\,, \\
\gamma_3(\mathbf{k}_1,\mathbf{k}_2,\mathbf{k}_3) &= 1+2\left(\hat{\mathbf{k}}_1\cdot\hat{\mathbf{k}}_2\right)\left(\hat{\mathbf{k}}_1\cdot\hat{\mathbf{k}}_3\right)\left(\hat{\mathbf{k}}_2\cdot\hat{\mathbf{k}}_3\right)-\left(\hat{\mathbf{k}}_1\cdot\hat{\mathbf{k}}_3\right)^2-\left(\hat{\mathbf{k}}_2\cdot\hat{\mathbf{k}}_3\right)^2-\left(\hat{\mathbf{k}}_1\cdot\hat{\mathbf{k}}_2\right)^2\,.
\end{aligned}
\tag{3.16}
$$

For completeness, we have included above the cubic vertex proportional to ν_3. However, since in the PS at 1-loop it enters as $\gamma_3(\mathbf{k},\mathbf{q},-\mathbf{q})=0$ [30] it does not contribute to the power spectrum at one loop and we will discard it. Therefore, removing this term the perturbation equations above become

$$
a\delta'_{\mathbf{k}}(a)-f_+(a)\theta_{\mathbf{k}}(a)=S^{\delta}_{\mathbf{k}}(a)\,, \tag{3.17}
$$

$$
a\theta'_{\mathbf{k}}(a)-f_+(a)\theta_{\mathbf{k}}(a)+\frac{3}{2}\frac{\nu(a)\Omega_{\mathrm{m},a}(a)}{f_+(a)}\left(\theta_{\mathbf{k}}(a)-\delta_{\mathbf{k}}(a)\right)=S^{\theta}_{\mathbf{k}}(a)\,, \tag{3.18}
$$

with

$$
S^{\delta}_{\mathbf{k}}=(2\pi)^3\int_{\mathbf{k}_1\mathbf{k}_2}\delta_D(\mathbf{k}-\mathbf{k}_{12})f_+\alpha(\mathbf{k}_1,\mathbf{k}_2)\theta_{\mathbf{k}_1}\delta_{\mathbf{k}_2}\,, \tag{3.19}
$$

$$
\begin{aligned}
S^{\theta}_{\mathbf{k}} &= (2\pi)^3\int_{\mathbf{k}_1\mathbf{k}_2}\delta_D(\mathbf{k}-\mathbf{k}_{12})\left[f_+\beta(\mathbf{k}_1,\mathbf{k}_2)\theta_{\mathbf{k}_1}\theta_{\mathbf{k}_2}+\frac{\nu_2}{f_+}\left(\frac{3\Omega_{\mathrm{m},a}}{2}\right)^2\gamma(\mathbf{k}_1,\mathbf{k}_2)\delta_{\mathbf{k}_1}\delta_{\mathbf{k}_2}\right] \\
&+(2\pi)^3\int_{\mathbf{k}_1\mathbf{k}_2\mathbf{q}_1\mathbf{q}_2}\delta_D(\mathbf{k}_2-\mathbf{q}_{12})\delta_D(\mathbf{k}-\mathbf{k}_{12})\frac{\nu_{22}}{f_+}\left(\frac{3\Omega_{\mathrm{m},a}}{2}\right)^3\gamma(\mathbf{q}_1,\mathbf{q}_2)\gamma(\mathbf{k}_1,\mathbf{k}_2)\delta_{\mathbf{k}_1}\delta_{\mathbf{q}_1}\delta_{\mathbf{q}_2}\,.
\end{aligned}
\tag{3.20}
$$

Moreover, for later purposes it is convenient to define the symmetrized α as $\alpha_s(\mathbf{k}_1,\mathbf{k}_2)=\frac{1}{2}(\alpha(\mathbf{k}_1,\mathbf{k}_2)+\alpha(\mathbf{k}_2,\mathbf{k}_1))$ and notice that

$$
\gamma(\mathbf{k}_1,\mathbf{k}_2)=\alpha_s(\mathbf{k}_1,\mathbf{k}_2)-\beta(\mathbf{k}_1,\mathbf{k}_2)\,. \tag{3.21}
$$

3.2.2 Perturbative solutions for dark matter

Following [259], to construct the higher-order solutions to eqs. (3.17) and (3.18), we need the Green's functions. For general scale-independent modified gravity models, where the deviations from GR are captured at linear order by the time-dependent function ν, these are defined as

$$a\frac{dG^{\delta}_{\sigma}(a,\tilde{a})}{da} - f_{+}G^{\theta}_{\sigma}(a,\tilde{a}) = \lambda_{\sigma}\delta_{D}(a-\tilde{a}), \tag{3.22}$$

$$a\frac{dG^{\theta}_{\sigma}(a,\tilde{a})}{da} - f_{+}G^{\theta}_{\sigma}(a,\tilde{a}) + \frac{3}{2}\frac{\nu\Omega_{\mathrm{m},a}}{f_{+}}\left(G^{\theta}_{\sigma}(a,\tilde{a}) - G^{\delta}_{\sigma}(a,\tilde{a})\right) = (1-\lambda_{\sigma})\delta_{D}(a-\tilde{a}), \tag{3.23}$$

where $\lambda_1 = 1$ and $\lambda_2 = 0$.

Explicitly, they are given by

$$G^{\delta}_{1}(a,\tilde{a}) = \frac{1}{\tilde{a}W(\tilde{a})}\left(\frac{dD_{-}(\tilde{a})}{d\tilde{a}}D_{+}(a) - \frac{dD_{+}(\tilde{a})}{d\tilde{a}}D_{-}(a)\right)\Theta(a-\tilde{a})\,, \tag{3.24}$$

$$G^{\delta}_{2}(a,\tilde{a}) = \frac{f_{+}(\tilde{a})/\tilde{a}^2}{W(\tilde{a})}\left(D_{+}(\tilde{a})D_{-}(a) - D_{-}(\tilde{a})D_{+}(a)\right)\Theta(a-\tilde{a})\,, \tag{3.25}$$

$$G^{\theta}_{1}(a,\tilde{a}) = \frac{a/\tilde{a}}{f_{+}(a)W(\tilde{a})}\left(\frac{dD_{-}(\tilde{a})}{d\tilde{a}}\frac{dD_{+}(a)}{da} - \frac{dD_{+}(\tilde{a})}{d\tilde{a}}\frac{dD_{-}(a)}{da}\right)\Theta(a-\tilde{a})\,, \tag{3.26}$$

$$G^{\theta}_{2}(a,\tilde{a}) = \frac{f_{+}(\tilde{a})a/\tilde{a}^2}{f_{+}(a)W(\tilde{a})}\left(D_{+}(\tilde{a})\frac{dD_{-}(a)}{da} - D_{-}(\tilde{a})\frac{dD_{+}(a)}{da}\right)\Theta(a-\tilde{a})\,, \tag{3.27}$$

where $W(\tilde{a})$ is the Wronskian of D_+ and D_-,

$$W(\tilde{a}) = \frac{dD_{-}(\tilde{a})}{d\tilde{a}}D_{+}(\tilde{a}) - \frac{dD_{+}(\tilde{a})}{d\tilde{a}}D_{-}(\tilde{a})\,, \tag{3.28}$$

$\Theta(a-\tilde{a})$ is the Heaviside step function and we impose the boundary conditions

$$G^{\delta}_{\sigma}(a,\tilde{a}) = 0 \qquad \text{and} \qquad G^{\theta}_{\sigma}(a,\tilde{a}) = 0 \qquad \text{for} \qquad \tilde{a} > a\,, \tag{3.29}$$

$$G^{\delta}_{\sigma}(\tilde{a},\tilde{a}) = \frac{\lambda_{\sigma}}{\tilde{a}} \qquad \text{and} \qquad G^{\theta}_{\sigma}(\tilde{a},\tilde{a}) = \frac{(1-\lambda_{\sigma})}{\tilde{a}}\,. \tag{3.30}$$

We write the dark matter density contrast and velocity divergence in a perturbative expansion of the form

$$\delta_{\mathbf{k}}(a) = \sum_{n=1}^{\infty}\delta^{(n)}_{\mathbf{k}}(a) \quad \text{and} \quad \theta_{\mathbf{k}}(a) = \sum_{n=1}^{\infty}\theta^{(n)}_{\mathbf{k}}(a), \tag{3.31}$$

which allows us to solve equations (3.17) and (3.18) order by order. The perturbative solution of these equations can then be written as an integral over time-dependent momentum kernels,

$$\begin{aligned}\delta^{(n)}_{\mathbf{k}}(a) &= \int \frac{d^3q_1}{(2\pi)^3}\cdots\frac{d^3q_n}{(2\pi)^3}(2\pi)^3\delta_D(\mathbf{k}-\mathbf{q}_{1n})K^{(n)}_{\delta}(\mathbf{q}_1,\ldots,\mathbf{q}_n,a)\delta^{(1)}_{\mathbf{q}_1}(a)\ldots\delta^{(1)}_{\mathbf{q}_n}(a)\,,\\ \theta^{(n)}_{\mathbf{k}}(a) &= \int \frac{d^3q_1}{(2\pi)^3}\cdots\frac{d^3q_n}{(2\pi)^3}(2\pi)^3\delta_D(\mathbf{k}-\mathbf{q}_{1n})K^{(n)}_{\theta}(\mathbf{q}_1,\ldots,\mathbf{q}_n,a)\delta^{(1)}_{\mathbf{q}_1}(a)\ldots\delta^{(1)}_{\mathbf{q}_n}(a)\,.\end{aligned} \tag{3.32}$$

Up to third order, the kernels are given by [64],[5]

$$K^{(1)}_{\lambda}(\mathbf{q}_1,a) = 1\,, \tag{3.33}$$

$$K^{(2)}_{\lambda}(\mathbf{q}_1,\mathbf{q}_2,a) = \alpha_s(\mathbf{q}_1,\mathbf{q}_2)\mathcal{G}^{\lambda}_1 + \beta(\mathbf{q}_1,\mathbf{q}_2)\mathcal{G}^{\lambda}_2\,, \tag{3.34}$$

$$K^{(3)}_{\lambda}(\mathbf{q}_1,\mathbf{q}_2,\mathbf{q}_3,a) = \alpha^{\sigma}(\mathbf{q}_1,\mathbf{q}_2,\mathbf{q}_3)\mathcal{U}^{\lambda}_{\sigma} + \beta^{\sigma}(\mathbf{q}_1,\mathbf{q}_2,\mathbf{q}_3)\mathcal{V}^{\lambda}_{\sigma 2} + \gamma^{\sigma}(\mathbf{q}_1,\mathbf{q}_2,\mathbf{q}_3)\mathcal{V}^{\lambda}_{\sigma 1} \tag{3.35}$$

where repeated $\sigma \in \{1,2\}$ are summed over and $\lambda \in \{\delta,\theta\}$. The six momentum kernels at third order $\{\alpha_\sigma,\beta_\sigma,\gamma_\sigma\}$ are products of α_s and β, while $\{\mathcal{G}^{\lambda}_1,\mathcal{G}^{\lambda}_2,\mathcal{U}^{\lambda}_{\sigma},\mathcal{V}^{\lambda}_{\sigma\tilde{\sigma}}\}$, where $\tilde{\sigma}\in\{1,2\}$, are time-dependent functions resulting from equations (3.17) and (3.18). All these functions are explicitly given in app. A. Moreover, in app. B.1 we discuss the relation between this expansion and the (equivalent) one derived using the bootstrap approach [209].

3.2.3 Biased tracers in redshift space

Galaxies are biased tracers of the long wavelength dark matter field distribution (see [226] for a review). As such, their density distribution δ_g can be related to the linear dark matter density distribution $\delta^{(1)}$ and its derivatives (see e.g. [219, 220, 221, 223, 222, 224, 225]). This relation is encoded by a bias expansion given in terms of the kernels $K^{(n)}_{\delta_g}$, defined by

$$\delta^{(n)}_{g,\mathbf{k}}(\eta) = \int \frac{d^3\mathbf{q}_1}{(2\pi)^3}\cdots\int \frac{d^3\mathbf{q}_n}{(2\pi)^3}(2\pi)^3\delta_D(\mathbf{k}-\mathbf{q}_{1\ldots n})K^{(n)}_{\delta_g}(\mathbf{q}_1,\ldots,\mathbf{q}_n,\eta)\delta^{(1)}_{\mathbf{q}_1}(\eta)\ldots\delta^{(1)}_{\mathbf{q}_n}(\eta)\,. \tag{3.36}$$

In what follows we use the same bias expansion and kernels introduced in [63] for a ΛCDM cosmology using the Einstein-de Sitter (EdS) approximation and extended to an exact time-dependent evolution in [64]. It was shown in [209], using the so-called bootstrap approach,

[5] In [64], eqs. (3.33)–(3.35) are derived assuming ΛCDM but their validity extends also to other models respecting the same symmetries, see [209].

that this bias expansion does not restrict to ΛCDM but can be straightforwardly applied to a large class of modified gravity models, i.e. all those models that share the same symmetries with ΛCDM. It can be thus applied to the nDGP model and to all single-field models within the Horndeski class.

Using this approach, one can show that the kernels up to third order can be expressed in terms of seven perturbative bias coefficients. However, for the calculation of the 1-loop power spectrum the third-order kernel appears with a particular combination of momenta, $K^{(3)}_{\delta_g}(\mathbf{q}, -\mathbf{q}, \mathbf{k}; a)$, from which we subtract its $|\mathbf{q}|/|\mathbf{k}| \to \infty$ limit. This reduces the effective number of bias parameters that enter the calculation to four, that we denote by b_1, b_2, b_3, and b_4.[6] See app. B.2 for details.

The relevant terms then are given by

$$K^{(1)}_{\delta_g}(\mathbf{k}; a) = b_1\,, \tag{3.37}$$

$$K^{(2)}_{\delta_g}(\mathbf{q}_1, \mathbf{q}_2; a) = (-b_1 + b_2 + b_4) + b_1\beta(\mathbf{q}_1, \mathbf{q}_2) + \left(b_1 - \frac{2}{7}b_2\right)\gamma(\mathbf{q}_1, \mathbf{q}_2)\,, \tag{3.38}$$

$$\begin{aligned} K^{(3)}_{\delta_g}(\mathbf{q}_1, \mathbf{q}_2, \mathbf{q}_3; a)\Big|_{\rm sub} &= \frac{b_1}{3}O_{\beta\beta}(\mathbf{q}_1, \mathbf{q}_2, \mathbf{q}_3) + \frac{1}{3}\left(\frac{g(a)b_1}{2} + \frac{b_3}{21}\right)O_{\gamma\beta}(\mathbf{q}_1, \mathbf{q}_2, \mathbf{q}_3) \\ &\quad + \frac{1}{3}\left(\frac{g(a)b_1}{2} - \frac{b_3}{21}\right)\left(O_{\gamma\gamma}(\mathbf{q}_1, \mathbf{q}_2, \mathbf{q}_3) + \frac{1}{2}O_{\gamma\alpha_a}(\mathbf{q}_1, \mathbf{q}_2, \mathbf{q}_3)\right) + \text{cyclic}, \end{aligned} \tag{3.39}$$

where we have defined,

$$O_{XY}(\mathbf{q}_1, \mathbf{q}_2, \mathbf{q}_3) \equiv X(\mathbf{q}_1, \mathbf{q}_2)\, Y(\mathbf{q}_{12}, \mathbf{q}_3)\,, \tag{3.40}$$

where X, Y are the kernels β, γ and α_a, with

$$\alpha_a(\mathbf{q}_1, \mathbf{q}_2) \equiv \alpha(\mathbf{q}_1, \mathbf{q}_2) - \alpha(\mathbf{q}_2, \mathbf{q}_1)\,, \tag{3.41}$$

and g is the *tracer-independent* time-dependent function,

$$g(a) = 2\,\mathcal{G}^{\delta}_1(a) - 1\,, \tag{3.42}$$

as shown in app. B.1.

[6] In the EdS-approximation limit, this bias expansion is equivalent to the one introduced in [63].

To derive the density contrast of the galaxies in redshift space, we can follow the usual procedure described in [260, 261], which gives

$$\delta_{g,s}^{(n)}(\mathbf{k};\eta) \equiv \int \frac{d^3\mathbf{q}_1}{(2\pi)^3}\cdots\int \frac{d^3\mathbf{q}_n}{(2\pi)^3}(2\pi)^3\delta_D\left(\mathbf{k}-\mathbf{q}_{1\ldots n}\right) Z^{(n)}(\mathbf{q}_1,\ldots,\mathbf{q}_n;\eta)\delta_{\mathbf{q}_1}^{(1)}(\eta)\ldots\delta_{\mathbf{q}_n}^{(1)}(\eta)\,, \tag{3.43}$$

where

$$Z^{(1)}(\mathbf{q}_1) = b_1 + f\mu_1^2\,, \tag{3.44}$$

$$\begin{aligned} Z^{(2)}(\mathbf{q}_1,\mathbf{q}_2) = {} & K_{\delta_g}^{(2)}(\mathbf{q}_1,\mathbf{q}_2) + f\mu_k^2 K_\theta^{(2)}(\mathbf{q}_1,\mathbf{q}_2) \\ & + f\mu_k k\left[\frac{\mu_1}{q_1}K_\theta^{(1)}(\mathbf{q}_1)\left(K_{\delta_g}^{(1)}(\mathbf{q}_2) + f\mu_2^2 K_\theta^{(1)}(\mathbf{q}_2)\right) + \text{cyclic}\right]\,, \end{aligned} \tag{3.45}$$

$$\begin{aligned} Z^{(3)}(\mathbf{q}_1,\mathbf{q}_2,\mathbf{q}_3) = {} & K_{\delta_g}^{(3)}(\mathbf{q}_1,\mathbf{q}_2,\mathbf{q}_3) + f\mu_k^2 K_\theta^{(3)}(\mathbf{q}_1,\mathbf{q}_2,\mathbf{q}_3) \\ & + \mu_k k f\Big\{\frac{\mu_1}{q_1}K_\theta^{(1)}(\mathbf{q}_1)\left[K_{\delta_g}^{(2)}(\mathbf{q}_2,\mathbf{q}_3) + f\mu_{23}^2 K_\theta^{(2)}(\mathbf{q}_2,\mathbf{q}_3)\right] \\ & + \frac{\mu_{23}}{q_{23}}K_\theta^{(3)}(\mathbf{q}_2,\mathbf{q}_3)\left[K_{\delta_g}^{(1)}(\mathbf{q}_1) + f\mu_1^2 K_\theta^{(1)}(\mathbf{q}_1)\right] + \text{cyclic}\Big\} \\ & + \mu_k^2 k^2 f^2\Big\{\frac{\mu_2}{q_2}\frac{\mu_3}{q_3}K_\theta^{(1)}(\mathbf{q}_2)K_\theta^{(1)}(\mathbf{q}_3)\left[K_{\delta_g}^{(1)}(\mathbf{q}_1) + f\mu_1^2 K_\theta^{(1)}(\mathbf{q}_1)\right] + \text{cyclic}\Big\}\,, \end{aligned} \tag{3.46}$$

where we have suppressed the dependence on a to simplify the notation, $\mathbf{k}$ is the sum over internal momenta as in (3.43), $\mu_k \equiv \hat{\mathbf{k}}\cdot\hat{\mathbf{z}}$, $\mu_i \equiv \hat{\mathbf{q}}_i\cdot\hat{\mathbf{z}}$, and $\mu_{ij} \equiv \hat{\mathbf{q}}_{ij}\cdot\hat{\mathbf{z}}$. A hat denotes the unit vector, e.g. $\hat{\mathbf{k}} \equiv \mathbf{k}/|\mathbf{k}|$.

3.2.4 Galaxy power spectrum in redshift space

The galaxy power spectrum in redshift space is defined by

$$\langle\delta_{g,s}(\mathbf{k};\eta)\delta_{g,s}(\mathbf{k}';\eta)\rangle = (2\pi)^3\delta_D(\mathbf{k}+\mathbf{k}')P_{g,s}(\mathbf{k};\eta)\,. \tag{3.47}$$

Using the perturbative expansion in eq. (3.43), it is possible to calculate the 1-loop power spectrum in perturbation theory as the sum of three contributions,

$$P_{g,s}^{1-\text{loop,PT}}(\mathbf{k};\eta) = P_{11}(\mathbf{k};\eta) + P_{22}(\mathbf{k};\eta) + P_{13}(\mathbf{k};\eta)\,. \tag{3.48}$$

The first term on the right-hand side is given by

$$P_{11}(\mathbf{k};\eta) = Z_1(\mathbf{k})^2 P_L(k;\eta)\,, \tag{3.49}$$

where $P_L(k;\eta)$ is the linear power spectrum, defined by

$$\langle \delta^{(1)}_{\mathbf{k}}(\eta)\delta^{(1)}_{\mathbf{k}'}(\eta)\rangle = (2\pi)^3\delta_D(\mathbf{k}+\mathbf{k}')P_L(k;\eta)\,. \tag{3.50}$$

Moreover,

$$P_{22}(\mathbf{k};\eta) = 2\int \frac{d^3\mathbf{q}}{(2\pi)^3}\left[Z_2(\mathbf{k}-\mathbf{q},\mathbf{q})\right]^2 P_L(q;\eta)P_L(|\mathbf{k}-\mathbf{q}|;\eta)\,, \tag{3.51}$$

and

$$P_{13}(\mathbf{k};\eta) = 6Z_1(\mathbf{k})P_L(k;\eta)\int \frac{d^3\mathbf{q}}{(2\pi)^3}Z_3(\mathbf{k},\mathbf{q},-\mathbf{q})P_L(q;\eta)\,. \tag{3.52}$$

The result in eq. (3.48) needs to be corrected with terms that account for the effects of the UV physics on the long modes, namely the counterterms and the stochastic terms resulting from the stress-energy tensor in eq. (3.4) and from the bias and redshift-space expansions [261, 62, 64],

$$P^{1-\text{loop}}_{g,s}(\mathbf{k};\eta) = P^{1-\text{loop,PT}}_{g,s}(\mathbf{k};\eta) + P^{\text{CT}}_{g,s}(\mathbf{k};\eta) + P^{\epsilon}_{g,s}(\mathbf{k};\eta)\,. \tag{3.53}$$

At this order, the counterterms in redshift space are

$$P^{\text{CT}}_{g,s}(\mathbf{k};\eta) = 2P_L(k;\eta)Z^{(1)}(\mathbf{k};\eta)\left(\frac{k}{k_{\text{M}}}\right)^2\left(c_{\text{ct}} + c_{r,1}\mu_k^2 + c_{r,2}\mu_k^4\right)\,, \tag{3.54}$$

where k_{M} is the typical comoving scale of halos, and the stochastic contribution is given by

$$P^{\epsilon}_{g,s}(\mathbf{k};\eta) = \frac{1}{\bar{n}_g}\left(c_{\epsilon,0} + \left(\frac{k}{k_{\text{M}}}\right)^2 c_{\epsilon,1} + f\mu_k^2\left(\frac{k}{k_{\text{M}}}\right)^2 c_{\epsilon,2}\right)\,, \tag{3.55}$$

where $\bar{n}_g$ is the mean number density of galaxies. From the anisotropic galaxy power spectrum, $P^{1-\text{loop}}_{g,s}(k,\mu_k)$, we can then calculate the multipoles,

$$P^{1-\text{loop},(l)}_{g,s}(k,z) = \frac{2l+1}{2}\int_{-1}^{1} d\mu_k P^{1-\text{loop}}_{g,s}(k,\mu_k;z)\mathcal{P}_l(\mu_k)\,, \tag{3.56}$$

where $\mathcal{P}_l(\mu)$ are the Legendre polynomials of order l. In this chapter we will only consider the monopole and the quadrupole of the galaxy power spectrum.

In addition, we perform the resummation of IR modes to account for the effect of long wavelength bulk motions on small scales [262, 263]. Again, as for the bias expansion, for scale-indepedent models the IR resummation procedure is not modified in nDGP with respect to ΛCDM [209], and therefore we follow the scheme described in [264], already implemented in the `PyBird` code.

3.3 PyBird meets nDGP

In this section we specify the equations used to implement the nDGP model. Finally, in sec. 3.3.3, we present the parameters used in the analysis and their priors.

3.3.1 The code

We have already discussed in sec. 3.2 the changes to the perturbation theory equations required by scale-independent modifications of gravity. Fortunately, thanks to the modular nature of the code it is easy to implement these extensions. In particular, the task is greatly facilitated by the fact that the perturbation theory kernels in the latest version of PyBird are computed taking into account their time dependence exactly, as opposed to the commonly used Einstein-de Sitter approximation. One of the main modifications consists in solving numerically the differential equation for the growth function and the Green's functions in the nDGP case and replacing the ones computed in ΛCDM. We refer the reader to app. C for a discussion on how to choose the initial conditions of the linear solutions. The procedure, explained here for nDGP, can be easily extended to any modified gravity model with scale-independent linear growth: Jordan Brans-Dicke [27] and scalar-tensor theories with scalar fields of horizon-sized Compton wavelengths, clustering quintessence [28, 29] (see [234] for the implementation of this model in PyBird and constraints on it with BOSS data in combination with BAO), the EFT of dark energy beyond linear order [30, 31, 32], dark scattering models [33], k-mouflage theories [34, 35, 36, 37], etc.

3.3.2 The model

In nDGP,[7] it is customary to introduce the dimensionless cosmological parameter $\Omega_{\rm rc}$ to measure the strength of modifications of gravity in the effective 4d theory. This is defined in eq. (3.1), where r_c is the cross-over scale between the 5d and 4d cosmological behaviour, appearing in the effective 4d Friedman equation as $H^2 + \frac{H}{r_c} = \frac{8\pi G}{3}\sum_i \rho_i$ [242], where ρ_i are the background energy densities, including dark energy.

[7] See [265, 248, 249, 250] for a treatment of cosmological perturbations of nDGP.

In this chapter we are interested in constraining the effect of modified gravity on perturbations *only*. We will therefore assume that the background expansion is exactly the one of a flat-ΛCDM model, that is,

$$H(a) = H_0\sqrt{\Omega_{\rm m}(a/a_0)^{-3} + 1 - \Omega_{\rm m}}\,, \tag{3.57}$$

where $\Omega_{\rm m}$ is the present matter abundance. Such a behaviour can be realized by considering a dark energy component with fine-tuned dynamics [250]. Modifications of gravity are therefore restricted to linear and higher-order perturbations, described by the single parameter $\Omega_{\rm rc}$.

Indeed, it can be shown (see e.g. [32] and references therein for details) that the modified Poisson equation in Fourier space is given by eq. (3.15) with

$$\nu(a) = 1 + \frac{1}{3\beta(a)}\,, \tag{3.58}$$

$$\nu_2(a) = -\frac{1}{2}\left(\frac{H(a)}{H_0}\right)^2\frac{1}{\Omega_{\rm rc}}\left(\frac{1}{3\beta(a)}\right)^3\,, \tag{3.59}$$

$$\nu_{22}(a) = 2\left(\frac{H(a)}{H_0}\right)^4\frac{1}{\Omega_{\rm rc}^2}\left(\frac{1}{3\beta(a)}\right)^5 \tag{3.60}$$

(as discussed above, we do not need to specify ν_3), where

$$\beta(a) \equiv 1 + \frac{H(a)}{H_0}\frac{1}{\sqrt{\Omega_{\rm rc}}}\left(1 + \frac{aH'(a)}{3H(a)}\right)\,. \tag{3.61}$$

One sees that GR is recovered by sending $H_0 r_c \to \infty$ or, equivalently, $\Omega_{\rm rc} \to 0$, which implies $\beta \to \infty$ and consequently $\nu = 1$, $\nu_2 = \nu_{22} = 0$.

To solve the perturbation equations we need an expression for the time-dependent $\Omega_{{\rm m},a}(a)$ in terms of its value today, $\Omega_{\rm m} = \Omega_{{\rm m},a}(a=0)$. Since in this model M is constant, from eq. (3.6) we find

$$\Omega_{{\rm m},a}(a) = \Omega_{\rm m}\left(\frac{H_0}{H(a)}\right)^2\left(\frac{a_0}{a}\right)^3\,. \tag{3.62}$$

3.3.3 Parameters and priors

Following [63], we perform the analysis using the bias parameters

$$c_2 \equiv \frac{1}{\sqrt{2}}(b_2 + b_4)\,, \qquad c_4 \equiv \frac{1}{\sqrt{2}}(b_2 - b_4)\,, \tag{3.63}$$

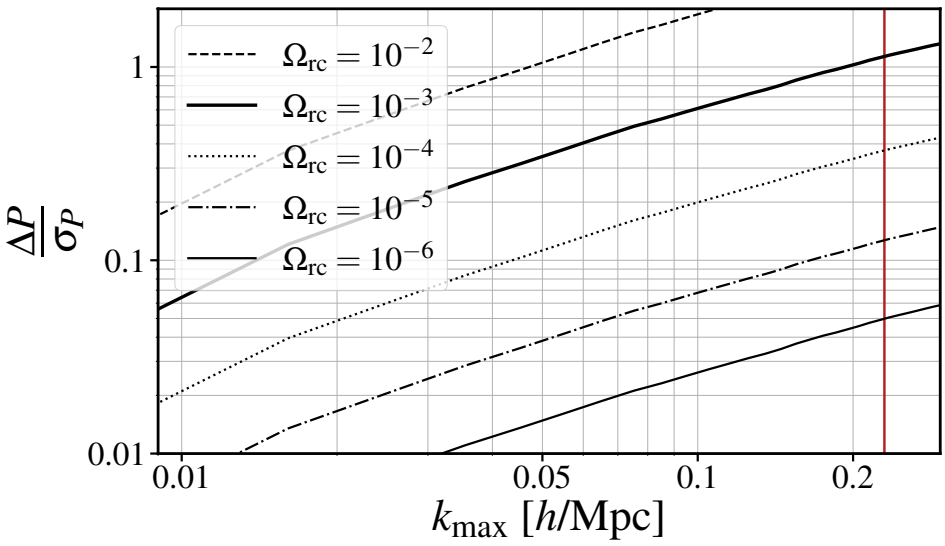

Figure 3.1: Ratio between $\Delta P \equiv P_{g,s}^{\rm nDGP,(0)} - P_{g,s}^{\Lambda{\rm CDM},(0)}$ and the error σ_P for the BOSS covariance at redshift $z = 0.61$, for different values of $\Omega_{\rm rc}$, and with bias parameters fixed to reproduce the monopole of the PT challenge simulations [208]. The red vertical line represents the $k_{\rm max}$ used in our analysis. Similar results are obtained at redshift $z = 0.38$.

instead of b_2 and b_4. Indeed, it was shown in that reference that b_2 and b_4 are highly degenerate in the data because they enter eqs. (3.38) and (3.39) in such a way that their difference, c_4, multiplies a term that is too small to be constrained by BOSS-like data. Here we set $c_4 = 0$. The parameters used in the analysis are

$$\{\omega_{\rm b},\ \omega_{\rm cdm},\ h,\ A_s,\ n_s,\ \log_{10}\Omega_{\rm rc},\ b_1,\ c_2, b_3, c_{\rm ct}, c_{\rm r,1}, c_{\epsilon,0}, c_{\epsilon,1}, c_{\epsilon,2}\}\ . \tag{3.64}$$

Since $\Omega_{\rm rc} \geq 0$, we decide to use $\log_{10}\Omega_{\rm rc}$ to scan many orders of magnitude. We then marginalize analytically on the remaining bias parameter, b_3, and on the parameters appearing in eqs. (3.54) and (3.55), see below.

Let us now discuss the priors on these parameters. Using the BBN constraint of Ref. [266], we adopt a Gaussian prior on the absolute density of baryonic matter $\omega_{\rm b} = 0.02237 \pm 0.00036$. We assume a flat prior for all the other parameters, except A_s discussed below. In the BOSS analysis, the priors are

$$\begin{aligned} &\omega_{\rm cdm} \in [0.04, 0.25]\ , \qquad h \in [0.5, 1.0]\ , \qquad n_s \in [0.5, 1.5]\ , \\ &\log_{10}\Omega_{\rm rc} \in [-3, 2]\ , \qquad b_1 \in [0.8, 4]\ , \qquad c_2 \in [-4, 4]\ . \end{aligned} \tag{3.65}$$

The lower and upper limits for the priors on b_1 and c_2 are motivated by previous analysis, see [208]. As can be seen in fig. D.1, the 2-σ posterior distributions for these parameters are well inside the priors bounds, and therefore we conclude that these priors are very uninformative. Moreover, we choose $\min\left[\log_{10}\Omega_{\rm rc}\right] = -3$ because our analysis is insensitive to lower values. Indeed, fig. 3.1 shows $\Delta P/\sigma_P$, where $\Delta P \equiv P_{g,s}^{\rm nDGP,(0)} - P_{g,s}^{\Lambda{\rm CDM},(0)}$, and σ_P is the error on $P_{g,s}^{(0)}$ for the BOSS volumes and galaxy densities, as a function of $k_{\rm max}$, for different values of $\Omega_{\rm rc}$. For $\Omega_{\rm rc} \lesssim 10^{-3}$, $\Delta P/\sigma_P \lesssim 1$, i.e. the effect of modified gravity on the monopole is smaller than the error. Adding the quadrupole does not change this conclusion. We discuss the implications of a different choice of $\min\left[\log_{10}\Omega_{\rm rc}\right]$ in sec. 3.5.

Assuming that the typical comoving scale of halos appearing in eqs. (3.54) and (3.55) is $k_{\rm M} = 0.7\,h/{\rm Mpc}$, we set Gaussian priors centered on 0 on the EFT parameters, with widths given by

$$\begin{aligned} &\sigma(b_3) = 2\,, \qquad \sigma(c_{\rm ct}) = 2\,, \qquad \sigma(c_{r,1}) = 8\,, \\ &\sigma(c_{\epsilon,0}) = 2\,, \qquad \sigma(c_{\epsilon,1}) = 2\,, \qquad \sigma(c_{\epsilon,2}) = 2\,, \end{aligned} \tag{3.66}$$

and we analytically marginalize over them, as described in [61]. Since we do not compute the hexadecapole, $c_{r,1}$ and $c_{r,2}$ are completely degenerate: we absorb the latter into the former and enlarge the prior width to 8. We choose a galaxy number density $\bar{n}_g = 3\times10^{-4}({\rm Mpc}/h)^3$ for the analysis of the synthetic data and the PT Challenge simulations at redshifts $z = 0.38$ and $z = 0.61$ respectively, and we use $\bar{n}_g = 4\times10^{-4}({\rm Mpc}/h)^3$ and $\bar{n}_g = 4.5\times10^{-4}({\rm Mpc}/h)^3$ for the analysis of the BOSS catalogues [267], at redshifts $z = 0.38$ and $z = 0.57$ respectively. We apply the Alcock-Paczynski effect to all the analyses performed in this chapter.

Finally, for the primordial amplitude of scalar fluctuations, A_s, we present two cases:

1. Assuming a flat prior in the range $A_s \in [0.1,\ 5.0]\times10^{-9}$;

2. Fixing it to the Planck central value [268]: $A_s = 2.0989\times10^{-9}$.

For the second case, given the smallness of Planck's error on A_s, 1.4%, fixing it or assuming a Gaussian prior with $1\,\sigma$ width essentially gives the same results, as we have explicitly checked.

We run MCMC's based on the Metropolis-Hastings sampler as implemented in `MontePython 3` [269, 270], with the theory model evaluated using `CLASS` [271] and `PyBird`. We declare

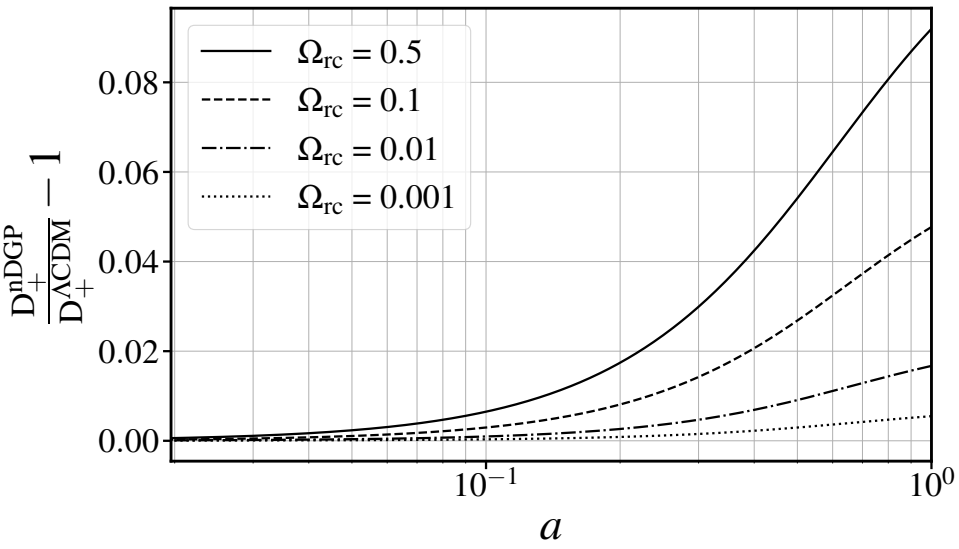

Figure 3.2: Growth function for nDGP with various values of $\Omega_{\rm rc}$ as a function of the scale factor a, rescaled to the ΛCDM one, with $\Omega_{\rm m}$ fixed to Planck's best-fit value.

convergence of the chains when the Gelman-Rubin $R-1$ value [272] is lower than 0.02. We used `GetDist` [273] package to create the plots and calculate the summary statistics.

3.4 Testing the pipeline

Before applying our pipeline to the real BOSS data, we have performed several tests on synthetic data and simulations. The aim is twofold: exploring projection effects due to strong degeneracy between parameters, such as for instance between A_s and $\Omega_{\rm rc}$ as explained in the next subsection, and assessing the maximal wavenumber that we can use in our analysis, $k_{\rm max}$. Indeed, in sec. 3.4.2 we test our pipeline on synthetic data and in sec. 3.4.3 we analyse the PT Challenge simulations. Finally, in sec. 3.4.4 we discuss projection effects in more details.

3.4.1 Degeneracy between A_s and $\Omega_{\rm rc}$

We expect the nDGP parameter $\Omega_{\rm rc}$ to be degenerate with the amplitude of primordial fluctuations A_s. Indeed, the former enters the modified linear growth equation, eq. (3.8), via the function $\nu(a)$ introduced in (3.15). In fig. 3.2 we show the effect of modified gravity on the linear growth function for different values of $\Omega_{\rm rc}$.

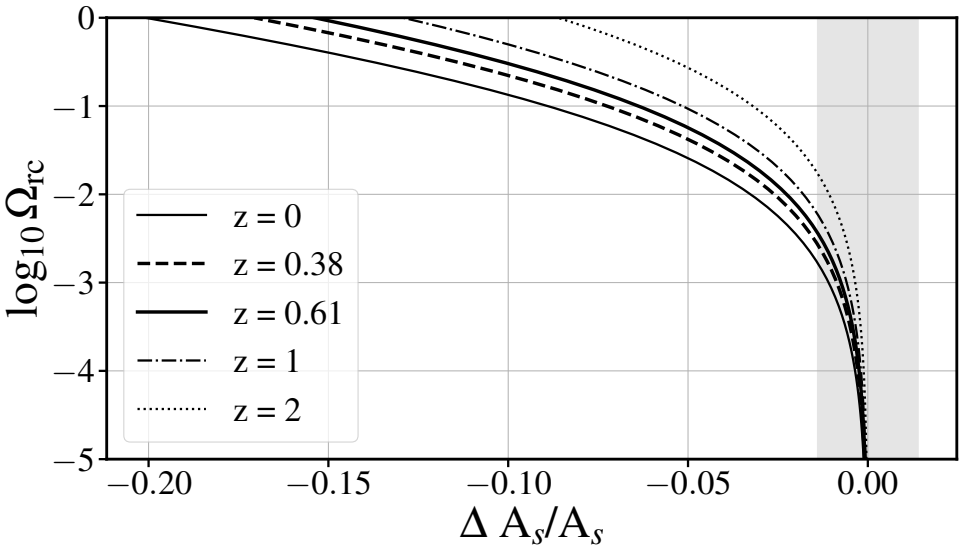

Figure 3.3: Curves of constant $D_+^2(z)A_s$ in the $\Delta A_s/A_s$-$\Omega_{\rm rc}$ plane, where $\Delta A_s/A_s \equiv \left(A_s^{\rm nDGP} - A_s^{\Lambda{\rm CDM}}\right)/A_s^{\Lambda{\rm CDM}}$ defines the shift in A_s required to compensate the change in $D_+^2(z)$, for different redshifts. The two thick lines represent the central redshifts of the PT simulations data samples considered in our analysis, which are very close to the BOSS catalogs analyzed in this chapter. The shaded region represents the Planck $\pm 1\sigma$ error.

Since the time dependence of the linear density power spectrum is given by $P(k;z) \propto D_+^2(z)A_s$, the effect of $\Omega_{\rm rc}$ on the linear growth function is exactly degenerate with the primordial amplitude A_s. To show the degeneracy as a function of the redshift, in fig. 3.3 we plot curves of constant $D_+^2(z)A_s$ in the $\Delta A_s/A_s$-$\log_{10}\Omega_{\rm rc}$ plane, where we have defined the shift in A_s required to compensate the change in $D_+^2(z)$ as

$$\frac{\Delta A_s}{A_s} \equiv \frac{A_s^{\rm nDGP} - A_s^{\Lambda{\rm CDM}}}{A_s^{\Lambda{\rm CDM}}}\,. \tag{3.67}$$

Combining data at different redshifts can, in principle, break this degeneracy but this does not work if $\Omega_{\rm rc}$ is too small or if the redshift bins are too close. In fig. 3.3 we also show the curves for $z = 1$ and $z = 2$.

3.4.2 Null test on synthetic data

Using the EFTofLSS model described in sec. 3.2, we have created synthetic data, with known cosmology and bias parameters, for ΛCDM (i.e. $\Omega_{\rm rc} = 0$), and we have tested our pipeline

	Synthetic data	PT-Challenge sims	BOSS data
Low-z sample	$z = 0.38$ $k_{\rm max} = 0.20h\,{\rm Mpc}^{-1}$	$z = 0.38$ $k_{\rm max} = 0.20h\,{\rm Mpc}^{-1}$	$z = 0.32$ $k_{\rm max} = 0.20h\,{\rm Mpc}^{-1}$
High-z sample	$z = 0.61$ $k_{\rm max} = 0.23h\,{\rm Mpc}^{-1}$	$z = 0.61$ $k_{\rm max} = 0.23h\,{\rm Mpc}^{-1}$	$z = 0.57$ $k_{\rm max} = 0.23h\,{\rm Mpc}^{-1}$

Table 3.1: Summary of the data samples considered for our analyses, with their respective redshifts and $k_{\rm max}$ used.

on these data. The goal of this preliminary analysis is to verify if the marginalized posterior probability are affected by strong projection effects, such as the one discussed above. See also e.g. [274, 238] for a discussion on this topic.

We fixed the cosmological parameters[8] of the synthetic data to be the same as those of the PT Challenge mocks, while the bias and EFT parameters were chosen using the best-fit values obtained by fitting the mocks. We generated samples at the two redshifts of the simulations dataset analyzed below, $z = 0.38$ and $z = 0.61$. We have analyzed the monopole and quadrupole of the synthetic galaxy power spectrum for both redshift samples and for the combination of the two. We have used a Gaussian covariance provided in the PT-Challenge website[9], rescaled in order to match the volume and number densities of the BOSS catalogues [267]. We have fixed the maximum wavenumber included in the analysis to $k_{\rm max} = 0.23\,h$/Mpc for $z = 0.61$ and $k_{\rm max} = 0.20\,h$/Mpc for $z = 0.38$; for a summary, see tab. 3.1. As explained in sec. 3.4.4, when analyzing the simulations we find that the theoretical systematic error on cosmological parameters is negligible.

The results are shown in fig. 3.4, with a flat prior on A_s (top) and with fixed A_s (bottom). The expected degeneracy between $\Omega_{\rm rc}$ and A_s is visible (top panel) for $\Omega_{\rm rc} \gtrsim 10^{-2}$, which results in a biased determination of A_s and a spurious peak in the $\Omega_{\rm rc}$ posterior, induced by projection effects. As anticipated, the shape of the 2d posterior in the $\log_{10}\Omega_{\rm rc}$-A_s plane is only mildly

[8] Following the philosophy of [208], we do not disclose their values here.

[9] https://www2.yukawa.kyoto-u.ac.jp/takahiro.nishimichi/data/PTchallenge

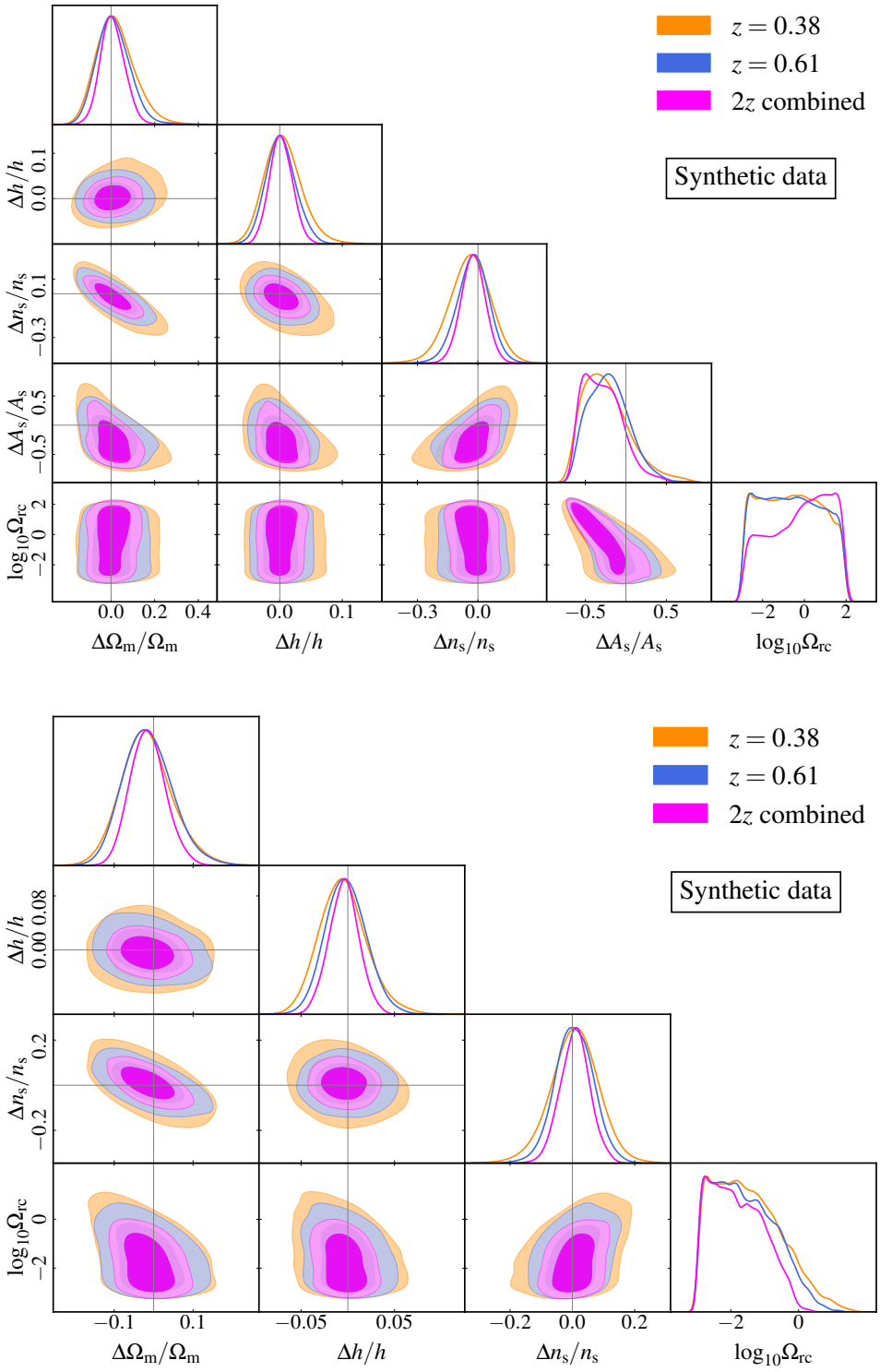

Figure 3.4: Marginalized posteriors for the cosmological parameters from ΛCDM-synthetic data, with flat-A_s priors (top panel) and fixed A_s (bottom panel), with two different sky-cuts and their combination. The covariances used have been rescaled to match that of BOSS data.

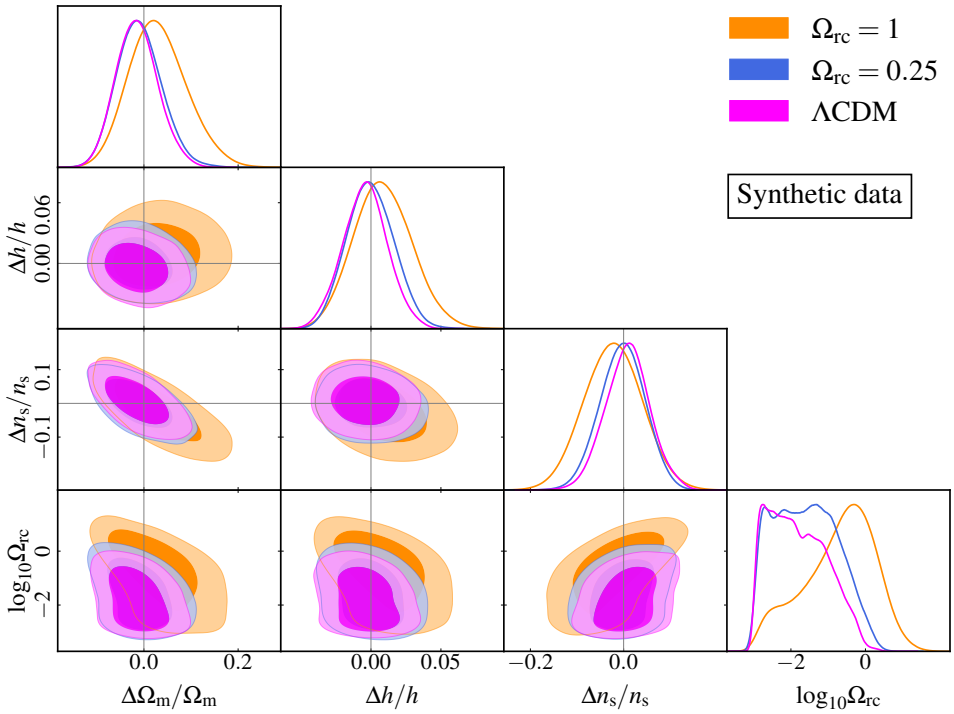

Figure 3.5: Marginalized posteriors for the cosmological parameters for nDGP with $\Omega_{\rm rc} = 0.25$ and $\Omega_{\rm rc} = 1$, compared to ΛCDM, for the combined sky-cuts and with A_s fixed to Planck's value.

redshift dependent; therefore, combining the two relatively close redshift samples does not help in reducing the degeneracy. Fixing A_s to Planck's value (botton panel) clearly reduces the degeneracy and removes projection effects. Moreover, increasing $\Omega_{\rm rc}$ while keeping A_s fixed lifts the amplitude of the linear power spectrum, and therefore the relative weight of the 1-loop effects with respect to the linear ones, which is instrumental in lifting degeneracies among cosmological and bias parameters. Furthermore, it is now possible to observe that there is also a moderate degeneracy between $\log_{10}\Omega_{\rm rc}$, n_s and Ω_m that it is less relevant in the case in which A_s is varied.

Additionally, we have performed an analysis of synthetic data in nDGP combining two redshift samples. To observe a clear effect of nDGP we have considered large values of $\Omega_{\rm rc}$, $\Omega_{\rm rc} = 1$ and $\Omega_{\rm rc} = 0.25$, leaving the other parameters as above and fixing A_s to the Planck central value. In fig. 3.5 we compare the marginalized posteriors of these two cases with the

ΛCDM case. A clear detection is present only for values bigger than $\Omega_{\rm rc} \gtrsim 1$.[10]

We also note that for the cosmology with large $\Omega_{\rm rc}$ the uncertainties of the other cosmological parameters are larger due to the different degeneracies with the other cosmological parameters around the central value.

3.4.3 Tests on simulations

We tested our pipeline on the PT Challenge simulations [208], which are ten realizations in periodic comoving boxes of side length of $3840\,\mathrm{Mpc}/h$ with 3072^3 particles each. The total volume, $566\,(\mathrm{Gpc}/h)^3$, is about a hundred times that of the BOSS catalogues. A flat ΛCDM cosmology is assumed, with Ω_ν set to zero. Dark matter halos are identified with the Rockstar halo finder [275] and then populated with mock galaxies matched to reproduce the observed clustering properties of the BOSS samples. Further details can be found in [208]. We analyzed these simulations with $k_{\rm max} = 0.23\,h/\mathrm{Mpc}$ for $z = 0.61$ and $k_{\rm max} = 0.20\,h/\mathrm{Mpc}$ for $z = 0.38$, as already described in the previous section.

The results are shown in fig. 3.6 for two cases: varying A_s with a flat prior (top) and for A_s fixed to the Planck central value (bottom). In the top panel we observe, again, the degeneracy between $\Omega_{\rm rc}$ and A_s and the presence of a peak in the $\log_{10}\Omega_{\rm rc}$ posterior, which indicates the presence of projection effects. These effects disappear when fixing A_s to Planck's value (bottom panel). As for synthetic data, a moderate degeneracy between $\log_{10}\Omega_{\rm rc}$, n_s and Ω_m emerges when A_s is fixed.

3.4.4 Projection effects and theoretical errors

The above analysis shows a large difference between the mean (or the median) of the 1d marginalized posterior and the true value of A_s. Following [238], to estimate the importance of other systematic biases due to projection effects, in tab. 3.2 we show the ratio between $\Delta(x) = \bar{x} - x_{\rm truth}$, i.e. the difference between the marginalized mean value $\bar{x}$ of a parameter x and its true value $x_{\rm truth}$, and the error associated to the data for the same parameter, $\sigma_{\rm data}(x)$.

[10] With *detection* here we mean the following: we subtract the 2-σ error to the measured best fit value and we compare it with the lower bound of the prior used for the analysis.

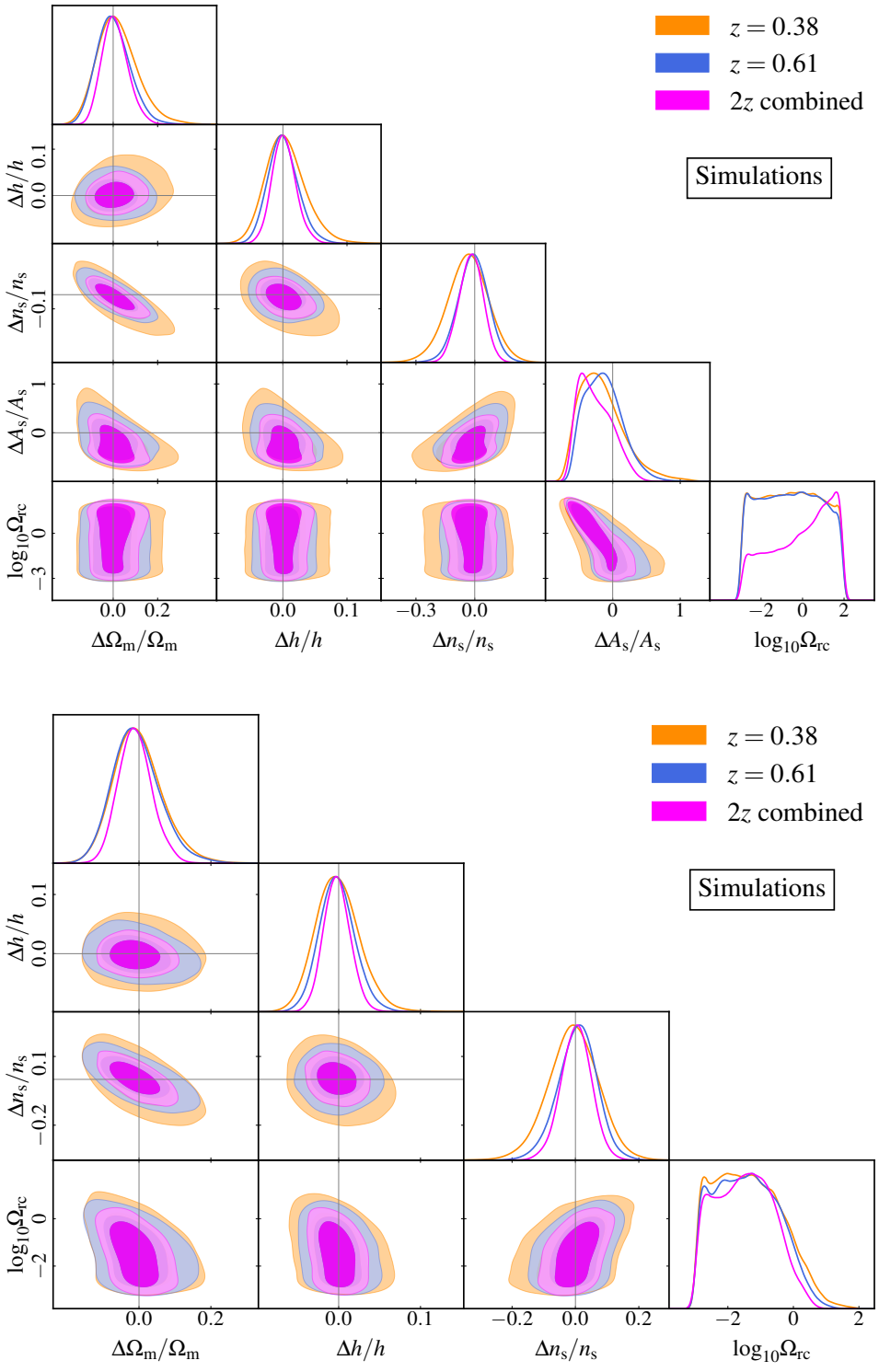

Figure 3.6: Marginalized posteriors for the cosmological parameters from the PT Challenge simulations, with flat-A_s priors (top panel) and fixed A_s (bottom panel), with two different sky-cuts and their combination. The covariances used have been rescaled to match those of BOSS data.

x	$\Omega_{\rm m}$	h	n_s
$\Delta_{\rm synth}(x)/\sigma_{\rm synth}(x)$	-0.2333	-0.0903	0.0938
$\Delta_{\rm sims}(x)/\sigma_{\rm sims}(x)$	-0.1053	-0.0826	0.0901
$\Delta_{\rm sims}(x)/\sigma_{\rm sims}(x) - \Delta_{\rm synth}(x)/\sigma_{\rm synth}(x)$	0.1280	0.0077	-0.0038

Table 3.2: Ratio $\Delta_{\rm data}(x)/\sigma_{\rm data}(x)$, where $\Delta(x) = \bar{x} - x_{\rm truth}$ is the difference between the marginalized mean and the true value, and $\sigma_{\rm data}$ is the data error, measured on synthetic data (first row) and the PT Challenge simulations (second row), for $x = \Omega_{\rm m}$, h and n_s. We consider only the high-z sample and we fix A_s to the Planck central value. We report also the difference between the two cases (third row).

These are computed for the synthetic data and for the simulations analyses, considering only one sky-cut (i.e. the high-z case), for the case in which A_s is fixed to the Planck value. We find that the deviations due to projection effects are negligible with respect the dataset errors, i.e., $\Delta_{\rm data}/\sigma_{\rm data}(x) \lesssim 1/3$.

For the simulation analysis, there are two contributions to the deviations of the means from their true values: the projection effects and the theory error. To estimate the importance of the theory error, we subtract the shift measured with synthetic data (which are exempt from theoretical errors) divided by the error from the same ratio measured with simulations: this is safely negligible in our analysis, as shown in the table.

3.5 Results

3.5.1 BOSS analysis

In this section we apply our pipeline to the analysis of real data from the SDSS-III BOSS [276]. In particular, we have analyzed the full-shape BOSS DR12 power spectrum measurements. The theory model is the same EFTofLSS used in the fit of synthetic data and simulations, with the same priors. We convolve the power spectrum multipoles with the survey window function measured with the technique outlined in [277], with a consistent normalization for the power

Param	best-fit	mean $\pm 1\sigma$
$\omega_{\rm cdm}$	0.1169	$0.1182^{+0.0084}_{-0.01}$
h	0.6791	$0.6794^{+0.013}_{-0.015}$
n_s	0.9793	$0.976^{+0.062}_{-0.056}$
$\Omega_{\rm m}$	0.3075	$0.3058^{+0.016}_{-0.02}$

Table 3.3: Best-fit and mean values with $1\,\sigma$ deviations measured on BOSS data, high-z sample. The bounds are obtained with A_s fixed to the Planck central value and using BOSS covariances.

spectrum estimator.[11]

We analyze the monopole and quadrupole power spectra of the redshift cuts, $z_{\rm eff} = 0.57$ and $z_{\rm eff} = 0.32$, using both North Galactic Cap and South Galactic Cap sky-cuts for each redshift bin. We cut the power spectra at $k_{\rm max} = 0.23\,h/{\rm Mpc}$ for the higher redshift and at $k_{\rm max} = 0.20h/{\rm Mpc}$ for the lower one. When analyzing BOSS data, we also include the effects of neutrinos in the linear power spectrum. We use the Planck prescription of one massive neutrino species with $m_\nu = 0.06$ eV and two massless ones contributing to the number of effective relativistic species as $N_{\rm eff} = 2.0328$.

We show the marginalized posteriors in figs. 3.7 and the best-fit and mean values of the cosmological parameters in tab. 3.3. The posteriors are in qualitative agreement with those obtained from synthetic data and simulations. In particular, they show the same error size and degeneracy among parameters.

3.5.2 Dependence on priors

We now discuss upper bounds on the nDGP parameter $\Omega_{\rm rc}$ from the analyses on BOSS data

$$x \equiv \log_{10}\Omega_{\rm rc}\,, \tag{3.68}$$

that is, $\mathcal{P}(x|d,{\rm p})$, where d and p denote the data and the priors, respectively. We considered

[11] See here for the public GitHub repository for the evaluation of the window function.

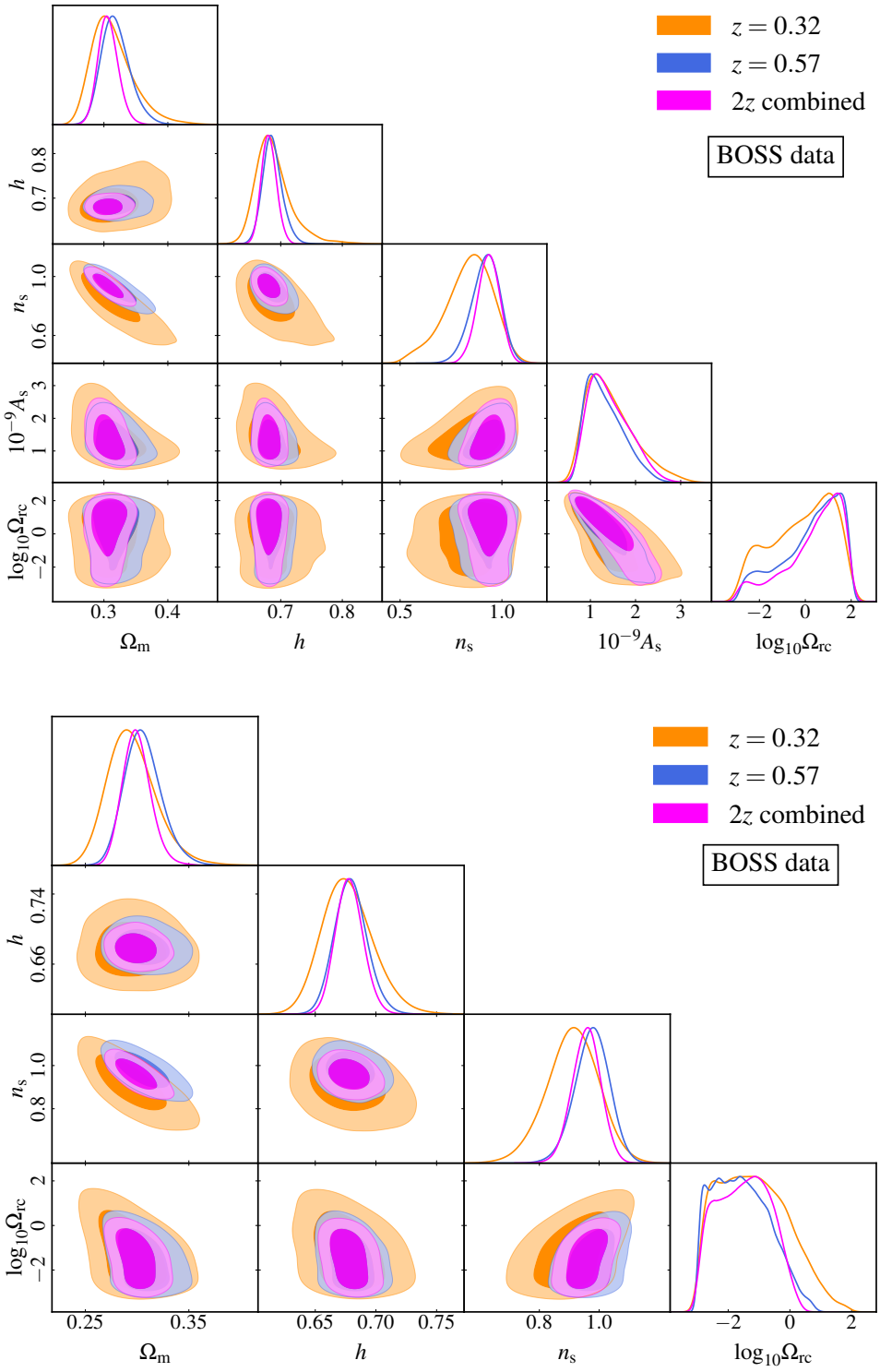

Figure 3.7: Marginalized posteriors for the cosmological parameter from the analysis of BOSS data for all the sky-cuts with flat prior on A_s (top panel) and A_s fixed to Planck central value (bottom panel), using BOSS covariances.

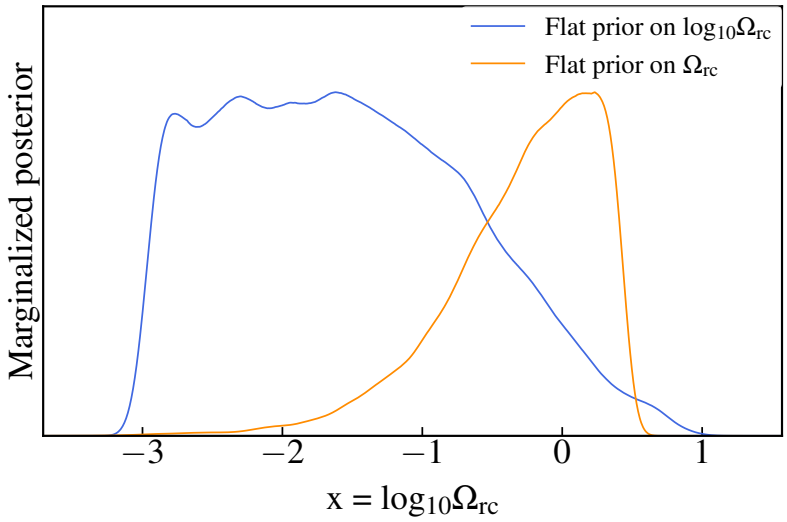

Figure 3.8: Marginalized posteriors of $\log_{10}\Omega_{\rm rc}$ from the BOSS analysis (high-z sample only) with a flat prior on $\Omega_{\rm rc}$ (yellow line) and with a flat prior on $\log_{10}\Omega_{\rm rc}$ (blue line), with A_s fixed to Planck central value.

two types of priors: a flat prior on x (log-flat prior) on an interval $[-a,\ 2]$([12]), that is

$$\mathrm{p}_a^x(x) = \mathrm{flat}_{x\in[-a,\,2]}\,, \tag{3.69}$$

and a flat prior on $\Omega_{\rm rc} = 10^x$ on the interval $[0,\ 100]$,

$$\mathrm{p}^{\Omega}(x) = \mathrm{flat}_{\Omega_{\rm rc}\in[0,\,100]}\,. \tag{3.70}$$

Due to the Jacobian of the transformation between $\Omega_{\rm rc}$ and x, when expressed in the x variable the second prior is proportional to $10^x\ \ln 10$. For the log-flat prior, the choice of the lower bound is important. In this case, as the x parameter goes to zero, it scans an infinite volume. But since the model has a smooth limit to GR in the $\Omega_{\rm rc}\to 0$ limit, allowing a very low lower bound introduces a large parameter space in which we are effectively sampling the ΛCDM model, thus biasing the marginalized 1-d posteriors. To remove this effect, for the log-flat prior we must choose a lower bound a such that, fixing all parameters, the differences in power spectra between the case $\Omega_{\rm rc}=0$ and the case in which $\Omega_{\rm rc}=10^{-a}$ is comparable to the standard deviation of the data, see fig. 3.1. In fig. 3.8 we show the 1d marginalized posteriors

[12]The *upper* bounds in both priors are values of the parameters for which the posteriors are practically zero, so the results are independent on the precise choices for them.

obtained with the flat prior on x, and lower bound in $x = -3$, $\mathrm{p}_3^x(x)$, as in fig. 3.7, and with the flat prior on $\Omega_{\rm rc}$, $\mathrm{p}^\Omega(x)$. Notice that the former tends to a plateau for large negative x, while the latter is exponentially suppressed in the same region, given the 10^x dependence on the prior. These behaviors are expected: data are insensitive to small $\Omega_{\rm rc}$ values, therefore the posterior in those region is just proportional to the prior.

We can define upper bounds on $\Omega_{\rm rc}$ from the integral,

$$\mathcal{I}[x_{\rm lim};\mathrm{p}] = \int_{x^p_{\rm min}}^{x_{\rm lim}} \mathcal{P}(x|d,\mathrm{p})dx\,, \tag{3.71}$$

where $x^p_{\rm min}$ is the lower bound of the prior $\mathrm{p}(x)$, that is, -3 for $\mathrm{p}_3^x(x)$ and $-\infty$ for $\mathrm{p}^\Omega(x)$. Setting $\mathcal{I}[x_{\rm lim};\mathrm{p}] = 0.68,\, 0.95$ gives the $x_{\rm lim}$ values corresponding to the upper limits on the parameter x at the $68\,\%$ or $95\,\%$ confidence level.

Translated back to $\Omega_{\rm rc}$, these values correspond to

$$\Omega_{\rm rc} < 0.0919 \quad \text{at } 68\%\text{ C.L.} \quad (< 0.646 \text{ at } 95\%\text{ C.L.}) \qquad \text{for } \mathrm{p}_3^x(x)\,, \tag{3.72}$$

$$\Omega_{\rm rc} < 0.9967 \quad \text{at } 68\%\text{ C.L.} \quad (< 2.185 \text{ at } 95\%\text{ C.L.}) \qquad \text{for } \mathrm{p}^\Omega(x)\,. \tag{3.73}$$

These upper bounds are clearly prior-dependent. In particular, considering the flat prior on x, p_a^x, they depend on the value of the lower extreme $x = -a$, as shifting it to $x = -b$ changes the value of the integral (3.71) by a quantity proportional to $b - a$, since the posterior is constant in that region. For instance, the lower extreme $x = -6$ gives

$$\Omega_{\rm rc} < 0.0187 \quad \text{at } 68\%\text{ C.L.} \quad (< 0.4087 \text{ at } 95\%\text{ C.L.}) \qquad \text{for } \mathrm{p}_6^x(x)\,. \tag{3.74}$$

We stress that such a low lower bound on x is not a very sensible choice. When calculating the bound as an integral over x, we are taking into account a large volume of parameter space that is simply ΛCDM. In the next subsection, we discuss a less prior-dependent method to extract a bound on how much we are allowed to deviate from the ΛCDM cosmology.

3.5.3 Bound using the Bayes factor

As an alternative criterion to quantify an upper bound to $\Omega_{\rm rc}$, consider the ratio between the 1d posterior and its corresponding prior,

$$b(x;d,\,\mathrm{p}) = \frac{\mathcal{P}(x|d,\mathrm{p})}{\mathrm{p}(x)}\,. \tag{3.75}$$

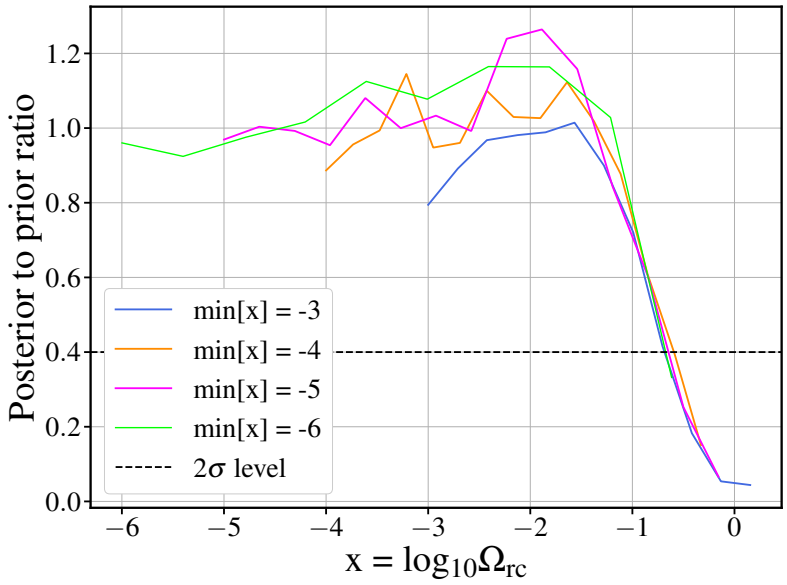

Figure 3.9: Normalized posterior-to-prior ratios of $\log_{10}\Omega_{\rm rc}$ from the BOSS analysis ($2z$-combined sky-cuts), assuming a flat prior on $\log_{10}\Omega_{\rm rc}$, with all the cosmological parameters fixed to their respective Planck central values, for different lower bounds of $\min[\log_{10}\Omega_{\rm rc}]$: $-6, -5, -4$ and -3. The dashed line denotes p-value $= 0.05$.

Taking two different values of x and the ratio between the corresponding b functions, gives

$$\frac{b(x_1; d,\ \mathrm{p})}{b(x_2; d,\ \mathrm{p})} = \frac{\mathcal{P}(d|x_1)}{\mathcal{P}(d|x_2)} \equiv B(x_1, x_2)\,, \tag{3.76}$$

where $\mathcal{P}(d|x)$ is the likelihood of the data d when the parameter is fixed at x, and the first equality is a consequence of Bayes theorem. $B(x_1, x_2)$, also known as the odds, or Bayes factor, gives the change in relative probability between the model with $x = x_1$ and $x = x_2$, supported by the data (see, for instance, [39]), and is prior independent by construction.

Values of $B(x_1, x_2)$ of order unity are associated to 'inconclusive' evidence of x_1 over x_2. Following tab. 1 of [39], we associate, for instance, a p-value of 0.05 ($2\,\sigma$) preference of x_1 over x_2 to odds in the range $B(x_1, x_2) > 2.5$ and a p-value of 0.003 ($3\,\sigma$) to $B(x_1, x_2) > 21$. If we fix x_1 to the low x plateau, we can then plot $B(x_1, x_2)$ as a function of x_2 and derive upper bounds on x. This is shown in fig. 3.9, where we plot the functions $B(x_{\rm plateau},\ x)$ obtained from different MCMC chains in which we imposed flat priors on x, $\mathrm{p}^x_a(x)$, with different values for the lower bound a. The different curves have been normalized in order to have $b(x_{\rm plateau}; d,\ \mathrm{p}^x_a) = 1$ on the plateau, correcting by the differences between the evidences

($\int_{-a}^{2} \mathcal{P}(d|x) p_a^x(x)$) due to the different lower limit of integration. As we can see, while the plateau is clear for $x^p_{\rm min} = -5$ and -6, it is only marginally visible for higher values of $x^p_{\rm min}$. However, we also see that the different curves have a descent which is to a great extent independent on the assumed value for $x^p_{\rm min}$. The $1\,\sigma$ bound extracted with the criteria described above corresponds to the tail of the distributions, which is difficult to sample numerically. Therefore, we only quote the $2\,\sigma$ bound corresponding to $B(x_{\rm plateau}, x) = 2.5$, obtained from the smallest available value for $x_{\rm plateau}$, that is -6, and from the largest value, -3. Apart from that, we use the same data and priors on the other parameters as those used to obtain fig. 3.7 and the bounds in (3.73).

We obtain, for $x_{\rm plateau} = -6$,

$$\Omega_{\rm rc} < 0.2113 \qquad \text{at } 95\% \text{ C.L.} \tag{3.77}$$

and, for $x_{\rm plateau} = -3$,

$$\Omega_{\rm rc} < 0.2047 \qquad \text{at } 95\% \text{ C.L. .} \tag{3.78}$$

These two bounds are very close, showing the robustness of our approach. A more detailed review of this method is illustrated in F.

3.6 Summary

We have constrained cosmological modifications of gravity with the full-shape power spectrum of BOSS data. As shown in sec. 3.2, we have modeled the galaxy distribution in redshift space by extending perturbation theory and the bias expansion to general scale-independent modified gravity models and using the EFTofLSS to capture the effect of the short-scale physics.

To be specific, we have then restricted our analysis to the normal branch of the DGP scenario, assuming the background expansion of a flat ΛCDM model. The relation between the gravitational potential and the density contrast, which in ΛCDM is given by the Poisson equation, is now modified by an enhancement of the effective Newton constant and by the presence of new non-linear terms. These effects are parameterized by a single quantity, $\Omega_{\rm rc}$. We perform the analysis with the code `PyBird`, that we have adapted to include the new effects (see sec. 3.3).

As discussed in sec. 3.4, in linear theory $\Omega_{\rm rc}$ is degenerate with A_s and, since we assume a flat ΛCDM background expansion, it is also degenerate with $\Omega_{\rm m}$. Furthermore, the new non-linear kernels affect the power spectrum on short scales and can be degenerate with the primordial tilt of fluctuations n_s. These strong degeneracies, in particular the one with A_s, shift the 1-d marginalized posteriors of the cosmological parameters from their true values. We have quantified this shift by analyzing synthetic data generated with the EFTofLSS, which has allowed us to estimate how degeneracy affects the marginalized posteriors through projection effects on the parameter volume.

The effect of parameter volume projection effects on the power spectrum amplitude A_s has also been investigated in [278, 210], showing that different choices of the priors for the EFT parameters can induce a shift on the measured A_s. We have reduced this effect by fixing A_s to the Planck central value, combined with a BBN prior on ω_b. Even when A_s is fixed, there are still residual degeneracies, such as the one between $\Omega_{\rm m}$ and n_s.

The results of the analysis on BOSS data are discussed in sec. 3.5. For fixed A_s, the marginalized posteriors are shown in fig. 3.7. The contours of the nDGP parameter $\Omega_{\rm rc}$ are prior-dependent. In order to obtain prior-independent constraints, we have considered the ratio between the 1d posterior and its corresponding prior, the so-called Bayes factor. The resulting upper bound on the nDGP parameter is $\Omega_{\rm rc} \lesssim 0.2$ at 95% C.L.. This is the first measurement of the nDGP parameter performed using the full shape galaxy power spectrum from the BOSS data.

Our analysis shows that competitive constraints using galaxy clustering data can be obtained only with volumes higher than BOSS and/or more information about the parameters, either from other datasets, such as the CMB, or by narrowing the priors on the EFT or bias parameters [278]. This could be done, for instance, by modelling the bias expansion using analytical constructs, such as the peak-background split [279, 280], the excursion-set approach [281, 282] or the consistency relations of LSS [283, 284], or by using more phenomenological models informed by simulation measurements.

In this respect, the bispectrum is receiving growing interest [285, 286, 287]. A joint analysis with the bispectrum could, in principle, help break some degeneracies, for example the one between the growth rate f (and thus $\Omega_{\rm m}$), the linear bias, b_1, and the primordial amplitude,

A_s. Reference [288] showed that by performing a joint analysis of the power spectrum and the bispectrum one could reach a 10% accuracy on f, while [289] has shown that using only the bispectrum monopole significantly reduces the information content of the bispectrum, allowing only for a better estimation of the bias parameters. The analysis using the EFT model for the tree-level bispectrum has been recently performed on numerical simulations [290], which showed an improvement of 5-15% on the constraints on cosmological parameters. The same analysis was performed using the 1-loop bispectrum on simulations [291] and using the BOSS data [238], showing a $\sim$ 10-30% improvement with respect to the power spectrum-only analysis.

The procedure introduced in this thesis can be straightforwardly extended to other models with a scale-independent growth of perturbations, such as those described by the EFT of dark energy. Modifications of gravity can also be scale dependent if the range of the scalar force becomes of the order of the sample size, such as for instance in the Hu-Sawicki $f(R)$ model [292]. Other scale-dependent effects on the growth are expected from massive neutrinos or baryonic feedback (see e.g. [293, 294]). The implementation of these effects in a fast code requires more work and is left for the future.

Chapter 4

Cosmological constraints on non-standard cosmologies from simulated *Euclid* probes

The *Euclid* satellite mission [77] is set to provide unmatched accuracy in measuring the large-scale galaxy clustering and lensing, presenting a unique opportunity to investigate deviations from the ΛCDM model.

In this chapter we focus on the extraction of cosmological parameters beyond ΛCDM from simulated galaxy mocks with different volumes. The theoretical model for our analysis is the EFTofLSS, which provides a robust perturbative description of the non-linear effects of dark matter clustering, short-scale physics, galaxy bias, redshift-space distortions, and large-scale bulk flows. The analysis is performed with Markov-Chain Monte-Carlo techniques and with the code `PyBird`.

In the following we present the theoretical model implemented and the results for two different simulated galaxy mocks, RayGal and DEMNUni, focusing on three different models: ΛCDM, nDGP and wCDM.

4.1 Euclid in a nutshell

The *Euclid* mission [77, 295], an initiative of the European Space Agency (ESA), is strategically designed to explore the Universe through the methodologies of weak gravitational lensing and galaxy clustering. The goal of this mission is to conduct a comprehensive imaging and spectroscopy survey across both visible and near-infrared wavelengths. It aims to cover an expansive area of approximately $15,000\,\mathrm{deg}^2$ of the extragalactic sky over a period of six years. Central to Euclid's design is a telescope equipped with a $1.2\,\mathrm{m}$ diameter Silicon Carbide (SiC) mirror, which channels data to two primary instruments developed by the Euclid Consortium. These include a high-resolution panoramic visible imager and a near-infrared photometer-spectrograph.

The Euclid spacecraft, during its mission, is set to conduct an extensive imaging and spectroscopic exploration of the visible and near-infrared spectrum through the Euclid Wide Survey (EWS) [296]. At the heart of Euclid's objectives is the EWS, which plays a pivotal role in the mission. Its primary purpose is to detect and analyze the clustering properties of galaxies, thereby contributing to a more profound understanding of the Universe's accelerated expansion and the essence of dark energy. The EWS employs two principal methodologies: galaxy clustering (GC) and weak lensing (WL), to achieve its scientific goals.

GC will comprise a substantial dataset of tens of millions of galaxy angular positions and spectroscopic redshifts. These redshifts fall within the interval $0.7 < z < 1.8$ and are expected to maintain an accuracy of $0.001 \times (1+z)$ at a confidence level of $68\,\%$. In parallel, WL will be assessed by analyzing approximately 1.5 billion galaxy shapes, which will be integrated with photometric redshifts (photo-z). This analysis will be further enhanced by complementary ground-based photometry. The near-infrared passbands are instrumental in determining the average photo-z for the tomographic redshift bins, aiming for an accuracy of $0.002 \times (1 + z)$ [297]. Additionally, WL observations will be augmented by various other cosmological probes derived from the same dataset, and these will be synergized with external data sources, such as clusters of galaxies and cross-correlation with the CMB.

The EWS is set to encompass over one-third of the celestial sphere, strategically avoiding the Galactic and ecliptic planes. The survey's anticipated average limiting magnitude is

gauged to be $26.5\,\mathrm{mag}$ in the visible I_E band, and $24.5\,\mathrm{mag}$ in the near-infrared bands Y_E, J_E, and H_E. On the spectroscopic front [296], the H_α line flux threshold is projected to be 2×10^{-16} erg^{-1} cm^{-2} s^{-1} at a wavelength of $1600\,\mathrm{nm}$. Complementarily, the Deep Survey (DS) is tailored to observe more faint objects across smaller regions, aiming to cover a minimum of $40\,\mathrm{deg}^2$ across three distinct fields in both the northern and southern Galactic hemispheres. The DS will not only furnish calibration data sets for the EWS but also contribute data for legacy science endeavors, encompassing the study of faint high-redshift galaxies, quasars, and active galactic nuclei (AGN). It will also provide Galaxy Clustering data, that is the main focus, in our case, for the extraction of cosmological parameters beyond ΛCDM.

4.2 Theoretical Model

As already illustrated in 3.1, we make use of the advanced theoretical modeling of galaxy clustering provided by the EFTofLSS, focusing on the power spectrum. An accurate power spectrum modeling can be achieved through perturbation theory up to the 1-loop level [213], with a systematic bias scheme and counterterms to describe the effects of small-scale physics [214, 215, 216, 217, 218, 219, 220, 221, 222, 223, 224, 225, 226].

We apply this EFTofLSS treatment [214, 216], which has been recently used to model the power spectrum at 1-loop for the analysis of the BOSS dataset [11], giving constraints on cosmological parameters with a good level of accuracy, see [63, 227, 228].

Building on these approach, it is possible to investigate the limits of neutrino masses [229, 230], to examine the inconsistency in measurements of the universe's expansion rate (known as the H_0 tension [231, 232, 233]) and to explore theories that go beyond the standard ΛCDM cosmological model [61, 234]. Looking into RSD [235, 236] and using both simple and complex EFTofLSS methods to analyze the BOSS bispectrum, could provide new insights into the early universe's structure [63, 237, 238, 239, 240, 241].

We report the priors used for the analysis of the cosmological parameters. We adopt a Gaussian prior on the absolute density of baryonic matter, centered on the true value of the simulations. For the RayGal simulations we have $\omega_b = 0.02258\pm0.00036$ and $\omega_b = 0.022445\pm 0.00036$ for the DEMNuni simulations. We assume a flat prior for all the other parameters,

except for A_s in the nDGP and wCDM cases, which we discuss in 4.3. In the analysis, the priors for the cosmological parameters are

$$\omega_{\rm cdm} \in [0.04, 0.25] \ , \qquad h \in [0.5, 0.9] \ , \qquad n_s \in [0.5, 1.5] \ . \tag{4.1}$$

For the bias parameters b_1 and c_2 have flat priors with the following bounds, motivated by previous analyses, see [208]:

$$b_1 \in [0.8, 4] \ , \qquad c_2 \in [-4, 4] \ . \tag{4.2}$$

For the other parameters we use Gaussian priors centered at 0 with the following standard deviations:

$$\begin{aligned} \sigma(b_3) = 2, \quad \sigma(c_{\rm ct}) = 2, \quad \sigma(c_{r,1}) = 8, \\ \sigma(c_{\epsilon,0}) = 2, \quad \sigma(c_{\epsilon,1}) = 2, \quad \sigma(c_{\epsilon,2}) = 2 \, . \end{aligned} \tag{4.3}$$

These are integrate over analytically as described in [61]. Given that the hexadecapole is not computed, $c_{r,1}$ and $c_{r,2}$ are indistinguishable; we combine them into $c_{r,1}$ and adjust the prior width to 8.

4.3 The RayGal simulations

The RayGalGroupSims suite (RayGal) [298] consists of two N-body simulations of $2625\ (\mathrm{Gpc}/h)^3$ volume with 4096^3 particles of a standard flat ΛCDM model and a non-standard wCDM phantom dark energy model with a constant equation of state. The optimal compromise between mass resolution (of order $\sim 2 \times 10^{10}\, h^{-1} M_\odot$) and large statistics makes these simulations well-suited for investigating the cosmological dependence of halo properties. This is particularly relevant for halos on the scale of galaxy groups, which play a crucial role in weak-lensing studies[1].

The initial conditions were generated with a modified version of *MPGRAFIC* [299]. Simulations were conducted using an enhanced version of the parallel AMR N-body code, RAMSES2 [300]. Dark matter halos are identified with the `rockstar` halo finder [301].

[1]It is worth mentioning that, even we do not make use of these in our work, the fundamental aspect of these simulations is the integration of relativistic ray tracing inside gravitational light cones. This aspect facilitates the generation of realistic catalogs containing dark-matter particles and halos, accounting for relativistic effects

Param	best-fit	mean $\pm 1\sigma$
$\omega_{\rm cdm}$	0.1163	$0.1178^{+0.0057}_{-0.0069}$
h	0.7257	$0.728^{+0.0084}_{-0.0096}$
$10^{+9}A_s$	1.991	$2.003^{+0.17}_{-0.19}$
n_s	0.943	$0.9366^{+0.051}_{-0.048}$
$\Omega_{\rm m}$	0.3075	$0.3058^{+0.016}_{-0.02}$

Table 4.1: Best-fit and mean values with $1\,\sigma$ deviations measured from the analysis of ΛCDM RayGal simulations.

In ΛCDM, we have snapshots at $z = 1$ and we analyzed these simulations with $k_{\rm max} = 0.20\,h$/Mpc. The values of the cosmological parameters are

$$\{\Omega_{\rm b,0}, \Omega_{\rm m,0}, h, n_{\rm s}, A_{\rm s}\} = \{0.04356, 0.25733, 0.72, 0.963, 2.0232 \times 10^{-9}\}. \tag{4.4}$$

The ΛCDM results from the MCMC analysis performed in the EFTofLSS theoretical framework are shown in fig. 4.1: the cosmological parameters fitted by the posterior distribution are in good agreement with the true values of the simulations. The best-fit and mean values of the cosmological parameters are reported in 4.1. For the nDGP analysis, illustrated in fig. 4.2, we have set a flat prior on $\log_{10}\Omega_{\rm rc} \in [-3, 2]$. We observe that here, as in chapter 3, there is strong degeneracy between $\Omega_{\rm rc}$ and A_s. Thus we performed two different analysis: one varying A_s with a flat prior and one with A_s fixed to the true value of the simulation. The results for the nDGP parameter Ω_{rc} are fully in agreement with the ones obtained in chapter 3. The best-fit and mean values are reported in 4.1. The constraint obtained fixing A_s to the true value of the simulations is $\Omega_{\rm rc} \lesssim 0.2054$ at 95% C.L., improving w.r.t. the BOSS analysis shown in 3.5. In the near future we plan to apply the Bayes factor method to obtain a prior-indipendent measure of the nDGP parameter, as previously explained in 3.5.3.

The RayGal simulations present also a different cosmology for the so-called wCDM model. The wCDM model is an extended version of the standard ΛCDM cosmological model: in this cosmology we assume Gaussian initial conditions, pure CDM with no WDM/HDM admixture,

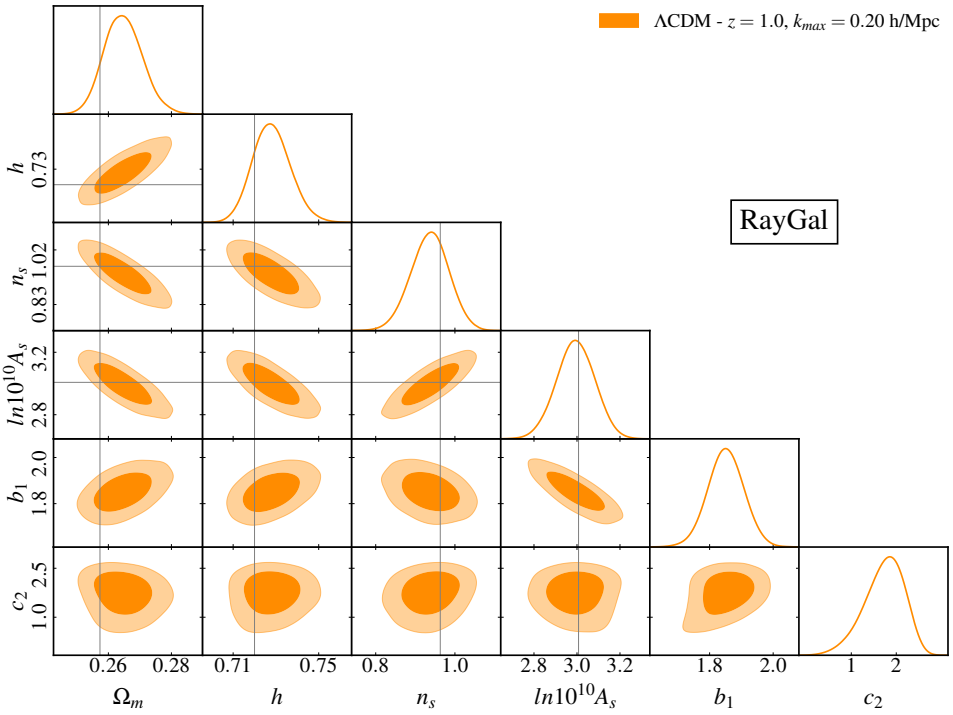

Figure 4.1: Marginalized posteriors for the cosmological parameters from the RayGal simulations.

Param	best-fit	mean $\pm 1\sigma$
$\omega_{\rm cdm}$	0.1145	$0.1121^{+0.0045}_{-0.0041}$
h	0.7256	$0.7218^{+0.0072}_{-0.0062}$
n_s	0.9434	$0.9647^{+0.038}_{-0.042}$
$\Omega_{\rm m}$	0.2602	$0.2583^{+0.0047}_{-0.0044}$

Table 4.2: Best-fit and mean values with $1\,\sigma$ deviations measured from the nDGP analysis of RayGal simulations. These bounds are obtained with A_s fixed to the simulation true value.

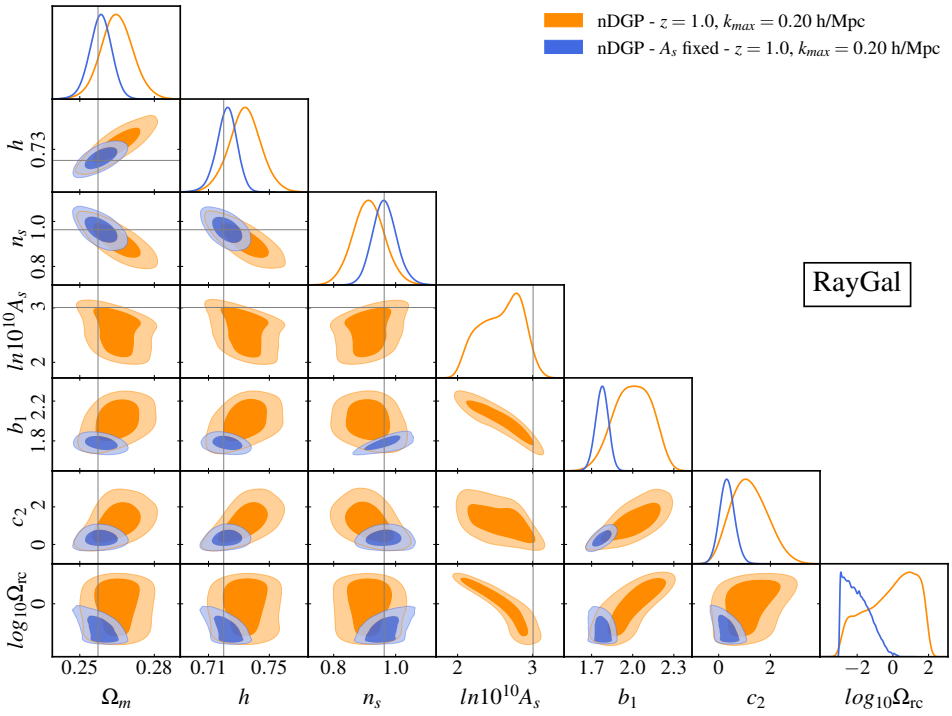

Figure 4.2: Marginalized posteriors for the cosmological parameters from the RayGal simulations for the nDGP model, with the comparison between a flat-A_s prior and the fixed A_s case.

and a dark energy fluid component described by constant-in-time equation of state $p = w\rho$ and negligible perturbations. The impact of this parameter is on the linear growth function and the angular diameter distance, which in turn modifies the observed angular scale of the BAO peak. Estimating these quantities would in principle enable us to deduce the cosmological parameters within the wCDM framework using only data derived from large-scale structures [61].

The capacity to estimate w using the power spectrum and observations like Ly-α BAO data stands in contrast to supernova (SN) measurements, which typically require external data, often from the CMB, to reach a comparable level of precision and to disrupt the degeneracy in the w-Ω_m plane. The SN constraint on w and Ω_m comes from their ability to provide measurements of the luminosity distance, $D_L(z)$. Hence, a possible combination of power spectrum measurements, BAO and SN would allow us to get significantly smaller constraints on w [61]. We expect that a combination of spectroscopic and photometric surveys in the future will enable unprecedented constraints on the nature of dark energy.

The wCDM results are shown in fig. 4.3, where we set a flat prior for $w \in [-3, -0.4]$. The parameter w, for which the true value is $w = -1.2$[2], is completely unconstrained. There is a strong degeneracy with the A_s parameter, similarly to what already observed in the nDGP model. We solve this problem by fixing A_s to its true value, thus recovering the w parameter with good precision. In tab. 4.3 we show the best-fit and mean values obtained with A_s fixed to the simulation true value.

4.4 The *DEMNuni* Simulations

The Dark Energy and Massive Neutrino Universe (DEMNUni) simulations [302, 303] are designed to study the impact of massive neutrinos and dynamical dark energy on large-scale cosmic structures. Created specifically for nonlinear analyses, they cover observational probes such as dark matter, halo, and galaxy clustering [304, 305, 306, 307, 308, 309, 303, 310, 311, 312], as well as weak lensing, CMB lensing, SZ, and ISW effects [313, 302, 314, 315]. Additionally, they aid in studying cosmic void metrics [316, 317, 318, 319, 320, 321] and in understanding cross-correlations between different observational metrics [322].

[2]It is important to highlight that this value, in a standard quintessence scenario, is nonphysical.

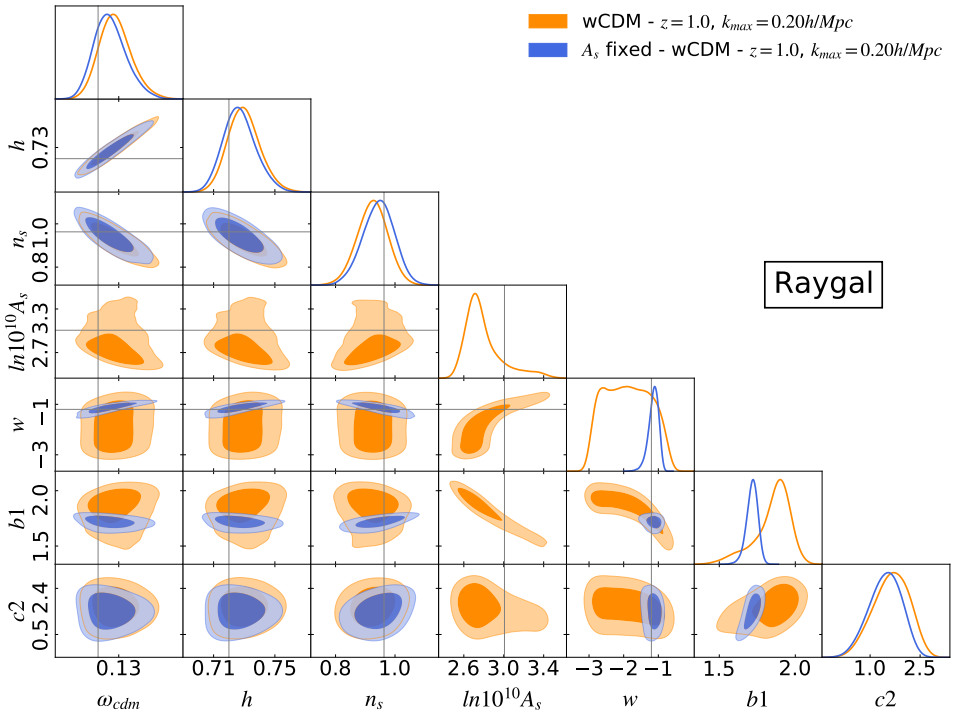

Figure 4.3: Marginalized posteriors for the cosmological parameters from the RayGal simulations for the wCDM model, with the comparison between a flat-A_s prior and the fixed A_s case..

Param	best-fit	mean $\pm$ 1σ
$\omega_{\rm cdm}$	0.1276	$0.1259^{+0.0068}_{-0.0089}$
h	0.7289	$0.727^{+0.0095}_{-0.012}$
n_s	0.9324	$0.9444^{+0.057}_{-0.052}$
w	-1.065	$-1.139^{+0.18}_{-0.11}$

Table 4.3: Best-fit and mean values with $1\,\sigma$ deviations measured from the analysis of wCDM RayGal simulations. The bounds are obtained with A_s fixed to the simulation true value.

These simulations have a comoving volume of $2\,h^{-3}\,\mathrm{Gpc}^3$, teeming with 2048^3 dark matter particles and, when included, an equivalent number of neutrino particles. These simulations are initialized at redshift $z_\mathrm{i} = 99$ using the Zel'dovich approximation. Generation of the Gaussian initial conditions utilizes an adapted N-GenIC toolset.

These simulations were run with the *P-Gadget3* code, built upon tree particle mesh and smoothed particle hydrodynamics principles (TreePM-SPH) [323]. The software was enhanced based on the method described in [324] to support massive neutrinos, allowing for the parallel progression of both CDM and neutrino particles without interaction.

The cosmological parameters are taken from Planck 2013 best fit [325]:

$$\{\Omega_{\mathrm{b},0}, \Omega_{\mathrm{m},0}, h, n_\mathrm{s}, A_\mathrm{s}\} = \{0.05, 0.32, 0.67, 0.96, 2.127 \times 10^{-9}\}. \tag{4.5}$$

In context, the reference CDM-particle mass resolution for the neutrino-free scenario is $m^p_\mathrm{CDM} = 8.27{\times}10^{10}\,h^{-1}\,M_\odot$. We use halo power spectra in redshift space in the mass bin $10^{12.7}h^{-1}M_\odot < M_\mathrm{halo} < 10^{13.2}h^{-1}M_\odot$, and we consider the monopole and quadrupole power spectra of the redshift cuts $z = 1.05$ and $z = 1.45$.

The ΛCDM analysis performed with MCMC in the EFTofLSS framework gave the results shown in fig. 4.4. The cosmological parameters are in good agreement with the simulated true values, as indicated by the posterior distribution. The best-fit and mean values of the cosmological parameters are reported in 4.4 for the lowest redshift only.

We have also analyzed the simulations with massive neutrinos. In accord with the simulation cosmology, we have considered 3 degenerate massive neutrinos with mass m_ν and total mass $M_{\nu,\mathrm{tot}} = 3m_\nu$. The prior is a flat prior $m_\nu \in [0.02\,\mathrm{eV}, 0.35\,\mathrm{eV}]$, such that we have $M_{\nu,\mathrm{tot}} \in [0.6\,\mathrm{eV}, 1.05\,\mathrm{eV}]$. The true value for the massive neutrinos is $m_\nu = 0.32$.

The analysis was performed with $k_\mathrm{max} = 0.20\,h/\mathrm{Mpc}$. The results are shown in fig. 4.5. The best-fit and mean values of the cosmological parameters are shown in 4.5 for the lowest redshift only. As expected given the small volume, fig. 4.5 shows that we are not able to get any constraint on the neutrino mass m_ν. The posterior distribution is almost completely flat. A possible solution for this issue, to be explored in the near future, would be to do a multisky analysis. Another option would be to fix the A_s parameter to the true value of the simulations, as we previously did for nDGP and wCDM. Nevertheless, we expect to be able

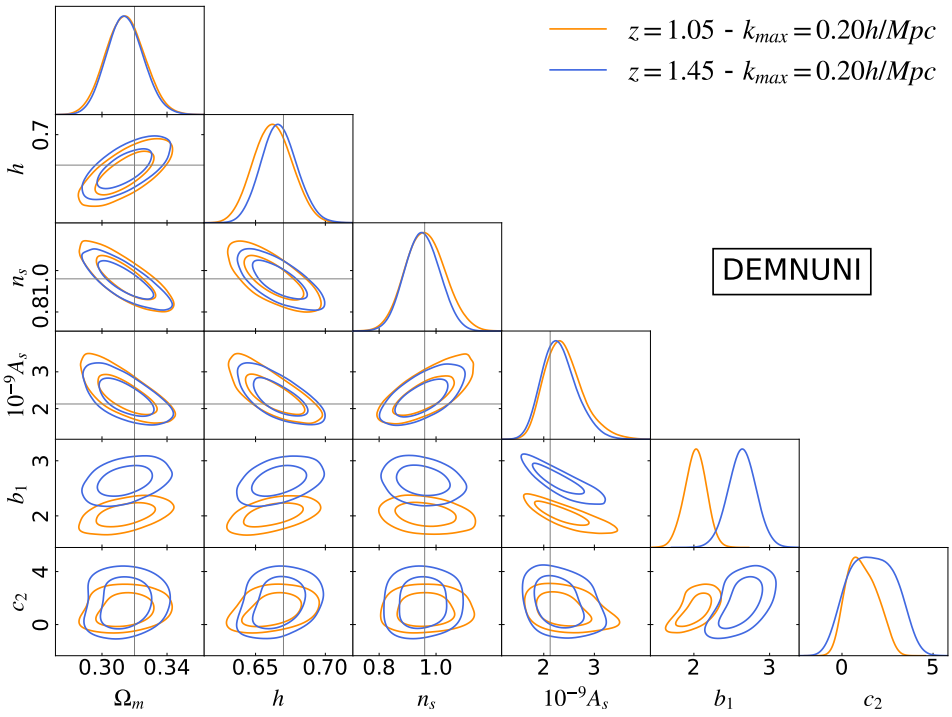

Figure 4.4: Marginalized posteriors for the cosmological parameters from the DEMNuni simulations.

Param	best-fit	mean $\pm$ 1σ
$\omega_{\rm cdm}$	0.1123	$0.1157^{+0.0098}_{-0.011}$
h	0.657	$0.6624^{+0.014}_{-0.015}$
$10^{+9}A_s$	2.459	$2.401^{+0.3}_{-0.44}$
n_s	0.977	$0.963^{+0.069}_{-0.075}$
Ω_m	0.312	$0.3143^{+0.012}_{-0.013}$

Table 4.4: Best-fit and mean values with $1\,\sigma$ deviations measured from the analysis $z = 1.05$ of ΛCDM DEMNuni simulation.

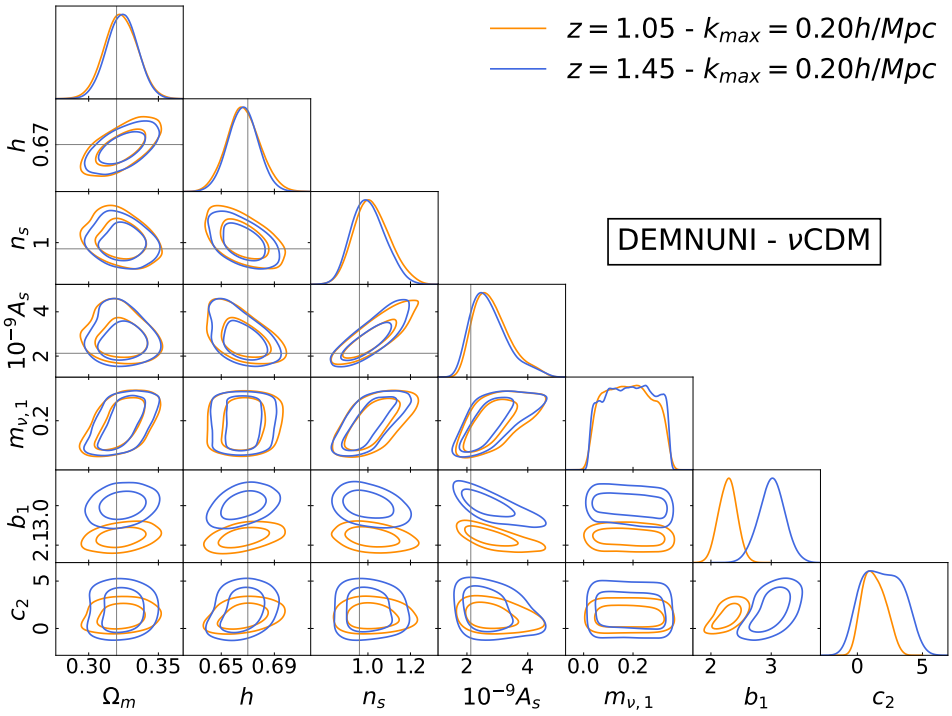

Figure 4.5: Marginalized posteriors for the cosmological parameters in Λ + massive neutrinos fitting the DEMNuni simulations.

to measure the mass of neutrinos when we analyze simulations with *Euclid*-like volumes and higher resolutions, and Euclid data.

4.5 Future perspectives

The *Euclid* space mission promises to deliver unparalleled precision in charting the clustering and gravitational lensing of galaxies on large scales, leading the way for probing potential deviations from the established ΛCDM framework.

The inference of cosmological parameters in models beyond the conventional ΛCDM using simulated galaxy datasets is necessary to prepare our pipelines for the future *Euclid* data releases. We plan to perform other analyses on simulations, e.g. on the Extended LEnsing PHysics using ANalaytic ray Tracing (ELEPHANT) [326].

We plan to test not only different volumes and redshifts, but also to get constraints on other beyond-ΛCDM models like w_0-w_a. Another intriguing possibility is to perform these

Param	best-fit	mean $\pm 1\sigma$
$\omega_{\rm cdm}$	0.1156	$0.1157^{+0.0085}_{-0.0099}$
h	0.666	$0.6669^{+0.012}_{-0.013}$
$10^{+9}A_s$	2.49	$2.803^{+0.44}_{-0.72}$
n_s	0.9867	$1.015^{+0.077}_{-0.091}$
Ω_m	0.32	$0.3233^{+0.012}_{-0.012}$

Table 4.5: Best-fit and mean values with $1\,\sigma$ deviations measured from the analysis at $z = 1.05$ in Λ + massive neutrinos fitting the DEMNuni simulations.

analyses with the perturbative expansions derived in the LSS bootstrap approach of [209].

The upcoming decade holds immense promise as a potential scientific golden age for cosmology. This optimism arises from the impending wave of galaxy surveys that will comprehensively sample the large-scale structure of the universe across vast cosmic volumes. These surveys offer an unprecedented opportunity to rigorously test cosmological models [77, 78, 79].

Chapter 5

Beyond-ΛCDM constraints from Lyman-α data

The main observable manifestation of the Inter-Galactic Medium (IGM) is the so-called Lyman-α forest, that is a pattern of absorption lines produced by the inhomogeneous distribution of the intergalactic neutral hydrogen along different line of sights to distant quasars (QSOs) [327, 328]. The Lyman-α forest has been proven to be an ideal tracer of the underlying dark matter (DM) distribution at relatively high redshifts ($2 \lesssim z \lesssim 5$) and small scales ($0.5\ \mathrm{Mpc}/h \lesssim \lambda \lesssim 50\ \mathrm{Mpc}/h$) [45, 46, 47, 329, 330, 331]. As such, its exploitation as a cosmological tool has allowed to establish tight constraints on a variety of non-standard DM (NSDM) models, such as thermal warm DM (WDM) [48, 72, 332, 333, 334, 335, 336, 337], axion-like particles [49, 338, 339, 340, 341, 342], (self-)interacting DM [50, 71, 73, 343, 344, 345, 346, 347, 348, 349, 350], as well as primordial black holes (PBHs) [51, 351]. The Lyman-α forest is also sensitive to the IGM thermal state and can thereby set limits on reionisation and its thermal history [352, 353, 354, 355, 356, 357, 358, 359, 360, 361].

The physical observable of interest in Lyman-α forest analyses is the *flux power spectrum*, the shape of which is determined by both astrophysics and cosmology. However, the relation between the astrophysical and cosmological parameters section determining the astrophysical and cosmological model (*astro/cosmo* parameters) and the expected Lyman-α flux is highly non-linear, hence dedicated N-Body hydrodynamic simulations are required in order to build a reliable grid of mock flux power spectra to be compared with observations [362]. Since the

aforementioned alternative scenarios deviate from the ΛCDM linear matter power spectrum on small scales only, accurate limits on the given DM model are generally established by adopting a phenomenological parameterisation capturing the small-scale departures induced by a large variety of models [52, 363, 364, 365, 366, 367, 368, 369]. On the other hand, the *astro/cosmo* parameters designed to capture the effects of varying the ΛCDM parameters are treated as nuisance parameters to marginalise over [70, 71, 73] sectionin that case. In other words, given that a broad variety of alternative DM models features the same asymptotic behaviour of the ΛCDM model on intermediate and large scales, their small-scale features can be modelled as independent of the underlying *astro/cosmo* parameters. Concretely, that means that to constrain these models it is not necessary to extend the *astro/cosmo* grid of simulations suitable for a purely ΛCDM analysis. Rather, one can simply augment such a grid by additional simulations designed to cover the added parameter space associated to the NSDM nature [71, 73]. Note, however, that even in a purely ΛCDM analysis Lyman-α data can deliver valuable information on longstanding tensions between early- and late- universe estimates of cosmological parameters [53, 370, 337], providing independent measurements of the amplitude of the linear power spectrum on 8 Mpc/h scales, σ_8 , and the primordial spectral index, n_s .

Furthermore, there is another class of extended cosmological scenarios that can be tested with Lyman-α data, i.e., models that show the same *qualitative* behaviour of ΛCDM in terms of the linear matter power spectrum. In this case, the introduction of additional parameter(s) capturing the detailed impact of the model on the Lyman-α flux power spectrum is not required. On the other hand, the additional parameters characterising such class of models may affect other cosmological observables in a non-trivial way, complementary to Lyman-α forest observations, such as the cosmic microwave background (CMB) or other early universe probes exploring a very different regime compared to the IGM. Therefore, the ΛCDM correlations between amplitude and tilt of the primordial power spectrum and amplitude and slope of the late-time linear matter power spectrum can be altered, so that the latter ones can be *quantitatively* very different from the ΛCDM predictions. For instance, this is the case for Early Dark Energy (EDE) models, as it was explicitly demonstrated in Ref. [371]. Indeed, such a deviation of the ΛCDM parameters is generically expected in the most promising solutions to the Hubble tension, in particular for early universe solutions changing the sound horizon [372].

One promising and still unexplored strategy to test such scenarios is to devise an expanded *astro/cosmo* grid, aimed at covering parameter values that would be excluded by the CMB within ΛCDM, yet being still allowed in more complex models as EDE or others. Through this approach, the amplitude and slope of the linear matter power spectrum – as traced by the Lyman-α flux power spectrum – can be used as a proxy to constrain a number of viable models beyond the standard ΛCDM paradigm.

The main goal of this section is to present a versatile and efficient tool[1] enabling to test a variety of alternative cosmological models with a joint set of Lyman-α forest data from both intermediate and high resolution surveys, covering a redshift interval $3.0 \leq z \leq 5.4$ and a wide range of different IGM thermal histories. This task has been achieved thanks to a novel set of N-Body hydrodynamic simulations, as well as a newly developed interpolation scheme refined with Machine Learning (ML) techniques, allowing to improve over past analyses in terms of accuracy, theoretical model coverage, and exploitation of additional data.

5.1 Numerical set-up

The impact on the flux power spectrum due to varying cosmological parameters within the ΛCDM model – and within alternative scenarios qualitatively indistinguishable in terms of the linear matter power spectrum $P_{\rm lin}(k, z)$ – can be parameterised via the amplitude and (effective) slope of $P_{\rm lin}(k, z)$ at scales that are probed by the Lyman-α forest [330, 329, 331]. Hence, we only need two parameters describing cosmology, namely σ_8 and $n_{\rm eff} \equiv {\rm d} \ln P_{\rm lin}/{\rm d} \ln k$, the latter being evaluated at $k = 0.009\,{\rm s/km}$ and $z_{\rm eff} = 3$[2] [70, 71, 73, 335]. As in previous works, we assume instantaneous reionisation, so that the only additional cosmological parameter to take into account in our analyses is the reionisation redshift $z_{\rm reio}$. We leave for a future work the implementation of inhomogeneous (patchy) reionisation, as it was shown that neglecting its effects does not bias the limits extracted from currently available Lyman-α data [373].

The Lyman-α forest flux power spectrum is also affected by the thermal equation of state of the IGM, that we parameterise as $T = T_0(1 + \delta_{\rm IGM})^{\gamma-1}$, with $\delta_{\rm IGM}$ being the IGM over-

[1] We dub the corresponding likelihood as `Lyajoint`, and we will make it publicly available upon publication of this work.

[2] conversion between s/km and h/Mpc.

density [352, 354]. We will thus vary its amplitude, $T_0(z)$, as well as its slope, $\gamma(z)$. We also consider ultraviolet (UV) fluctuations of the ionising background, which can be particularly important at high redshift and large scales [334, 335]. The amplitude of this effect is described by an effective parameter, $f_{\rm UV} \in [0, 1]$, defined as the fraction of the volume-averaged hydrogen photo-ionisation rate that arises from a fluctuating QSO component: the remaining fraction, $1 - f_{\rm UV}$, is attributed to a spatially uniform UV background arising from faint galaxies with a typical separation much less than the mean free path of ionising photons [70, 335]. Finally, for each simulation we vary the mean transmitted flux $\bar{F}(z)$ via a post-processing procedure aimed at capturing the uncertainty in the photo-ionisation rate. Since varying the mean flux does not require running other computationally expensive simulations, we build a very dense template in terms of $\bar{F}(z)$, and we extend it far beyond the parameter space allowed by observations. As described in detail in Section 5.1.3 and Appendix I, this strategy enables us to maximise the accuracy of the numerical routine that we have developed to interpolate within the *astro/cosmo* grid, which naturally improves when adding more grid-points.

The 7-dimensional parameter space that is scanned by our analyses is thus defined by 4 redshift-independent parameters, $\{\sigma_8, n_{\rm eff}, z_{\rm reio}, f_{\rm UV}\}$, in addition to 3 redshift-dependent ones $\{\bar{F}(z), T_0(z), \gamma(z)\}$. In Section 5.1.1 we will give a detailed description of the suite of hydrodynamic simulations that we have performed (or recycled from previous works) to efficiently sample this parameter space.

5.1.1 Simulations

We build a grid of mock flux power spectra extracted from a large selection of cosmological hydrodynamic simulations performed with GADGET-3, a modified version of the publicly available code GADGET-2 [323, 374] which includes Smoothed Particle Hydrodynamics (SPH). The initial conditions were produced by displacing the DM particles from a cubic Cartesian grid according to second-order Lagrangian Perturbation Theory, by means of the publicly available code `2LPTic` [375]. Each simulation, started at redshift $z = 99$ and evolved down to redshift $z = 2$, includes – besides one collisionless cold DM (CDM) species – gas particles treated with a simplified hydrodynamic prescription specifically devised for Lyman-α forest analyses, i.e. the so-called *Quick-Lyman-*α method [47, 48]. In practice this method consists in

converting into (collisionless) stars all gas particles that reach a density larger than 1000 times the mean density and a temperature below 10^5 K.

As the physical observable for our analyses is the 1-dimensional flux power spectrum $P_{\rm F}(k,z)$, the goal of our set of simulations is to provide a template of mock flux power spectra to be confronted with observations. We follow the approach of Refs. [51, 70, 71, 72, 73, 376] and build such a grid in terms of ratios of flux power spectra with respect to a given fiducial model. The main advantage for this choice is that a given grid can be expanded with additional simulations run with (slightly) different set-ups, provided that a reference simulation (i.e., corresponding to the fiducial model) having the same set-up is performed for each additional expansion set, in order to consistently compute the additional set of ratios.

Our fiducial model simulation is recycled from Ref. [335], and it has a box length of $20/h$ comoving Mpc with 2×768^3 gas and CDM particles, with gravitational softening $1.04/h$ comoving kpc, in a flat ΛCDM universe with cosmological parameters $\Omega_m = 0.301$, $\Omega_b = 0.0457$, $n_s = 0.961$, $H_0 = 70.2$ km s^{-1} Mpc^{-1} [377]. The reference IGM thermal history assumes $T_0(z = 4.2) \simeq 9200$ K and $\gamma(z = 4.2) \simeq 1.47$ [362], whereas the fiducial values of the redshift-independent parameters are $\sigma_8 = 0.829, n_{\rm eff} = -2.3074, z_{\rm reio} = 9$, and $f_{\rm UV} = 0$, the latter choice corresponding to a spatially uniform UV background. Concerning the mean transmitted flux $\bar{F}(z)$, we build a template of 17 different values as in Ref. [70]: 9 obtained by rescaling the optical depth $\tau_{\rm eff} \equiv -\ln \bar{F}$ to the observed values [378] with a multiplicative factor f (i.e., $\tau_{\rm eff} = f \cdot \tau_{\rm eff,obs}$) and 8 obtained by directly rescaling $f \cdot \bar{F}_{\rm obs}$, with $f \in [0.6, 1.4]$. From Refs. [335, 70] we also recycle a set of 3×3 simulations corresponding to 8 additional IGM thermal histories – in addition to the aforementioned reference one – sampling a range of values motivated by past observations [356]. The full set is given by the combination of 3 different temperatures at mean density, $T_0(z = 4.2) \simeq 6000, 9200, 12500$ K, with 3 values of the slope of the IGM equation of state, $\gamma(z = 4.2) = 0.88, 1.24, 1.47$. Concerning the template of simulations with varying cosmological parameters, we recycle two sets of 4 simulations, each of them bracketing the fiducial values of σ_8 and $n_{\rm eff}$, i.e., $\sigma_8 = 0.754, 0.804, 0.854, 0.904$, and $n_{\rm eff} = -2.3474, -2.3274, -2.2874, -2.2674$. We also recycle two pairs of simulations bracketing the fiducial values of $z_{\rm reio}$ and $f_{\rm UV}$, i.e., $z_{\rm reio} = 7, 15$, and $f_{\rm UV} = 0.5, 1$. All these simulations have been rescaled with the aforementioned 17 values of the mean transmitted flux

$\bar{F}$, as it was done for the fiducial model simulation. We have thus recycled from Refs. [70, 335] a total of 357 grid-points.

In order to expand the grid coverage of the *astro/cosmo* parameter space with respect to previous works, we also perform a new series of simulations, with a box length of $20/h$ comoving Mpc, and 512^3 gas and CDM particles: 6 of them aimed at extending the grid coverage in terms of cosmological parameters, corresponding to the following values of $n_{\rm eff} = -2.583, -2.453, -2.168, -2.043$ and $\sigma_8 = 0.697, 0.967$; 2 of them aimed at exploring colder and hotter IGM thermal histories, corresponding to the following values of the amplitude of the IGM equation of state $T_0(z = 4.2) \simeq 3800, 14200$ K – while the slope $\gamma(z = 4.2)$ is kept fixed to its fiducial value. Finally, a template of 2×2 simulations is built by simultaneously varying $n_{\rm eff}$ and $T_0(z)$: namely, we apply both the new hotter and colder IGM thermal choices to models with $n_{\rm eff} = -2.453, -2.168$. In Section 5.1.4 we will discuss in detail the specific purposes of these choices. Regarding the mean transmitted flux $\bar{F}(z)$, we build a template of 23 different values, obtained by rescaling the optical depth $\tau_{\rm eff} \equiv -\ln \bar{F} = f \cdot \tau_{\rm eff,obs}$, with $f \in [0.4, 1.5]$. We have thus produced 276 new grid-points, for a total of 633 (recycled plus new) flux power spectra ratios constituting the whole grid that we use in all our analyses.

5.1.2 Data

We make use of Lyman-α forest flux power spectrum measurements reconstructed from two different samples of QSO spectra: the XQ-100 and the MIKE/HIRES data-sets.

The XQ-100 data-set is constituted by a sample of medium resolution and intermediate signal-to-noise lo QSO spectra, obtained by the VLT/X-shooter survey, with emission redshifts $3.5 \leq z \leq 4.5$ [379]. The spectral resolution of the X-shooter spectrograph is $30 - 50$ km/s, depending on the wavelength. The flux power spectrum $P_{\rm F}(k, z)$ has been calculated for a total of 133 (k, z) data-points, at redshift bins $z = [3.0, 3.2, 3.4, 3.6, 3.8, 4.0, 4.2]$, in 19 bins in k-space in the range 0.003-0.057 s/km [380].

The second set of flux power spectra that we consider was obtained from the HIRES (Keck) and the MIKE (Magellan) high resolution spectrographs, in 10 k-bins in the interval 0.001-0.08 s/km, at redshift bins $z = [4.2, 4.6, 5.0, 5.4]$, with spectral resolution of 13.6 and 6.7 km/s, for HIRES and MIKE, respectively [334]. As in previous analyses [49, 51, 70, 71, 72, 73, 334, 335,

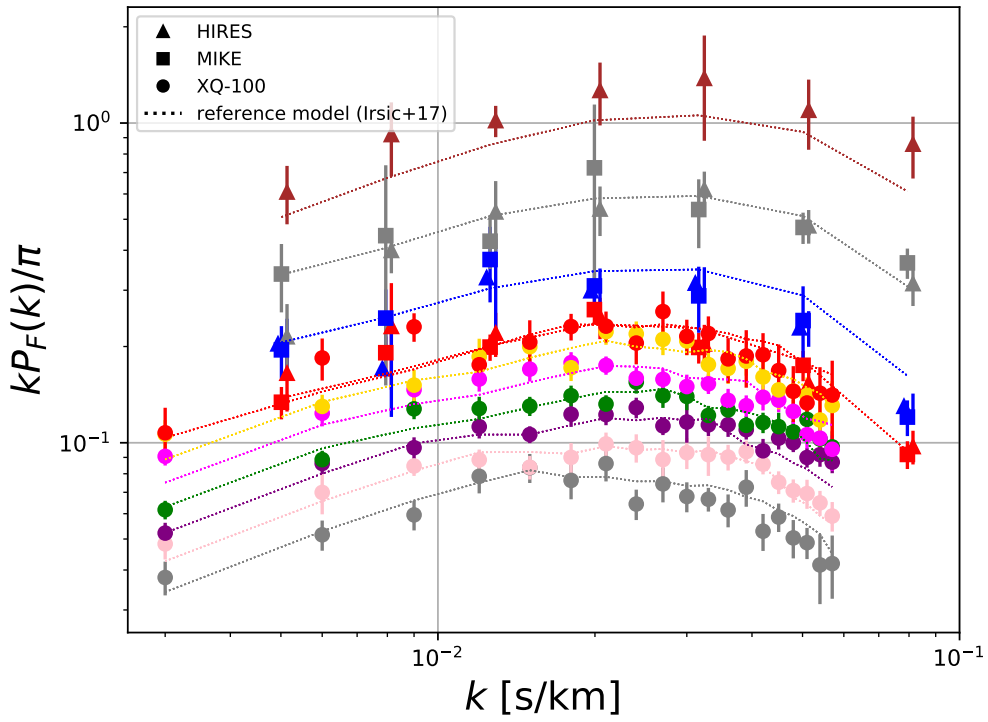

Figure 5.1: Here we show MIKE, HIRES and XQ-100 data-points and error bars, as well as our fiducial model 1D flux power spectra.

339, 376] we imposed a conservative cut on the flux power spectra obtained from MIKE/HIRES data, and only the measurements with $k > 0.005$ s/km have been used, in order to avoid possible systematic uncertainties on large scales due to continuum fitting. Furthermore, we do not use the highest redshift bin for MIKE data, for which the error bars are very large [334]. The MIKE/HIRES data-set is thus constitued by 49 (k, z) data-points, for a total of 182 data-points in the joint XQ-100+MIKE/HIRES analysis, as shown in Fig. 5.1.

5.1.3 The interpolation scheme

With the 633 mock flux power spectra obtained from the suite of hydrodynamic simulations described in Section 5.1.1, we have set a non-regular grid in terms of ratios to the flux power spectrum of the fiducial model, densely sampling the 7-dimensional parameter space of $\{\sigma_8, n_{\rm eff}, z_{\rm reio}, f_{\rm UV}, \bar{F}(z), T_0(z), \gamma(z)\}$.

In order to estimate the values of the ratios in regions of the parameter space that are not

sampled by simulations, it is indispensable to make use of an accurate interpolation procedure[3], such as the so-called Ordinary Kriging method [70, 71, 72, 73]. With this method, few known points are enough to reconstruct an unknown function, provided that it is a continuous function not varying too rapidly within a certain patch of the parameter space, so that it locally behaves as a constant value plus coordinate-dependent fluctuations that average out to zero. Given an unknown input model, the interpolation procedure consists in estimating a set of optimal weights λ_n's (one per each grid-point n), and use them to predict the flux power spectrum ratio corresponding to the input model, $f(\hat{x})$, through a weighted sum over the ratios of all the grid-points, i.e.,

$$f(\hat{x}) = \sum_{n=1}^{N_{\rm sims}} \lambda_n f(\hat{x}_n), \tag{5.1}$$

where $N_{\rm sims}$ is the number of simulations/grid-points (633), and $\hat{x}$ and $\hat{x}_n$ are 7-dimensional arrays containing the coordinates in parameter space of the unknown and known models, respectively[4]. This approach is based on the reasonable assumption that, even if the truly exact weights are specified only for the actual grid-points, an input model close to a grid-point should also return a flux power spectrum close to that obtained for that grid-point. The notion of *closeness* can be quantified in different ways: in the Ordinary Kriging method it is assumed that the weights are inversely proportional to some power β of the distance in parameter space, $D_\beta(\hat{x}, \hat{x}_n)$, i.e.,

$$\lambda_n \equiv \frac{1/D_\beta(\hat{x}, \hat{x}_n)}{\sum_{\ell=1}^{N_{\rm sims}} 1/D_\beta(\hat{x}, \hat{x}_\ell)} \quad \text{with} \quad \sum_{n=1}^{N_{\rm sims}} \lambda_n = 1. \tag{5.2}$$

While in Refs. [70, 71, 73] the distance was defined as a classical Euclidean distance, in this chapter we generalise its definition as follows:

$$D_\beta(\hat{x}, \hat{x}_n) \equiv \left(\left[\sum_{i=1}^{N_{\rm params}} \left(\left| x_i - x_{n,i} \right| \right)^p \cdot w_i \right]^{1/p} + \epsilon \right)^\beta \tag{5.3}$$

[3] A possible alternative is to use Gaussian Process optimisation emulators as in Refs. [381, 382, 383, 384].

[4] For this to work one also needs to make use of *normalised* coordinates, in order not to single out any direction in the parameter space. We do so by simply dividing each coordinate by its maximum range. Note that the Ordinary Kriging method usually fails to give very accurate predictions outside of the set of points supplied, so that indeed it makes sense to vary the parameters only within the grid boundaries [71, 73].

where $N_{\rm params}$ is the number of parameters (7), and x_i and $x_{n,i}$ represent the i-th elements of the 7-dimensional arrays in parameter space, $\hat{x}$ and $\hat{x}_n$. The exponent p generalises the definition of Euclidean distance (that is recovered when $p = 2$), ϵ is a minimal distance parameter to prevent $D_\beta = 0$ (we fix $\epsilon = 10^{-8}$), while β is an enhancement parameter that determines how strongly points far away from the one under consideration influence the estimated value of the function at that point. The 7-dimensional array of weights $\{w_1, .., w_i, .., w_{N_{\rm params}}\}$ has been introduced in order to be able to attribute a different weight to the importance of each i-th parameter when globally estimating the distance between $\hat{x}$ and $\hat{x}_n$ through Eq. (5.3): an advantageous choice when one has to deal with highly non-regular grids such as the one used in this work. To select the optimal values for the 9 hyperparameters (β, p, and the weights w_i's) we perform an optimisation process based on ML techniques, aimed at minimising the average relative error on the theoretical predictions obtained via Eq. (5.1). To do so, we make use of the Optuna package [74], interfaced with a *Tree of Parzen Estimator* (TPE) sampler [75, 76] for the choice of the hyperparameter values. We vary β with a uniform prior distribution in the interval $[2, 10]$, whereas p and each w_i are let free to vary with a logarithmic prior distribution in the ranges $[10^{-3}, 10]$ and $[10^{-2}, 1]$, respectively. At each step of the optimisation process, the i-th grid-point, identified by the set of hyperparameters selected by the TPE, is *left out* of the grid, i.e., the corresponding flux power spectra ratio is determined by interpolating among the remaining $N_{\rm sims} - 1$ grid-points. The mean relative uncertainty associated to the interpolation procedure is then determined by computing the root mean square error (MSQE) between the output of Eq. (5.1), obtained with the $(N_{\rm sims} - 1)$-grid, and the actual output of the i-th simulation that was left out of the grid. The procedure is iterated for 2000 trials. We refer the reader to Appendix I for further technical details.

5.1.4 The new likelihood

In order to perform our analyses, we designed a likelihood module[5] for the publicly available cosmological Monte Carlo Markov Chain (MCMC) sampler `MontePython-v3` [162, 163], building it upon the numerical routines developed in Refs. [71, 73]. The new likelihood has thus

[5] See footnote 1.

inherited the possibility to carry out combined analyses with a number of complementary cosmological probes, as well as the interfaceability with the publicly available Einstein-Boltzmann solver CLASS [55], allowing to test any theoretical model that is implemented within it. In addition, the likelihood module devised in this chapterimproves over the previous ones on several aspects, as summarised below:

- we have improved the Ordinary Kriging method adopted in previous studies to interpolate in the *astro/cosmo* grid, thanks to ML techniques, as illustrated in Section 5.1.3. In addition, we have made use of a finer and more extended grid in terms of values of the mean transmitted flux $\bar{F}(z)$, allowing to furtherly minimise the theoretical errors associated to our newly devised Optimized Kriging method (see also Appendix I).

- we have expanded the *astro/cosmo* grid by performing a new set of simulations corresponding to a very wide range of non-reference values of the cosmological parameters σ_8 and $n_{\rm eff}$, in order to cover regions of the parameter space that are relevant in beyond-ΛCDM analyses;

- we have extended the grid of simulations in terms of colder and hotter IGM thermal histories, in order to prevent the need for inaccurate linear extrapolation beyond the grid boundaries (see Refs. [350, 73] for a discussion on this issue);

- as in past studies, we assume a power law redshift evolution for the slope of the IGM equation of state, $\gamma(z) = \gamma^A[(1+z)/(1+z_p)]^{\gamma^S}$, where the pivot redshift z_p is the redshift at which most of the Lyman-α pixels are coming from ($z_p = 3.6, 4.5, 4.2$ for XQ-100, MIKE/HIRES, and their joint analysis, respectively). However, we have now implemented the possibility of two choices for the redshift evolution of the IGM temperature $T_0(z)$, i.e., (i) a (more conservative) freely floating evolution, where the amplitude of the IGM equation of state is free to vary at each redshift bin, (ii) a power law evolution, analogous to that assumed for $\gamma(z)$, namely $T_0(z) = T_0^A[(1+z)/(1+z_p)]^{T_0^S}$[6];

- we have added to the *astro/cosmo* grid a set of cross-simulations corresponding to simultaneous variations of $n_{\rm eff} \times T_0(z)$. Even if the majority of current NSDM limits were

[6]Note that in Refs. [71, 73] the power law temperature evolution was the only available option.

shown not to be biased by the absence of cross-simulations between correlated parameters [70], this may not always be the case when the cosmological models under study are characterised by very low values of $n_{\rm eff}$ [350];

- we have added the XQ-100 data-set, that enables to further break the degeneracies between the impact of the cosmological parameters and the heating effects due to different thermal and/or reionisation histories – due to its complementary redshift coverage with respect to MIKE/HIRES data [335, 336].

5.2 Results

The goal of this newly built interpolation scheme is to constrain the cosmological models under study by means of MCMC analyses with the `MontePython`[7] sampler [162, 163] in its default Metropolis-Hastings mode, interfaced with `CLASS` [55].

The results reported here are preliminary and focus only on the ΛCDM model with various data-set combinations, MIKE/HIRES, XQ-100 and their joint analysis. For the IGM thermal history we modelled $T_0(z)$ as a power law. The cosmological and astrophysical parameters, and their priors, involved in our analysis are discussed in the following. This is the first analysis performed and so it can be considered as a test to evaluate the performance of the interpolator and not to compare our results with past literature or to discuss implications for the σ_8. These considerations are left for future works, as is the analysis of non-standard cosmologies.

5.2.1 Analysis with the ΛCDM model

In our baseline configuration we scan the parameter space defined by the standard set of six ΛCDM parameters: namely, the baryon physical energy density (ω_b), the CDM abundance parameter ($\Omega_{\rm cdm}$), the angular size of the sound horizon at recombination (θ_s), the tilt and amplitude of the primordial power spectrum (n_s, A_s), and the optical depth at reionisation ($\tau_{\rm reio}$). The three parameters describing the impact of cosmology on the Lyman-α flux power spectrum ($\sigma_8, n_{\rm eff}, z_{\rm reio}$) are derived from this standard set of free parameters, while all the other

[7] https://github.com/brinckmann/montepythonpublic

(astrophysical) parameters are considered as nuisance parameters. We consider the MCMC chains to be converged when the Gelman-Rubin criterion [164] satisfies $R-1<0.02$.

Let us now discuss the priors on these parameters. Using the BBN constraint of Ref. [266], we adopt a Gaussian prior on the absolute density of baryonic matter $\omega_{\rm b}=0.02237\pm0.00036$. In the analysis, we set flat priors on $A_s>0.1$ and on n_s.

For all the other parameters we adopted Gaussian priors coming from Planck's analysis[268]. In particular:

- We assumed a Gaussian prior for $\Omega_{\rm cdm}<1$, with $\Omega_{\rm cdm}=0.2673\pm0.0026$;
- We have chosen a Gaussian prior for $\tau_{\rm reio}$ in range $\in[0.004,\ 0.1]$ with $\tau_{\rm reio}=0.0544\pm0.0073$;
- We have set a Gaussian prior for $100\theta_s$ with $100\theta_s=1.04092\pm0.00031$;

The choice of having multiple tight Gaussian priors on different cosmological parameters is to be considered as a first test for the interpolation scheme and the new likelihood: we are more interested in the overall performance of the interpolator rather than evaluating the cosmological constraints or tensions. In the future we plan to relax these priors and set a configuration comparable with past literature, e.g., Refs. [53, 335, 337].

Concerning the astrophysical (nuisance) parameter, we have opted for the following flat priors:

$$\begin{aligned}
T_0^A&\in[0.0,2.0]\ , & T_0^S&\in[-5.0,5.0]\ , & \gamma^A&\in[1.00,1.70]\ ,\\
\gamma^S&\in[-5.0,5.0]\ , & F(z_1)&\in[0.45,0.90]\ , & F(z_2)&\in[0.39,0.84]\ ,\\
F(z_3)&\in[0.33,0.77]\ , & F(z_4)&\in[0.29,0.73]\ , & F(z_5)&\in[0.21,0.66]\ ,\\
F(z_6)&\in[0.16,0.61]\ , & F(z_7)&\in[0.12,0.58]\ , & F(z_8)&\in[0.05,0.55]\ ,\\
F(z_9)&\in[0.01,0.40]\ , & F(z_{10})&\in[0.01,0.25]\ , & F_{UV}&\in[0.00,1.00]\ .
\end{aligned}\tag{5.4}$$

We show the marginalized posteriors for the cosmological parameters in figs. 5.2 and for the astrophysical ones in figs. 5.3. The best-fit and mean values of the cosmological and astrophysical parameters in tab. 5.1. The analysis seem promising since the results are coherent

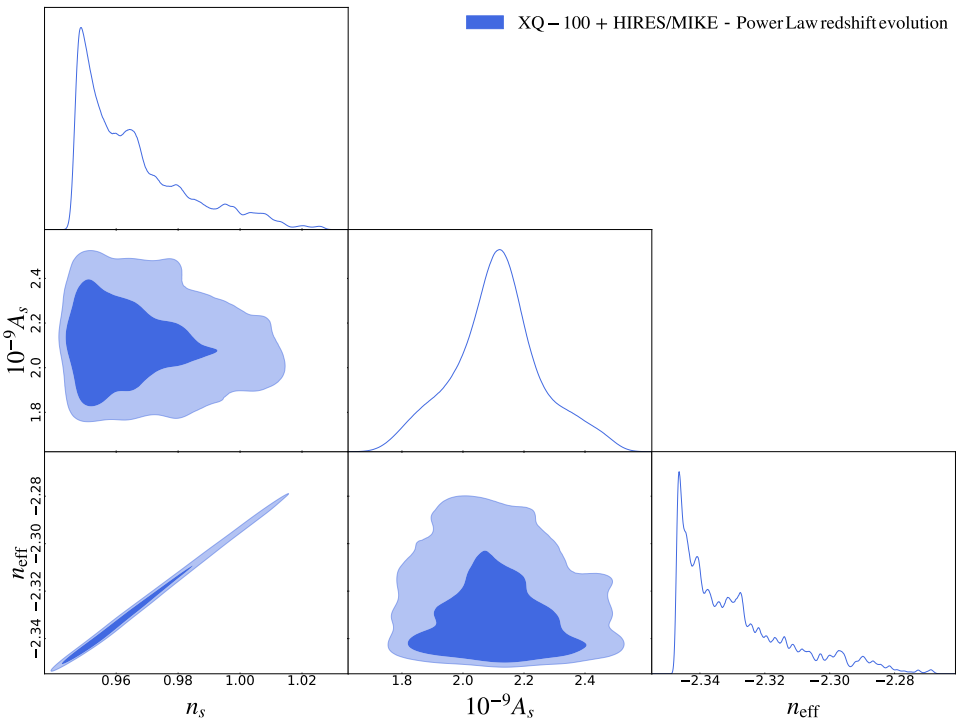

Figure 5.2: Marginalized posteriors for the cosmological parameter from the joint analysis of MIKE/HIRES and XQ-100 Lyman-α data.

with those obtained in past literature, e.g., Refs. [53, 335, 337]. This preliminary test, even if conducted with multiple tight Gaussian priors on different cosmological parameters, sets the way for a more extensive and general analysis with.

5.2.2 Future constraints on extended models: the case of Early Dark Energy

As a consequence of this newly built interpolation scheme, we plan to put constraints on one particular extended scenario, the impact of which on the Lyman-α forest is not *qualitatively* different from the ΛCDM impact. Namely, a scenario that affects the flux power spectrum only in terms of variations of σ_8, $n_{\rm eff}$, and to a less extent $z_{\rm reio}$. We will focus on the model known as Early Dark Energy (EDE), given what was shown in Ref. [371], with the goal to compare our results with those of Ref. [385].

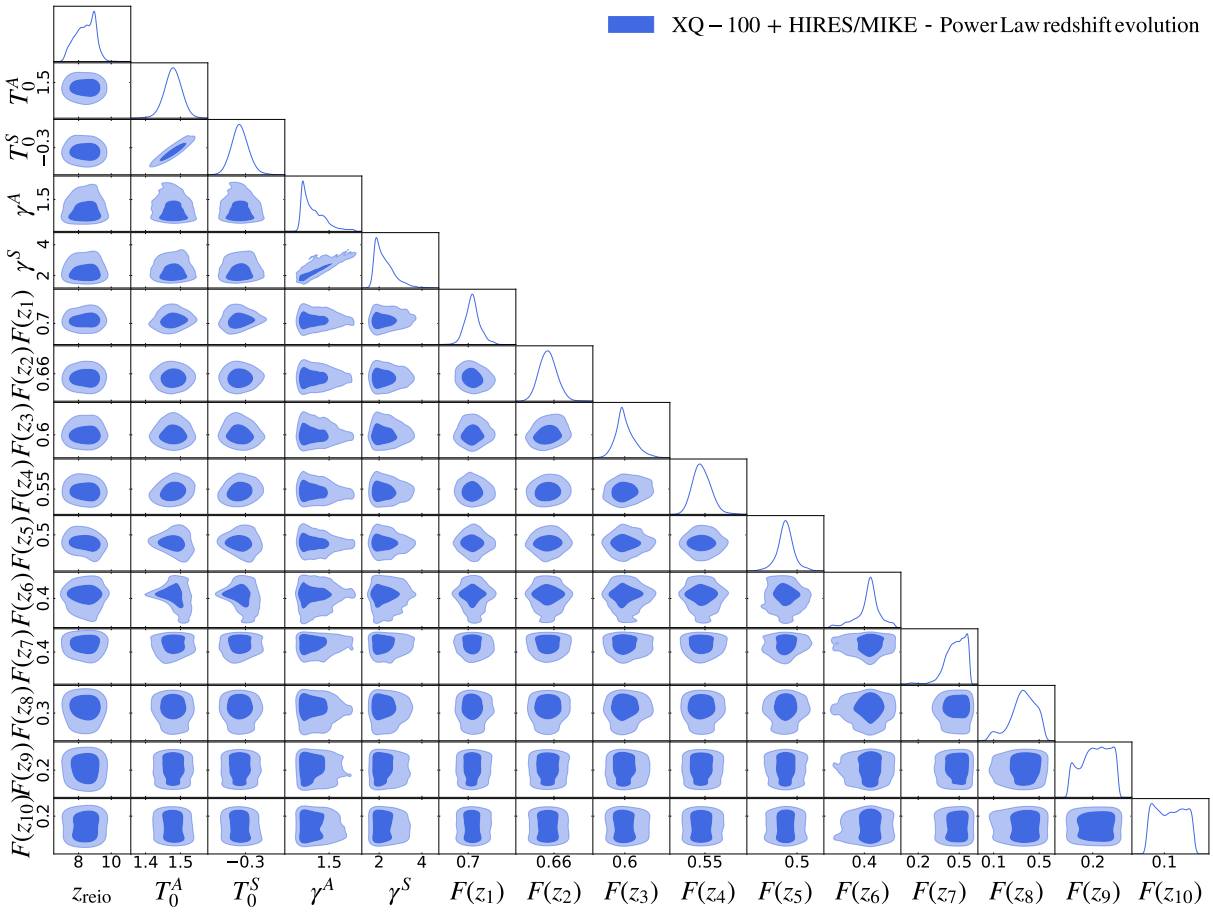

Figure 5.3: Marginalized posteriors for the astrophysical parameter from the joint analysis of MIKE/HIRES and XQ-100 Lyman-α data.

Param	best-fit	mean $\pm\, 1\sigma$
$10^{+9}A_{\rm s}$	2.114	$2.117^{+0.13}_{-0.14}$
$n_{\rm s}$	0.9519	0.9668
$n_{\rm eff}$	-2.342	-2.327
$z_{\rm reio}$	9.029	8.344
T_0^A	1.492	$1.48^{+0.025}_{-0.023}$
T_0^S	-0.3005	$-0.3555^{+0.086}_{-0.092}$
γ^A	1.306	$1.377^{+0.041}_{-0.099}$
γ^S	1.839	$2.216^{+0.22}_{-0.51}$
$F(z_1)$	0.7136	$0.7116^{+0.017}_{-0.023}$
$F(z_2)$	0.6567	$0.6538^{+0.0073}_{-0.0095}$
$F(z_3)$	0.5977	$0.6003^{+0.005}_{-0.0075}$
$F(z_4)$	0.5459	$0.5478^{+0.006}_{-0.0073}$
$F(z_5)$	0.4871	$0.4834^{+0.011}_{-0.012}$
$F(z_6)$	0.4711	$0.43^{+0.082}_{-0.054}$

Table 5.1: Best-fit and mean values with $1\,\sigma$ deviations measured from the joint analysis of MIKE/HIRES and XQ-100 Lyman-α data.

5.3 Towards a unified model-independent approach

There are models that we cannot describe only in terms of tilt and amplitude, because their small-scale behaviours is qualitatively different from that of ΛCDM. This is the case of models featuring sharp suppressions or power enhancement deviating from the simple ΛCDM-like behaviour.

In past literature, these scenarios have often been studied by adopting some flexible analytical parametrisation capable to accurately describe a variety of shapes in the primordial power spectrum on small scales, by varying its parameters. Thereafter, one generally builds an additional grid of hydrodynamic simulations exploring the additional parameter space, while keeping all other cosmological and astrophysical parameters fixed.

An alternative route is to add only one phenomenological parameter capturing in an agnostic way the *qualitative* deviations from ΛCDM, i.e., features that cannot be captured by σ_8 and $n_{\rm eff}$. Once introduced, on the one hand one can treat it as a nuisance parameter to marginalise over and look at constraints on other cosmological parameters; on the other hand, finding a preference for a non-zero value for this extra-parameter could in principle provide a model-independent evidence of new physics beyond ΛCDM.

This is outside the scope of this thesis, because it would require a further extension of the grid of simulations. However, this work represent a first important step, given that the numerical set-up presented here can readily be accommodated to include new simulations. We leave this task for future work.

A unified framework to test most of the alternative cosmological models implemented in CLASS requires to merge the ΛCDM+"area" likelihood with the $\{\alpha, \beta, \gamma, \delta\}$-likelihood introduced in Ref. [73]. This will also allow to perform a more in depth investigation of the hints of non-zero DM-neutrino and DM-baryon interactions claimed in Refs. [73, 350], respectively.

Finally, in the future, besides the Lyman-α forest data-sets illustrated in Section 5.1.2, for some of the runs we plan to make use of the following additional complementary data:

- the low-ℓ CMB TT, EE ($\ell < 30$), the high-ℓ TT, TE, EE ($30 \leq \ell \leq 2500$) data [9], and the gravitational lensing potential reconstruction ($8 \leq \ell \leq 400$) [386] from *Planck*;
- the BAO measurements from 6dFGS at $z = 0.106$ [387], SDSS DR7 at $z = 0.15$ [388],

BOSS DR12 at $z = 0.38, 0.51$ and 0.61 [389], and the joint constraints from eBOSS DR14 Lyman-α auto-correlation at $z = 2.34$ [390] and cross-correlation at $z = 2.35$ [391];

- the measurements of the growth function $f\sigma_8(z)$ (FS) from the CMASS and LOWZ galaxy samples of BOSS DR12 at $z = 0.38$, 0.51, and 0.61 [389];
- the Pantheon+ SnIa catalogue, spanning redshifts $0.01 < z < 2.3$ [392].

Chapter 6

Conclusions

In this thesis, our attention has been primarily directed towards non-standard cosmological frameworks and the influence of numerical instruments on deducing evidences of beyond-ΛCDM theories. Even though the ΛCDM model has achieved remarkable results in the understanding of many cosmological phenomena, it remains unclear the authentic nature of DM and DE. The models and approaches took in exam in this thesis may contribute to solve some of these discrepancies. For instance, PBHs represent a specific type of CDM, offering perspectives on its nature. Additionally, the normal branch of DGP gravity is an interesting model of modifications of General Relativity at large scales that has not yet been excluded. Lastly, obtaining constraints on theoretical models like EDE may contribute to resolve long-standing tensions like the one on the Hubble parameter H_0.

In this thesis we focused on one the most popular DM candidates, PBHs. We have obtained constraints associated with matter accretion into a PBH. The radiation emission that follows the accretion process influences the universe's thermal history, causing delays in recombination and early reionization. Consequently, these processes can be restricted by observations from the CMB. Nonetheless, the modeling of accretion comes with considerable theoretical uncertainties, leading to significant margins of error in the final constraints.

Beyond these uncertainties, the influence of outflows, whether in the form of winds or jets (based on their collimation), on accretion has not been thoroughly explored in existing literature. Both analytical and computational studies have indicated that even minor outflows

might escape the black hole's gravitational pull, displacing a portion of the surrounding cosmic medium, which in turn reduces the PBH's accretion rate. Concurrently, these outflows could potentially speed up non-thermal particles, amplifying the black hole's brightness. These intertwined effects can notably impact the system's overall brightness, adding another dimension of uncertainty. This added complexity needs consideration when deriving cosmological constraints based on PBH accretion.

In this work, our goal was to model these effects and to analyze how their interplay impacts the CMB constraints on PBH accretion. We explored various accretion geometries, such as spherical or disk-like configurations, alongside different ionization models, including photo-ionization and collisional ionization. Furthermore, we consider both singular and broad mass distributions. The insights from our analysis are depicted in figures 2.6-2.7, highlighting that our results are heavily influenced by the chosen efficiency of non-thermal emissions [25]. This inference is shown in figure 2.8, which presents the compounded uncertainty ranges on the actual constraints, both including and excluding the impact of outflows [25].

Our incomplete understanding of dark energy opens doors for alternative theories. Modified gravity models are examples of such scenarios, even if there is no alternative gravity theory that solves the cosmological constant problem. In fact the discrepancy between the observed value of the cosmological constant (or dark energy) and its theoretically predicted value remains and these theories often inadvertently introduce other naturalness or fine-tuning problems.

We have placed bounds on potential alterations to gravitational cosmology using the full power spectrum derived from BOSS data [38]. As detailed in Section 3.2, our approach to modeling galaxy distribution in redshift space has been based on the EFTofLSS and a perturbative bias expansion.

In particular we focused on the normal branch of the DGP framework, assuming the background expansion of a flat ΛCDM model. All the needed modifications are embodied by the parameter $\Omega_{\rm rc}$. The analysis have been conducted using the `PyBird` software, which, for our purposes, has been customized to incorporate these new effects (refer to Section 3.3 for details).

As elaborated in sec. 3.4, within the framework of linear theory, $\Omega_{\rm rc}$ exhibits degeneracy with A_s. This pronounced degeneracy cause a deviation in the 1-dimensional marginalized posteriors of the cosmological parameters from their true values. By utilizing synthetic data derived from the EFTofLSS, we have measured this deviation, providing insights into how degeneracy impacts the marginalized posteriors via projection effects. We have mitigated this influence by anchoring A_s to the central value reported by Planck. However, even with a fixed A_s, there remain underlying degeneracies, such as the relationship between $\Omega_{\rm rc}$ and n_s.

Our analysis of the BOSS data is detailed in sec.3.5. With a fixed A_s, the marginalized posteriors can be seen in fig.3.7. The bounds for the nDGP parameter, $\Omega_{\rm rc}$, depend on the chosen prior. To derive constraints that are not influenced by these priors, we evaluated the ratio of the 1d posterior to its associated prior, known as the Bayes factor. This analysis yields an upper limit for the nDGP parameter of $\Omega_{\rm rc} \lesssim 0.2$ at a confidence level of 95%. Notably, this represents the first constraints of the nDGP parameter utilizing the complete galaxy power spectrum from BOSS data [38].

Although our analysis is restricted to the nDGP model alone, it can be straightforwardly extended to other scale-independent models, such as those described by the general single-field framework of the EFT of dark energy extended beyond linear order [31]. Another intriguing possibility is to perform these analyses with the perturbative expansions derived in the LSS bootstrap approach of [209]. In any case, our analysis [38] shows that competitive constraints on the nDGP model using galaxy clustering data can be obtained only with volumes higher than BOSS.

The recent launch of the*Euclid* satellite [77], along with upcoming data releases, could be fundamental to test the methodologies introduced in this thesis. In chapter 4 we provided a preliminary insight into the results that will be presented in the future article "Cosmological constraints on non-standard cosmologies from simulated*Euclid* probes" by the*Euclid* Consortium [77]. We focused on deducing cosmological parameters that go beyond the ΛCDM, leveraging from the halo power spectrum of simulations. and performing the analysis through the use of the `PyBird` software.

The Lyman-α forest is a prominent observational manifestation of the IGM and it serves as

a tool in unveiling the nature of the underlying dark matter distribution across the universe. Through its pattern of absorption lines, it offers significant insights into the inhomogeneous distribution of intergalactic neutral hydrogen, making it fundamental for cosmological explorations, particularly within the realms of non-standard dark matter models.

In chapter 5 we elucidated how the Lyman-α forest provides valuable constraints, not just on ΛCDM cosmology but also on alternative cosmological models. We have highlighted how the Lyman-α forest data can shed light on long-standing tensions between early and late-universe estimates of cosmological parameters, such as the amplitude of the linear power spectrum, σ_8.

One of the central contributions of this work is the development of an adaptive interpolation tool designed for analyzing diverse cosmological models using an extensive Lyman-α forest dataset. The combination of N-Body hydrodynamic simulations and advanced interpolation methods, notably the Optimized Kriging technique, is fundamental for achieving this achievement. The modified distance metric in the interpolation process, given by Eq. (5.3), enhances the flexibility and scope of this framework.

In conclusion, in this thesis we focused on the significance of numerical tools with their potential in addressing some of the long-standing mysteries in cosmology.

Through these techniques we tried to optimize the constraints on deviations from the standard ΛCDM cosmology. These methods can be easily integrated into rapid analysis codes for cosmological data and some of these can be refined with ML tools to have faster and more precise computation.

Overall the ultimate goal of the thesis is to show that a synergistic approach between astrophysics, astroparticle physics, and cosmology, helps to constrain the fundamental properties of Dark Matter and Dark Energy through astrophysical and cosmological observations coming from different sources.

The expertise and numerical tools here developed can be adapted for testing a large variety of non-standard cosmologies with many other cosmological and astrophysical probes. The combination of different data sets, with complementary redshift and scale coverages, will improve the present constraints and possibly lead to discoveries.

The methods and results presented in this work emphasizes the importance of these new tools and approaches for the future of cosmology.

Appendix A

Kernels and time-dependent functions

The six kernels introduced in sec. 3.2.2 in eq. (3.35) are defined as

$$\alpha^1(\mathbf{q}_1,\mathbf{q}_2,\mathbf{q}_3) = \alpha(\mathbf{q}_3,\mathbf{q}_1+\mathbf{q}_2)\alpha_s(\mathbf{q}_1,\mathbf{q}_2) = O_{\alpha_s\alpha_s}(\mathbf{q}_1,\mathbf{q}_2,\mathbf{q}_3) - \frac{1}{2}O_{\alpha_s\alpha_a}(\mathbf{q}_1,\mathbf{q}_2,\mathbf{q}_3)\,, \tag{A.1}$$

$$\alpha^2(\mathbf{q}_1,\mathbf{q}_2,\mathbf{q}_3) = \alpha(\mathbf{q}_3,\mathbf{q}_1+\mathbf{q}_2)\beta(\mathbf{q}_1,\mathbf{q}_2) = O_{\beta\alpha_s}(\mathbf{q}_1,\mathbf{q}_2,\mathbf{q}_3) - \frac{1}{2}O_{\beta\alpha_a}(\mathbf{q}_1,\mathbf{q}_2,\mathbf{q}_3)\,, \tag{A.2}$$

$$\beta^1(\mathbf{q}_1,\mathbf{q}_2,\mathbf{q}_3) = 2\beta(\mathbf{q}_3,\mathbf{q}_1+\mathbf{q}_2)\alpha_s(\mathbf{q}_1,\mathbf{q}_2) = 2\,O_{\alpha_s\beta}(\mathbf{q}_1,\mathbf{q}_2,\mathbf{q}_3)\,, \tag{A.3}$$

$$\beta^2(\mathbf{q}_1,\mathbf{q}_2,\mathbf{q}_3) = 2\beta(\mathbf{q}_3,\mathbf{q}_1+\mathbf{q}_2)\beta(\mathbf{q}_1,\mathbf{q}_2) = 2\,O_{\beta\beta}(\mathbf{q}_1,\mathbf{q}_2,\mathbf{q}_3)\,, \tag{A.4}$$

$$\gamma^1(\mathbf{q}_1,\mathbf{q}_2,\mathbf{q}_3) = \alpha(\mathbf{q}_1+\mathbf{q}_2,\mathbf{q}_3)\alpha_s(\mathbf{q}_1,\mathbf{q}_2) = O_{\alpha_s\alpha_s}(\mathbf{q}_1,\mathbf{q}_2,\mathbf{q}_3) + \frac{1}{2}O_{\alpha_s\alpha_a}(\mathbf{q}_1,\mathbf{q}_2,\mathbf{q}_3)\,, \tag{A.5}$$

$$\gamma^2(\mathbf{q}_1,\mathbf{q}_2,\mathbf{q}_3) = \alpha(\mathbf{q}_1+\mathbf{q}_2,\mathbf{q}_3)\beta(\mathbf{q}_1,\mathbf{q}_2) = O_{\beta\alpha_s}(\mathbf{q}_1,\mathbf{q}_2,\mathbf{q}_3) + \frac{1}{2}O_{\beta\alpha_a}(\mathbf{q}_1,\mathbf{q}_2,\mathbf{q}_3)\,, \tag{A.6}$$

where $O_{\alpha_s\alpha_s}$, $O_{\alpha_s\alpha_a}$, $O_{\beta\alpha_s}$, and $O_{\alpha_s\beta}$, are defined analogously to eq. (3.40).

To shorten the following expressions, let us introduce the following notation,

$$M_1(a) \equiv \frac{1}{f_+(a)}\left(\frac{3\Omega_{\mathrm{m},a}(a)}{2}\right)^2\,, \qquad M_2(a) \equiv \frac{\nu_{22}(a)}{2}\frac{3\Omega_{\mathrm{m},a}(a)}{2}\,. \tag{A.7}$$

The time dependent functions that appear in the kernels up to third order are

$$\mathcal{G}_1^\lambda(a) = \int_0^1 \left[G_1^\lambda(a,\tilde{a})f_+(\tilde{a}) + G_2^\lambda(a,\tilde{a})\nu_2(\tilde{a})M_1(\tilde{a})\right]\frac{D_+^2(\tilde{a})}{D_+^2(a)}d\tilde{a}\,, \tag{A.8}$$

$$\mathcal{G}_2^\lambda(a) = \int_0^1 G_2^\lambda(a,\tilde{a})\left[f_+(\tilde{a}) - \nu_2(\tilde{a})M_1(\tilde{a})\right]\frac{D_+^2(\tilde{a})}{D_+^2(a)}d\tilde{a}\,, \tag{A.9}$$

and

$$\mathcal{U}_1^\lambda(a) = \int_0^1 \left\{ G_1^\lambda(a,\tilde{a}) f_+(\tilde{a}) \mathcal{G}_1^\delta(\tilde{a}) + G_2^\lambda(a,\tilde{a}) M_1(\tilde{a}) \left[\nu_2(\tilde{a}) \mathcal{G}_1^\delta(\tilde{a}) + M_2(\tilde{a}) \right] \right\} \frac{D_+^3(\tilde{a})}{D_+^3(a)} d\tilde{a} \,, \tag{A.10}$$

$$\mathcal{U}_2^\lambda(a) = \int_0^1 \left\{ G_1^\lambda(a,\tilde{a}) f_+(\tilde{a}) \mathcal{G}_2^\delta(\tilde{a}) + G_2^\lambda(a,\tilde{a}) M_1(\tilde{a}) \left[\nu_2(\tilde{a}) \mathcal{G}_2^\delta(\tilde{a}) - M_2(\tilde{a}) \right] \right\} \frac{D_+^3(\tilde{a})}{D_+^3(a)} d\tilde{a} \,, \tag{A.11}$$

$$\mathcal{V}_{11}^\lambda(a) = \int_0^1 \left\{ G_1^\lambda(a,\tilde{a}) f_+(\tilde{a}) \mathcal{G}_1^\theta(\tilde{a}) + G_2^\lambda(a,\tilde{a}) M_1(\tilde{a}) \left[\nu_2(\tilde{a}) \mathcal{G}_1^\delta(\tilde{a}) + M_2(\tilde{a}) \right] \right\} \frac{D_+^3(\tilde{a})}{D_+^3(a)} d\tilde{a} \,, \tag{A.12}$$

$$\mathcal{V}_{21}^\lambda(a) = \int_0^1 \left\{ G_1^\lambda(a,\tilde{a}) f_+(\tilde{a}) \mathcal{G}_2^\theta(\tilde{a}) + G_2^\lambda(a,\tilde{a}) M_1(\tilde{a}) \left[\nu_2(\tilde{a}) \mathcal{G}_2^\delta(\tilde{a}) - M_2(\tilde{a}) \right] \right\} \frac{D_+^3(\tilde{a})}{D_+^3(a)} d\tilde{a} \,, \tag{A.13}$$

$$\mathcal{V}_{12}^\lambda(a) = \int_0^1 G_2^\lambda(a,\tilde{a}) \left\{ f_+(\tilde{a}) \mathcal{G}_1^\theta(\tilde{a}) - M_1(\tilde{a}) \left[\nu_2(\tilde{a}) \mathcal{G}_1^\delta(\tilde{a}) + M_2(\tilde{a}) \right] \right\} \frac{D_+^3(\tilde{a})}{D_+^3(a)} d\tilde{a} \,, \tag{A.14}$$

$$\mathcal{V}_{22}^\lambda(a) = \int_0^1 G_2^\lambda(a,\tilde{a}) \left\{ f_+(\tilde{a}) \mathcal{G}_2^\theta(\tilde{a}) - M_1(\tilde{a}) \left[\nu_2(\tilde{a}) \mathcal{G}_2^\delta(\tilde{a}) - M_2(\tilde{a}) \right] \right\} \frac{D_+^3(\tilde{a})}{D_+^3(a)} d\tilde{a} \,. \tag{A.15}$$

In the previous expressions, G_i^λ, with $i = 1, 2$ and $\lambda = \delta, \theta$, are the Green's functions defined by eqs. (3.24)–(3.27) while ν_2 and ν_{22} are the nDGP functions that account for the non-linear corrections of the generalized Poisson equation (3.5). Their explicit expression for the nDGP case is given by eqs. (3.59) and (3.60).

Appendix B

Comparison with LSS bootstrap

In this appendix we discuss the relation between the perturbative expansions of [64] used in the main text and in `PyBird` with the one that can be derived in the LSS bootstrap approach [209]. This approach allows one to derive the analytic structure of the perturbative kernels of dark matter and biased tracers starting from symmetries. In this way, one can show that the expansion used in ΛCDM also applies to more general models, even in modified gravity, with the same symmetries (translational and rotational invariance, the equivalence principle, etc.) as in ΛCDM. Indeed, here we show that the two expansions are equivalent.

B.1 Dark matter kernels

Let us start by discussing the dark matter kernels. For the matter density contrast in the bootstrap basis we have, after imposing all the symmetries [209][1]

$$K_1^{(1)}(\mathbf{q}_1) = 1\,, \tag{B.1}$$

$$K_1^{(2)}(\mathbf{q}_1,\mathbf{q}_2) = \frac{1}{2}\big[2\beta(\mathbf{q}_1,\mathbf{q}_2) + a_\gamma\gamma(\mathbf{q}_1,\mathbf{q}_2)\big]\,, \tag{B.2}$$

$$\begin{aligned} K_1^{(3)}(\mathbf{q}_1,\mathbf{q}_2,\mathbf{q}_3) = \frac{1}{6}\big[&2\beta(\mathbf{q}_1,\mathbf{q}_2)\beta(\mathbf{q}_{12},\mathbf{q}_3) + a_{\gamma\gamma}\gamma(\mathbf{q}_1,\mathbf{q}_2)\gamma(\mathbf{q}_{12},\mathbf{q}_3) \\ &- 2\left(a_{\gamma\alpha}-g\right)\gamma(\mathbf{q}_1,\mathbf{q}_2)\beta(\mathbf{q}_{12},\mathbf{q}_3) + 2\left(a_\gamma + 2a_{\gamma\alpha} - g\right)\beta(\mathbf{q}_1,\mathbf{q}_2)\gamma(\mathbf{q}_{12},\mathbf{q}_3) \\ &+ a_{\gamma\alpha}\gamma(\mathbf{q}_1,\mathbf{q}_2)\alpha_a(\mathbf{q}_{12},\mathbf{q}_3) + \text{ cyclic}\big]\,, \end{aligned} \tag{B.3}$$

where $\alpha_a(\mathbf{q}_1,\mathbf{q}_2) \equiv \frac{\mathbf{q}_1\cdot\mathbf{q}_2}{q_1^2} - \frac{\mathbf{q}_1\cdot\mathbf{q}_2}{q_2^2}$ and a_γ, $a_{\gamma\gamma}$, etc.. are time-dependent coefficients that depend on the cosmological model. Analogous expressions can be given for the velocity divergence kernels. We denote the corresponding time-dependent coefficients by d_γ, $d_{\gamma\gamma}$, etc., i.e.,

$$K_2^{(1)}(\mathbf{q}_1) = 1\,, \tag{B.4}$$

$$K_2^{(2)}(\mathbf{q}_1,\mathbf{q}_2) = \frac{1}{2}\big[2\beta(\mathbf{q}_1,\mathbf{q}_2) + d_\gamma\gamma(\mathbf{q}_1,\mathbf{q}_2)\big]\,, \tag{B.5}$$

$$\begin{aligned} K_2^{(3)}(\mathbf{q}_1,\mathbf{q}_2,\mathbf{q}_3) = \frac{1}{6}\big[&2\beta(\mathbf{q}_1,\mathbf{q}_2)\beta(\mathbf{q}_{12},\mathbf{q}_3) + d_{\gamma\gamma}\gamma(\mathbf{q}_1,\mathbf{q}_2)\gamma(\mathbf{q}_{12},\mathbf{q}_3) \\ &- 2\left(d_{\gamma\alpha}-g\right)\gamma(\mathbf{q}_1,\mathbf{q}_2)\beta(\mathbf{q}_{12},\mathbf{q}_3) + 2\left(d_\gamma + 2d_{\gamma\alpha} - g\right)\beta(\mathbf{q}_1,\mathbf{q}_2)\gamma(\mathbf{q}_{12},\mathbf{q}_3) \\ &+ d_{\gamma\alpha}\gamma(\mathbf{q}_1,\mathbf{q}_2)\alpha_a(\mathbf{q}_{12},\mathbf{q}_3) + \text{ cyclic}\big]\,, \end{aligned} \tag{B.6}$$

With these definitions we find that the function h in the above expressions is given by [209]

$$g(a) \equiv \int_0^a d\ln\tilde{a}\; f_+(\tilde{a})\left[\frac{D_+(\tilde{a})}{D_+(a)}\right]^2 d_\gamma(\tilde{a})\,. \tag{B.7}$$

We can now compare this expansion with the one of eqs. (3.33)–(3.35) [64]. For instance, by comparing eq. (B.2) with eq. (3.34) we obtain

$$a_\gamma = 2\mathcal{G}_1^\delta\,, \qquad d_\gamma = 2\mathcal{G}_1^\theta\,. \tag{B.8}$$

[1] In [209] we define the nth-order perturbation theory kernel with a $1/n!$ with respect to the standard definition. Hence, the factor $1/2$ and $1/6$ in the second- and third-order kernels in these equations. Notice also that we have changed the name of the time-dependent coefficients.

Using the definitions (A.9) and the equations (3.23) we can verify the following relation, which enforces the continuity equation for the second order matter kernel,

$$\frac{1}{f_+(a)}\frac{d}{d\ln a}\mathcal{G}_1^\delta(a) = 1 - 2\mathcal{G}_1^\delta(a) + \mathcal{G}_1^\theta(a)\,, \tag{B.9}$$

and can be integrated to give

$$\mathcal{G}_1^\delta(a) = \frac{g(a)+1}{2}\,, \tag{B.10}$$

where we have used (B.7) and (B.8).

Finally, comparing the third-order kernels we have

$$a_{\gamma\gamma} = 2\mathcal{U}_1^\delta + g - 2\mathcal{V}_{12}^\delta\,, \qquad a_{\gamma\alpha} = \frac{g}{2} - \mathcal{V}_{12}^\delta - \mathcal{U}_1^\delta\,, \tag{B.11}$$

$$d_{\gamma\gamma} = 2\mathcal{U}_1^\theta + g - 2\mathcal{V}_{12}^\theta\,, \qquad d_{\gamma\alpha} = \frac{g}{2} - \mathcal{V}_{12}^\theta - \mathcal{U}_1^\theta\,. \tag{B.12}$$

In [64] a tracer-independent function $Y(a)$ was introduced, defined in terms of the functions $\mathcal{V}_{11}^\theta$ and $\mathcal{V}_{12}^\theta$, see eq. (3.35), as

$$Y(a) \equiv \mathcal{V}_{11}^\theta(a) + \mathcal{V}_{12}^\theta(a) - \frac{3}{14}\,. \tag{B.13}$$

It is related to the function $g(a)$ by

$$Y(a) = \frac{g(a)}{2} - \frac{3}{14}\,. \tag{B.14}$$

B.2 Biased tracers kernels

For the tracer's kernels in the bootstrap approach we have [209]

$$K_{\delta_g}^{(1)}(\mathbf{q}_1) = a_0^{(g)}\,, \tag{B.15}$$

$$K_{\delta_g}^{(2)}(\mathbf{q}_1,\mathbf{q}_2) = \frac{1}{2}\big[a_1^{(g)} + 2\,a_0^{(g)}\,\beta(\mathbf{q}_1,\mathbf{q}_2) + a_{\gamma_2}^{(g)}\,\gamma(\mathbf{q}_1,\mathbf{q}_2)\big]\,, \tag{B.16}$$

$$\begin{aligned} K_{\delta_g}^{(3)}(\mathbf{q}_1,\mathbf{q}_2,\mathbf{q}_3) = \frac{1}{6}\big[&a_2^{(g)}/3 + a_{\gamma_3}^{(g)}\gamma(\mathbf{q}_1,\mathbf{q}_2) + 2a_1^{(g)}\beta(\mathbf{q}_1,\mathbf{q}_2) \\ &+ a_{\gamma\gamma}^{(g)}\gamma(\mathbf{q}_1,\mathbf{q}_2)\gamma(\mathbf{q}_{12},\mathbf{q}_3) + 2\,a_0^{(g)}\beta(\mathbf{q}_1,\mathbf{q}_2)\beta(\mathbf{q}_{12},\mathbf{q}_3) \\ &+ 2(g\,a_0^{(g)} - a_{\gamma\alpha}^{(g)})\gamma(\mathbf{q}_1,\mathbf{q}_2)\beta(\mathbf{q}_{12},\mathbf{q}_3) + 2(a_{\gamma_2}^{(g)} + 2\,a_{\gamma\alpha}^{(g)} - g\,a_0^{(g)})\beta(\mathbf{q}_1,\mathbf{q}_2)\gamma(\mathbf{q}_{12},\mathbf{q}_3) \\ &+ a_{\gamma\alpha}^{(g)}\gamma(\mathbf{q}_1,\mathbf{q}_2)\alpha_a(\mathbf{q}_{12},\mathbf{q}_3) + \text{cyclic}\big]\,. \end{aligned} \tag{B.17}$$

We wish to verify that these expressions reproduce eqs. (3.37), (3.38) and (3.39) [64]. This is obvious for $K^{(1)}_{\delta_g}$ and for $K^{(2)}_{\delta_g}$ if these relations hold,

$$a_0^{(g)} = b_1\,, \qquad a_1^{(g)} = -2(b_1 - b_2 - b_4)\,, \qquad a_{\gamma_2}^{(g)} = 2\left(b_1 - \frac{2}{7}b_2\right)\,. \tag{B.18}$$

To do the same comparison on the third-order kernel, it is convenient to rewrite eq. (B.17) in the following form,

$$\begin{aligned} K^{(3)}_{\delta_g}(\mathbf{q}_1,\mathbf{q}_2,\mathbf{q}_3) = \frac{1}{6}\Bigg[&\frac{1}{3}\,a_2^{(g)} + a_{\gamma_3}^{(g)}\gamma(\mathbf{q}_1,\mathbf{q}_2) + 2a_1^{(g)}\beta(\mathbf{q}_1,\mathbf{q}_2) \\ &+ 2\,a_0^{(g)}\beta(\mathbf{q}_1,\mathbf{q}_2)\beta(\mathbf{q}_{12},\mathbf{q}_3) + \left[2a_{\gamma_2}^{(g)} + a_{\gamma a}^{(g)} - 2\left(a_{\gamma b}^{(g)} + g a_0^{(g)}\right)\right]\beta(\mathbf{q}_1,\mathbf{q}_2)\gamma(\mathbf{q}_{12},\mathbf{q}_3) \\ &+ \left(\frac{1}{4}a_{\gamma a}^{(g)} - \frac{1}{2}a_{\gamma b}^{(g)}\right)\gamma(\mathbf{q}_1,\mathbf{q}_2)\alpha_a(\mathbf{q}_{12},\mathbf{q}_3) + \left(a_{\gamma b}^{(g)} - \frac{1}{2}a_{\gamma a}^{(g)} + 2g a_0^{(g)}\right)\gamma(\mathbf{q}_1,\mathbf{q}_2)\beta(\mathbf{q}_{12},\mathbf{q}_3) \\ &+ \left(\frac{1}{2}a_{\gamma a}^{(g)} + a_{\gamma b}^{(g)}\right)\gamma(\mathbf{q}_1,\mathbf{q}_2)\gamma(\mathbf{q}_{12},\mathbf{q}_3) + \text{cyclic}\Bigg]\,. \end{aligned} \tag{B.19}$$

To compare this expression with (3.39), we need first to replace $\mathbf{q}_1 \to \mathbf{q}$, $\mathbf{q}_2 \to -\mathbf{q}$ and $\mathbf{q}_3 \to \mathbf{k}$ and then subtract the UV part, i.e. the finite part of the kernel in the limit $q/k \to \infty$. Subtracting the UV part removes the first line of the above equation, while the term proportional to $\beta(\mathbf{q}_1,\mathbf{q}_2)\gamma(\mathbf{q}_{12},\mathbf{q}_3)$ and its permutations cancel. Moreover, also the combination of terms multiplying $a_{\gamma b}^{(g)}$ vanishes under this replacement.

Comparing what remains with eq. (3.39), using the notation eq. (3.40), eq. (B.18) and the relation between Y and g, eq. (B.14), we obtain

$$b_3 = \frac{21}{2}\left(g a_0^{(g)} - \frac{a_{\gamma a}^{(g)}}{2}\right)\,. \tag{B.20}$$

Before concluding, let us compare this bias expansion with another commonly used one [393],

$$\delta_g = \hat{b}_1\delta + \frac{\hat{b}_2}{2}\delta^2 + \hat{b}_{\mathcal{G}_2}\mathcal{G}_2 + \hat{b}_{\mathcal{G}_N}\mathcal{G}_N + \dots\,, \tag{B.21}$$

where

$$\mathcal{G}_2 = (\nabla_i\nabla_j\varphi_1)^2 - (\nabla^2\varphi_1)^2\,, \qquad \mathcal{G}_N = \nabla_i\nabla_j\varphi_1\nabla_i\nabla_j\varphi_2 - \nabla^2\varphi_1\nabla^2\varphi_2\,, \tag{B.22}$$

with $\nabla^2\varphi_1 = \delta$ and $\nabla^2\varphi_2 = \mathcal{G}_2$. The ellipses denote bias operators that do not enter in the

1-loop calculation. Using the results of [209], we find

$$
\begin{aligned}
b_1 &= \hat{b}_1 \ , \quad b_2 = \frac{7}{2}\left[\left(1-\frac{a_\gamma}{2}\right)\hat{b}_1 + \hat{b}_{\mathcal{G}_2}\right] \ , \\
b_3 &= \frac{21}{2}\left[\left(g-\frac{a_{\gamma a}}{2}\right)\hat{b}_1 + a_\gamma \hat{b}_{\mathcal{G}_2} - \hat{b}_{\mathcal{G}_N}\right] \ , \\
b_4 &= -\frac{1}{2}\left[\left(5-\frac{7}{2}a_\gamma\right)\hat{b}_1 - \hat{b}_2 + 7\hat{b}_{\mathcal{G}_2}\right] \ .
\end{aligned}
\tag{B.23}
$$

Appendix C

Initial conditions in nDGP

The Green's functions, eqs. (3.24)–(3.27), are defined in terms of the two independent solutions of the growth equation, eq. (3.8). Here we discuss how to select these two solutions in nDGP.

In general relativity, for matter domination, $\nu = 1$ and $\Omega_{\mathrm{m},a} = \Omega_{\mathrm{m}}$, one has two independent solutions, a growing and a decaying one, respectively

$$D_+(a) \propto a \ , \qquad D_-(a) \propto a^{-3/2} \ . \tag{C.1}$$

In ΛCDM one can express the two solutions in terms of hypergeometric functions with the above initial conditions, see e.g. [64, 394].

In nDGP, one needs to solve the differential equation for the growth function eq. (3.8) numerically. To get an idea of its solutions, let us expand it for small a. Up to order $a^{9/2}$, one finds

$$\frac{d^2D}{d\ln a^2} + \frac{1+3\zeta a^3}{2}\frac{dD}{d\ln a} - \left[\frac{3}{2} + \xi a^{3/2} - \frac{3\zeta+4\xi^2}{2}a^3 + \frac{-5\zeta\xi+8\xi^3}{2}a^{9/2}\right] D = 0 \ , \tag{C.2}$$

where we have defined two dimensionless parameters,

$$\zeta \equiv \frac{1-\Omega_{\mathrm{m}}}{\Omega_{\mathrm{m}}} \ , \qquad \xi = \sqrt{\frac{\Omega_{\mathrm{rc}}}{\Omega_{\mathrm{m}}}} \ , \tag{C.3}$$

that parametrize the effect of deviating from matter dominance and general relativity, respectively. We notice that terms proportional to ξ in the bracket start at order $a^{3/2}$ while those proportional to ζ start at a^3. Thus, for comparable values of ζ and ξ, the effect of modifying gravity dominates over the effect of not being in matter domination. Thus, it is crucial to include the nDGP corrections proportional to ξ.

We can solve the above equation perturbatively and we obtain two modes,

$$D_+(a) \propto a\left(1+\frac{\xi}{6}a^{3/2}+\frac{-18\zeta-11\xi^2}{99}a^3+\frac{-2817\zeta\xi+2816\xi^2}{24948}a^{9/2}+\mathcal{O}(a^4)\right)\,, \tag{C.4}$$

$$D_-(a) \propto a^{-3/2}\left(1-\frac{2\xi}{3}a^{3/2}+\frac{9\zeta-32\xi^2}{18}a^3+\frac{-9\zeta\xi+32\xi^2}{81}a^{9/2}+\mathcal{O}(a^4)\right)\,, \tag{C.5}$$

that we can call the "growing" and "decaying", respectively, because at early times they match the usual growing and decaying solutions. However, both grow at large a ([1]) and separating the two solutions at late time requires infinite numerical precision.

To bypass this problem in `PyBird`, we consider also the asymptotic behaviour of eq. (3.8) at late time, i.e. for $a \gg a_0$, where it becomes

$$\frac{d^2D}{d\ln a^2}+2\frac{dD}{d\ln a}=0\,, \tag{C.6}$$

with solutions

$$\tilde{D}_+(a) \propto \text{const.}\,, \qquad \tilde{D}_-(a) \propto \left(\frac{a_0}{a}\right)^2\,. \tag{C.7}$$

The second solution grows going backward in time and can be easily selected numerically, independently from D_+. Thus, to compute the Green's functions we use D_+ and $\tilde{D}_-$ as two independent solutions.

[1] For $\xi \neq 0$, the growing of $D_-(a)$ is not an artifact of the expansion but the effect of having a time dependent Newton's constant.

Appendix D

Additional parameter posteriors

In fig. D.1 we show the two full triangle plots obtained fitting BOSS 4 skies and including the effects of neutrinos in the linear power spectrum.

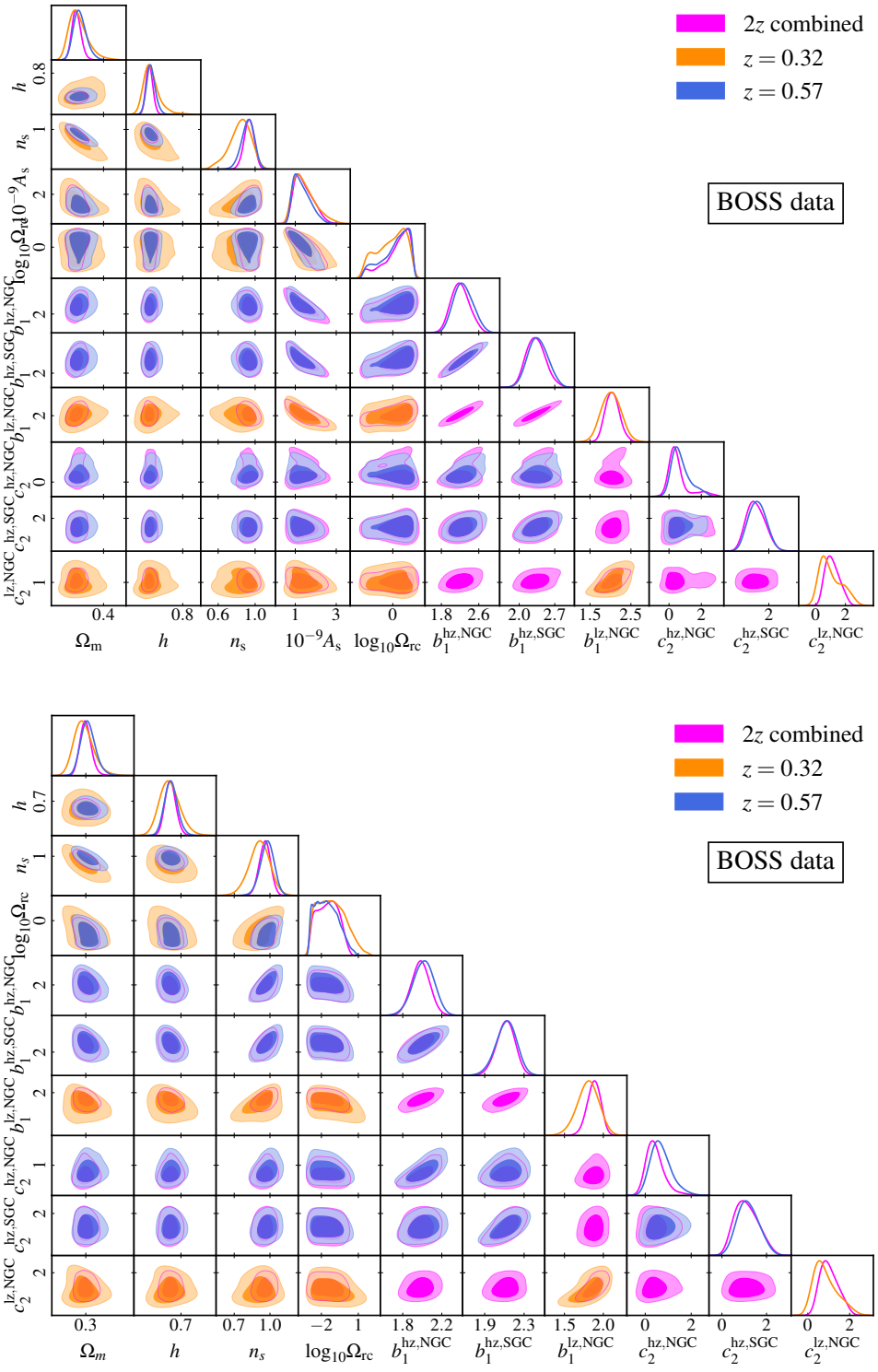

Figure D.1: Full triangle plots of the marginalized posteriors for the cosmological parameter from the analysis of BOSS data for all the sky-cuts with flat prior on A_s (top panel) and A_s fixed to Planck central value (bottom panel), using BOSS covariances.

Appendix E

Perturbation Theory and the EFTofLSS

The effective field theory of LSS (EFTofLSS) [214, 216] provides an accurate method for the calculation of the effect of non-linear scale physics on large, perturbative, scales, adding appropriate counterterms to the standard perturbative expansion, to incorporate physics beyond the perfect fluid approximation and poorly-known physics of galaxy formation. In this appendix, we provide a simple overview of the perturbative approach to the large-scale structure of the universe. Our focus will be on the linear and non-linear perturbation theory of dark matter overdensity.

E.1 Perturbation Theory

For the LSS we are interested in the motion of non-relativistic DM particles in the Newtonian limit, since we are considering sub-horizon scales.

The development of the matter particles can be characterized through its phase space density function, denoted as $f(\mathbf{x}, \mathbf{p}; \tau)$. In this context, τ is conformal time, $\mathbf{x}$ is the comoving coordinate, $\mathbf{p}$ represents the comoving momentum. The (microscopic) distribution function for dark matter particles is ultimately a sum of Dirac delta functions:

$$f(\mathbf{x}, \mathbf{p}; \tau) = \sum_n \delta_D(\mathbf{x} - \mathbf{x}_n(\tau))\delta_D(\mathbf{p} - \mathbf{p}_n(\tau)), \tag{E.1}$$

where the summation extends over all N particles in the system, and $x_n(\tau)$ and $p_n(\tau)$ satisfy Newton's equations.

This function satisfies the conservation equation in phase-space:

$$\frac{Df}{D\tau} = \frac{\partial f}{\partial t} + \frac{\vec{p}}{ma}\frac{\partial f}{\partial \vec{x}} - ma\sum_{n\neq\bar{n}}\frac{\partial \phi_{\bar{n}}}{\partial \vec{x}}\frac{\partial f_n}{\partial \vec{p}} = 0, \tag{E.2}$$

where the gravitational potential ϕ_n is given by:

$$\phi_n = -G\,m\sum_i \frac{1}{|\mathbf{r}_i - \mathbf{r}_n|}. \tag{E.3}$$

In cosmological contexts, our interest lies in scales much larger than the average distance between particles. To accommodate this, we smooth the microscopic distribution function by averaging over a certain resolution scale R:

$$\bar{f}(\mathbf{x},\mathbf{p};\tau,R) = \int d^3\mathbf{y}\, W\left(\left|\frac{\mathbf{y}}{R}\right|\right) f(\mathbf{x}+\mathbf{y},\mathbf{p};\tau), \tag{E.4}$$

with $W(|\mathbf{x}|)$ being a smoothing window function normalized to unity:

$$\int d^3\mathbf{y}\, W\left(\left|\frac{\mathbf{y}}{R}\right|\right) = 1. \tag{E.5}$$

To get a more manageable fluid description, we will use velocity moments of the smoothed distribution function. The first three moments of are:

$$\begin{aligned}
\rho_\ell(\mathbf{x},\tau) &= \frac{m}{a^3}\int d^3p\,\bar{f}(\mathbf{x},p,\tau) = \frac{m}{a^3}\rho_0(\tau)(1+\delta_\ell(\mathbf{x},\tau))\,,\\
\pi^i_\ell(\mathbf{x},\tau) &= \frac{m}{a^3}\int d^3p\,\frac{p^i}{am}\bar{f}(\mathbf{x},p,\tau)\,,\\
{\sigma_\ell}^{ij}(\mathbf{x},\tau) &= \frac{m}{a^3}\int d^3p\,\frac{p^i}{am}\frac{p^j}{am}\bar{f}(\mathbf{x},p,\tau)\,,
\end{aligned} \tag{E.6}$$

where ρ_0 indicates the mean background density, $\bar{u}^i_\ell = \frac{\bar{\pi}^i}{\rho_\ell}$ is the comoving velocity, and the subscript $_\ell$ stands for longwave field (from now on we will drop the $_\ell$ notation for simplicity).

Taking momentum moments of the smoothed Vlasov equation, one gets the usual continuity and Euler equations:

$$\frac{\partial\delta(\mathbf{x},\tau)}{\partial\tau} + \nabla_{\mathbf{x}}\cdot[(1+\delta(\mathbf{x},\tau))\mathbf{u}(\mathbf{x},\tau)] = 0, \tag{E.7}$$

$$\frac{\partial u^i(\mathbf{x},\tau)}{\partial\tau} + \mathcal{H}(\tau)u^i(\mathbf{x},\tau) + (u^j(\mathbf{x},\tau)\nabla_j)u^i(\mathbf{x},\tau) + \nabla_i\phi(\mathbf{x},\tau) = -\frac{\nabla_i\tau^{ij}(\mathbf{x},\tau)}{\rho(\mathbf{x},\tau)} \tag{E.8}$$

where ϕ satisfies the Poisson equation

$$\nabla^2\phi(\mathbf{x},\tau) = \frac{3}{2}\Omega_m(\tau)\mathcal{H}^2(\tau)\delta(\mathbf{x},\tau)\,, \tag{E.9}$$

and τ^{ij} is an effective stress-tensor induced by short-wavelength fluctuations.

E.1.1 SPT solutions in EdS approximation

If we neglect for the moment the effective stress-tensor, we have a perfect fluid approximation and we will study the perturbative solutions of this system. At linear and second order level the vorticity goes to 0 and it would be generated only at higher orders. First, the velocity field decomposes into divergence and vorticity components, and one can check from eq. (E.8) that the vorticity is driven to zero at linear and second order. The solution at linear order is then simply

$$\delta^{(1)}(\boldsymbol{x},\tau) = D(\tau)\delta_1(\boldsymbol{x})\,, \qquad \theta^{(1)}(\boldsymbol{x},\tau) = \nabla\cdot\boldsymbol{u}(\boldsymbol{x},\tau) = -\mathcal{H}(\tau)f(\tau)D(\tau)\delta_1(\boldsymbol{x})\,, \tag{E.10}$$

where $D(\tau)$ is the growth factor, and $f(\tau) = \frac{d\ln D}{d\ln a}$ is the growth rate, and $\boldsymbol{\nabla}_0(\boldsymbol{x})$ is the initial density field.

Going to Fourier space, eqs. (E.7) and (E.8) read:

$$\frac{d\delta(\mathbf{k})}{d\tau} + \theta(\mathbf{k}) = -\int \frac{d^3q}{(2\pi)^3}\alpha(\mathbf{q},\mathbf{k}-\mathbf{q})\delta(\mathbf{k}-\mathbf{q})\theta(\mathbf{q}), \tag{E.11}$$

$$\frac{d\theta(\mathbf{k})}{d\tau} + \mathcal{H}\theta(\mathbf{k}) + \frac{3}{2}\mathcal{H}^2\Omega_m\delta(\mathbf{k}) = -\int \frac{d^3q}{(2\pi)^3}\beta(\mathbf{q},\mathbf{k}-\mathbf{q})\theta(\mathbf{k}-\mathbf{q})\theta(\mathbf{q}), \tag{E.12}$$

where α and β encode the non-linear coupling between different modes in the evolution of the density and the velocity fields, and are given by:

$$\alpha(\mathbf{q}_1,\mathbf{q}_2) \equiv \frac{\mathbf{q}_1\cdot(\mathbf{q}_1+\mathbf{q}_2)}{q_1^2}\,, \qquad \beta(\mathbf{q}_1,\mathbf{q}_2) \equiv \frac{|\mathbf{q}_1+\mathbf{q}_2|^2\,\mathbf{q}_1\cdot\mathbf{q}_2}{2\mathbf{q}_1^2\mathbf{q}_2^2}\,. \tag{E.13}$$

The equations become separable in an EdS universe, that is, $\Omega_m = 1$ and $D \propto a$, $f = 1$. For ΛCDM we make the very good approximation $\Omega_m \sim f^2$ and we can separate the time dependence as $\delta(\boldsymbol{k},\tau) = \sum_n D^n(\tau)\delta_n(\boldsymbol{k})$, $\theta(\boldsymbol{k},\tau) = -\mathcal{H}(\tau)f(\tau)\sum_n D^n(\tau)\theta_n(\boldsymbol{k})$. The $\delta_n(\boldsymbol{k})$, $\theta_n(\boldsymbol{k})$ are written in terms of linear fluctuations via

$$\delta_n(\boldsymbol{k}) = \int_{\boldsymbol{q}_1}\cdots\int_{\boldsymbol{q}_n}(2\pi)^3\delta_D(\boldsymbol{k}-\boldsymbol{q}_1\cdots-\boldsymbol{q}_n)F_n(\boldsymbol{q}_1,\ldots,\boldsymbol{q}_n)\delta_1(\boldsymbol{q}_1)\ldots\delta_1(\boldsymbol{q}_n)\,, \tag{E.14}$$

$$\theta_n(\boldsymbol{k}) = \int_{\boldsymbol{q}_1}\cdots\int_{\boldsymbol{q}_n}(2\pi)^3\delta_D(\boldsymbol{k}-\boldsymbol{q}_1\cdots-\boldsymbol{q}_n)G_n(\boldsymbol{q}_1,\ldots,\boldsymbol{q}_n)\delta_1(\boldsymbol{q}_1)\ldots\delta_1(\boldsymbol{q}_n)\,. \tag{E.15}$$

The kernels F_n, G_n are given by

$$\begin{aligned} F_n(\mathbf{q}_1,\ldots,\mathbf{q}_n) = &\sum_{m=1}^{n-1}\frac{G_m(\mathbf{q}_1,\ldots,\mathbf{q}_m)}{(2n+3)(n-1)}[(2n+1)\alpha(\mathbf{q}_{1\ldots m},\mathbf{q}_{m+1\ldots n})F_{n-m}(\mathbf{q}_{m+1},\ldots,\mathbf{q}_n) \\ &+ 2\beta(\mathbf{q}_{1\ldots m},\mathbf{q}_{m+1\ldots n})G_{n-m}(\mathbf{q}_{m+1},\ldots,\mathbf{q}_n)]\,, \end{aligned} \tag{E.16}$$

$$G_n(\mathbf{q}_1,\ldots,\mathbf{q}_n) = \sum_{m=1}^{n-1} \frac{G_m(\mathbf{q}_1,\ldots,\mathbf{q}_m)}{(2n+3)(n-1)} [3\alpha(\mathbf{q}_{1\ldots m},\mathbf{q}_{m+1\ldots n}) F_{n-m}(\mathbf{q}_{m+1},\ldots,\mathbf{q}_n) + 2n\beta(\mathbf{q}_{1\ldots m},\mathbf{q}_{m+1\ldots n}) G_{n-m}(\mathbf{q}_{m+1},\ldots,\mathbf{q}_n)] \,. \tag{E.17}$$

This perturbative solution, however, is not well-defined. In fact, higher orders involve integrals over high k's, where the perfect fluid approximation, and perturbation theory itself, breaks down. So we need to consider the effective stress tensor and do a renormalization of the perturbative expansion.

E.2 Loops and Counterterms

The effective stress tensor depends on short-wavelength fluctuations, which we do not control analytically. So we will evaluate it by averaging over realizations of the short-wavelength modes in the presence of long-wavelength modes, and write it as a perturbative expansion in terms of the long-wavelength modes and their gradients (see [214, 216]). We can write all terms respecting symmetries of the problem, which are the rotational symmetry and the equivalence principle:

$$\langle \tau_{ij} \rangle_{\delta_\ell} = p_b \delta_{ij} + \rho_0 \left[c_s^2 \delta_\ell \, \delta_{ij} - \frac{c_{bv}^2}{\mathcal{H}} \delta_{ij} \, \nabla_k u^k - \frac{3}{4} \frac{c_{sv}^2}{\mathcal{H}} \left(\nabla_i u_{\ell,j} + \nabla_j u_{\ell,i} - \frac{3}{2} \delta_{ij} \, \nabla_k u_\ell^k \right) \right] + \ldots , \tag{E.18}$$

where p_b, c_s, c_{bv}, and c_{sv} represent effective pressure, adiabatic sound speed, bulk viscosity, and shear viscosity coefficients, dependent on the smoothing scale R (see eq. (E.4)). These coefficients, not determined by SPT, could be estimated from N-body simulations but, commonly, they are fit to data as nuisance parameters.

The simplest statistics that we can measure is the power spectrum, that is the Fourier transform of the 2-point function.

The linear power spectrum, denoted as $P_{\rm L}(k)$, is determined by the initial conditions. As structures in the universe evolve, interactions become increasingly non-linear. To account for these, we have to consider higher orders in perturbation theory, so we consider loop corrections to the power spectrum:

$$P_{1-\rm loop}(k) = P_{\rm L}(k) + P_{22}(k) + P_{13}(k), \tag{E.19}$$

where $P_{22}(k)$ and $P_{13}(k)$ represent the two possible one-loop contributions.

The loop integrals depend on integration over all k but at high k values the standard perturbative approach breaks down. To have a consistent perturbation theory one needs to introduce counterterms. For the matter power spectrum, the counterterms are the operators in τ^{ij}. These counterterms absorb the divergences and allow the definition of a renormalized perturbation theory, independent on the regularization procedure. At lowest order, we will have

$$P_{\rm ct}(k) = 2c_s^2 k^2 P_{\rm L}(k), \tag{E.20}$$

where c_s^2 is the effective sound speed and is a linear combination of some of the coefficients of τ^{ij}.

In the EFTofLSS, counterterms are of two kinds: response and stochastic. Response counterterms depend on the long-wavelength power spectrum $P(k)$ and renormalize interactions between long-wavelength and short-wavelength modes. A typical example of response counterterm is $P_{\rm ct}(k)$, that renormalizes P_{13}. On the other hand, stochastic counterterms represent the large-scale effects generated by small-scale random motions that are uncorrelated with the large-scale structure: at lowest order they would renormalize $P_{22}(k)$. They are important for biased tracers, where they take the form of shot-noise terms, while for matter they start at $O(k^4)$.

E.3 Biased tracers

In the universe, we cannot observe dark matter. Rather, we observe tracers such as galaxies, intergalactic gas, or dark matter halos. On large scales, we can consider these fields (denoted by $\delta_g(\mathbf{x}, \tau)$ as biased tracers of the underlying matter and velocity fields. They can be expressed as a sum of operators in δ, v^i and their derivatives respecting the symmetries of the problem, in this case rotational invariance and the equivalence principle. There is one subtlety to be considered. The EFTofLSS is non-local in time, as the timescale for galaxy formation is of the order of the Hubble scale, which is typical timescale of the evolution of the fields. Therefore, we have to integrate in time arbitrary functions against operators evaluated along the fluid

trajectory (so that Galilean invariance is respected) [222, 395]:

$$\delta_g(\mathbf{x},t) = \sum_{\mathcal{O}} \int^t dt' H(t') c_{\mathcal{O}}(t,t') \mathcal{O}(\mathbf{x}_{fl}(\mathbf{x},t,t'),t') \,, \tag{E.21}$$

where

$$\mathbf{x}_{fl}(\mathbf{x},t,t') = \mathbf{x} + \int_t^{t'} \frac{d\tilde{t}}{a(\tilde{t})} \mathbf{v}(\mathbf{x}_{fl}(\mathbf{x},t,\tilde{t}),\tilde{t}) \,. \tag{E.22}$$

We can simplify this expression by noting that, in perturbation theory, the t' dependence comes through powers of growth factors $D(t')$. Therefore, we can formally define bias coefficients that depend only on t as integrals of $c_{\mathcal{O}}(t,t')$ and growth factors, to finally get the expansion:

$$\delta_g(\mathbf{x},t) = \sum_{\mathcal{O}} \sum_n b_{\mathcal{O}}^{(n)}(t) C_{\mathcal{O}}^{(n)}(\mathbf{x},t) \,, \tag{E.23}$$

where the $C_{\mathcal{O}}^{(n)}$ are operators at n-th order in perturbation theory that result from expanding the $\mathcal{O}$.

To have a consistent perturbation theory, also the loops of biased tracers will need to be renormalized. One needs to write all possible counterterms in a gradient expansion, getting coefficients that need to be fit to data in addition to the bias parameters.

E.3.1 Redshift-space distortions

Observationally, we observe the redshfit of galaxies, which at zeroth order is related to their distance by the Hubble law.

The distortions are caused by peculiar velocities of galaxies superimposed on the Hubble flow, resulting in anisotropies in the observed galaxy distribution. The mapping from real space position $\mathbf{x}$ to redshift space position s is given by:

$$s = \mathbf{x} + \frac{v_\parallel(\mathbf{x})}{aH} \hat{z}, \tag{E.24}$$

where $v_\parallel(\mathbf{x})$ is the component of the peculiar velocity along the line of sight, a is the scale factor, H is the Hubble parameter, and $\hat{z}$ is the unit vector along the line of sight.

We then define the redshift-space overdensity:

$$\delta_{g,r}(\boldsymbol{k},\hat{\boldsymbol{z}}) = \delta_g(\boldsymbol{k}) + \int d^3x\, e^{-i\boldsymbol{k}\cdot\boldsymbol{x}} \left[\exp\left(-\frac{i(\hat{\boldsymbol{z}}\cdot\boldsymbol{k})}{aH} (\hat{\boldsymbol{z}}\cdot\boldsymbol{v}(\boldsymbol{x})) \right) - 1 \right] [1+\delta_g(\boldsymbol{x})] \,, \tag{E.25}$$

where δ_g is the real-space overdensity of the tracer.

We expand this equation in $\boldsymbol{v}$, to get $\delta^{(n)}_{g,r}(\boldsymbol{k}, \hat{z})$. We see that redshift space distortions break the rotational symmetry of the problem, so they allow us to have information about the velocity along the line of sight. At linear order, we find the usual Kaiser formula [279]:

$$P_{g,r}(k,\mu) = \left(b_1 + f\mu^2\right)^2 P_L(k), \tag{E.26}$$

where $\mu = \hat{\boldsymbol{k}} \cdot \hat{\boldsymbol{z}}$, b_1 is the linear bias and f the growth rate.

At higher orders, we see that $\delta_{g,r}$ depends on the product of velocities at the same point. In fact, redshift-space distortions are more sensitive to short-scale physics [396, 236, 235]. In the EFTofLSS, product of velocities at the same point need to be renormalized, giving rise to additional response and stochastic counterterms [261, 397, 395].

Appendix F

Bayes factor for competing theoretical models

Bayesian model selection offers a systematic approach to assess and compare the odds of different theoretical models based on observed data and any prior beliefs. Frequently, one is interested in extending an existing model by incorporating additional parameters, and in comparing if the new model is preferred by the data [39]). These cases are often referred to as "nested" models, meaning that the extended model reverts to the original one when the new parameters assume specific values. This is the case of the nDGP model we studied, which becomes ΛCDM in the limit $\Omega_{rc} \to 0$.

In a Bayesian framework we have to choose a prior for the parameters, and there can be many possible choices. To see if the new model is preferred, a strategy is to select the prior for the new parameters such that one maximizes the likelihood of the new model for the available data. If, even in this most favorable situation, the new model does not exhibit a notably higher probability than the original model, it can be confidently concluded that the data does not justify the inclusion of the additional parameters.

To do a comparative analysis of a baseline model M_0 against an alternative model with additional parameters M_1, it is common to introduce the Bayes factor as the ratio of (marginal) likelihoods

$$B = \frac{p(d|M_1)}{p(d|M_0)} \tag{F.1}$$

where d are the data, and the parameters for the models have been integrated over. The Bayes factor, B, quantifies the shift in relative probabilities between the two models due to the evidence provided by the data d. Using Bayes' theorem, we can write the ratio of the posteriors of the two models as

$$\frac{p(M_1|d)}{p(M_0|d)} = B\frac{P(M_1)}{P(M_0)} \tag{F.2}$$

where $P(M_i)(i = 0, 1)$ are the prior probabilities for the two models and $P(M_i|d)$ the posterior probabilities. In the case in which the prior belief is agnostic, that is $P(M_1) = P(M_0) = \frac{1}{2}$, the Bayes factor gives us directly the ratio of model probabilities after considering the available data. The level of support is usually categorized as either 'inconclusive' ($|\ln B| < 1$), 'weak' ($1 < |\ln B| < 2.5$), 'moderate' ($2.5 < |\ln B| < 5$), or 'strong' ($|\ln B| > 5$).

The problem is that the ratio of marginal likelihoods is, in most cases, computationally expensive. Assuming that the parameter priors are separable as usually done in cosmology, we get the Savage–Dickey density ratio [398, 399, 39]:

$$\mathrm{B} = \frac{p(\theta_*|M_1)}{p(\theta_*|d, M_1)}\,, \tag{F.3}$$

where θ denotes the additional parameter(s) and θ_* is the value for which one recovers the simpler model M_0. For a broad $p(\theta|M_1)$, the dependence of the posterior $p(\theta_*|d, M_1)$ on θ^* comes predominantly from the likelihood. As a consequence, the Bayes factor B can be considered arbitrarily small by assuming $p(\theta|M_1)$ sufficiently broad, because $p(\theta|M_1)$ needs to be normalized over a large interval of θ. Therefore, if we are agnostic about the prior on θ, but we would like to understand if the new model is justified, we can derive an upper limit for B by selecting $p(\theta|M_1)$ as a delta function centered at the maximum likelihood estimate, θ_{max}. This choice maximally favors M_1, leading to an upper bound on the odds:

$$\bar{B} = \frac{p(d|\theta_{\mathrm{max}}, M_1)}{p(d|\theta^*, M_0)}\,. \tag{F.4}$$

This equation represents the likelihood ratio between θ_{max} and θ^*, but it is still expensive to compute.

In our case, we use a procedure meant to approximate this method. As explained in sec. 3.5.3, we take the ratio of marginal likelihoods for two different values of the new parameter Ω_{rc}:

$$B(x_1, x_2) = \frac{\mathcal{P}(d|x_1)}{\mathcal{P}(d|x_2)}\,; \tag{F.5}$$

the x_1 value is fixed to be small enough such that the model is effectively ΛCDM, and we consider the Bayes factor as a function of x_2. In this way, we are able to explore a large range of $\Omega_{\rm rc}$ in a prior-independent way and therefore we get an upper bound on the odds that the nDGP model is preferred over ΛCDM. We then check that this procedure is consistent changing the lower limit of the prior of $\Omega_{\rm rc}$.

An alternative approach to bypass the prior dependence would be the frequentist method of computing the profiled likelihood, i.e., maximize the likelihood over all parameters except the added one. One then considers the likelihood ratio with respect to the maximum of the new parameter. We expect this approach to give similar results, and we did not explore it because of its computational complexity.

Appendix G

Converting abundance constraints from MMD to EMD

Abundance constraint conversion formulas accounting for PBH effects on CMB anisotropies exist only for the spherical accretion case [165, 103]. However, different accretion geometries or energy emission efficiencies require the development (and testing) of new conversion relations, which we present in this appendix. Furthermore, in this appendix we focus on lognormal EMDs, given the large interest on this specific EMD coming from the theoretical modelling of PBH formation. We note, however, that the procedure presented in this appendix is easily applicable also to other EMDs.

In the most general setup, as for instance in equation (2.9), we have that the injected and deposited energy are proportional to

$$\frac{L_{\rm tot}}{M_{\rm PBH}} = \left(\epsilon_{\rm non-th} + \epsilon_{\rm rad}\right) \frac{\dot{M}_{\rm PBH}}{M_{\rm PBH}}, \tag{G.1}$$

which is weighted by the PBH EMD of choice, as shown in equation (2.17). In the spherical accretion case we have that

$$\frac{L_{\rm tot}}{M_{\rm PBH}} \propto \left[\epsilon_{\rm non-th} + \gamma_{\rm sph} \lambda M_{\rm PBH}\right] \lambda M_{\rm PBH}, \tag{G.2}$$

where in the redshift range of interest the mass-independent quantity $\gamma_{\rm sph}$ takes values in the range $\gamma_{\rm sph} \simeq [2-19] \times 10^{-10}$ and $\gamma_{\rm sph} \simeq [3-24] \times 10^{-8}$ for the collisional and photoionization models, respectively. The effect of the dimensionless accretion rate can be effectively

parametrized (neglecting its redshift dependence) as $\lambda \propto M^{\alpha/2}$ [165], where α is a parameter to be tuned numerically a posteriori to minimize the differences in the relevant observable quantity between the EMD case and the equivalent monochromatic case. Therefore, for the purpose of obtaining an accurate conversion, the equivalent mass is given by

$$\left[\epsilon_{\rm non-th} + \gamma_{\rm sph} M_{\rm eq}^{1+\alpha/2}\right] M_{\rm eq}^{1+\alpha/2} = \mu^{1+\alpha/2} e^{(2+\alpha)^2\sigma^2/8} \left[\epsilon_{\rm non-th} + \gamma_{\rm sph} \mu^{1+\alpha/2} e^{3(2+\alpha)^2\sigma^2/8}\right], \tag{G.3}$$

where, for a lognormal distribution, $\alpha = 0.2$. From the equation above we see that in the limit of zero non-thermal emission ($\epsilon_{\rm non-th} \to 0$) we recover the known result [165]

$$M_{\rm eq}^{2+\alpha} = \mu^{2+\alpha} e^{(2+\alpha)^2\sigma^2/2}, \tag{G.4}$$

while in the limit of dominant non-thermal emission ($\gamma_{\rm sph} \to 0$), we find that

$$M_{\rm eq}^{1+\alpha/2} = \mu^{1+\alpha/2} e^{(2+\alpha)^2\sigma^2/8}. \tag{G.5}$$

On the other hand, in the case of disk accretion we have

$$\frac{L_{\rm tot}}{M_{\rm PBH}} \propto \left[\epsilon_{\rm non-th} + \gamma_{\rm disk} M_{\rm PBH}^a\right] M_{\rm PBH}, \tag{G.6}$$

where in this case the mass-independent quantity $\gamma_{\rm disk} \simeq 6 \times 10^{-4}$ and the exponent a is given in ref. [122]. In this case the equivalent mass relation reads as

$$\left[\epsilon_{\rm non-th} + \gamma_{\rm disk} M_{\rm eq}^a\right] M_{\rm eq} = \mu \left[\epsilon_{\rm non-th} e^{\sigma^2/2} + \gamma_{\rm disk} \mu^a e^{(1+a)^2\sigma^2/2}\right] \tag{G.7}$$

which reduces to

$$M_{\rm eq}^{1+a} = \mu^{1+a} e^{(1+a)^2\sigma^2/2}, \tag{G.8}$$

and

$$M_{\rm eq} = \mu e^{\frac{\sigma^2}{2}} \tag{G.9}$$

in the radiation-emission and non-thermal-emission dominated regimes, respectively.

Appendix H

PBH accretion physics

Here we will discuss in detail the two main accretion models that are present in the literature: the spherical accretion and the disk formation model. In particular we will refer to [96] for the spherical accretion and to [97] for the disk accretion.

The first aspect to consider is the geometry of the accretion. If the characteristic angular momentum of the accreted gas at the Bondi radius is smaller than the angular momentum at the innermost stable circular orbit (ISCO), the accretion presents a spherical symmetry. Otherwise, there could be the formation of a disk: this accretion is tipically much more efficient than spherical in the mass-radiation conversion. In the spherical case, the dominant radiative process is free-free emission from the hot ionized plasma near the event horizon of the black hole, while in the disk accretion process the large viscous heating required to dissipate angular momentum leads to radiating a significant fraction of the rest-mass energy. It is difficult to estimate the angular momentum of the accreted gas: this would require to know the relative velocity of the PBH-baryon components on scales of the Bondi radius and accounting also for the (non-linear) clustering of PBHs.

H.1 Spherical accretion onto PBHs

We start by considering a stationary system where a PBH is steadily accreting the surrounding baryonic gas on the cosmological background. The assumption is that the accretion time-scale is shorter than the Hubble time: this picture is valid for $M_{\rm PBH} \leq 3 \times 10^4 M_\odot$ and we

focus on this mass range. Far from the PBH, the baryonic gas is little attracted by the black hole and its density becomes equal to the cosmological density. An important feature of the accretion model is the Bondi radius: it is the distance found for setting escape velocity equal to the sound speed and solving for radius and it represents the boundary between subsonic and supersonic infall. Down to this radius, the cooling of the baryonic gas by the background CMB is efficient and the temperature of the gas remains the same as that of CMB. Below this radius, the cooling by the CMB becomes negligible and the gas temperature increases as the inverse of the radius by the adiabatic compression as the gas falls. When the temperature exceeds $10^4 K$, the collisional ionization starts to be important. After the gas is completely ionized, the temperature again increases as the inverse of the radius until the electrons become relativistic. Finally, the gas is swallowed by the PBH at the event horizon. Near the event horizon, the gas temperature is enormous and the Bremsstrahlung radiation produces the intense outgoing radiation which eventually heats or ionizes the background gas. It is possible that the gas ionization near the PBH is caused not by the collisions of gas particles but by the radiation emanating from the vicinity of the BH horizon.

The accretion rate is affected also by local feedbacks: there could be ionization and/or heating of the accreted gas from the radiation emitted by the accreted material generating a radiative output. The result of the work of [96] is that the thermal and ionization feedback are negligible for all masses and redshifted considered, with the Strömgren radius, the size of the idealized ionized region around the PBH, being always significantly smaller than the Bondi radius r_B. It is possible to assume that the ionization fraction is approximately equal to the background value in the outermost region of the accretion flow. Getting close enough to the black hole, there is the full ionization of the gas by two possible processes: photoionization or/and collisional ionization. To avoid a complicated calculation of the luminosity and ionization profile, [96] considered the two limiting cases with one process dominant: either neglecting all radiative feedback and assuming the ionizazion fraction x_e as the background value $\bar{x}_e$ until $T \sim 10^4 K$, when the gas gets collisionally ionized; or having photoionization of the gas up to a radius beyond which $T \sim 10^4 K$, yet inside the Bondi radius. The first is the collisional ionization case, the second the photoionization one. The correct result lies between these two limiting cases.

We will analyze the hydrodynamics and the thermodynamics of the physical system under consideration in three regions around the BH: the outermost region, with a constant x_e equal to the background $\bar{x}_e$, accounting for Compton drag and Compton cooling by CMB photons; the intermediate region, in which we take into account the (re)ionization of H in the collisional ionizazion case for a gas that has reached $T_{ion} = 10^4 K$; the innermost region, where the gas is fully ionized and adiabatically compressed. The outcome of this reasoning is the gas temperature near the event horizon which, together with $\dot{M}$, determines the luminosity of the accreting BH.

H.1.1 Outermost, constant-ionization-fraction region

As stated before, the model under consideration is the spherical accretion of a pure H gas onto an isolated point mass M, bathed in the quasi-uniform CMB radiation field. The main and first assumption is that the constant ionization fraction is equal to the background value of the medium in this region, $x_e = \bar{x}_e$. Because the Hubble time t_H is much longer than the characteristic accretion timescale, the approximation of stationarity is valid for $M \lessapprox 3 \times 10^4 M_\odot$ [123]. The calculation outline of the work of [96] neglects the self-gravity of the accreted gas, valid for $M \lessapprox 3 \times 10^5 M_\odot$.

Indicating with $v \equiv v_r < 0$ the peculiar radial velocity (i.e. the velocity with respect to the Hubble flow) of the accreted gas, we can describe the system with the steady-state mass and momentum equation:

$$4\pi r^2 |v| = \dot{M} = const, \tag{H.1}$$

$$v\frac{dv}{dr} = -\frac{GM}{r^2} - \frac{1}{\rho}\frac{dP}{d\rho} - \frac{4}{3}\frac{\bar{x}_e \sigma_T \rho_{\rm CMB}}{m_p c} v \tag{H.2}$$

where G is the gravitational constant, c is the speed of light, $\sigma_{\rm T}$ is the Thomson cross-section, $m_{\rm p}$ is the proton mass, $\rho_{\rm CMB}$ is the density of the CMB and P is the pressure value:

$$P = \frac{\rho}{m_p}(1 + \bar{x}_e)T. \tag{H.3}$$

where T is the temperature.

The drag effect due to inverse Compton scattering of free electrons by CMB photons is the last term in the right-hand side of H.2. It is possible to reduce the accretion rate onto PBHs if the gas behaves as a viscous fluid: the photon viscosity may also be important in removing angular momentum from the gas [400].

Also the Hubble expansion acts as a viscous term that tends to reduce the accretion rate, independent of the ionization fraction of the gas: this effect may be non-negligible and could alter the rate of accretion. We can rewrite the previous hydrodynamical equations to include the cosmological term due to the Hubble expansion, using a comoving frame of reference:

$$\begin{cases} r = a(t)x \\ v = \frac{d}{dt}(ax) = Hr + v_p \end{cases} \tag{H.4}$$

where a(t) is the scale factor, $H = \dot{a}/a$ is the Hubble parameter and the peculiar velocity is defined as $v_p = a\dot{x}$. We could then rewrite the hydrodynamical equations as:

$$\begin{cases} 4\pi r^2 |v| = \dot{M} = const, \\ v\frac{dv}{dr} = -\frac{GM}{r^2} - \frac{1}{\rho}\frac{dP}{d\rho} - (\beta + H)v \end{cases} \tag{H.5}$$

with β the Compton drag term and H accounting for the universe expansion. In the following calculations we would not account for this effect that could still be relevant at early times [95].

The thermodynamical equations complement the hydrodynamical ones: in the work we have been following, one considers only the Compton cooling by CMB photons as a heat sink in this region. The steady state heat equation is then:

$$v\rho^{2/3}\frac{d}{dr}\left(\frac{T}{\rho^{2/3}}\right) = \frac{8\bar{x}_e\sigma_T\rho_{\rm cmb}}{3m_e c(1+\bar{x}_e)}(T_{\rm cmb} - T) \tag{H.6}$$

where $T_{\rm cmb}$ is the temperature of CMB photons. Anyway, given the range of masses we consider, the timescale of accretion is always shorter than t_H and this enforces $T_\infty = T_{\rm cmb}$. The classical Bondi accretion solution assumes instead that Compton drag and cooling are negligible, and it is described by the characteristic velocity, length and time scales:

$$v_B \equiv \sqrt{P_\infty/\rho_\infty}, \quad r_B \equiv \frac{GM}{v_B^2}, \quad t_B \equiv \frac{GM}{v_B^3} \tag{H.7}$$

It is possible to express the problem with dimensionless variables: $x \equiv r/r_B$, $u \equiv v/v_B$, $\hat{\rho} \equiv \rho/\rho_\infty$, $\hat{T} \equiv T/T_\infty$. So what defines the physics of this system are the dimensionless constants:

$$\begin{cases} \lambda \equiv \frac{\dot{M}}{4\pi\rho_\infty r_B^2 v_B} \\ \beta \equiv \frac{4}{3}\frac{\bar{x}_e \sigma_T \rho_{CMB}}{m_p c} t_B \\ \gamma \equiv \frac{8\bar{x}_e \sigma_T \rho_{cmb}}{3 m_e c (1+\bar{x}_e)} t_B = \frac{2m_p}{m_e(1+\bar{x}_e}\beta \gg \beta \end{cases} \tag{H.8}$$

We can then finally rewrite the hydro-thermodynamics problem in terms of the previous parameters:

$$\begin{cases} \hat{\rho} x^2 |u| = \lambda, \\ u\frac{du}{dx} = -\frac{1}{x^2} - \frac{1}{\hat{\rho}\frac{d}{dx}(\hat{\rho}\hat{T})} - \beta u, \\ u\hat{\rho}^{2/3}\frac{d}{dx}\left(\frac{\hat{T}}{\hat{\rho}^{2/3}}\right) = \gamma(1-\hat{T}), \end{cases} \tag{H.9}$$

with asymptotic conditions $\hat{\rho} \to$ and $\hat{T} \to 1$ at $x \to \infty$.

It is important to underline that the PBH mass doesn't grow significantly in a Hubble time.

$$\frac{\dot{M}}{HM} = \frac{4\pi\lambda\bar{\rho_b}(GM)^2}{HMv_B^3} = \frac{4\pi\lambda\bar{\rho_b}Gt_B}{H} = \frac{3}{2}\lambda\frac{\bar{\rho_b}}{\bar{\rho_t}ot}Ht_B, \tag{H.10}$$

where the Friedman's equation for the Hubble rate H has been used in the last equality and we assumed steady-state: $\dot{M} \ll HM$.

H.1.2 Collisional ionization region

In the case in which the radiation induced by the accretion is not intense enough to photoionize the gas, the collisions due to compression and heating can anyway ionize the surrounding medium. For this happening at constant temperature $T \approx T_{ion} \approx 1.5 \times 10^4$, the corresponding ionization fraction is $x_e = 0.5$ and the transition between neutral and ionized medium is sharp. At small radii:

$$T(r) \approx \tau T_\infty \frac{r_B}{r}, \tag{H.11}$$

with τ a dimensionless constant at most equal to 0.3, and smaller when Compton cooling is important:

$$\tau \approx \frac{1.5}{5+\gamma^{2/3}}. \tag{H.12}$$

Once the global $\bar{x}_e$ falls significantly below unity, i.e. for $T_\infty \lessapprox 3000K \ll T_{\rm ion}$, the effect of the ionization region is relevant. We get then that the ionization region is completely enclosed in the Bondi radius. The distance at which the ionization region starts is:

$$r_{ion}^{start} \approx \tau \frac{T_\infty}{T_{ion}} r_B, \tag{H.13}$$

where the density field is:

$$\hat{\rho}(x) \approx \frac{\lambda}{\sqrt{2-5\tau}} x^{-3/2} \Rightarrow \rho_{ion}^{start} \approx \frac{\lambda}{\sqrt{2-5\tau}} \rho_\infty \left(\frac{T_{ion}}{\tau T_\infty}\right)^{3/2} \tag{H.14}$$

Here we are assuming that collisions are the mechanisms for ionization of neutral hydrogen atoms with free electrons. To have a constant temperature throughout the ionization region, this effect must be compensated by the temperature increase due to the adiabatic compression of the gas.

Between the end of the ionization region and the beginning we have a density ratio:

$$\frac{\rho_{ion}^{end}}{\rho_{ion}^{start}} \approx \left(\frac{1}{1+\bar{x}_e}\right)^{12}. \tag{H.15}$$

Assuming that $\rho \propto r^{-3/2}$ throughout the region, the region of ionization is indicated by:

$$\frac{r_{ion}^{end}}{r_{ion}^{start}} \approx \left(\frac{1+\bar{x}_e}{2}\right)^{8}. \tag{H.16}$$

In the case in which $\bar{x}_e \ll 1$ there's the possibility of extending the ionization region by even a factor ~ 300 in radius, not taking into account the heat loss due to collisional excitations followed by radiative decays that are not simple to include. The Compton cooling here is also not considered, but it could be relevant for high x_e. In fact adding these cooling mechanisms would imply a larger density contrast ρ^{end}/ρ^{start}, hence a more extended ionization region.

For powerful enough radiation, it is possible to obtain the photoionization beyond r_{ion}: it is defined such as $\rho_{ion}^{start} = \rho_{ion}^{end}$. The general case is then included between these two limits:

$$\rho_{ion}^{start}/\rho_{ion}^{end} = \chi \equiv 1 \qquad \text{(photoionization)} \tag{H.17}$$

or

$$\chi \equiv 1\left(\frac{2}{1+\bar{x}_e}\right)^8 \qquad \text{(collisional ionization)}\,. \tag{H.18}$$

H.1.3 Innermost adiabatic region

Once it reaches the condition of full ionization, the gas resumes adiabatic compression and the thermal energy density u of the ionized plasma is:

$$u = \frac{3}{2}n_e\left(1 + f(T/m_e c^2)\right)T, \tag{H.19}$$

where the dimensionless function $f(X)$, with $X \equiv \frac{T}{m_e c^2}$, accounts for the fact that electrons are potentially relativistic and varies between 1 ($X \ll 1$) and 2 ($X \gg 1$). Here m_e is the electron mass and with n_e the electronic density. The explicit value computed by [96] of $f(X)$ is:

$$f(x) \approx 1 + \frac{X}{X + 0.73} \tag{H.20}$$

The pressure remains unchanged $P = 2n_e T$ and the first law of thermodynamics can be written as:

$$\frac{3}{2}[1 + f(x) + Xf'(X)]\frac{dT}{T} = 2\frac{d\rho}{\rho} \tag{H.21}$$

Integrating this relation, it is possible to obtain the density field and the ratio:

$$\frac{\rho_2}{\rho_1} = \frac{3}{4}\int_{X_1}^{X_2}[1 + f(X) + Xf'(X)]\frac{dX}{X} \tag{H.22}$$

Inverting this relation numerically, [96] obtained the following approximation, valid for $T_1 \ll m_e c^2$ and arbitrary T_2:

$$\frac{T_2}{m_e c^2} \approx F\left(\frac{T_1}{m_e c^2}\left(\frac{\rho_2}{\rho_1}\right)^{2/3}\right) \tag{H.23}$$

$$F(Y) \equiv Y\left(1+\frac{Y}{0.27}\right)^{-1/3}. \tag{H.24}$$

Since the velocity is almost c, the density is then:

$$\rho_S = \frac{\lambda}{(c/v_B)(r_S/r_B)^2}\rho_\infty = \frac{\lambda}{4(v_B/c)^3}\rho_\infty = \frac{\lambda}{4}\left(\frac{m_p c^2}{(1+\bar{x}_e T_\infty}\right)^{3/2}\rho_\infty. \tag{H.25}$$

At the end of the ionization, the temperature is T_{ion} and the density becomes:

$$\rho_{ion}^{end} = \chi\frac{\lambda}{\sqrt{2-5\tau}}\left(\frac{T_{ion}}{\tau T_\infty}\right)^{3/2}\rho_\infty. \tag{H.26}$$

Using then $F(Y)$ for $T_1 = T_{ion}$ and $\rho_1 = \rho_{ion}^{end}$, the temperature near the Schwartzschild radius is then:

$$T_S = m_e c^2 F(Y_S) \tag{H.27}$$

with

$$Y_S \equiv \frac{T_{ion}}{m_e c^2}\left(\frac{\rho_S}{\rho_{ion}^{end}}\right)^{2/3}. \tag{H.28}$$

H.2 Disk accretion

The main assumption for disk formation is that it happens during the dark ages, between recombination and reionization (possibly already at $z = 1000$) [97]. A firm proof would require deeper studies of non linear growth of structures at small scales, accounting for PBH clustering and formation of baryonic halos.

The first step is to consider a point mass Black Hole of mass M moving at constant speed v_{rel} in a homogeneous gas of number density n_∞. The standard Bondi accretion takes into account, in the medium, the sound speed far away from the point mass:

$$c_{s,\infty} = \sqrt{\frac{\gamma P_\infty}{\rho_\infty}} = \sqrt{\frac{\gamma(1+x_e)T}{m_p}} \simeq 5.7 \frac{\text{km}}{\text{s}} \sqrt{\frac{1+z}{1000}} \qquad \text{for } z \gg 132. \tag{H.29}$$

This approximation holds for $100 \leq z \leq 1000$. Accounting for the motion of the BH, it is reasonable to have an effective speed given by the quadratic sum of the relative velocity and the sound speed at infinity: $v_{eff}^2 = c_{s,\infty}^2 + v_{rel}^2$. We get an important drop for the sound velocity at the Recombination and the baryons, originally coupled to photons, acquire a supersonic relative stream with respect to the Dark Matter, coherent over tens of Mpc scales. The linear component of the relative baryon-DM velocity is basically constant [401, 402] before recombination and then drops linearly with z:

$$\sqrt{< v_L^2 >} \simeq \min\left[1, \frac{1+z}{1000}\right] \times 30 \text{ km/s}. \tag{H.30}$$

The result is a delay for small-scale structure formation and for the baryon settling into the DM potential wells. Considering the luminosity of accreting BH over the velocity distribution, it is possible to rewrite the previous relation as:

$$v_{eff} \equiv \left\langle \frac{1}{(c_{s,\infty}^2 + v_L^2)^3} \right\rangle^{-1/6} \simeq \sqrt{c_{s,\infty} \sqrt{< v_L^2 >}} \tag{H.31}$$

with the last approximation valid if $c_{s,\infty} \ll \sqrt{< v_L^2 >}$. These results are acceptable at early epochs after recombination.

One hypothesis is that PBH formation mechanism is a non-linear phenomenon and the peaks theory suggests that PBHs are likely already born in clusters during radiation era [403, 404]: this would imply that PBH formation then becomes more subtle as the PBH is now no longer in an isolated region, as shown in [404]. If this is the case, it is reasonable to expect that the PBHs can generically accrete from two components: from the high-velocity, free-streaming fraction at cosmological density and from a virialized component, of initial negligible density but growing with time and eventually dominating, with typical relative velocity of the order of the virial ones ($10^{-3}c$ in the MW halo). When the density of the virialized baryon component attains values comparable to the cosmological average density (unavoidable for $z \leq 100$), the virialized component eventually dominates at late times.

The usual criterion to assess if a disk forms is the angular momentum of the material at the accretion distance [405]: if this is sufficient to keep the matter in Keplerian rotation at $r_D \gg 3r_S$, a disk will form. To build up angular momentum, the material accreted at the Hoyle-Bondi distance along different directions must have appreciable velocity or density differences. The angular momentum per unit mas of the accreted gas scales like:

$$l \simeq \left(\frac{\delta\rho}{\rho} + \frac{\delta v}{v_{\rm eff}}\right) v_{\rm eff} r_{\rm HB} \tag{H.32}$$

where $\delta\rho/\rho$ represents typical inhomogeneities at the scale r_{HB} in the direction orthogonal to the relative motion PBH-baryons, and $\delta v_{\rm eff}/v_{\rm eff}$ the analogous typical velocity gradient at the same scale. The above quantity can be compared to the specific angular momentum of a Keplerian orbit:

$$l_D \simeq r_D v_{kep}(r_D) \simeq \sqrt{GMr_D} \tag{H.33}$$

to extract r_D. In the case of inhomogeneities, it is possible to adopt the effective velocity at the RHS of $v_{\rm eff}$, and then obtain, as a benchmark, that for r_D/r_S already after recombination the density gradient is $\gg 10^{-4}$ in the baryon flow on the scale of the Bondi radius, sufficient for a disk to form, largely satisfied already at $z \sim 1000$ because of the "granular" potential due to neighboring PBHs.

If we consider a free-streaming homogenous gas, hypothetically ideal as composition, that moves a bulk motion comparable to $\sqrt{< v_L^2 >}$ without any velocity dispersion, then the disk formation criterion is likely satisfied if the non-linear PBH motions at small scales are taken into account. This is a reasonable situation, as usually the BH motion at very small scale within its halo is influenced by it nearest neighbors. The simplest scenario is that a sizable fraction of PBH forms binary systems with their nearest partner, under the tidal effect of the next-to-nearest. It is sufficient [23] that PBHs have a distance slightly below the average distance at matter-radiation equality for a binary to form. This is valid for PBH constituting a sizable fraction of the DM: under the assumption of an isotropic PBH distribution and monochromatic PBH mass function M, this distance can be estimated as:

$$d \sim \left(\frac{3M}{4\pi\rho_{PBH}}\right)^{1/3} = \frac{1}{1+z_{eq}}\left(\frac{2GM}{H_0^2 f_{pbh}\Omega_{DM}}\right)^{1/3} \sim 0.05pc\left(\frac{M}{f_{pbh}M_\odot}\right)^{1/3}\frac{3400}{1+z_{eq}} \quad \text{(H.34)}$$

If bound in a system, the two PBH (each of mass M) orbit around the common center with keplerian angular velocity ω so that the angular momentum:

$$l \simeq \omega r_{HB}^2 \quad \text{(H.35)}$$

Adopting v_{eff}, we get the disk formation condition ($z \leq 1000$):

$${f_{pbh}}^{1/2}\frac{M}{M_\odot} >> \left(\frac{1+z}{730}\right)^3 \quad \text{(H.36)}$$

If $M \gtrsim M_\odot$ and PBH constitute a sizable fraction of the DM, this is satisfied at the epoch of interest for CMB bounds.

The main impact on the CMB (polarization) anisotropies from accreting PBHs comes from redshifts 1000 and below, rather around redshift 300, scaling the costraining power to lower redshifts.

All the disk formation discussion so far is based on the main assumption that stellar mass PBHs are clustered in non-linear structures at small scales and early times, greatly differing from WIMPs in that respect.

Appendix I

Testing the performance of the interpolation scheme

This Appendix is dedicated to the *leave-one-out* tests that we performed to ensure both the accuracy of the newly developed interpolation scheme and the adequate grid coverage of the parameter space. In order to check whether our interpolation routine is working as expected, we use all simulations except for a single simulation i, and predict with these remaining simulations the flux power spectrum corresponding to the simulation i. The goal is to always find a relative theoretical error (associated to the interpolation) lower than the relative experimental uncertainty on the flux power spectrum data-points used in our analyses. These tests are expected to provide better results in regions where there are more simulations, given that the interpolation routine is intrinsically less accurate for simulations that are close to the grid boundaries. However, given that our grid of simulations extends far beyond the prior ranges that we have adopted in all our analyses, it is sufficient to satisfy this condition within our prior ranges. Therefore, instead of applying the *leave-one-out* tests to the whole grid, constituted by 633 simulations, we only apply it to those simulations associated to parameter values within our prior ranges. We thus compute the flux power spectrum for the model i from the remaining 632 grid-points, and compare it to the flux power spectrum of the i-th simulation, by computing the root mean square error (MSQE). The values of the MSQEs are listed in Table I.1, where we also report the mean relative uncertainties on the Lyman-α data-points, for each redshift bin. For comparison, we report the MSQEs obtained with the Optimized Kriging

method developed in this work, as well as the MSQEs obtained when applying the same tests to the Ordinary Kriging method. Note that, when the two errors are not equal, the latter ones are always larger than those obtained with our optimized method. Regarding the Optimized Kriging method, in Fig. I.1 we show a histogram per each redshift bin of the MSQE for the grid-points that we left out one-by-one. Note that most of the grid-points can be recovered with a MSQE $\lesssim 1\% - 10\%$, showing the excellent accuracy of our interpolation routine. Only a very limited number of simulations shows a MSQE $\gtrsim 10\%$. Furthermore, as it was already manifest from Table I.1, the theoretical errors associated to the interpolation are practically always smaller than the mean experimental uncertainties, that are reported as vertical lines in Fig. I.1 – except for a few cases in the highest redshift bin (which however do not bias our results, since they sample regions of the parameter space that are anyhow excluded by data).

	Mean theoretical relative error		Mean experimental relative error		
z	Ordinary Kriging	Optimized Kriging	XQ-100	MIKE	HIRES
3.0	0.02	0.01	0.13	–	–
3.2	0.01	0.01	0.10	–	–
3.4	0.02	0.01	0.08	–	–
3.6	0.02	0.01	0.08	–	–
3.8	0.02	0.01	0.09	–	–
4.0	0.01	0.01	0.12	–	–
4.2	0.03	0.03	0.16	0.10	0.19
4.6	0.10	0.07	–	0.21	0.19
5.0	0.14	0.08	–	0.30	0.18
5.4	0.12	0.10	–	–	0.23

Table I.1: Here we report the values of the theoretical MSQE associated to the interpolation procedure within our prior ranges, per each redshift bin covered by our analyses, for both the Ordinary and Optimized Kriging methods. We also report the mean relative experimental uncertainties on the Lyman-α flux power spectrum data-points. See Section 5.1.3 and Appendix I for further details.

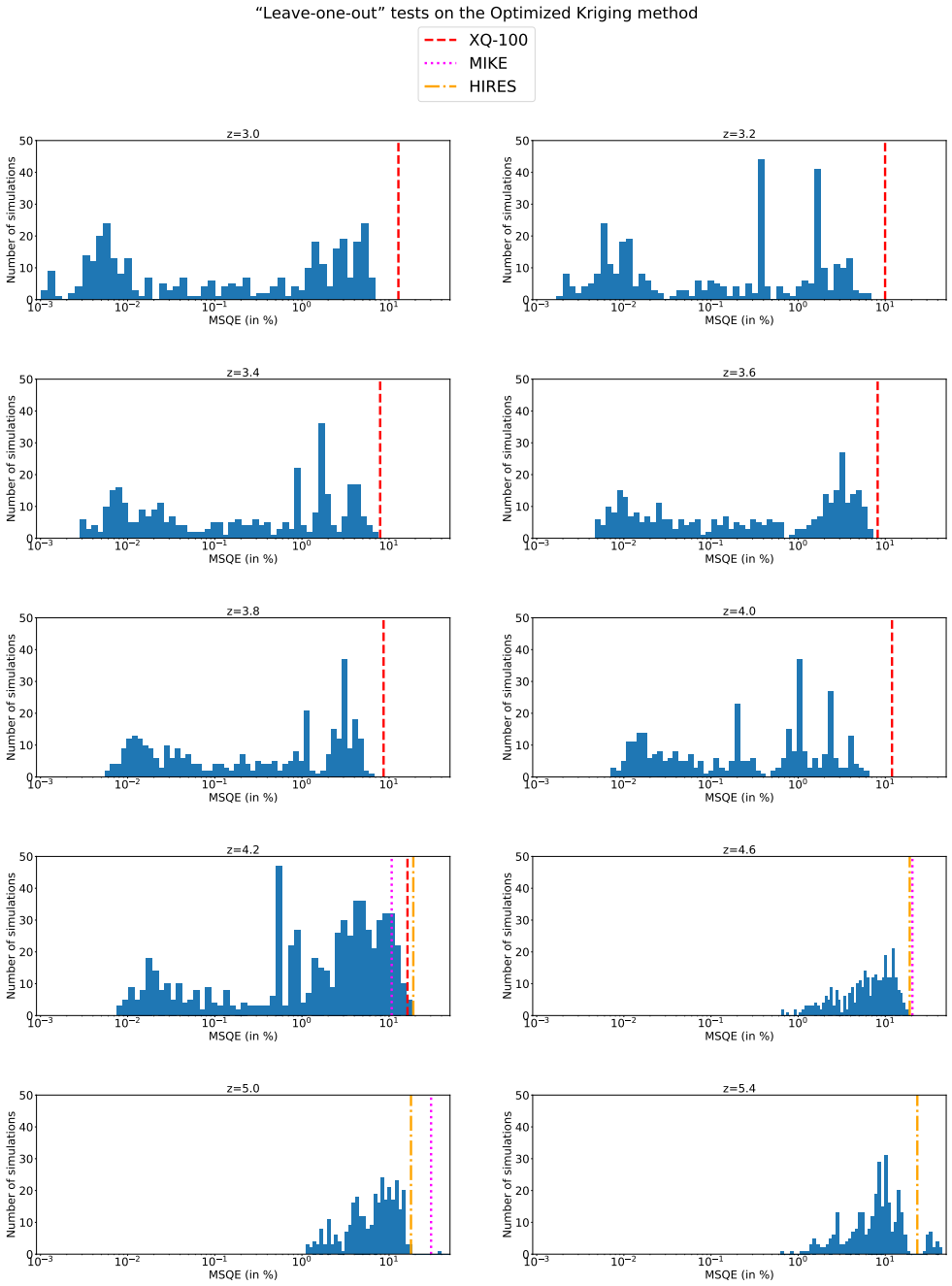

Figure I.1: Here we show a histogram per redshift bin of the MSQE associated to the grid-points within our prior ranges. They are obtained by applying the *leave-one-out* tests described in Appendix I. Vertical lines indicate the mean experimental relative error from XQ-100 (red dashed), MIKE (pink dotted), and HIRES (golden dot-dashed).

Bibliography

[1] P. Kumar Aluri, P. Cea, P. Chingangbam, M.-C. Chu, R. G. Clowes, D. Hutsemékers, J. P. Kochappan, A. M. Lopez, L. Liu, N. C. M. Martens, C. J. A. P. Martins, K. Migkas, E. Ó Colgáin, P. Pranav, L. Shamir, A. K. Singal, M. M. Sheikh-Jabbari, J. Wagner, S.-J. Wang, D. L. Wiltshire, S. Yeung, L. Yin, and W. Zhao, "Is the observable Universe consistent with the cosmological principle?," *Classical and Quantum Gravity* **40** (May, 2023) 094001, 2207.05765.

[2] S. Dodelson, *Modern cosmology*. Academic Press, San Diego, CA, 2003.

[3] P. Coles and F. Lucchin, *Cosmology: The Origin and evolution of cosmic structure*. 1995.

[4] L. Perivolaropoulos and F. Skara, "Challenges for ΛCDM: An update," *New Astron. Rev.* **95** (2022) 2105.05208.

[5] **Supernova Cosmology Project** Collaboration, S. Perlmutter *et. al.*, "Measurements of Ω and Λ from 42 high redshift supernovae," *Astrophys. J.* **517** (1999) 565–586, astro-ph/9812133.

[6] **Supernova Search Team** Collaboration, A. G. Riess *et. al.*, "Observational evidence from supernovae for an accelerating universe and a cosmological constant," *Astron. J.* **116** (1998) 1009–1038, astro-ph/9805201.

[7] **Planck** Collaboration, N. Aghanim *et. al.*, "Planck 2018 results. I. Overview and the cosmological legacy of Planck," *Astron. Astrophys.* **641** (2020) A1, 1807.06205.

[8] **Planck** Collaboration, N. Aghanim *et. al.*, "Planck 2018 results. VI. Cosmological parameters," *Astron. Astrophys.* **641** (2020) A6, 1807.06209. [Erratum: Astron.Astrophys. 652, C4 (2021)].

[9] **Planck Collaboration** Collaboration, N. Aghanim *et. al.*, "Planck 2018 results. VI. Cosmological parameters," *Astron. Astrophys.* **641** (2020) A6, 1807.06209.

[10] **SDSS** Collaboration, D. J. Eisenstein *et. al.*, "Detection of the Baryon Acoustic Peak in the Large-Scale Correlation Function of SDSS Luminous Red Galaxies," *Astrophys. J.* **633** (2005) 560–574, astro-ph/0501171.

[11] **BOSS** Collaboration, S. Alam *et. al.*, "The clustering of galaxies in the completed SDSS-III Baryon Oscillation Spectroscopic Survey: cosmological analysis of the DR12 galaxy sample," *Mon. Not. Roy. Astron. Soc.* **470** (2017), no. 3 2617–2652, 1607.03155.

[12] **BOSS Collaboration** Collaboration, S. Alam *et. al.*, "The clustering of galaxies in the completed SDSS-III Baryon Oscillation Spectroscopic Survey: cosmological analysis of the DR12 galaxy sample," *Mon. Not. Roy. Astron. Soc.* **470** (2017), no. 3 2617–2652, 1607.03155.

[13] **DES Collaboration** Collaboration, T. M. C. Abbott *et. al.*, "Dark Energy Survey year 1 results: Cosmological constraints from galaxy clustering and weak lensing," *Phys. Rev.* **D98** (2018), no. 4 043526, 1708.01530.

[14] H. Hildebrandt *et. al.*, "KiDS+VIKING-450: Cosmic shear tomography with optical and infrared data," *Astron. Astrophys.* **633** (2020) A69, 1812.06076.

[15] C. Alcock, R. A. Allsman, D. R. Alves, T. S. Axelrod, A. C. Becker, D. P. Bennett, K. H. Cook, N. Dalal, A. J. Drake, K. C. Freeman, M. Geha, K. Griest, M. J. Lehner, S. L. Marshall, D. Minniti, C. A. Nelson, B. A. Peterson, P. Popowski, M. R. Pratt, P. J. Quinn, C. W. Stubbs, W. Sutherland, A. B. Tomaney, T. Vandehei, and D. Welch, "The MACHO Project: Microlensing Results from 5.7 Years of Large Magellanic Cloud Observations," **542** (Oct., 2000) 281–307, astro-ph/0001272.

[16] R. D. Peccei and H. R. Quinn, "CP Conservation in the Presence of Instantons," *Phys. Rev. Lett.* **38** (1977) 1440–1443.

[17] S. Dodelson and L. M. Widrow, "Sterile neutrinos as dark matter," **72** (Jan., 1994) 17–20, hep-ph/9303287.

[18] G. Jungman, M. Kamionkowski, and K. Griest, "Supersymmetric dark matter," *Physics Reports* **267** (1996), no. 5 195–373.

[19] E. W. Kolb and M. S. Turner, *The Early Universe*, vol. 69. 1990.

[20] H. E. Haber and G. L. Kane, "The Search for Supersymmetry: Probing Physics Beyond the Standard Model," *Phys. Rept.* **117** (1985) 75–263.

[21] S. Bird, I. Cholis, J. B. Muñoz, Y. Ali-Haïmoud, M. Kamionkowski, E. D. Kovetz, A. Raccanelli, and A. G. Riess, "Did ligo detect dark matter?," *Phys. Rev. Lett.* **116** (May, 2016) 201301, 1603.00464.

[22] S. Clesse and J. García-Bellido, "The clustering of massive primordial black holes as dark matter: Measuring their mass distribution with advanced ligo," *Physics of the Dark Universe* **15** (2017), no. Supplement C 142 – 147, 1603.05234.

[23] M. Sasaki, T. Suyama, T. Tanaka, and S. Yokoyama, "Primordial black hole scenario for the gravitational-wave event gw150914," *Phys. Rev. Lett.* **117** (Aug, 2016) 061101, 1603.08338.

[24] **LIGO Scientific and Virgo Collaboration** Collaboration, B. P. Abbott *et. al.*, "Observation of Gravitational Waves from a Binary Black Hole Merger," *Phys. Rev. Lett.* **116** (2016), no. 6 061102, 1602.03837.

[25] L. Piga, M. Lucca, N. Bellomo, V. Bosch-Ramon, S. Matarrese, A. Raccanelli, and L. Verde, "The effect of outflows on CMB bounds from Primordial Black Hole accretion," 2210.14934.

[26] L. Amendola *et. al.*, "Cosmology and fundamental physics with the Euclid satellite," *Living Rev. Rel.* **21** (2018), no. 1 2, 1606.00180.

[27] C. Brans and R. H. Dicke, "Mach's principle and a relativistic theory of gravitation," *Phys. Rev.* **124** (1961) 925–935.

[28] E. Sefusatti and F. Vernizzi, "Cosmological structure formation with clustering quintessence," *JCAP* **03** (2011) 047, 1101.1026.

[29] S. Anselmi, G. Ballesteros, and M. Pietroni, "Non-linear dark energy clustering," *JCAP* **11** (2011) 014, 1106.0834.

[30] G. Cusin, M. Lewandowski, and F. Vernizzi, "Dark Energy and Modified Gravity in the Effective Field Theory of Large-Scale Structure," *JCAP* **04** (2018) 005, 1712.02783.

[31] G. Cusin, M. Lewandowski, and F. Vernizzi, "Nonlinear Effective Theory of Dark Energy," *JCAP* **04** (2018) 061, 1712.02782.

[32] B. Bose, K. Koyama, M. Lewandowski, F. Vernizzi, and H. A. Winther, "Towards Precision Constraints on Gravity with the Effective Field Theory of Large-Scale Structure," *JCAP* **04** (2018) 063, 1802.01566.

[33] P. Carrilho, C. Moretti, B. Bose, K. Markovič, and A. Pourtsidou, "Interacting dark energy from redshift-space galaxy clustering," *JCAP* **10** (2021) 004, 2106.13163.

[34] E. Babichev *et. al.*, "k-Mouflage gravity," *IJMPD* **18** (2009) 2147–2154, 0905.2943.

[35] P. Brax and P. Valageas, "K-mouflage cosmology: The background evolution," *Physical Review D* **90** (Jul, 2014).

[36] P. Brax and P. Valageas, "The effective field theory of K-mouflage," *JCAP* **01** (2016) 020, 1509.00611.

[37] G. Benevento, M. Raveri, A. Lazanu, N. Bartolo, M. Liguori, P. Brax, and P. Valageas, "K-mouflage Imprints on Cosmological Observables and Data Constraints," *JCAP* **05** (2019) 027, 1809.09958.

[38] L. Piga, M. Marinucci, G. D'Amico, M. Pietroni, F. Vernizzi, and B. S. Wright, "Constraints on modified gravity from the BOSS galaxy survey," 2211.12523.

[39] C. Gordon and R. Trotta, "Bayesian Calibrated Significance Levels Applied to the Spectral Tilt and Hemispherical Asymmetry," *Mon. Not. Roy. Astron. Soc.* **382** (2007) 1859–1863, 0706.3014.

[40] P. Creminelli, G. D'Amico, J. Norena, and F. Vernizzi, "The Effective Theory of Quintessence: the w<-1 Side Unveiled," *JCAP* **02** (2009) 018, 0811.0827.

[41] G. Gubitosi, F. Piazza, and F. Vernizzi, "The Effective Field Theory of Dark Energy," *JCAP* **1302** (2013) 032, 1210.0201. [JCAP1302,032(2013)].

[42] J. K. Bloomfield, E. E. Flanagan, M. Park, and S. Watson, "Dark energy or modified gravity? An effective field theory approach," *JCAP* **08** (2013) 010, 1211.7054.

[43] J. Gleyzes, D. Langlois, F. Piazza, and F. Vernizzi, "Essential Building Blocks of Dark Energy," *JCAP* **08** (2013) 025, 1304.4840.

[44] J. Bloomfield, "A Simplified Approach to General Scalar-Tensor Theories," *JCAP* **12** (2013) 044, 1304.6712.

[45] V. K. Narayanan, D. N. Spergel, R. Dave, and C.-P. Ma, "Constraints on the mass of warm dark matter particles and the shape of the linear power spectrum from the Lyα forest," *Astrophys. J. Lett.* **543** (2000) L103–L106, astro-ph/0005095.

[46] M. Viel, S. Matarrese, H. J. Mo, M. G. Haehnelt, and T. Theuns, "Probing the intergalactic medium with the lyman alpha forest along multiple lines of sight to distant qsos," *Mon. Not. Roy. Astron. Soc.* **329** (2002) 848, astro-ph/0105233.

[47] M. Viel, M. G. Haehnelt, and V. Springel, "Inferring the dark matter power spectrum from the Lyman-alpha forest in high-resolution QSO absorption spectra," *Mon. Not. Roy. Astron. Soc.* **354** (2004) 684, astro-ph/0404600.

[48] M. Viel, J. Lesgourgues, M. G. Haehnelt, S. Matarrese, and A. Riotto, "Constraining warm dark matter candidates including sterile neutrinos and light gravitinos with WMAP and the Lyman-alpha forest," *Phys. Rev.* **D71** (2005) 063534, astro-ph/0501562.

[49] V. Iršič, M. Viel, M. G. Haehnelt, J. S. Bolton, and G. D. Becker, "First constraints on fuzzy dark matter from Lyman-α forest data and hydrodynamical simulations," *Phys. Rev. Lett.* **119** (2017), no. 3 031302, 1703.04683.

[50] R. Krall, F.-Y. Cyr-Racine, and C. Dvorkin, "Wandering in the Lyman-alpha Forest: A Study of Dark Matter-Dark Radiation Interactions," *JCAP* **09** (2017) 003, 1705.08894.

[51] R. Murgia, G. Scelfo, M. Viel, and A. Raccanelli, "Lyman-α Forest Constraints on Primordial Black Holes as Dark Matter," *Phys. Rev. Lett.* **123** (2019), no. 7 071102, 1903.10509.

[52] R. Murgia, A. Merle, M. Viel, M. Totzauer, and A. Schneider, ""Non-cold" dark matter at small scales: a general approach," *JCAP* **11** (2017) 046, 1704.07838.

[53] M. Esposito, V. Iršič, M. Costanzi, S. Borgani, A. Saro, and M. Viel, "Weighing Cosmic Structures with Clusters of Galaxies and the Intergalactic Medium," 2202.00974.

[54] J. Lesgourgues, "The Cosmic Linear Anisotropy Solving System (CLASS) I: Overview," 1104.2932.

[55] D. Blas, J. Lesgourgues, and T. Tram, "The Cosmic Linear Anisotropy Solving System (CLASS) II: Approximation schemes," *JCAP* **1107** (2011) 034, 1104.2933.

[56] D. Blas, J. Lesgourgues, and T. Tram, "The Cosmic Linear Anisotropy Solving System (CLASS). Part II: Approximation schemes," **2011** (July, 2011) 034, 1104.2933.

[57] M. Lucca, N. Schöneberg, D. C. Hooper, J. Lesgourgues, and J. Chluba, "The synergy between CMB spectral distortions and anisotropies," *Journal of Cosmology and Astroparticle Physics* **2020** (feb, 2020) 026–026, 1909.08631.

[58] Stöcker, P. and Krämer, M. and Lesgourgues, J. and Poulin, V., "Exotic energy injection with ExoCLASS: Application to the Higgs portal model and evaporating black holes," *JCAP* **1803** (2018), no. 03 018, 1801.01871.

[59] Y. Ali-Haimoud and C. M. Hirata, "HyRec: A fast and highly accurate primordial hydrogen and helium recombination code," *Phys. Rev.* **D83** (2011) 043513, 1011.3758.

[60] N. Lee and Y. Ali-Haïmoud, "HYREC-2: a highly accurate sub-millisecond recombination code," *Phys. Rev. D* **102** (2020), no. 8 083517, 2007.14114.

[61] G. D'Amico, L. Senatore, and P. Zhang, "Limits on wCDM from the EFTofLSS with the PyBird code," *JCAP* **01** (2021) 006, 2003.07956.

[62] A. Perko, L. Senatore, E. Jennings, and R. H. Wechsler, "Biased Tracers in Redshift Space in the EFT of Large-Scale Structure," 1610.09321.

[63] G. D'Amico, J. Gleyzes, N. Kokron, K. Markovic, L. Senatore, P. Zhang, F. Beutler, and H. Gil-Marín, "The Cosmological Analysis of the SDSS/BOSS data from the Effective Field Theory of Large-Scale Structure," *JCAP* **05** (2020) 005, 1909.05271.

[64] Y. Donath and L. Senatore, "Biased Tracers in Redshift Space in the EFTofLSS with exact time dependence," *JCAP* **10** (2020) 039, 2005.04805.

[65] M. Simonović, T. Baldauf, M. Zaldarriaga, J. J. Carrasco, and J. A. Kollmeier, "Cosmological perturbation theory using the FFTLog: formalism and connection to QFT loop integrals," *JCAP* **04** (2018) 030, 1708.08130.

[66] A. Chudaykin, M. M. Ivanov, O. H. E. Philcox, and M. Simonović, "Nonlinear perturbation theory extension of the Boltzmann code CLASS," *Phys. Rev. D* **102** (2020), no. 6 063533, 2004.10607.

[67] S.-F. Chen, Z. Vlah, and M. White, "Consistent Modeling of Velocity Statistics and Redshift-Space Distortions in One-Loop Perturbation Theory," *JCAP* **07** (2020) 062, 2005.00523.

[68] S.-F. Chen, Z. Vlah, E. Castorina, and M. White, "Redshift-Space Distortions in Lagrangian Perturbation Theory," *JCAP* **03** (2021) 100, 2012.04636.

[69] C. Howlett, A. Lewis, A. Hall, and A. Challinor, "CMB power spectrum parameter degeneracies in the era of precision cosmology," *Journal of Cosmology and Astroparticle Physics* **2012** (apr, 2012) 027–027.

[70] R. Murgia, V. Iršič, and M. Viel, "Novel constraints on noncold, nonthermal dark matter from Lyman- α forest data," *Phys. Rev. D* **98** (2018), no. 8 083540, 1806.08371.

[71] M. Archidiacono, D. C. Hooper, R. Murgia, S. Bohr, J. Lesgourgues, and M. Viel, "Constraining Dark Matter-Dark Radiation interactions with CMB, BAO, and Lyman-α," *JCAP* **10** (2019) 055, 1907.01496.

[72] W. Enzi *et. al.*, "Joint constraints on thermal relic dark matter from strong gravitational lensing, the Ly α forest, and Milky Way satellites," *Mon. Not. Roy. Astron. Soc.* **506** (2021), no. 4 5848–5862, 2010.13802.

[73] D. C. Hooper, N. Schöneberg, R. Murgia, M. Archidiacono, J. Lesgourgues, and M. Viel, "One likelihood to bind them all: Lyman-α constraints on non-standard dark matter," *JCAP* **10** (2022) 032, 2206.08188.

[74] T. Akiba, S. Sano, T. Yanase, T. Ohta, and M. Koyama, "Optuna: A next-generation hyperparameter optimization framework," in *Proceedings of the 25rd ACM SIGKDD International Conference on Knowledge Discovery and Data Mining*, 2019.

[75] J. Bergstra, R. Bardenet, Y. Bengio, and B. Kégl, "Algorithms for hyper-parameter optimization," *Advances in neural information processing systems* **24** (2011).

[76] J. Bergstra, D. Yamins, and D. Cox, "Making a science of model search: Hyperparameter optimization in hundreds of dimensions for vision architectures," in *International conference on machine learning*, pp. 115–123, PMLR, 2013.

[77] R. Laureijs, J. Amiaux, S. Arduini, J. L. Augueres, J. Brinchmann, R. Cole, M. Cropper, C. Dabin, L. Duvet, A. Ealet, B. Garilli, P. Gondoin, L. Guzzo, J. Hoar, H. Hoekstra, R. Holmes, T. Kitching, T. Maciaszek, Y. Mellier, F. Pasian, W. Percival, J. Rhodes, G. S. Criado, M. Sauvage, R. Scaramella, L. Valenziano, S. Warren, R. Bender, F. Castander,

A. Cimatti, O. L. Fèvre, H. Kurki-Suonio, M. Levi, P. Lilje, G. Meylan, R. Nichol, K. Pedersen, V. Popa, R. R. Lopez, H. W. Rix, H. Rottgering, W. Zeilinger, F. Grupp, P. Hudelot, R. Massey, M. Meneghetti, L. Miller, S. Paltani, S. Paulin-Henriksson, S. Pires, C. Saxton, T. Schrabback, G. Seidel, J. Walsh, N. Aghanim, L. Amendola, J. Bartlett, C. Baccigalupi, J. P. Beaulieu, K. Benabed, J. G. Cuby, D. Elbaz, P. Fosalba, G. Gavazzi, A. Helmi, I. Hook, M. Irwin, J. P. Kneib, M. Kunz, F. Mannucci, L. Moscardini, C. Tao, R. Teyssier, J. Weller, G. Zamorani, M. R. Z. Osorio, O. Boulade, J. J. Foumond, A. D. Giorgio, P. Guttridge, A. James, M. Kemp, J. Martignac, A. Spencer, D. Walton, T. Blümchen, C. Bonoli, F. Bortoletto, C. Cerna, L. Corcione, C. Fabron, K. Jahnke, S. Ligori, F. Madrid, L. Martin, G. Morgante, T. Pamplona, E. Prieto, M. Riva, R. Toledo, M. Trifoglio, F. Zerbi, F. Abdalla, M. Douspis, C. Grenet, S. Borgani, R. Bouwens, F. Courbin, J. M. Delouis, P. Dubath, A. Fontana, M. Frailis, A. Grazian, J. Koppenhöfer, O. Mansutti, M. Melchior, M. Mignoli, J. Mohr, C. Neissner, K. Noddle, M. Poncet, M. Scodeggio, S. Serrano, N. Shane, J. L. Starck, C. Surace, A. Taylor, G. Verdoes-Kleijn, C. Vuerli, O. R. Williams, A. Zacchei, B. Altieri, I. E. Sanz, R. Kohley, T. Oosterbroek, P. Astier, D. Bacon, S. Bardelli, C. Baugh, F. Bellagamba, C. Benoist, D. Bianchi, A. Biviano, E. Branchini, C. Carbone, V. Cardone, D. Clements, S. Colombi, C. Conselice, G. Cresci, N. Deacon, J. Dunlop, C. Fedeli, F. Fontanot, P. Franzetti, C. Giocoli, J. Garcia-Bellido, J. Gow, A. Heavens, P. Hewett, C. Heymans, A. Holland, Z. Huang, O. Ilbert, B. Joachimi, E. Jennins, E. Kerins, A. Kiessling, D. Kirk, R. Kotak, O. Krause, O. Lahav, F. van Leeuwen, J. Lesgourgues, M. Lombardi, M. Magliocchetti, K. Maguire, E. Majerotto, R. Maoli, F. Marulli, S. Maurogordato, H. McCracken, R. McLure, A. Melchiorri, A. Merson, M. Moresco, M. Nonino, P. Norberg, J. Peacock, R. Pello, M. Penny, V. Pettorino, C. D. Porto, L. Pozzetti, C. Quercellini, M. Radovich, A. Rassat, N. Roche, S. Ronayette, E. Rossetti, B. Sartoris, P. Schneider, E. Semboloni, S. Serjeant, F. Simpson, C. Skordis, G. Smadja, S. Smartt, P. Spano, S. Spiro, M. Sullivan, A. Tilquin, R. Trotta, L. Verde, Y. Wang, G. Williger, G. Zhao, J. Zoubian, and E. Zucca, "Euclid definition study report," 2011.

[78] **LSST** Collaboration, v. Ivezić *et. al.*, "LSST: from Science Drivers to Reference Design

and Anticipated Data Products," *Astrophys. J.* **873** (2019), no. 2 111, 0805.2366.

[79] **DESI** Collaboration, A. Aghamousa *et. al.*, "The DESI Experiment Part I: Science,Targeting, and Survey Design," 1611.00036.

[80] V. Bosch-Ramon and N. Bellomo, "Mechanical feedback effects on primordial black hole accretion," *Astron. Astrophys.* **638** (2020) A132, 2004.11224.

[81] V. Bosch-Ramon, "3D hydrodynamical simulations of the impact of mechanical feedback on accretion in supersonic stellar-mass black holes," *Astron. Astrophys.* **660** (2022) A5, 2201.09601.

[82] Y. B. Zel'dovich and I. D. Novikov, "The Hypothesis of Cores Retarded during Expansion and the Hot Cosmological Model," **10** (Feb., 1967) 602.

[83] S. Hawking, "Gravitationally collapsed objects of very low mass," *Mon. Not. Roy. Astron. Soc.* **152** (1971) 75.

[84] B. J. Carr and S. W. Hawking, "Black holes in the early universe," *Monthly Notices of the Royal Astronomical Society* **168** (aug, 1974) 399–415.

[85] G. F. Chapline, "Cosmological effects of primordial black holes," *Nature* **253** (jan, 1975) 251.

[86] M. Sasaki, T. Suyama, T. Tanaka, and S. Yokoyama, "Primordial black holes—perspectives in gravitational wave astronomy," *Class. Quant. Grav.* **35** (2018), no. 6 063001, 1801.05235.

[87] B. Carr, K. Kohri, Y. Sendouda, and J. Yokoyama, "Constraints on primordial black holes," *Rept. Prog. Phys.* **84** (2021), no. 11 116902, 2002.12778.

[88] B. Carr and F. Kuhnel, "Primordial Black Holes as Dark Matter: Recent Developments," *Ann. Rev. Nucl. Part. Sci.* **70** (2020) 355–394, 2006.02838.

[89] P. Villanueva-Domingo, O. Mena, and S. Palomares-Ruiz, "A brief review on primordial black holes as dark matter," *Front. Astron. Space Sci.* **8** (2021) 87, 2103.12087.

[90] J. Silk, "Feedback by Massive Black Holes in Gas-rich Dwarf Galaxies," **839** (Apr., 2017) L13, 1703.08553.

[91] K. Kohri, T. Nakama, and T. Suyama, "Testing scenarios of primordial black holes being the seeds of supermassive black holes by ultracompact minihalos and CMB μ-distortions," *Phys. Rev. D* **90** (2014), no. 8 083514, 1405.5999.

[92] J. L. Bernal, A. Raccanelli, L. Verde, and J. Silk, "Signatures of primordial black holes as seeds of supermassive black holes," *JCAP* **05** (2018) 017, 1712.01311. [Erratum: JCAP 01, E01 (2020)].

[93] B. Carr, S. Clesse, J. García-Bellido, and F. Kühnel, "Cosmic conundra explained by thermal history and primordial black holes," *Phys. Dark Univ.* **31** (2021) 100755, 1906.08217.

[94] J. I. Juan, P. D. Serpico, and G. Franco-Abellán, "The QCD phase transition behind a PBH origin of LIGO/virgo events?," *Journal of Cosmology and Astroparticle Physics* **2022** (jul, 2022) 009, 2204.07027.

[95] M. Ricotti, J. P. Ostriker, and K. J. Mack, "Effect of Primordial Black Holes on the Cosmic Microwave Background and Cosmological Parameter Estimates," *Astrophys. J.* **680** (2008) 829, 0709.0524.

[96] Y. Ali-Haïmoud and M. Kamionkowski, "Cosmic microwave background limits on accreting primordial black holes," *Phys. Rev.* **D95** (2017), no. 4 043534, 1612.05644.

[97] V. Poulin, P. D. Serpico, F. Calore, S. Clesse, and K. Kohri, "CMB bounds on disk-accreting massive primordial black holes," *Phys. Rev.* **D96** (2017), no. 8 083524, 1707.04206.

[98] K. J. Mack, J. P. Ostriker, and M. Ricotti, "Growth of structure seeded by primordial black holes," *Astrophys. J.* **665** (2007) 1277–1287, astro-ph/0608642.

[99] P. D. Serpico, V. Poulin, D. Inman, and K. Kohri, "Cosmic microwave background bounds on primordial black holes including dark matter halo accretion," *Phys. Rev. Res.* **2** (2020), no. 2 023204, 2002.10771.

[100] M. V. Barkov, D. V. Khangulyan, and S. B. Popov, "Jets and gamma-ray emission from isolated accreting black holes," *Mon. Not. Roy. Astron. Soc.* **427** (2012) 589–594, 1209.0293.

[101] A. Sadowski, J.-P. Lasota, M. A. Abramowicz, and R. Narayan, "Energy flows in thick accretion discs and their consequences for black hole feedback," *Mon. Not. Roy. Astron. Soc.* **456** (2016), no. 4 3915–3928, 1510.08845.

[102] X. Li, P. Chang, Y. Levin, C. D. Matzner, and P. J. Armitage, "Simulation of a compact object with outflows moving through a gaseous background," *Mon. Not. Roy. Astron. Soc.* **494** (2020), no. 2 2327–2336, 1912.06864. [Erratum: Mon.Not.Roy.Astron.Soc. 504, 3166–3167 (2021)].

[103] J. L. Bernal, N. Bellomo, A. Raccanelli, and L. Verde, "Cosmological implications of primordial black holes," **2017** (Oct., 2017) 052, 1709.07465.

[104] D. Gaggero, G. Bertone, F. Calore, R. M. T. Connors, M. Lovell, S. Markoff, and E. Storm, "Searching for primordial black holes in the radio and x-ray sky," *Phys. Rev. Lett.* **118** (2017), no. 24 241101, 1612.00457.

[105] J. Manshanden, D. Gaggero, G. Bertone, R. M. T. Connors, and M. Ricotti, "Multi-wavelength astronomical searches for primordial black holes," *Journal of Cosmology and Astroparticle Physics* **2019** (jun, 2019) 026, 1812.07967.

[106] Hektor, Andi, Hütsi, Gert, and Raidal, Martti, "Constraints on primordial black hole dark matter from galactic center x-ray observations," *A&A* **618** (2018) A139, 1805.06513.

[107] V. Takhistov, P. Lu, G. B. Gelmini, K. Hayashi, Y. Inoue, and A. Kusenko, "Interstellar gas heating by primordial black holes," *JCAP* **03** (2022), no. 03 017, 2105.06099.

[108] A. Hektor, G. Hütsi, L. Marzola, M. Raidal, V. Vaskonen, and H. Veermäe, "Constraining primordial black holes with the edges 21-cm absorption signal," *Phys. Rev. D* **98** (Jul, 2018) 023503, 1803.09697.

[109] G. Hütsi, M. Raidal, and H. Veermäe, "Small-scale structure of primordial black hole dark matter and its implications for accretion," *Phys. Rev. D* **100** (Oct, 2019) 083016, 1907.06533.

[110] O. Mena, S. Palomares-Ruiz, P. Villanueva-Domingo, and S. J. Witte, "Constraining the primordial black hole abundance with 21-cm cosmology," *Phys. Rev. D* **100** (Aug, 2019) 043540, 1906.07735.

[111] **LIGO Scientific and Virgo Collaboration** Collaboration, B. P. Abbott *et. al.*, "GWTC-1: A Gravitational-Wave Transient Catalog of Compact Binary Mergers Observed by LIGO and Virgo during the First and Second Observing Runs," *Phys. Rev. X* **9** (2019), no. 3 031040, 1811.12907.

[112] K. W. K. Wong, G. Franciolini, V. De Luca, V. Baibhav, E. Berti, P. Pani, and A. Riotto, "Constraining the primordial black hole scenario with Bayesian inference and machine learning: the GWTC-2 gravitational wave catalog," *Phys. Rev. D* **103** (2021), no. 2 023026, 2011.01865.

[113] G. Franciolini, V. Baibhav, V. De Luca, K. K. Y. Ng, K. W. K. Wong, E. Berti, P. Pani, A. Riotto, and S. Vitale, "Searching for a subpopulation of primordial black holes in LIGO-Virgo gravitational-wave data," *Phys. Rev. D* **105** (2022), no. 8 083526, 2105.03349.

[114] B. Horowitz, "Revisiting Primordial Black Holes Constraints from Ionization History," 1612.07264.

[115] F. Hoyle and R. A. Lyttleton, "The effect of interstellar matter on climatic variation," *Mathematical Proceedings of the Cambridge Philosophical Society* **35** (1939), no. 3 405–415.

[116] H. Bondi and F. Hoyle, "On the mechanism of accretion by stars," *MNRAS* **104** (1944) 273.

[117] H. Bondi, "On spherically symmetrical accretion," *Mon. Not. Roy. Astron. Soc.* **112** (1952) 195.

[118] D. Inman and Y. Ali-Haïmoud, "Early structure formation in primordial black hole cosmologies," *Phys. Rev. D* **100** (2019), no. 8 083528, 1907.08129.

[119] T. R. Slatyer and C.-L. Wu, "General Constraints on Dark Matter Decay from the Cosmic Microwave Background," *Phys. Rev. D* **95** (2017), no. 2 023010, 1610.06933.

[120] M. Ricotti, J. P. Ostriker, and K. J. Mack, "Effect of Primordial Black Holes on the Cosmic Microwave Background and Cosmological Parameter Estimates," *Astrophys. J.* **680** (2008) 829, 0709.0524.

[121] M. Sasaki, T. Suyama, T. Tanaka, and S. Yokoyama, "Primordial Black Hole Scenario for the Gravitational-Wave Event GW150914," *Phys. Rev. Lett.* **117** (2016), no. 6 061101, 1603.08338. [Erratum: Phys.Rev.Lett. 121, 059901 (2018)].

[122] F.-G. Xie and F. Yuan, "The Radiative Efficiency of Hot Accretion Flows," *Mon. Not. Roy. Astron. Soc.* **427** (2012) 1580, 1207.3113.

[123] M. Ricotti, "Bondi accretion in the early universe," *Astrophys. J.* **662** (2007) 53–61, 0706.0864.

[124] L. Mayer, *Super-Eddington accretion; flow regimes and conditions in high-z galaxies.* World Scientific, 2019.

[125] M. Brightman *et. al.*, "Breaking the limit: Super-Eddington accretion onto black holes and neutron stars," 1903.06844.

[126] E. Takeo, K. Inayoshi, K. Ohsuga, H. R. Takahashi, and S. Mineshige, "Super-Eddington growth of black holes in the early universe: effects of disc radiation spectra," *Mon. Not. Roy. Astron. Soc.* **488** (2019), no. 2 2689–2700, 1901.04514.

[127] E. Takeo, K. Inayoshi, K. Ohsuga, H. R. Takahashi, and S. Mineshige, "Rapid growth of black holes accompanied with hot or warm outflows exposed to anisotropic super-Eddington radiation," *Mon. Not. Roy. Astron. Soc.* **476** (2018), no. 1 673–682, 1705.05382.

[128] D. Inman and Y. Ali-Haïmoud, "Early structure formation in primordial black hole cosmologies," *Phys. Rev. D* **100** (Oct, 2019) 083528, 1907.08129.

[129] P. Boldrini, Y. Miki, A. Y. Wagner, R. Mohayaee, J. Silk, and A. Arbey, "Cusp-to-core transition in low-mass dwarf galaxies induced by dynamical heating of cold dark matter by primordial black holes," *Monthly Notices of the Royal Astronomical Society* **492** (01, 2020) 5218–5225, 1909.07395.

[130] B. Liu, S. Zhang, and V. Bromm, "Effects of stellar-mass primordial black holes on first star formation," *Monthly Notices of the Royal Astronomical Society* **514** (05, 2022) 2376–2396, 2204.06330.

[131] B. Liu and V. Bromm, "Accelerating early massive galaxy formation with primordial black holes," 2208.13178.

[132] V. D. Luca, G. Franciolini, P. Pani, and A. Riotto, "The evolution of primordial black holes and their final observable spins," *Journal of Cosmology and Astroparticle Physics* **2020** (apr, 2020) 052–052, 2003.02778.

[133] V. De Luca, G. Franciolini, P. Pani, and A. Riotto, "Constraints on Primordial Black Holes: the Importance of Accretion," *Phys. Rev. D* **102** (2020), no. 4 043505, 2003.12589.

[134] J. Adamek, C. T. Byrnes, M. Gosenca, and S. Hotchkiss, "WIMPs and stellar-mass primordial black holes are incompatible," *Phys. Rev.* **D100** (2019), no. 2 023506, 1901.08528.

[135] Y. Ali-Haïmoud, "Correlation function of high-threshold regions and application to the initial small-scale clustering of primordial black holes," *Phys. Rev. Lett.* **121** (Aug, 2018) 081304, 1805.05912.

[136] V. D. Luca, G. Franciolini, A. Riotto, and H. Veermäe, "Ruling out initial primordial black hole clustering," 2208.01683.

[137] Y. Ali-Haïmoud, E. D. Kovetz, and M. Kamionkowski, "Merger rate of primordial black-hole binaries," *Phys. Rev. D* **96** (Dec, 2017) 123523, 1709.06576.

[138] K. Jedamzik, "Primordial black hole dark matter and the LIGO/virgo observations," *Journal of Cosmology and Astroparticle Physics* **2020** (sep, 2020) 022–022, 2006.11172.

[139] K. Jedamzik, "Consistency of primordial black hole dark matter with ligo/virgo merger rates," *Phys. Rev. Lett.* **126** (Feb, 2021) 051302, 2007.03565.

[140] S. L. Shapiro, "Accretion onto Black Holes: the Emergent Radiation Spectrum. III. Rotating (kerr) Black Holes," **189** (Apr., 1974) 343–352.

[141] T. Chiba and S. Yokoyama, "Spin Distribution of Primordial Black Holes," *PTEP* **2017** (2017), no. 8 083E01, 1704.06573.

[142] V. D. Luca, V. Desjacques, G. Franciolini, A. Malhotra, and A. Riotto, "The initial spin probability distribution of primordial black holes," *Journal of Cosmology and Astroparticle Physics* **2019** (may, 2019) 018–018, 1903.01179.

[143] T. Harada, C.-M. Yoo, K. Kohri, and K.-I. Nakao, "Spins of primordial black holes formed in the matter-dominated phase of the Universe," *Phys. Rev. D* **96** (2017), no. 8 083517, 1707.03595. [Erratum: Phys.Rev.D 99, 069904 (2019)].

[144] F. Kuhnel, "Enhanced Detectability of Spinning Primordial Black Holes," *Eur. Phys. J. C* **80** (2020), no. 3 243, 1909.04742.

[145] J. A. de Freitas Pacheco and J. Silk, "Primordial Rotating Black Holes," *Phys. Rev. D* **101** (2020), no. 8 083022, 2003.12072.

[146] T. W. Jensen and Y. Ali-Haïmoud, "Perturbed recombination from inhomogeneous photon injection and application to accreting primordial black holes," *Phys. Rev. D* **104** (2021), no. 6 063534, 2106.10266.

[147] M. Safarzadeh, "Primordial black holes as seeds of magnetic fields in the universe," *MNRAS* **479** (Sept., 2018) 315–318, 1701.03800.

[148] R. D. Blandford and R. L. Znajek, "Electromagnetic extraction of energy from Kerr black holes.," *MNRAS* **179** (May, 1977) 433–456.

[149] R. D. Blandford and D. G. Payne, "Hydromagnetic flows from accretion disks and the production of radio jets.," *MNRAS* **199** (June, 1982) 883–903.

[150] M. V. Barkov and D. V. Khangulyan, "Direct wind accretion and jet launch in binary systems," *MNRAS* **421** (Apr., 2012) 1351–1359, 1109.5810.

[151] M. V. Barkov, D. V. Khangulyan, and S. B. Popov, "Jets and gamma-ray emission from isolated accreting black holes," *Monthly Notices of the Royal Astronomical Society* **427** (11, 2012) 589–594.

[152] S. M. Ressler, E. Quataert, C. J. White, and O. Blaes, "Magnetically modified spherical accretion in GRMHD: reconnection-driven convection and jet propagation," *MNRAS* **504** (July, 2021) 6076–6095, 2102.01694.

[153] T. R. Slatyer, "Indirect dark matter signatures in the cosmic dark ages. I. Generalizing the bound on s-wave dark matter annihilation from Planck results," *Phys. Rev. D* **93** (2016), no. 2 023527, 1506.03811.

[154] T. R. Slatyer, N. Padmanabhan, and D. P. Finkbeiner, "CMB Constraints on WIMP Annihilation: Energy Absorption During the Recombination Epoch," *Phys. Rev.* **D80** (2009) 043526, 0906.1197.

[155] T. R. Slatyer, "Energy Injection And Absorption In The Cosmic Dark Ages," *Phys. Rev.* **D87** (2013), no. 12 123513, 1211.0283.

[156] X.-L. Chen and M. Kamionkowski, "Particle decays during the cosmic dark ages," *Phys. Rev.* **D70** (2004) 043502, astro-ph/0310473.

[157] N. Padmanabhan and D. P. Finkbeiner, "Detecting dark matter annihilation with cmb polarization: Signatures and experimental prospects," *Phys. Rev. D* **72** (Jul, 2005) 023508, astro-ph/0503486.

[158] S. Galli, T. R. Slatyer, M. Valdes, and F. Iocco, "Systematic Uncertainties In Constraining Dark Matter Annihilation From The Cosmic Microwave Background," *Phys. Rev.* **D88** (2013) 063502, 1306.0563.

[159] T. R. Slatyer, "Indirect dark matter signatures in the cosmic dark ages. II. Ionization, heating, and photon production from arbitrary energy injections," *Phys. Rev.* **D93** (Jan., 2016) 023521, 1506.03812.

[160] V. Poulin, J. Lesgourgues, and P. D. Serpico, "Cosmological constraints on exotic injection of electromagnetic energy," *JCAP* **1703** (2017), no. 03 043, 1610.10051.

[161] H. Liu, G. W. Ridgway, and T. R. Slatyer, "Code package for calculating modified cosmic ionization and thermal histories with dark matter and other exotic energy injections," *Phys. Rev. D* **101** (Jan, 2020) 023530, 1904.09296.

[162] B. Audren, J. Lesgourgues, K. Benabed, and S. Prunet, "Conservative Constraints on Early Cosmology: an illustration of the Monte Python cosmological parameter inference code," *JCAP* **1302** (2013) 001, 1210.7183.

[163] T. Brinckmann and J. Lesgourgues, "MontePython 3: boosted MCMC sampler and other features," 1804.07261.

[164] A. Gelman and D. B. Rubin, "Inference from iterative simulation using multiple sequences," *Statist. Sci.* **7** (11, 1992) 457–472.

[165] N. Bellomo, J. L. Bernal, A. Raccanelli, and L. Verde, "Primordial Black Holes as Dark Matter: Converting Constraints from Monochromatic to Extended Mass Distributions," *JCAP* **01** (2018) 004, 1709.07467.

[166] B. J. Carr, "The primordial black hole mass spectrum," *Astrophysical Journal* **201** (1975) 1.

[167] S. W. Hawking, "Black holes from cosmic strings," *Physics Letters B* **231** (1989) 237.

[168] P. Ivanov, P. Naselsky, and I. Novikov, "Inflation and primordial black holes as dark matter," *Phys. Rev. D* **50** (dec, 1994) 7173–7178.

[169] J. García-Bellido, A. Linde, and D. Wands, "Density perturbations and black hole formation in hybrid inflation," *Phys. Rev. D* **54** (Nov, 1996) 6040–6058, astro-ph/9605094.

[170] P. Ivanov, "Nonlinear metric perturbations and production of primordial black holes," *Phys. Rev. D* **57** (Jun, 1998) 7145–7154, astro-ph/9708224.

[171] S. M. Leach, I. J. Grivell, and A. R. Liddle, "Black hole constraints on the running-mass inflation model," *Phys. Rev. D* **62** (Jul, 2000) 043516, astro-ph/0004296.

[172] M. Drees and E. Erfani, "Running-mass inflation model and primordial black holes," *Journal of Cosmology and Astroparticle Physics* **2011** (2011), no. 04 005, 1102.2340.

[173] M. Drees and E. Erfani, "Running spectral index and formation of primordial black hole in single field inflation models," *Journal of Cosmology and Astroparticle Physics* **2012** (jan, 2012) 035, 1110.6052.

[174] M. Kawasaki, N. Kitajima, and T. T. Yanagida, "Primordial black hole formation from an axionlike curvaton model," *Phys. Rev. D* **87** (Mar, 2013) 063519, 1207.2550.

[175] K. Kohri, C.-M. Lin, and T. Matsuda, "Primordial black holes from the inflating curvaton," *Phys. Rev. D* **87** (May, 2013) 103527, 1211.2371.

[176] J. Garcia-Bellido and E. Ruiz Morales, "Primordial black holes from single field models of inflation," *Physics of the Dark Universe* **18** (2017) 47–54, 1702.03901.

[177] C. Germani and T. Prokopec, "On primordial black holes from an inflection point," *Physics of the Dark Universe* **18** (2017) 6–10, 1706.04226.

[178] K. Kannike, L. Marzola, M. Raidal, and H. Veermäe, "Single field double inflation and primordial black holes," *Journal of Cosmology and Astroparticle Physics* **2017** (sep, 2017) 020, 1705.06225.

[179] H. Motohashi and W. Hu, "Primordial black holes and slow-roll violation," *Phys. Rev. D* **96** (Sep, 2017) 063503, 1706.06784.

[180] G. Ballesteros and M. Taoso, "Primordial black hole dark matter from single field inflation," *Phys. Rev. D* **97** (Jan, 2018) 023501, 1709.05565.

[181] O. Özsoy, S. Parameswaran, G. Tasinato, and I. Zavala, "Mechanisms for primordial black hole production in string theory," *Journal of Cosmology and Astroparticle Physics* **2018** (jul, 2018) 005, 1803.07626.

[182] M. Cicoli, V. A. Diaz, and F. G. Pedro, "Primordial black holes from string inflation," *Journal of Cosmology and Astroparticle Physics* **2018** (jun, 2018) 034, 1803.02837.

[183] I. Dalianis, A. Kehagias, and G. Tringas, "Primordial black holes from α-attractors," *Journal of Cosmology and Astroparticle Physics* **2019** (jan, 2019) 037, 1805.09483.

[184] **Planck Collaboration** Collaboration, P. A. R. Ade *et. al.*, "Planck 2013 results. xxii. constraints on inflation," *A&A* **571** (2014) A22, 1303.5082.

[185] **Planck Collaboration** Collaboration, P. A. R. Ade *et. al.*, "Planck 2015 results. XX. Constraints on inflation," *Astron. Astrophys.* **594** (2016) A20, 1502.02114.

[186] **Planck Collaboration** Collaboration, Y. Akrami *et. al.*, "Planck 2018 results. x. constraints on inflation," *A&A* **641** (2020) A10, 1807.06211.

[187] B. J. Carr, "The primordial black hole mass spectrum," *The Astrophysical Journal* **201** (oct, 1975) 1–19.

[188] B. J. Carr and J. E. Lidsey, "Primordial black holes and generalized constraints on chaotic inflation," *Phys. Rev. D* **48** (Jul, 1993) 543–553.

[189] B. J. Carr, J. H. Gilbert, and J. E. Lidsey, "Black hole relics and inflation: Limits on blue perturbation spectra," *Phys. Rev. D* **50** (Oct, 1994) 4853–4867, astro-ph/9405027.

[190] A. S. Josan, A. M. Green, and K. A. Malik, "Generalized constraints on the curvature perturbation from primordial black holes," *Phys. Rev. D* **79** (May, 2009) 103520, 0903.3184.

[191] P. S. Cole and C. T. Byrnes, "Extreme scenarios: the tightest possible constraints on the power spectrum due to primordial black holes," *Journal of Cosmology and Astroparticle Physics* **2018** (2018), no. 02 019, 1706.10288.

[192] J. Mifsud and C. van de Bruck, "Complementary probes of inflationary cosmology," 1904.09590.

[193] G. Sato-Polito, E. D. Kovetz, and M. Kamionkowski, "Constraints on the primordial curvature power spectrum from primordial black holes," *Phys. Rev. D* **100** (Sep, 2019) 063521, 1904.10971.

[194] Y. Akrami, F. Kuhnel, and M. Sandstad, "Uncertainties in primordial black-hole constraints on the primordial power spectrum," *Physics of the Dark Universe* **19** (2018) 124 – 128, 1611.10069.

[195] A. Kalaja, N. Bellomo, N. Bartolo, D. Bertacca, S. Matarrese, I. Musco, A. Raccanelli, and L. Verde, "From primordial black holes abundance to primordial curvature power spectrum (and back)," *Journal of Cosmology and Astroparticle Physics* **2019** (oct, 2019) 031–031, 1908.03596.

[196] A. D. Gow, C. T. Byrnes, P. S. Cole, and S. Young, "The power spectrum on small scales: robust constraints and comparing PBH methodologies," *Journal of Cosmology and Astroparticle Physics* **2021** (feb, 2021) 002–002, 2008.03289.

[197] N. Schöneberg, M. Lucca, and D. C. Hooper, "Constraining the inflationary potential with spectral distortions," 2010.07814.

[198] A. D. Gow, C. T. Byrnes, and A. Hall, "Accurate model for the primordial black hole mass distribution from a peak in the power spectrum," *Phys. Rev. D* **105** (Jan, 2022) 023503, 2009.03204.

[199] B. Carr, F. Kühnel, and M. Sandstad, "Primordial black holes as dark matter," *Phys. Rev. D* **94** (Oct, 2016) 083504, 1607.06077.

[200] B. Carr, M. Raidal, T. Tenkanen, V. Vaskonen, and H. Veermäe, "Primordial black hole constraints for extended mass functions," *Phys. Rev. D* **96** (Jul, 2017) 023514, 1705.05567.

[201] R. Abbott *et. al.*, "Population properties of compact objects from the second ligo-virgo gravitational-wave transient catalog," *The Astrophysical Journal Letters* **913** (may, 2021) L7, 2010.14533.

[202] M. Zumalacárregui and U. Seljak, "Limits on stellar-mass compact objects as dark matter from gravitational lensing of type ia supernovae," *Phys. Rev. Lett.* **121** (Oct, 2018) 141101, 1712.02240.

[203] T. D. Brandt, "Constraints on macho dark matter from compact stellar systems in ultra-faint dwarf galaxies," *The Astrophysical Journal* **824** (jun, 2016) L31, 1605.03665.

[204] S. M. Koushiappas and A. Loeb, "Dynamics of dwarf galaxies disfavor stellar-mass black holes as dark matter," *Phys. Rev. Lett.* **119** (Jul, 2017) 041102, 1704.01668.

[205] Zoutendijk, Sebastiaan L. *et. al.*, "The muse-faint survey - i. spectroscopic evidence for a star cluster in eridanus 2 and constraints on machos as a constituent of dark matter," *A&A* **635** (2020) A107, 2001.08790.

[206] N. Afshordi, P. McDonald, and D. N. Spergel, "Primordial black holes as dark matter: The power spectrum and evaporation of early structures," *The Astrophysical Journal* **594** (aug, 2003) L71–L74, astro-ph/0302035.

[207] M. A. Monroy-Rodríguez and C. Allen, "The end of the macho era revisited: new limits on macho masses from halo wide binaries," *The Astrophysical Journal* **790** (jul, 2014) 159, 1406.5169.

[208] T. Nishimichi, G. D'Amico, M. M. Ivanov, L. Senatore, M. Simonović, M. Takada, M. Zaldarriaga, and P. Zhang, "Blinded challenge for precision cosmology with large-scale structure: results from effective field theory for the redshift-space galaxy power spectrum," *Phys. Rev. D* **102** (2020), no. 12 123541, 2003.08277.

[209] G. D'Amico, M. Marinucci, M. Pietroni, and F. Vernizzi, "The large scale structure bootstrap: perturbation theory and bias expansion from symmetries," *JCAP* **10** (2021) 069, 2109.09573.

[210] P. Carrilho, C. Moretti, and A. Pourtsidou, "Cosmology with the EFTofLSS and BOSS: dark energy constraints and a note on priors," 2207.14784.

[211] F. Simpson, "Scattering of dark matter and dark energy," *Phys. Rev. D* **82** (2010) 083505, 1007.1034.

[212] S. Ferraro, N. Sailer, A. Slosar, and M. White, "Snowmass2021 Cosmic Frontier White Paper: Cosmology and Fundamental Physics from the three-dimensional Large Scale Structure," 2203.07506.

[213] F. Bernardeau, S. Colombi, E. Gaztanaga, and R. Scoccimarro, "Large scale structure of the universe and cosmological perturbation theory," *Phys. Rept.* **367** (2002) 1–248, astro-ph/0112551.

[214] D. Baumann, A. Nicolis, L. Senatore, and M. Zaldarriaga, "Cosmological Non-Linearities as an Effective Fluid," *JCAP* **07** (2012) 051, 1004.2488.

[215] M. Pietroni, G. Mangano, N. Saviano, and M. Viel, "Coarse-Grained Cosmological Perturbation Theory," *JCAP* **01** (2012) 019, 1108.5203.

[216] J. J. M. Carrasco, M. P. Hertzberg, and L. Senatore, "The Effective Field Theory of Cosmological Large Scale Structures," *JHEP* **09** (2012) 082, 1206.2926.

[217] A. Manzotti, M. Peloso, M. Pietroni, M. Viel, and F. Villaescusa-Navarro, "A coarse grained perturbation theory for the Large Scale Structure, with cosmology and time independence in the UV," *JCAP* **09** (2014) 047, 1407.1342.

[218] P. McDonald and A. Roy, "Clustering of dark matter tracers: generalizing bias for the coming era of precision LSS," *JCAP* **08** (2009) 020, 0902.0991.

[219] K. C. Chan, R. Scoccimarro, and R. K. Sheth, "Gravity and Large-Scale Non-local Bias," *Phys. Rev. D* **85** (2012) 083509, 1201.3614.

[220] S. Saito, T. Baldauf, Z. Vlah, U. Seljak, T. Okumura, and P. McDonald, "Understanding higher-order nonlocal halo bias at large scales by combining the power spectrum with the bispectrum," *Phys. Rev. D* **90** (2014), no. 12 123522, 1405.1447.

[221] V. Assassi, D. Baumann, D. Green, and M. Zaldarriaga, "Renormalized Halo Bias," *JCAP* **08** (2014) 056, 1402.5916.

[222] L. Senatore, "Bias in the Effective Field Theory of Large Scale Structures," *JCAP* **11** (2015) 007, 1406.7843.

[223] M. Mirbabayi, F. Schmidt, and M. Zaldarriaga, "Biased Tracers and Time Evolution," *JCAP* **07** (2015) 030, 1412.5169.

[224] R. Angulo, M. Fasiello, L. Senatore, and Z. Vlah, "On the Statistics of Biased Tracers in the Effective Field Theory of Large Scale Structures," *JCAP* **09** (2015) 029, 1503.08826.

[225] T. Fujita, V. Mauerhofer, L. Senatore, Z. Vlah, and R. Angulo, "Very Massive Tracers and Higher Derivative Biases," *JCAP* **01** (2020) 009, 1609.00717.

[226] V. Desjacques, D. Jeong, and F. Schmidt, "Large-Scale Galaxy Bias," *Phys. Rept.* **733** (2018) 1–193, 1611.09787.

[227] M. M. Ivanov, M. Simonović, and M. Zaldarriaga, "Cosmological Parameters from the BOSS Galaxy Power Spectrum," *JCAP* **05** (2020) 042, 1909.05277.

[228] S.-F. Chen, Z. Vlah, and M. White, "A new analysis of galaxy 2-point functions in the BOSS survey, including full-shape information and post-reconstruction BAO," *JCAP* **02** (2022), no. 02 008, 2110.05530.

[229] T. Colas, G. D'amico, L. Senatore, P. Zhang, and F. Beutler, "Efficient Cosmological Analysis of the SDSS/BOSS data from the Effective Field Theory of Large-Scale Structure," *JCAP* **06** (2020) 001, 1909.07951.

[230] M. M. Ivanov, M. Simonović, and M. Zaldarriaga, "Cosmological Parameters and Neutrino Masses from the Final Planck and Full-Shape BOSS Data," *Phys. Rev. D* **101** (2020), no. 8 083504, 1912.08208.

[231] O. H. Philcox, M. M. Ivanov, M. Simonović, and M. Zaldarriaga, "Combining Full-Shape and BAO Analyses of Galaxy Power Spectra: A 1.6% CMB-independent constraint on H0," *JCAP* **05** (2020) 032, 2002.04035.

[232] G. D'Amico, L. Senatore, P. Zhang, and H. Zheng, "The Hubble Tension in Light of the Full-Shape Analysis of Large-Scale Structure Data," 2006.12420.

[233] M. M. Ivanov, E. McDonough, J. C. Hill, M. Simonović, M. W. Toomey, S. Alexander, and M. Zaldarriaga, "Constraining Early Dark Energy with Large-Scale Structure," *Phys. Rev. D* **102** (2020), no. 10 103502, 2006.11235.

[234] G. D'Amico, Y. Donath, L. Senatore, and P. Zhang, "Limits on Clustering and Smooth Quintessence from the EFTofLSS," 2012.07554.

[235] M. M. Ivanov, O. H. E. Philcox, M. Simonović, M. Zaldarriaga, T. Nischimichi, and M. Takada, "Cosmological constraints without nonlinear redshift-space distortions," *Phys. Rev. D* **105** (2022), no. 4 043531, 2110.00006.

[236] G. D'Amico, L. Senatore, P. Zhang, and T. Nishimichi, "Taming redshift-space distortion effects in the EFTofLSS and its application to data," 2110.00016.

[237] O. H. E. Philcox and M. M. Ivanov, "BOSS DR12 full-shape cosmology: ΛCDM constraints from the large-scale galaxy power spectrum and bispectrum monopole," *Phys. Rev. D* **105** (2022), no. 4 043517, 2112.04515.

[238] G. D'Amico, Y. Donath, M. Lewandowski, L. Senatore, and P. Zhang, "The BOSS bispectrum analysis at one loop from the Effective Field Theory of Large-Scale Structure," 2206.08327.

[239] G. D'Amico, M. Lewandowski, L. Senatore, and P. Zhang, "Limits on primordial non-Gaussianities from BOSS galaxy-clustering data," 2201.11518.

[240] G. Cabass, M. M. Ivanov, O. H. E. Philcox, M. Simonović, and M. Zaldarriaga, "Constraints on Single-Field Inflation from the BOSS Galaxy Survey," *Phys. Rev. Lett.* **129** (2022), no. 2 021301, 2201.07238.

[241] G. Cabass, M. M. Ivanov, O. H. E. Philcox, M. Simonović, and M. Zaldarriaga, "Constraints on Multi-Field Inflation from the BOSS Galaxy Survey," 2204.01781.

[242] C. Deffayet, "Cosmology on a brane in Minkowski bulk," *Phys. Lett. B* **502** (2001) 199–208, hep-th/0010186.

[243] M. A. Luty, M. Porrati, and R. Rattazzi, "Strong interactions and stability in the DGP model," *JHEP* **09** (2003) 029, hep-th/0303116.

[244] C. Charmousis, R. Gregory, N. Kaloper, and A. Padilla, "DGP Specteroscopy," *JHEP* **10** (2006) 066, hep-th/0604086.

[245] K. Koyama, "Ghosts in the self-accelerating universe," *Class. Quant. Grav.* **24** (2007), no. 24 R231–R253, 0709.2399.

[246] G. R. Dvali, G. Gabadadze, and M. Porrati, "4-D gravity on a brane in 5-D Minkowski space," *Phys. Lett. B* **485** (2000) 208–214, hep-th/0005016.

[247] C. Hernández-Aguayo, C. Arnold, B. Li, and C. M. Baugh, "Galaxy formation in the brane world I: overview and first results," *Mon. Not. Roy. Astron. Soc.* **503** (2021), no. 3 3867–3885, 2006.15467.

[248] L. Lombriser, W. Hu, W. Fang, and U. Seljak, "Cosmological Constraints on DGP Braneworld Gravity with Brane Tension," *Phys. Rev. D* **80** (2009) 063536, 0905.1112.

[249] L. Xu, "Confronting DGP braneworld gravity with cosmico observations after Planck data," *JCAP* **02** (2014) 048, 1312.4679.

[250] F. Schmidt, "Cosmological Simulations of Normal-Branch Braneworld Gravity," *Phys. Rev. D* **80** (2009) 123003, 0910.0235.

[251] A. Raccanelli, D. Bertacca, D. Pietrobon, F. Schmidt, L. Samushia, N. Bartolo, O. Doré, S. Matarrese, and W. J. Percival, "Testing gravity using large-scale redshift-space distortions," *MNRAS* **436** (Nov., 2013) 89–100, 1207.0500.

[252] A. Barreira, A. G. Sánchez, and F. Schmidt, "Validating estimates of the growth rate of structure with modified gravity simulations," *Phys. Rev. D* **94** (2016), no. 8 084022, 1605.03965.

[253] **BOSS** Collaboration, A. G. Sanchez *et. al.*, "The clustering of galaxies in the completed SDSS-III Baryon Oscillation Spectroscopic Survey: cosmological implications of the configuration-space clustering wedges," *Mon. Not. Roy. Astron. Soc.* **464** (2017), no. 2 1640–1658, 1607.03147.

[254] A. Taruya, T. Nishimichi, F. Bernardeau, T. Hiramatsu, and K. Koyama, "Regularized cosmological power spectrum and correlation function in modified gravity models," *Phys. Rev. D* **90** (2014), no. 12 123515, 1408.4232.

[255] G. W. Horndeski, "Second-order scalar-tensor field equations in a four-dimensional space," *Int. J. Theor. Phys.* **10** (1974) 363–384.

[256] C. Deffayet, X. Gao, D. A. Steer, and G. Zahariade, "From k-essence to generalised Galileons," *Phys. Rev. D* **84** (2011) 064039, 1103.3260.

[257] A. Nicolis, R. Rattazzi, and E. Trincherini, "The Galileon as a local modification of gravity," *Phys. Rev. D* **79** (2009) 064036, 0811.2197.

[258] A. I. Vainshtein, "To the problem of nonvanishing gravitation mass," *Phys. Lett. B* **39** (1972) 393–394.

[259] M. Lewandowski, A. Maleknejad, and L. Senatore, "An effective description of dark matter and dark energy in the mildly non-linear regime," *JCAP* **05** (2017) 038, 1611.07966.

[260] R. Scoccimarro, H. M. P. Couchman, and J. A. Frieman, "The Bispectrum as a Signature of Gravitational Instability in Redshift-Space," *Astrophys. J.* **517** (1999) 531–540, astro-ph/9808305.

[261] L. Senatore and M. Zaldarriaga, "Redshift Space Distortions in the Effective Field Theory of Large Scale Structures," 1409.1225.

[262] T. Baldauf, M. Mirbabayi, M. Simonović, and M. Zaldarriaga, "Equivalence Principle and the Baryon Acoustic Peak," *Phys. Rev. D* **92** (2015), no. 4 043514, 1504.04366.

[263] L. Senatore and G. Trevisan, "On the IR-Resummation in the EFTofLSS," *JCAP* **05** (2018) 019, 1710.02178.

[264] M. Lewandowski and L. Senatore, "An analytic implementation of the IR-resummation for the BAO peak," *JCAP* **03** (2020) 018, 1810.11855.

[265] K. Koyama and R. Maartens, "Structure formation in the dgp cosmological model," *JCAP* **01** (2006) 016, astro-ph/0511634.

[266] R. J. Cooke, M. Pettini, and C. C. Steidel, "One Percent Determination of the Primordial Deuterium Abundance," *Astrophys. J.* **855** (2018), no. 2 102, 1710.11129.

[267] **BOSS** Collaboration, F. Beutler *et. al.*, "The clustering of galaxies in the completed SDSS-III Baryon Oscillation Spectroscopic Survey: Anisotropic galaxy clustering in Fourier-space," *Mon. Not. Roy. Astron. Soc.* **466** (2017), no. 2 2242–2260, 1607.03150.

[268] **Planck** Collaboration, N. Aghanim *et. al.*, "Planck 2018 results. VI. Cosmological parameters," *Astron. Astrophys.* **641** (2020) A6, 1807.06209.

[269] B. Audren, J. Lesgourgues, K. Benabed, and S. Prunet, "Conservative Constraints on Early Cosmology: an illustration of the Monte Python cosmological parameter inference code," *JCAP* **1302** (2013) 001, 1210.7183.

[270] T. Brinckmann and J. Lesgourgues, "MontePython 3: boosted MCMC sampler and other features," *Phys. Dark Univ.* **24** (2019) 100260, 1804.07261.

[271] D. Blas, J. Lesgourgues, and T. Tram, "The Cosmic Linear Anisotropy Solving System (CLASS) II: Approximation schemes," *JCAP* **07** (2011) 034, 1104.2933.

[272] A. Gelman and D. B. Rubin, "Inference from Iterative Simulation Using Multiple Sequences," *Statist. Sci.* **7** (1992) 457–472.

[273] A. Lewis, "GetDist: a Python package for analysing Monte Carlo samples," 1910.13970.

[274] A. Gómez-Valent, "A fast test to assess the impact of marginalization in Monte Carlo analyses, and its application to cosmology," 2203.16285.

[275] P. S. Behroozi, R. H. Wechsler, and H.-Y. Wu, "The ROCKSTAR Phase-space Temporal Halo Finder and the Velocity Offsets of Cluster Cores," *ApJ* **762** (Jan., 2013) 109, 1110.4372.

[276] H. Gil-Marín, W. J. Percival, J. R. Brownstein, C.-H. Chuang, J. N. Grieb, S. Ho, F.-S. Kitaura, C. Maraston, F. Prada, S. Rodríguez-Torres, A. J. Ross, L. Samushia, D. J. Schlegel, D. Thomas, J. L. Tinker, and G.-B. Zhao, "The clustering of galaxies in the SDSS-III Baryon Oscillation Spectroscopic Survey: RSD measurement from the LOS-dependent power spectrum of DR12 BOSS galaxies," *Monthly Notices of the Royal Astronomical Society* **460** (05, 2016) 4188–4209, https://academic.oup.com/mnras/article-pdf/460/4/4188/8116112/stw

[277] F. Beutler and P. McDonald, "Unified galaxy power spectrum measurements from 6dFGS, BOSS, and eBOSS," *JCAP* **11** (2021) 031, 2106.06324.

[278] T. Simon, P. Zhang, V. Poulin, and T. L. Smith, "On the consistency of effective field theory analyses of BOSS power spectrum," 2208.05929.

[279] N. Kaiser, "On the Spatial correlations of Abell clusters," *Astrophys. J. Lett.* **284** (1984) L9–L12.

[280] J. M. Bardeen, J. R. Bond, N. Kaiser, and A. S. Szalay, "The Statistics of Peaks of Gaussian Random Fields," *Astrophys. J.* **304** (1986) 15–61.

[281] V. Desjacques, M. Crocce, R. Scoccimarro, and R. K. Sheth, "Modeling scale-dependent bias on the baryonic acoustic scale with the statistics of peaks of Gaussian random fields," *Phys. Rev. D* **82** (2010) 103529, 1009.3449.

[282] M. Musso and R. K. Sheth, "One step beyond: The excursion set approach with correlated steps," *Mon. Not. Roy. Astron. Soc.* **423** (2012) L102–L106, 1201.3876.

[283] M. Marinucci, T. Nishimichi, and M. Pietroni, "Measuring Bias via the Consistency Relations of the Large Scale Structure," *Phys. Rev. D* **100** (2019), no. 12 123537, 1907.09866.

[284] M. Marinucci, T. Nishimichi, and M. Pietroni, "Model independent measurement of the growth rate from the consistency relations of the LSS," *JCAP* **07** (2020) 054, 2005.09574.

[285] H. Gil-Marín, J. Noreña, L. Verde, W. J. Percival, C. Wagner, M. Manera, and D. P. Schneider, "The power spectrum and bispectrum of SDSS DR11 BOSS galaxies – I. Bias and gravity," *Mon. Not. Roy. Astron. Soc.* **451** (2015), no. 1 539–580, 1407.5668.

[286] H. Gil-Marín, L. Verde, J. Noreña, A. J. Cuesta, L. Samushia, W. J. Percival, C. Wagner, M. Manera, and D. P. Schneider, "The power spectrum and bispectrum of SDSS DR11 BOSS galaxies – II. Cosmological interpretation," *Mon. Not. Roy. Astron. Soc.* **452** (2015), no. 2 1914–1921, 1408.0027.

[287] H. Gil-Marín, W. J. Percival, L. Verde, J. R. Brownstein, C.-H. Chuang, F.-S. Kitaura, S. A. Rodríguez-Torres, and M. D. Olmstead, "The clustering of galaxies in the SDSS-III Baryon Oscillation Spectroscopic Survey: RSD measurement from the power spectrum and bispectrum of the DR12 BOSS galaxies," *Mon. Not. Roy. Astron. Soc.* **465** (2017), no. 2 1757–1788, 1606.00439.

[288] N. Agarwal, V. Desjacques, D. Jeong, and F. Schmidt, "Information content in the redshift-space galaxy power spectrum and bispectrum," *JCAP* **03** (2021) 021, 2007.04340.

[289] V. Yankelevich and C. Porciani, "Cosmological information in the redshift-space bispectrum," *Mon. Not. Roy. Astron. Soc.* **483** (2019), no. 2 2078–2099, 1807.07076.

[290] M. M. Ivanov, O. H. E. Philcox, T. Nishimichi, M. Simonović, M. Takada, and M. Zaldarriaga, "Precision analysis of the redshift-space galaxy bispectrum," *Phys. Rev. D* **105** (2022), no. 6 063512, 2110.10161.

[291] O. H. E. Philcox, M. M. Ivanov, G. Cabass, M. Simonović, M. Zaldarriaga, and T. Nishimichi, "Cosmology with the Redshift-Space Galaxy Bispectrum Monopole at One-Loop Order," 2206.02800.

[292] W. Hu and I. Sawicki, "Models of f(R) Cosmic Acceleration that Evade Solar-System Tests," *Phys. Rev. D* **76** (2007) 064004, 0705.1158.

[293] A. Aviles, A. Banerjee, G. Niz, and Z. Slepian, "Clustering in massive neutrino cosmologies via Eulerian Perturbation Theory," *JCAP* **11** (2021) 028, 2106.13771.

[294] G. Parimbelli, M. Viel, and E. Sefusatti, "On the degeneracy between baryon feedback and massive neutrinos as probed by matter clustering and weak lensing," *JCAP* **01** (2019) 010, 1809.06634.

[295] R. Laureijs, J. Amiaux, S. Arduini, J. L. Augueres, J. Brinchmann, R. Cole, M. Cropper, C. Dabin, L. Duvet, A. Ealet, B. Garilli, P. Gondoin, L. Guzzo, J. Hoar, H. Hoekstra, R. Holmes, T. Kitching, T. Maciaszek, Y. Mellier, F. Pasian, W. Percival, J. Rhodes, G. S. Criado, M. Sauvage, R. Scaramella, L. Valenziano, S. Warren, R. Bender, F. Castander, A. Cimatti, O. L. Fèvre, H. Kurki-Suonio, M. Levi, P. Lilje, G. Meylan, R. Nichol, K. Pedersen, V. Popa, R. R. Lopez, H. W. Rix, H. Rottgering, W. Zeilinger, F. Grupp, P. Hudelot, R. Massey, M. Meneghetti, L. Miller, S. Paltani, S. Paulin-Henriksson, S. Pires, C. Saxton, T. Schrabback, G. Seidel, J. Walsh, N. Aghanim, L. Amendola, J. Bartlett, C. Baccigalupi, J. P. Beaulieu, K. Benabed, J. G. Cuby, D. Elbaz, P. Fosalba, G. Gavazzi, A. Helmi, I. Hook, M. Irwin, J. P. Kneib, M. Kunz, F. Mannucci, L. Moscardini, C. Tao, R. Teyssier, J. Weller, G. Zamorani, M. R. Z. Osorio, O. Boulade, J. J. Foumond, A. D. Giorgio, P. Guttridge, A. James, M. Kemp, J. Martignac, A. Spencer, D. Walton, T. Blümchen, C. Bonoli, F. Bortoletto, C. Cerna, L. Corcione, C. Fabron, K. Jahnke, S. Ligori, F. Madrid, L. Martin, G. Morgante, T. Pamplona, E. Prieto, M. Riva, R. Toledo, M. Trifoglio, F. Zerbi, F. Abdalla, M. Douspis, C. Grenet, S. Borgani,

R. Bouwens, F. Courbin, J. M. Delouis, P. Dubath, A. Fontana, M. Frailis, A. Grazian, J. Koppenhöfer, O. Mansutti, M. Melchior, M. Mignoli, J. Mohr, C. Neissner, K. Noddle, M. Poncet, M. Scodeggio, S. Serrano, N. Shane, J. L. Starck, C. Surace, A. Taylor, G. Verdoes-Kleijn, C. Vuerli, O. R. Williams, A. Zacchei, B. Altieri, I. E. Sanz, R. Kohley, T. Oosterbroek, P. Astier, D. Bacon, S. Bardelli, C. Baugh, F. Bellagamba, C. Benoist, D. Bianchi, A. Biviano, E. Branchini, C. Carbone, V. Cardone, D. Clements, S. Colombi, C. Conselice, G. Cresci, N. Deacon, J. Dunlop, C. Fedeli, F. Fontanot, P. Franzetti, C. Giocoli, J. Garcia-Bellido, J. Gow, A. Heavens, P. Hewett, C. Heymans, A. Holland, Z. Huang, O. Ilbert, B. Joachimi, E. Jennins, E. Kerins, A. Kiessling, D. Kirk, R. Kotak, O. Krause, O. Lahav, F. van Leeuwen, J. Lesgourgues, M. Lombardi, M. Magliocchetti, K. Maguire, E. Majerotto, R. Maoli, F. Marulli, S. Maurogordato, H. McCracken, R. McLure, A. Melchiorri, A. Merson, M. Moresco, M. Nonino, P. Norberg, J. Peacock, R. Pello, M. Penny, V. Pettorino, C. D. Porto, L. Pozzetti, C. Quercellini, M. Radovich, A. Rassat, N. Roche, S. Ronayette, E. Rossetti, B. Sartoris, P. Schneider, E. Semboloni, S. Serjeant, F. Simpson, C. Skordis, G. Smadja, S. Smartt, P. Spano, S. Spiro, M. Sullivan, A. Tilquin, R. Trotta, L. Verde, Y. Wang, G. Williger, G. Zhao, J. Zoubian, and E. Zucca, "Euclid definition study report," 1110.3193.

[296] R. Scaramella, J. Amiaux, Y. Mellier, C. Burigana, C. S. Carvalho, J.-C. Cuillandre, A. Da Silva, A. Derosa, J. Dinis, E. Maiorano, M. Maris, I. Tereno, R. Laureijs, T. Boenke, G. Buenadicha, X. Dupac, L. M. Gaspar Venancio, P. Gómez-Álvarez, J. Hoar, J. Lorenzo Alvarez, G. D. Racca, G. Saavedra-Criado, J. Schwartz, R. Vavrek, M. Schirmer, H. Aussel, R. Azzollini, V. F. Cardone, M. Cropper, A. Ealet, B. Garilli, W. Gillard, B. R. Granett, L. Guzzo, H. Hoekstra, K. Jahnke, T. Kitching, T. Maciaszek, M. Meneghetti, L. Miller, R. Nakajima, S. M. Niemi, F. Pasian, W. J. Percival, S. Pottinger, M. Sauvage, M. Scodeggio, S. Wachter, A. Zacchei, N. Aghanim, A. Amara, T. Auphan, N. Auricchio, S. Awan, A. Balestra, R. Bender, C. Bodendorf, D. Bonino, E. Branchini, S. Brau-Nogue, M. Brescia, G. P. Candini, V. Capobianco, C. Carbone, R. G. Carlberg, J. Carretero, R. Casas, F. J. Castander, M. Castellano, S. Cavuoti, A. Cimatti, R. Cledassou, G. Congedo, C. J. Conselice, L. Conversi, Y. Copin,

L. Corcione, A. Costille, F. Courbin, H. Degaudenzi, M. Douspis, F. Dubath, C. A. J. Duncan, S. Dusini, S. Farrens, S. Ferriol, P. Fosalba, N. Fourmanoit, M. Frailis, E. Franceschi, P. Franzetti, M. Fumana, B. Gillis, C. Giocoli, A. Grazian, F. Grupp, S. V. H. Haugan, W. Holmes, F. Hormuth, P. Hudelot, S. Kermiche, A. Kiessling, M. Kilbinger, R. Kohley, B. Kubik, M. Kümmel, M. Kunz, H. Kurki-Suonio, O. Lahav, S. Ligori, P. B. Lilje, I. Lloro, O. Mansutti, O. Marggraf, K. Markovic, F. Marulli, R. Massey, S. Maurogordato, M. Melchior, E. Merlin, G. Meylan, J. J. Mohr, M. Moresco, B. Morin, L. Moscardini, E. Munari, R. C. Nichol, C. Padilla, S. Paltani, J. Peacock, K. Pedersen, V. Pettorino, S. Pires, M. Poncet, L. Popa, L. Pozzetti, F. Raison, R. Rebolo, J. Rhodes, H.-W. Rix, M. Roncarelli, E. Rossetti, R. Saglia, P. Schneider, T. Schrabback, A. Secroun, G. Seidel, S. Serrano, C. Sirignano, G. Sirri, J. Skottfelt, L. Stanco, J. L. Starck, P. Tallada-Crespí, D. Tavagnacco, A. N. Taylor, H. I. Teplitz, R. Toledo-Moreo, F. Torradeflot, M. Trifoglio, E. A. Valentijn, L. Valenziano, G. A. Verdoes Kleijn, Y. Wang, N. Welikala, J. Weller, M. Wetzstein, G. Zamorani, J. Zoubian, S. Andreon, M. Baldi, S. Bardelli, A. Boucaud, S. Camera, D. Di Ferdinando, G. Fabbian, R. Farinelli, S. Galeotta, J. Graciá-Carpio, D. Maino, E. Medinaceli, S. Mei, C. Neissner, G. Polenta, A. Renzi, E. Romelli, C. Rosset, F. Sureau, M. Tenti, T. Vassallo, E. Zucca, C. Baccigalupi, A. Balaguera-Antolínez, P. Battaglia, A. Biviano, S. Borgani, E. Bozzo, R. Cabanac, A. Cappi, S. Casas, G. Castignani, C. Colodro-Conde, J. Coupon, H. M. Courtois, J. Cuby, S. de la Torre, S. Desai, H. Dole, M. Fabricius, M. Farina, P. G. Ferreira, F. Finelli, P. Flose-Reimberg, S. Fotopoulou, K. Ganga, G. Gozaliasl, I. M. Hook, E. Keihanen, C. C. Kirkpatrick, P. Liebing, V. Lindholm, G. Mainetti, M. Martinelli, N. Martinet, M. Maturi, H. J. McCracken, R. B. Metcalf, G. Morgante, J. Nightingale, A. Nucita, L. Patrizii, D. Potter, G. Riccio, A. G. Sánchez, D. Sapone, J. A. Schewtschenko, M. Schultheis, V. Scottez, R. Teyssier, I. Tutusaus, J. Valiviita, M. Viel, W. Vriend, and L. Whittaker, "Euclid preparation: I. the euclid wide survey," *Astronomy amp; Astrophysics* **662** (June, 2022) A112.

[297] M. Schirmer, K. Jahnke, G. Seidel, H. Aussel, C. Bodendorf, F. Grupp, F. Hormuth, S. Wachter, P. N. Appleton, R. Barbier, J. Brinchmann, J. M. Carrasco, F. J. Castander,

J. Coupon, F. De Paolis, A. Franco, K. Ganga, P. Hudelot, E. Jullo, A. Lançon, A. A. Nucita, S. Paltani, G. Smadja, F. Strafella, L. M. G. Venancio, M. Weiler, A. Amara, T. Auphan, N. Auricchio, A. Balestra, R. Bender, D. Bonino, E. Branchini, M. Brescia, V. Capobianco, C. Carbone, J. Carretero, R. Casas, M. Castellano, S. Cavuoti, A. Cimatti, R. Cledassou, G. Congedo, C. J. Conselice, L. Conversi, Y. Copin, L. Corcione, A. Costille, F. Courbin, A. Da Silva, H. Degaudenzi, M. Douspis, F. Dubath, X. Dupac, S. Dusini, A. Ealet, S. Farrens, S. Ferriol, P. Fosalba, M. Frailis, E. Franceschi, P. Franzetti, M. Fumana, B. Garilli, W. Gillard, B. Gillis, C. Giocoli, A. Grazian, L. Guzzo, S. V. H. Haugan, H. Hoekstra, W. Holmes, A. Hornstrup, M. Kümmel, S. Kermiche, A. Kiessling, M. Kilbinger, T. Kitching, R. Kohley, M. Kunz, H. Kurki-Suonio, R. Laureijs, S. Ligori, P. B. Lilje, I. Lloro, T. Maciaszek, E. Maiorano, O. Mansutti, O. Marggraf, K. Markovic, F. Marulli, R. Massey, S. Maurogordato, Y. Mellier, M. Meneghetti, E. Merlin, G. Meylan, M. Moresco, L. Moscardini, E. Munari, R. Nakajima, R. C. Nichol, S. M. Niemi, C. Padilla, F. Pasian, K. Pedersen, W. J. Percival, V. Pettorino, S. Pires, M. Poncet, L. Popa, L. Pozzetti, E. Prieto, F. Raison, J. Rhodes, H.-W. Rix, M. Roncarelli, E. Rossetti, R. Saglia, B. Sartoris, R. Scaramella, P. Schneider, A. Secroun, S. Serrano, C. Sirignano, G. Sirri, L. Stanco, P. Tallada-Crespí, A. N. Taylor, H. I. Teplitz, I. Tereno, R. Toledo-Moreo, F. Torradeflot, M. Trifoglio, E. A. Valentijn, L. Valenziano, Y. Wang, J. Weller, G. Zamorani, J. Zoubian, S. Andreon, S. Bardelli, A. Boucaud, S. Camera, R. Farinelli, J. Graciá-Carpio, D. Maino, E. Medinaceli, S. Mei, N. Morisset, G. Polenta, A. Renzi, E. Romelli, M. Tenti, T. Vassallo, A. Zacchei, E. Zucca, C. Baccigalupi, A. Balaguera-Antolínez, A. Biviano, A. Blanchard, S. Borgani, E. Bozzo, C. Burigana, R. Cabanac, A. Cappi, C. S. Carvalho, S. Casas, G. Castignani, C. Colodro-Conde, A. R. Cooray, H. M. Courtois, M. Crocce, J.-G. Cuby, S. Davini, S. de la Torre, D. Di Ferdinando, J. A. Escartin, M. Farina, P. G. Ferreira, F. Finelli, S. Fotopoulou, S. Galeotta, J. Garcia-Bellido, E. Gaztanaga, K. George, G. Gozaliasl, I. M. Hook, S. Ilić, V. Kansal, A. Kashlinsky, E. Keihanen, C. C. Kirkpatrick, V. Lindholm, G. Mainetti, R. Maoli, M. Martinelli, N. Martinet, M. Maturi, N. Mauri, H. J. McCracken, R. B. Metcalf, P. Monaco, G. Morgante, J. Nightingale, L. Patrizii, A. Peel, V. Popa, C. Porciani, D. Potter, P. Reimberg, G. Riccio, A. G. Sánchez,

D. Sapone, V. Scottez, E. Sefusatti, R. Teyssier, I. Tutusaus, C. Valieri, J. Valiviita, M. Viel, and H. Hildebrandt, "Euclid preparation: Xviii. the nisp photometric system," *Astronomy amp; Astrophysics* **662** (June, 2022) A92.

[298] Y. Rasera *et. al.*, "The RayGalGroupSims cosmological simulation suite for the study of relativistic effects: An application to lensing-matter clustering statistics," *Astron. Astrophys.* **661** (2022) A90, 2111.08745.

[299] S. Prunet, C. Pichon, D. Aubert, D. Pogosyan, R. Teyssier, and S. Gottloeber, "Initial conditions for large cosmological simulations," *The Astrophysical Journal Supplement Series* **178** (oct, 2008) 179.

[300] R. Teyssier, "Cosmological hydrodynamics with adaptive mesh refinement. A new high resolution code called RAMSES," **385** (Apr., 2002) 337–364, astro-ph/0111367.

[301] P. S. Behroozi, R. H. Wechsler, and H.-Y. Wu, "The Rockstar Phase-Space Temporal Halo Finder and the Velocity Offsets of Cluster Cores," *ApJ* **762** (2013) 109, 1110.4372.

[302] C. Carbone, M. Petkova, and K. Dolag, "DEMNUni: ISW, Rees-Sciama, and weak-lensing in the presence of massive neutrinos," *JCAP* **07** (2016) 034, 1605.02024.

[303] G. Parimbelli, C. Carbone, J. Bel, B. Bose, M. Calabrese, E. Carella, and M. Zennaro, "DEMNUni: comparing nonlinear power spectra prescriptions in the presence of massive neutrinos and dynamical dark energy," *JCAP* **11** (2022) 041, 2207.13677.

[304] E. Castorina, C. Carbone, J. Bel, E. Sefusatti, and K. Dolag, "DEMNUni: The clustering of large-scale structures in the presence of massive neutrinos," *JCAP* **07** (2015) 043, 1505.07148.

[305] M. Moresco *et. al.*, "The VIMOS Public Extragalactic Redshift Survey (VIPERS). Exploring the dependence of the three-point correlation function on stellar mass and luminosity at $0.5 < z < 1.1$," *A&A* **604** (2017) A133, 1603.08924.

[306] M. Zennaro, J. Bel, J. Dossett, C. Carbone, and L. Guzzo, "Cosmological constraints from galaxy clustering in the presence of massive neutrinos," *MNRAS* **477** (2018), no. 1 491–506, 1712.02886.

[307] R. Ruggeri, E. Castorina, C. Carbone, and E. Sefusatti, "DEMNUni: Massive neutrinos and the bispectrum of large scale structures," *JCAP* **03** (2018) 003, 1712.02334.

[308] J. Bel, A. Pezzotta, C. Carbone, E. Sefusatti, and L. Guzzo, "Accurate fitting functions for peculiar velocity spectra in standard and massive-neutrino cosmologies," *A&A* **622** (2019) A109, 1809.09338.

[309] G. Parimbelli, S. Anselmi, M. Viel, C. Carbone, F. Villaescusa-Navarro, P. S. Corasaniti, Y. Rasera, R. Sheth, G. D. Starkman, and I. Zehavi, "The effects of massive neutrinos on the linear point of the correlation function," *JCAP* **01** (2021) 009, 2007.10345.

[310] M. Guidi, A. Veropalumbo, E. Branchini, A. Eggemeier, and C. Carbone, "Modelling the next-to-leading order matter three-point correlation function using FFTLog," *JCAP* **08** (2023) 066, 2212.07382.

[311] P. Baratta, J. Bel, S. Gouyou Beauchamps, and C. Carbone, "COVMOS: a new Monte Carlo approach for galaxy clustering analysis," *A&A* **673** (2023) A1, 2211.13590.

[312] S. Gouyou Beauchamps, P. Baratta, S. Escoffier, W. Gillard, J. Bel, J. Bautista, and C. Carbone, "Cosmological inference including massive neutrinos from the matter power spectrum: biases induced by uncertainties in the covariance matrix," 2306.05988.

[313] M. Roncarelli, C. Carbone, and L. Moscardini, "The effect of massive neutrinos on the Sunyaev–Zel'dovich and X-ray observables of galaxy clusters," *MNRAS* **447** (2015), no. 2 1761–1773, 1409.4285.

[314] G. Fabbian, M. Calabrese, and C. Carbone, "CMB weak-lensing beyond the Born approximation: a numerical approach," *JCAP* **02** (2018) 050, 1702.03317.

[315] B. Hernández-Molinero, C. Carbone, R. Jimenez, and C. Peña Garay, "Cosmic Background Neutrinos Deflected by Gravity: DEMNUni Simulation Analysis," 2301.12430.

[316] C. D. Kreisch, A. Pisani, C. Carbone, J. Liu, A. J. Hawken, E. Massara, D. N. Spergel, and B. D. Wandelt, "Massive Neutrinos Leave Fingerprints on Cosmic Voids," *MNRAS* **488** (2019), no. 3 4413–4426, 1808.07464.

[317] N. Schuster, N. Hamaus, A. Pisani, C. Carbone, C. D. Kreisch, G. Pollina, and J. Weller, "The bias of cosmic voids in the presence of massive neutrinos," *JCAP* **12** (2019) 055, 1905.00436.

[318] G. Verza, A. Pisani, C. Carbone, N. Hamaus, and L. Guzzo, "The Void Size Function in Dynamical Dark Energy Cosmologies," *JCAP* **12** (2019) 040, 1906.00409.

[319] G. Verza, C. Carbone, and A. Renzi, "The Halo Bias inside Cosmic Voids," *ApJLett.* **940** (2022), no. 1 L16, 2207.04039.

[320] G. Verza, C. Carbone, A. Pisani, and A. Renzi, "DEMNUni: disentangling dark energy from massive neutrinos with the void size function," 2212.09740.

[321] P. Vielzeuf, M. Calabrese, C. Carbone, G. Fabbian, and C. Baccigalupi, "DEMNUni: the imprint of massive neutrinos on the cross-correlation between cosmic voids and CMB lensing," *JCAP* **08** (2023) 010, 2303.10048.

[322] V. Cuozzo, C. Carbone, M. Calabrese, E. Carella, and M. Migliaccio, "DEMNUni: cross-correlating the nonlinear ISWRS effect with CMB-lensing and galaxies in the presence of massive neutrinos," 2307.15711.

[323] V. Springel, "The Cosmological simulation code GADGET-2," *Mon. Not. Roy. Astron. Soc.* **364** (2005) 1105–1134, astro-ph/0505010.

[324] M. Viel, M. G. Haehnelt, and V. Springel, "The effect of neutrinos on the matter distribution as probed by the intergalactic medium," *JCAP* **10** (jun, 2010) 015–015.

[325] **Planck** Collaboration, P. A. R. Ade *et. al.*, "Planck 2013 results. XVI. Cosmological parameters," *A&A* **571** (2014) A16, 1303.5076.

[326] M. Cautun, E. Paillas, Y.-C. Cai, S. Bose, J. Armijo, B. Li, and N. Padilla, "The Santiago–Harvard–Edinburgh–Durham void comparison – I. SHEDding light on chameleon gravity tests," *MNRAS* **476** (2018), no. 3 3195–3217, 1710.01730.

[327] A. A. Meiksin, "The Physics of the Intergalactic Medium," *Rev. Mod. Phys.* **81** (2009) 1405–1469, 0711.3358.

[328] M. McQuinn, "The Evolution of the Intergalactic Medium," *Ann. Rev. Astron. Astrophys.* **54** (2016) 313–362, 1512.00086.

[329] **SDSS** Collaboration, P. McDonald *et. al.*, "The Lyman-alpha forest power spectrum from the Sloan Digital Sky Survey," *Astrophys. J. Suppl.* **163** (2006) 80–109, astro-ph/0405013.

[330] U. Seljak, A. Slosar, and P. McDonald, "Cosmological parameters from combining the lyman-alpha forest with cmb, galaxy clustering and sn constraints," *JCAP* **0610** (2006) 014, astro-ph/0604335.

[331] A. Arinyo-i Prats, J. Miralda-Escudé, M. Viel, and R. Cen, "The Non-Linear Power Spectrum of the Lyman Alpha Forest," *JCAP* **1512** (2015), no. 12 017, 1506.04519.

[332] M. Viel, G. D. Becker, J. S. Bolton, M. G. Haehnelt, M. Rauch, and W. L. W. Sargent, "How cold is cold dark matter? Small scales constraints from the flux power spectrum of the high-redshift Lyman-alpha forest," *Phys. Rev. Lett.* **100** (2008) 041304, 0709.0131.

[333] A. Boyarsky, J. Lesgourgues, O. Ruchayskiy, and M. Viel, "Lyman-alpha constraints on warm and on warm-plus-cold dark matter models," *JCAP* **05** (2009) 012, 0812.0010.

[334] M. Viel, G. D. Becker, J. S. Bolton, and M. G. Haehnelt, "Warm dark matter as a solution to the small scale crisis: New constraints from high redshift Lyman- forest data," *Phys. Rev.* **D88** (2013) 043502, 1306.2314.

[335] V. Iršič *et. al.*, "New Constraints on the free-streaming of warm dark matter from intermediate and small scale Lyman-α forest data," *Phys. Rev. D* **96** (2017), no. 2 023522, 1702.01764.

[336] A. Garzilli *et. al.*, "The Lyman-α forest as a diagnostic of the nature of the dark matter," *Mon. Not. Roy. Astron. Soc.* **489** (2019), no. 3 3456–3471, 1809.06585.

[337] N. Palanque-Delabrouille, C. Yèche, N. Schöneberg, J. Lesgourgues, M. Walther, S. Chabanier, and E. Armengaud, "Hints, neutrino bounds and WDM constraints from SDSS DR14 Lyman-α and Planck full-survey data," *JCAP* **04** (2020) 038, 1911.09073.

[338] E. Armengaud, N. Palanque-Delabrouille, C. Yèche, D. J. E. Marsh, and J. Baur, "Constraining the mass of light bosonic dark matter using SDSS Lyman-α forest," *Mon. Not. Roy. Astron. Soc.* **471** (2017), no. 4 4606–4614, 1703.09126.

[339] T. Kobayashi, R. Murgia, A. De Simone, V. Iršič, and M. Viel, "Lyman-α constraints on ultralight scalar dark matter: Implications for the early and late universe," *Phys. Rev. D* **96** (2017), no. 12 123514, 1708.00015.

[340] M. Nori, R. Murgia, V. Iršič, M. Baldi, and M. Viel, "Lyman α forest and non-linear structure characterization in Fuzzy Dark Matter cosmologies," *Mon. Not. Roy. Astron. Soc.* **482** (2019), no. 3 3227–3243, 1809.09619.

[341] V. Iršič, H. Xiao, and M. McQuinn, "Early structure formation constraints on the ultralight axion in the postinflation scenario," *Phys. Rev. D* **101** (2020), no. 12 123518, 1911.11150.

[342] K. K. Rogers and H. V. Peiris, "Strong Bound on Canonical Ultralight Axion Dark Matter from the Lyman-Alpha Forest," *Phys. Rev. Lett.* **126** (2021), no. 7 071302, 2007.12705.

[343] S. Bose, M. Vogelsberger, J. Zavala, C. Pfrommer, F.-Y. Cyr-Racine, S. Bohr, and T. Bringmann, "ETHOS – an Effective Theory of Structure Formation: detecting dark

matter interactions through the Lyman-α forest," *Mon. Not. Roy. Astron. Soc.* **487** (2019), no. 1 522–536, 1811.10630.

[344] M. Garny, T. Konstandin, L. Sagunski, and S. Tulin, "Lyman-α forest constraints on interacting dark sectors," *JCAP* **09** (2018) 011, 1805.12203.

[345] F. D'Eramo and A. Lenoci, "Lower mass bounds on FIMP dark matter produced via freeze-in," *JCAP* **10** (2021) 045, 2012.01446.

[346] K. K. Rogers, C. Dvorkin, and H. V. Peiris, "Limits on the Light Dark Matter–Proton Cross Section from Cosmic Large-Scale Structure," *Phys. Rev. Lett.* **128** (2022), no. 17 171301, 2111.10386.

[347] M. A. Buen-Abad, R. Essig, D. McKeen, and Y.-M. Zhong, "Cosmological constraints on dark matter interactions with ordinary matter," *Phys. Rept.* **961** (2022) 1–35, 2107.12377.

[348] D. Egana-Ugrinovic, R. Essig, D. Gift, and M. LoVerde, "The Cosmological Evolution of Self-interacting Dark Matter," *JCAP* **05** (2021) 013, 2102.06215.

[349] Q. Decant, J. Heisig, D. C. Hooper, and L. Lopez-Honorez, "Lyman-α constraints on freeze-in and superWIMPs," *JCAP* **03** (2022), no. 03 041, 2111.09321.

[350] D. C. Hooper and M. Lucca, "Hints of dark matter-neutrino interactions in Lyman-α data," *Phys. Rev. D* **105** (2022), no. 10 103504, 2110.04024.

[351] N. Afshordi, P. McDonald, and D. N. Spergel, "Primordial black holes as dark matter: The Power spectrum and evaporation of early structures," *Astrophys. J. Lett.* **594** (2003) L71–L74, astro-ph/0302035.

[352] L. Hui and N. Y. Gnedin, "Equation of state of the photoionized intergalactic medium," *Mon. Not. Roy. Astron. Soc.* **292** (1997) 27, astro-ph/9612232.

[353] M. Zaldarriaga, L. Hui, and M. Tegmark, "Constraints from the Lyman alpha forest power spectrum," *Astrophys. J.* **557** (2001) 519–526, astro-ph/0011559.

[354] J. S. Bolton, M. Viel, T. S. Kim, M. G. Haehnelt, and R. F. Carswell, "Possible evidence for an inverted temperature-density relation in the intergalactic medium from the flux distribution of the Lyman-alpha forest," *Mon. Not. Roy. Astron. Soc.* **386** (2008) 1131–1144, 0711.2064.

[355] J. S. Bolton and G. D. Becker, "Resolving the high redshift Lyman-alpha forest in smoothed particle hydrodynamics simulations," *Mon. Not. Roy. Astron. Soc.* **398** (2009) 26, 0906.2861.

[356] G. D. Becker, J. S. Bolton, M. G. Haehnelt, and W. L. W. Sargent, "Detection of Extended He II Reionization in the Temperature Evolution of the Intergalactic Medium," *Mon. Not. Roy. Astron. Soc.* **410** (2011) 1096, 1008.2622.

[357] G. D. Becker and J. S. Bolton, "New Measurements of the Ionizing Ultraviolet Background over $2 < z < 5$ and Implications for Hydrogen Reionization," *Mon. Not. Roy. Astron. Soc.* **436** (2013) 1023, 1307.2259.

[358] K.-G. Lee *et. al.*, "IGM Constraints from the SDSS-III/BOSS DR9 Lyα Forest Flux Probability Distribution Function," *Astrophys. J.* **799** (2015), no. 2 196, 1405.1072.

[359] E. Boera, G. D. Becker, J. S. Bolton, and F. Nasir, "Revealing Reionization with the Thermal History of the Intergalactic Medium: New Constraints from the Lyα Flux Power Spectrum," *Astrophys. J.* **872** (2019), no. 1 101, 1809.06980.

[360] M. Walther, J. Oñorbe, J. F. Hennawi, and Z. Lukić, "New Constraints on IGM Thermal Evolution from the Lyα Forest Power Spectrum," *Astrophys. J.* **872** (2019), no. 1 13, 1808.04367.

[361] P. Gaikwad, R. Srianand, M. G. Haehnelt, and T. R. Choudhury, "A consistent and robust measurement of the thermal state of the IGM at $2 \leq z \leq 4$ from a large sample of Ly α forest spectra: evidence for late and rapid He ii reionization," *Mon. Not. Roy. Astron. Soc.* **506** (2021), no. 3 4389–4412, 2009.00016.

[362] J. S. Bolton *et. al.*, "The Sherwood simulation suite: overview and data comparisons with the Lyman α forest at redshifts $2 \leq z \leq 5$," *Mon. Not. Roy. Astron. Soc.* **464** (2017), no. 1 897–914, 1605.03462.

[363] M. Leo, C. M. Baugh, B. Li, and S. Pascoli, "Nonlinear growth of structure in cosmologies with damped matter fluctuations," *JCAP* **08** (2018) 001, 1712.02742.

[364] S. Bohr, J. Zavala, F.-Y. Cyr-Racine, M. Vogelsberger, T. Bringmann, and C. Pfrommer, "ETHOS – an effective parametrization and classification for structure formation: the non-linear regime at $z \gtrsim 5$," *Mon. Not. Roy. Astron. Soc.* **498** (2020), no. 3 3403–3419, 2006.01842.

[365] G. Ballesteros, M. A. G. Garcia, and M. Pierre, "How warm are non-thermal relics? Lyman-α bounds on out-of-equilibrium dark matter," *JCAP* **03** (2021) 101, 2011.13458.

[366] S. Baumholzer and P. Schwaller, "Probing non-thermal light DM with structure formation and N_{eff}," *JCAP* **06** (2022), no. 06 013, 2112.03993.

[367] K. R. Dienes, F. Huang, J. Kost, S. Su, and B. Thomas, "Deciphering the archaeological record: Cosmological imprints of nonminimal dark sectors," *Phys. Rev. D* **101** (2020), no. 12 123511, 2001.02193.

[368] K. R. Dienes, F. Huang, J. Kost, B. Thomas, and H.-B. Yu, "Evaluating Lyman-α Constraints for General Dark-Matter Velocity Distributions: Multiple Scales and Cautionary Tales," 2112.09105.

[369] C. M. Vogel and K. N. Abazajian, "Entering the Era of Measuring Sub-Galactic Dark Matter Structure: Accurate Transfer Functions for Axino, Gravitino & Sterile Neutrino Thermal Warm Dark Matter," 2210.10753.

[370] A. Amon and G. Efstathiou, "A non-linear solution to the S_8 tension?," 2206.11794.

[371] R. Murgia, G. F. Abellán, and V. Poulin, "Early dark energy resolution to the Hubble tension in light of weak lensing surveys and lensing anomalies," *Phys. Rev. D* **103** (2021), no. 6 063502, 2009.10733.

[372] N. Schöneberg, G. F. Abellán, A. P. Sánchez, S. J. Witte, V. Poulin, and J. Lesgourgues, "The h_0 olympics: A fair ranking of proposed models," *Physics Reports* **984** (2022) 1–55, 2107.10291.

[373] M. Molaro, V. Iršič, J. S. Bolton, L. C. Keating, E. Puchwein, P. Gaikwad, M. G. Haehnelt, G. Kulkarni, and M. Viel, "The effect of inhomogeneous reionization on the Lyman α forest power spectrum at redshift z $>$ 4: implications for thermal parameter recovery," *Mon. Not. Roy. Astron. Soc.* **509** (2021), no. 4 6119–6137, 2109.06897.

[374] V. Springel, N. Yoshida, and S. D. M. White, "GADGET: A Code for collisionless and gasdynamical cosmological simulations," *New Astron.* **6** (2001) 79, astro-ph/0003162.

[375] M. Crocce, S. Pueblas, and R. Scoccimarro, "Transients from Initial Conditions in Cosmological Simulations," *Mon. Not. Roy. Astron. Soc.* **373** (2006) 369–381, astro-ph/0606505.

[376] C. Miller, A. L. Erickcek, and R. Murgia, "Constraining nonthermal dark matter's impact on the matter power spectrum," *Phys. Rev. D* **100** (2019), no. 12 123520, 1908.10369.

[377] **Planck Collaboration** Collaboration, P. A. R. Ade *et. al.*, "Planck 2015 results. XIII. Cosmological parameters," *Astron. Astrophys.* **594** (2016) A13, 1502.01589.

[378] N. Palanque-Delabrouille *et. al.*, "The one-dimensional Ly-alpha forest power spectrum from BOSS," *Astron. Astrophys.* **559** (2013) A85, 1306.5896.

[379] López, S., D´Odorico, V., Ellison, S. L., Becker, G. D., Christensen, L., Cupani, G., Denney, K. D., Pâris, I., Worseck, G., Berg, T. A. M., Cristiani, S., Dessauges-Zavadsky, M., Haehnelt, M., Hamann, F., Hennawi, J., Irsic, V., Kim, T.-S., López, P., Lund Saust, R., Ménard, B., Perrotta, S., Prochaska, J. X., Sánchez-Ramírez, R., Vestergaard, M., Viel, M., and Wisotzki, L., "Xq-100: A legacy survey of one hundred 3.5 5 quasars observed with vlt/x-shooter," *A&A* **594** (2016) A91.

[380] V. Iršič *et. al.*, "The Lyman α forest power spectrum from the XQ-100 Legacy Survey," *Mon. Not. Roy. Astron. Soc.* **466** (2017), no. 4 4332–4345, 1702.01761.

[381] S. Bird, K. K. Rogers, H. V. Peiris, L. Verde, A. Font-Ribera, and A. Pontzen, "An Emulator for the Lyman-alpha Forest," *JCAP* **02** (2019) 050, 1812.04654.

[382] K. K. Rogers, H. V. Peiris, A. Pontzen, S. Bird, L. Verde, and A. Font-Ribera, "Bayesian emulator optimisation for cosmology: application to the Lyman-alpha forest," *JCAP* **02** (2019) 031, 1812.04631.

[383] C. Pedersen, A. Font-Ribera, K. K. Rogers, P. McDonald, H. V. Peiris, A. Pontzen, and A. Slosar, "An emulator for the Lyman-α forest in beyond-ΛCDM cosmologies," *JCAP* **05** (2021) 033, 2011.15127.

[384] M. A. Fernandez, M.-F. Ho, and S. Bird, "A Multi-Fidelity Emulator for the Lyman-α Forest Flux Power Spectrum," 2207.06445.

[385] S. Goldstein, J. C. Hill, V. Iršič, and B. D. Sherwin, "Canonical Hubble-Tension-Resolving Early Dark Energy Cosmologies are Inconsistent with the Lyman-α Forest," 2303.00746.

[386] **Planck Collaboration** Collaboration, N. Aghanim *et. al.*, "Planck 2018 results. VIII. Gravitational lensing," 1807.06210.

[387] F. Beutler, C. Blake, M. Colless, D. H. Jones, L. Staveley-Smith, L. Campbell, Q. Parker, W. Saunders, and F. Watson, "The 6dF Galaxy Survey: Baryon Acoustic Oscillations and the Local Hubble Constant," *Mon. Not. Roy. Astron. Soc.* **416** (2011) 3017–3032, 1106.3366.

[388] A. J. Ross, L. Samushia, C. Howlett, W. J. Percival, A. Burden, and M. Manera, "The clustering of the SDSS DR7 main Galaxy sample – I. A 4 per cent distance measure at $z = 0.15$," *Mon. Not. Roy. Astron. Soc.* **449** (2015), no. 1 835–847, 1409.3242.

[389] **BOSS** Collaboration, S. Alam *et. al.*, "The clustering of galaxies in the completed SDSS-III Baryon Oscillation Spectroscopic Survey: cosmological analysis of the DR12

galaxy sample," *Mon. Not. Roy. Astron. Soc.* **470** (2017), no. 3 2617–2652, 1607.03155.

[390] V. de Sainte Agathe *et. al.*, "Baryon acoustic oscillations at z = 2.34 from the correlations of Lyα absorption in eBOSS DR14," *Astron. Astrophys.* **629** (2019) A85, 1904.03400.

[391] M. Blomqvist *et. al.*, "Baryon acoustic oscillations from the cross-correlation of Lyα absorption and quasars in eBOSS DR14," *Astron. Astrophys.* **629** (2019) A86, 1904.03430.

[392] D. M. Scolnic *et. al.*, "The Complete Light-curve Sample of Spectroscopically Confirmed SNe Ia from Pan-STARRS1 and Cosmological Constraints from the Combined Pantheon Sample," *Astrophys. J.* **859** (2018), no. 2 101, 1710.00845.

[393] A. Eggemeier, R. Scoccimarro, and R. E. Smith, "Bias Loop Corrections to the Galaxy Bispectrum," *Phys. Rev. D* **99** (2019), no. 12 123514, 1812.03208.

[394] S. Lee and K.-W. Ng, "Growth index with the exact analytic solution of sub-horizon scale linear perturbation for dark energy models with constant equation of state," *Phys. Lett. B* **688** (2010) 1–3, 0906.1643.

[395] G. D'Amico, Y. Donath, M. Lewandowski, L. Senatore, and P. Zhang, "The one-loop bispectrum of galaxies in redshift space from the Effective Field Theory of Large-Scale Structure," 2211.17130.

[396] R. Scoccimarro, "Redshift-space distortions, pairwise velocities and nonlinearities," *Phys. Rev.* **D70** (2004) 083007, astro-ph/0407214.

[397] M. Lewandowski, L. Senatore, F. Prada, C. Zhao, and C.-H. Chuang, "On the EFT of Large Scale Structures in Redshift Space," 1512.06831.

[398] J. M. Dickey, "The Weighted Likelihood Ratio, Linear Hypotheses on Normal Location Parameters," *The Annals of Mathematical Statistics* **42** (1971), no. 1 204 – 223.

[399] R. Trotta, "Applications of bayesian model selection to cosmological parameters," *Monthly Notices of the Royal Astronomical Society* **378** (June, 2007) 72–82.

[400] M. Umemura, A. Loeb, and E. L. Turner, "Early Cosmic Formation of Massive Black Holes," *The Astrophysical Journal* **419** (Dec, 1993) 459, astro-ph/9303004.

[401] D. Tseliakhovich and C. Hirata, "Relative velocity of dark matter and baryonic fluids and the formation of the first structures," *Phys. Rev. D* **82** (Oct, 2010) 083520.

[402] C. Dvorkin, K. Blum, and M. Kamionkowski, "Constraining dark matter-baryon scattering with linear cosmology," *Phys. Rev. D* **89** (Jan, 2014) 023519.

[403] J. R. Chisholm, "Clustering of primordial black holes: Basic results," *Physical Review D* **73** (Apr., 2006).

[404] J. R. Chisholm, "Clustering of primordial black holes. ii. evolution of bound systems," *Physical Review D* **84** (Dec., 2011).

[405] E. Agol and M. Kamionkowski, "X-rays from isolated black holes in the Milky Way," *Monthly Notices of the Royal Astronomical Society* **334** (08, 2002) 553–562.